SEARCHES FOR SUPERSYMMETRIC PARTICLES IN EVENTS WITH TWO OPPOSITE-SIGN SAME-FLAVOR LEPTONS, JETS, AND LARGE MISSING TRANSVERSE ENERGY

BY

RUO YU SHANG

DISSERTATION

Submitted in partial fulfillment of the requirements
for the degree of Doctor of Philosophy in Physics
in the Graduate College of the
University of Illinois at Urbana-Champaign, 2018

Urbana, Illinois

Doctoral Committee:

Professor Mark Neubauer, Chair
Professor Benjamin Hooberman, Director of Research
Professor Brian Fields
Assistant Professor Jessie Shelton

ABSTRACT

This thesis presents the search for Supersymmetric particles, in both strong and electroweak productions, in the same-flavor opposite-sign dilepton channel. The SUSY analyses usually require large missing transverse energy $E_{\mathrm{T}}^{\mathrm{miss}}$ for the presence of invisible LSPs. One of the most difficult background processes to estimate in these searches is due to artificial *etmiss* from hadronic object (jet) energy mismeasurements, which are difficult to model in simulation due to the complexity of detector defects. One major focus of this thesis is to estimate such mismeasurements in the crucial background originating from SM production of Z boson in association with jets ($Z+\text{jets}$), where Z decays to two leptons. In addition to the jet mismeasurement, the artificial $E_{\mathrm{T}}^{\mathrm{miss}}$ in $Z+\text{jets}$ events also convolves the mismeasurement of lepton energy. A data-driven method is developed using photon data ($\gamma+\text{jets}$) events to model the jet mismeasurements in $Z+\text{jets}$ events. To model the lepton resolution, I developed a data-driven deconvolution method, which deconvolves jet and lepton resolutions in a control region, to derive a resolution correction for the photons. The results of this thesis probe the gluino masses as large as ~ 2 TeV, and gaugino masses as large as ~ 600 GeV. However, the analyses are not yet sensitive to the parameter space of light electroweak gauginos. A new background method and a new analysis variable are also proposed in this thesis to improve the sensitivity to the light higgsinos, which are crucial for the SUSY solution to the hierarchy problem.

To my parents and my sister, for their love and support.

ACKNOWLEDGMENTS

Foremost, I would like to express my sincere gratitude to my advisor Prof. Ben Hooberman for the continuous support of my Ph.D study and job applications, for his patience, motivation, enthusiasm, and immense knowledge. Prof. Hooberman has been always flexible and allows me to pursue my creativities, even when sometimes these ideas are not directly related to his research projects.. I enjoyed my Ph.D life working with Prof. Hooberman, and I am very glad that we produced many good scientific results.

I thank my another advisor, Prof. Tony Liss, who continues guiding me with my study after he left Illinois. With Prof. Tony's guidance, I establish my confidence in science research.

I would also like to thank Dr. Zach Marshall, Dr. Emma Kuwertz, and Dr. Jon Long for their help in developing the photon template method. I especially thank Dr. Marshall for his supports and advises on the career in science and his time and energy on providing me feedback on some of my original ideas on particle physics.

TABLE OF CONTENTS

LIST OF TABLES

LIST OF FIGURES

CHAPTER 1

SEARCH FOR SUPERSYMMETRY: INTRODUCTION

1.1 The Higgs boson and the hierarchy problem

High energy physics has entered a new era since the discovery of the Higgs boson in 2012. The Higgs boson was the last element in the Standard model to be found, and the discovery of which is an important milestone in the history of science. The field of Higgs boson explains how elementary fermions and gauge bosons, whose intrinsic masses were predicted to be zero in the Standard Model, to acquire their masses. With the complement of the Higgs boson, the Standard Model provides excellent descriptions of experimental phenomena that we have observed in the laboratories. Nevertheless, there are still deeper mysteries in the Universe which the Standard Model cannot answer. One of these mysteries is the mass of Higgs boson itself. Since its discovery, the mass of Higgs boson has been carefully measured to be 125.09 ± 0.24 GeV by dozens of analyses using LHC data. However, according to the quantum field theory, this observed mass should receive corrections from particles produced in the quantum fluctuations of the vacuum, which are 16 orders of magnitude larger than the measured value. The disappearance of the enormous quantum corrections is a puzzle called 'hierarchy problem' for particle physicists to solve. To understand why the Higgs boson is needed in the Standard Model and why its mass is so problematic, we will review the basics of these problems and how the theory of supersymmetry can provide an answer to the hierarchy problem.

1.2 The gauge theory of fields

The Standard Model, which describes the electroweak and strong interactons, is built on the concept of 'gauge invariance'. The concept of gauge invariance originated from the classical theory of electrodynamics, in which the electromagnetic force is described by a set of Maxwell's equations. The solutions of the observable forces in the Maxwell equations have the following forms

$$\vec{B} = \vec{\nabla} \times \vec{A} \tag{1.1}$$

$$\vec{E} = -\vec{\nabla}\Phi - \partial_t \vec{A}. \tag{1.2}$$

It was then discovered that different forms of the potentials $\vec{A}$ and Φ could result in the same observable force, if they follow the transformation

$$\vec{A} \to \vec{A}_0 + \vec{\nabla}\chi \tag{1.3}$$

$$\Phi \to \Phi_0 - \partial_t \chi \tag{1.4}$$

where χ is a scalar function known as the gauge function. Furthermore, the relativistic wave equation for a spin 0, charged particle in the presence of an electromagnetic field is written as

$$(\partial^\mu + ieA^\mu)(\partial_\mu + ieA_\mu)\phi = m^2\phi \tag{1.5}$$

where m is the mass of the particle, and $A^\mu = (\Phi, \vec{A})$ is the 4-vector electromagnetic potential. This equation is also unchanged under the transformations of

$$A^\mu \to A_0^\mu - \partial^\mu \chi \tag{1.6}$$

and

$$\phi \to \phi_0 exp(ie\chi). \tag{1.7}$$

The gauge invariance is then recognized as a basic principle, and in electrodynamics the gauge invariance is connected to the fundamental law of the conservation of electromagnetic current (or conservation of charge in general).

1.3 The masses of particles

In the field theory, the wave equation is derived from a Lagrangian density $\mathcal{L}$ (or just Lagrangian) by following the principle of least action. In quantum electrodynamics (QED), the Lagrangian for a photon field is

$$\mathcal{L}_\gamma = -\frac{1}{4}F_{\mu\nu}F^{\mu\nu} + m_\gamma^2 A_\mu A^\mu \tag{1.8}$$

where $F^{\mu\nu} = \partial^\mu A^\nu - \partial^\nu A^\mu$ is the EM field tensor. When the principle of gauge invariance is imposed on the Lagrangian, it results in a consequence that a mass term for the EM field is forbidden:

$$m_\gamma^2 A_\mu A^\mu(\text{under a gauge transform}) \rightarrow \mathrm{m}_\gamma^2(\mathrm{A}_\mu+\frac{1}{\mathrm{e}}\partial_\mu\alpha)(\mathrm{A}^\mu+\frac{1}{\mathrm{e}}\partial^\mu\alpha) \neq \mathrm{m}_\gamma^2\mathrm{A}_\mu\mathrm{A}^\mu. \tag{1.9}$$

This result implies that all force carriers (photons, W and Z bosons) in the Standard Model are massless. While this is true for photons, the result is problematic for W and Z bosons, which have masses of 80.385 ± 0.015 GeV and 91.1876 ± 0.0021 GeV respectively. Furthermore, it is also forbidden to have massive fermions, which would have a mass term like this:

$$m_f^2\bar{\psi}\psi = m\left[\bar{\psi}_R\psi_L + \bar{\psi}_L\psi_R\right] \tag{1.10}$$

where $\psi_L = (e_L, \nu_L)$ is an isospin doublet and $\psi_R = (e_R, 0)$ is an isospin singlet. Since ψ_L and ψ_R transform differently under rotations:

$$\psi_L \rightarrow \psi_L^0 exp(i\alpha(x)T + i\beta(x)Y) \tag{1.11}$$

$$\psi_R \rightarrow \psi_R^0 exp(i\beta(x)Y) \tag{1.12}$$

the term $m_f^2\bar{\psi}\psi$ is not gauge invariant.

1.4 The Higgs mechanism and the Yukawa coupling

The solution to the problem of the gauge boson masses is to introduce a new complex scalar field $\phi = \frac{1}{\sqrt{2}}(\phi_1 + i\phi_2)$ to the Lagrangian, which becomes

$$\mathcal{L} = -\frac{1}{4}F_{\mu\nu}F^{\mu\nu} + (D_\mu\phi)^*(D^\mu\phi) - V(\phi) \tag{1.13}$$

with $D^\mu = \partial^\mu + ieA^\mu$ and $V = \mu^2(\phi^*\phi) + \lambda(\phi^*\phi)^2$. This Lagrangian is gauge invariant. Expanding the Lagrangian further, we find

$$(D_\mu\phi)^*(D^\mu\phi) = (\partial_\mu\phi)^2 + e^2 A_\mu^2 \phi^2 + \cdots . \tag{1.14}$$

When $\mu^2 < 0$, this potential V creates an infinite number of vacuum of located at

$$\sqrt{\phi_1^2 + \phi_2^2} = \sqrt{\frac{-\mu^2}{\lambda}} = v. \tag{1.15}$$

We can define a small perturbation field h around the vacuum as

$$\phi = \frac{1}{\sqrt{2}}(\phi_1 + i\phi_2) = \frac{1}{\sqrt{2}}(v + h + i\xi) \tag{1.16}$$

and carefully choose a specific gauge $\alpha = \xi/v$ (the local gauge symmetry is broken), so that

$$\phi \to \phi e^{-i\xi/v} = \frac{1}{\sqrt{2}}(v + h + i\xi)e^{-i\xi/v} = \frac{1}{\sqrt{2}}(v + h)e^{i\xi/v}e^{-i\xi/v} = \frac{1}{\sqrt{2}}(v + h). \tag{1.17}$$

Here two things happened: (1) a new field h (Higgs field) is introduced, and (2) the ξ field (Goldstone field) vanishes when the gauge $\alpha = \xi/v$ is chosen. Then we plug $\phi = v + h$ back in the Lagrangian, the Lagrangian can be written as

$$\mathcal{L} = -\frac{1}{4}F_{\mu\nu}F^{\mu\nu} + \frac{1}{2}e^2 v^2 A_\mu^2 + \frac{1}{2}(\partial_\mu h)^2 - \lambda v^2 h^2 + (\text{interactions}). \tag{1.18}$$

By introducing a massive Higgs boson field h with a broken symmetry potential, the gauge boson acquires a mass of ev. Fermions also acquire their masses by interacting with the ϕ field through the Yukawa coupling

$$\mathcal{L}_{\text{Yukawa}} = -\lambda_f(\bar{\psi}_L\phi\psi_R + \bar{\psi}_R\phi\psi_L) \tag{1.19}$$

which is gauge invariant under rotations. For example, a lepton will acquire a mass if the ϕ-doublet has a non-zero expectation value $\phi_0 = \begin{pmatrix} 0 & v + h \end{pmatrix}$.

We expand the Yukawa coupling term for a lepton as

$$\mathcal{L}_{\text{Yukawa}} = -\frac{\lambda_e}{\sqrt{2}}\left[\begin{pmatrix}\bar{\nu} & \bar{e}\end{pmatrix}_L \begin{pmatrix}0 \\ v+h\end{pmatrix} e_R + \bar{e}_R \begin{pmatrix}0 & v+h\end{pmatrix} \begin{pmatrix}\nu \\ e\end{pmatrix}_L\right] \tag{1.20}$$

$$= -\frac{\lambda_e}{\sqrt{2}}(v+h)(\bar{e}_L e_R + \bar{e}_R e_L) = -\frac{\lambda_e}{\sqrt{2}}(v+h)\bar{e}e \tag{1.21}$$

where $\lambda_e v/\sqrt{2}$ can be understood as the lepton mass and $\lambda_e h/\sqrt{2}$ as the interaction coupling between the lepton and the Higgs field. Note that the lepton-higgs coupling is proportional to the mass of the lepton. The Higgs field $\phi = \begin{pmatrix}0 & v+h\end{pmatrix}$ gives masses to electrons and 'down' type quarks. To give masses to neutrinos and 'up' type quarks, we need another Higgs field $\tilde{\phi}^c = -\begin{pmatrix}v+h & 0\end{pmatrix}$, which is paired with ϕ to form a complex Higgs doublet in the Standard Model.

1.5 The divergence of quantum loop corrections

While fermions and gauge bosons acquire masses through their couplings with the Higgs boson, the Higgs also receives mass corrections from the couplings with fermions and gauge bosons. For example, a quantum loop of the top quark field can contribute to the Higgs mass term ϕ^2 through the diagram in Figure 1.1. An one-loop diagram integral is quadratically divergent and is proportional to

$$I_1 = \int \frac{d^4p}{(2\pi)^4}\frac{1}{p^2} \tag{1.22}$$

where p is a four momentum. The total quadratic divergence corrections that a Higgs field receives are from gauge bosons, fermions, and the Higgs itself. This quadratic divergence is confined if we choose a cut-off value Λ, the kinematic region beyond which is no longer applicable for the electroweak theory, and $I_1 \propto \Lambda^2$. With this cut-off, the one-loop mass correction to the Higgs mass is proportional to

$$(\lambda_{\text{H}} + \frac{1}{8}g_1^2 + \frac{3}{8}g_2^2 - \lambda_{\text{f}}^2)\Lambda^2 \tag{1.23}$$

where λ_{H} is the Higgs self-coupling constant, g_1 and g_2 are $U(1)$ and $SU(2)$ gauge couplings, and λ_{f} is the Yukawa coupling between Higgs and fermion.

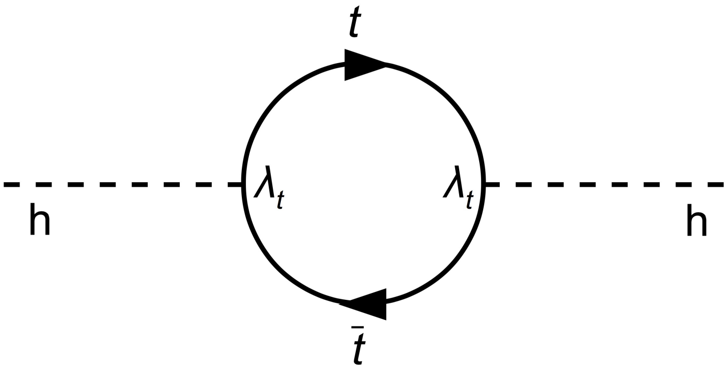

Figure 1.1: The mass of the Higgs boson receives corrections from quantum fluctuations of a fermion field.

Using an expression in terms of particle masses, the one-loop correction is proportional to

$$(m_{\mathrm{H}}^2 + 2m_{\mathrm{W}}^2 + m_{\mathrm{Z}}^2 - 4\sum m_{\mathrm{f}}^2)\Lambda^2. \tag{1.24}$$

The corrections from fermions are large (which come mainly from top quarks). If Λ is chosen to be at the Planck scale, it is unnatural for the Higgs mass to be around electroweak scale (a few hundred GeV). The question about why the mass of Higgs boson is much smaller than the Planck scale is referred as the hierarchy problem.

1.6 The theory of Supersymmetry

The theory of supersymmetry (SUSY) is the most popular solution to the hierarchy problem, which states the existence of superpartners of each SM field, whose spins differ from the SM field by 1/2 unit. Since fermions and bosons contribute to the quantum correctons of Higgs mass with opposite magnitudes, the quadratic divergences would be cancelled if the superpartners and the SM field have the similar masses, and leave us with the radiative corrections $\propto \log(\Lambda/m_{\mathrm{EW}})$ to the Higgs mass, which increase slowly with kinematic scale.

In the minimal supersymmetric extension to the Standard Model (MSSM), the superpartners are only different from their corresponding SM partners by 1/2 unit of spin, otherwise they have the same properties and quantum numbers. There are scalar quarks (squark $\tilde{q}$) and scalar leptons (sleptons $\tilde{l}$ and $\tilde{\nu}$), which are superpartners of quarks and leptons. There are fermionic gauginos such as gluinos, which are superpartners of SM gauge boson gluons. The MSSM has two Higgs doublets instead of one doublet for 'up' and 'down'-type quarks and leptons. The superprtners of the Higgs doublets are higgsinos. The charged higgsinos and electroweak gauginos are mixed to form the charginos ($\tilde{\chi}^{\pm}$), the neutral higgsinos and gauginos are mixed to form neutralinos ($\tilde{\chi}^0$).

However, we know that Supersymmetry is also broken in someway, and the masses of a SM field and a superpartner are not equal, otherwise we would have observed superpartners long ago. The breaking mechanism and scale of Supersymmetry determine the mass spectrum of SUSY particles. Although the SUSY breaking is unclear to us, we believe that naturalness is the key motivation for SUSY to solve the hierarchy problem, which also imposes constraints on some of SUSY particles. As it is pointed out in [3], the naturalness requirement is summarized by the following relation in MSSM,

$$-\frac{m_Z^2}{2} = \mid \mu \mid^2 + m_{H_u}^2. \tag{1.25}$$

Equation 1.25 ensures that the quantum corrections that Higgs bosons receive are not sensitive to the cut-off value Λ, and it also provides a guideline to the mass spectrum of Natural SUSY. In particular, the masses of higgsinos are controlled by μ and thus cannot be too far away from m_Z, otherwise Equation 1.25 will have to be fine-tuned. The masses of stop quarks and gluinos, which contribute to m_{H_u} through one-loop and two-loop diagrams, also cannot to be too heavy. Furthermore, the phenomenology of SUSY also depends on whether the R-parity $R = (-1)^{3(B-L)+2S}$, where B and L are baryon and lepton numbers and S is spin, is violated or not. If R-parity is violated, it would imply either baryon or lepton number is violated. If R-parity is conserved, the lightest SUSY particle (LSP) is often assumed to be stable and a weakly interacting massive particle, which makes SUSY an ideal solution to dark matter.

1.7 The experimental results on searches for supersymmetry

Prior to LHC, the lower limits on squark masses are set by the Tevatron experiments to be > 310 GeV for all squarks and > 390 GeV in the scenario with $m_{\tilde{q}} = m_{\tilde{g}}$ [4, 5]. Using the LHC Run-1 8 TeV data, ATLAS and CMS experiments further extended the squark mass limit to 1300 GeV for all squarks and 1700 GeV for the case of $m_{\tilde{q}} = m_{\tilde{g}}$. The lower limits on chargino and neutralino masses are also set to be as large as 420 GeV in the $\tilde{\chi}_2^0 \tilde{\chi}_1^\pm$ pair production model via W/Z decay channels by Run-1 ATLAS and CMS data [6, 7].

The LHC 13 TeV Run-2 data is expected to provide more comprehensive limits on the SUSY particle masses. In this thesis, we will review the experiment setup of the LHC machine and the ATLAS detector. We will discuss the background estimation methods in the events with two leptons and multiple jets and large missing transverse energy. Finally, we will discuss the results of the searches on gluinos and squarks in strong productions, as well as charginos and neutralinos in elecroweak productions, using 13 TeV data collected at the ATLAS detector.

CHAPTER 2

THE LHC AND THE ATLAS DETECTOR

2.1 The Large Hadron Collider

The Large Hadron Collider (LHC) is a superconducting hadron accelerator and collider based at European Organization for Nuclear Research (CERN) in Switzerland. The LHC is the most powerful machine that produces proton collisions at highest energy and luminosity by far. The LHC is designed to collide protons at a center mass energy of 14 TeV to study the physics at the smallest scale and the conditions at the earliest moment of the Universe.

As shown in Figure 2.1, the LHC is hosted in a tunnel that previously hosted the Large Electron Positron experiment (LEP). The LHC is a circular collider with a circumference of 26.7 km. The circular collider has two rings, which conduct two counter-rotating proton beams. The LHC is the lastest part of a large chain of accelerators at CERN. The acceleration begins at LINAC 2, a linear accelerator that uses radiofrequency cavities to accelerate charged particles and brings proton energy to 50 MeV. Then the proton beam is directed to the circular Booster (PSB), where the protons are accelerated to 1.4 GeV. At the Proton Synchrotron (PS), which is the CERN's first synchrotron, the proton beam reaches 26 GeV in energy and then sequentially enters the Super Proton Synchrotron (SPS) for an energy boost to 450 GeV before entering LHC. After SPS, the proton beam is split into two counter-direction beams in bunches to LHC, where the protons are accelerated for about 20 minutes to reach the nominal energy of 7 TeV each beam.

During the acceleration, to avoid collisions with air molecules, these beam pipes are kept in an ultrahigh vacuum of 10^{-13} atm when accelerating protons. A total of 9593 magnets, including dipole, quadrupole, and sextupole magnets, are used to direct the circulation of the proton beams. These magnets are superconducting and are maintained at a temperature of 1.9 K using

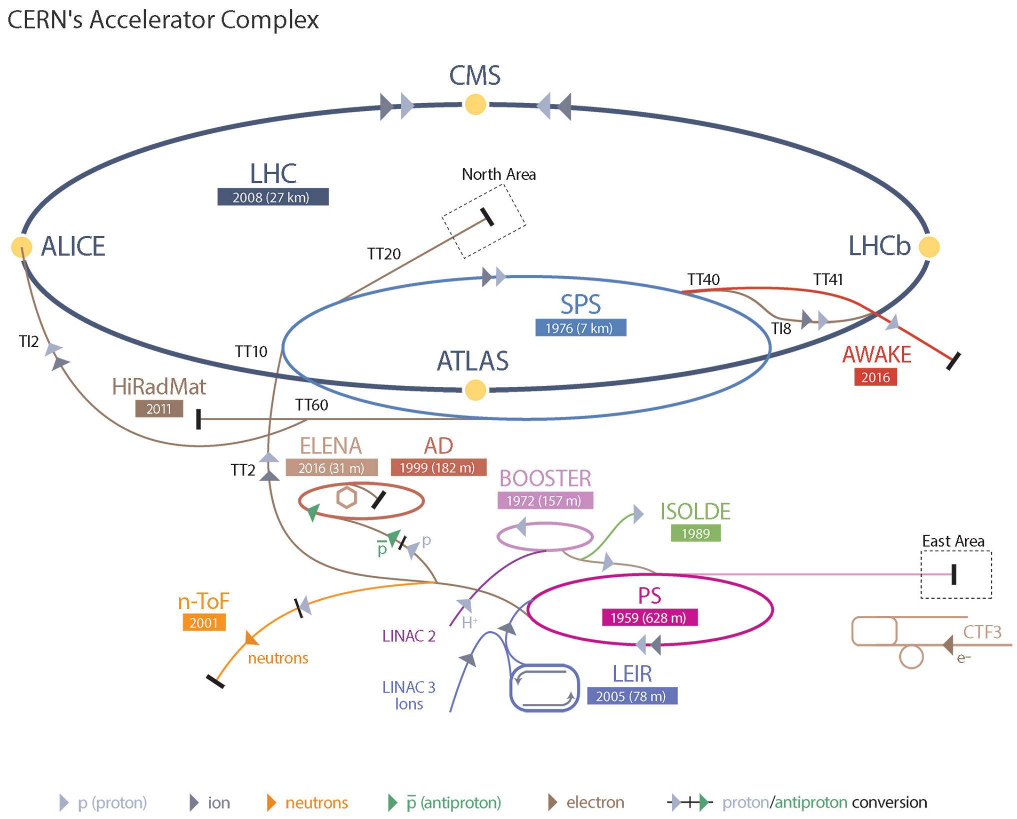

Figure 2.1: The CERN accelerator complex. The LHC is hosted in a 26.7 km tunnel and is the lastest part of the CERN accelerator chain, which includes privious accelerators, LINAC 2, PSB, PS, and SPS.

superfluid helium.

To keep the accelerated protons in the 26.7 km long vacuum tubes, 1232 superconducting dipole magnets are used to generate an 8.33 T magnetic field that bends the proton beams around the trajectory. The LHC dipole magnets are made of two sets of coils using niobium-titanium (NbTi) cables (see Figure 2.2), which become superconducting at temperatures below 10 K. A magnet field of 8.33 T is generated when a current of 11850 A flows in these coils, to bend the proton beams into the 26.7 km ring.

In addition to the dipole magnets that bend the proton beams in the LHC rings, there are 392 quadrupole magnets are used to bring the proton beams together at the interaction points (IPs), where the proton-proton collisions take place. These quadrupole magnets, as illustrated in Figure 2.3, are placed near IPs to adjust the proton beam focus. They squeeze the cross-section of

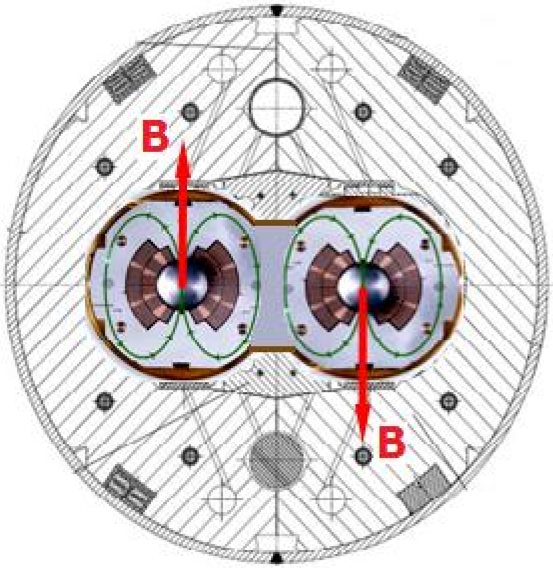

Figure 2.2: This is cross-section of an LHC dipole magnet. The LHC dipole magnets create magnetic fields on the proton beam pipes. The magnet fields are applied in opposite directions to the two pipes to make the two proton beams running in counter-direction.

the proton beams to increase the proton density and maximize the collision rate at IPs.

There are four interaction points (IPs) around the LHC, where the two LHC rings intersect and accelerated particles collide. At these IPs, four particle detectors are installed to record the moments of the particle collisions. The A Toroidal LHC ApparatuS (ATLAS) detector at IP1 and the Compact Muon Solenoid (CMS) detector at IP5 are general-purpose detectors, designed to perform standard model physics measurements, discover and measure Higgs boson properties, and probe new physics with the full potential of the LHC energy. The A Large Ion Collider Experiment (ALICE) and the Large Hadron Collider beauty (LHCb) are specialized detectors, built to study heavy ion physics and b-quark physics, respectively.

2.2 The ATLAS detector

The ATLAS detector has a dimension of 25 m high, 44 m long, and 7000 tonnes weight. The ATLAS detector is installed roughly 100 m under ground surface at the LHC IP1. The ATLAS detector has four layers of subdetectors

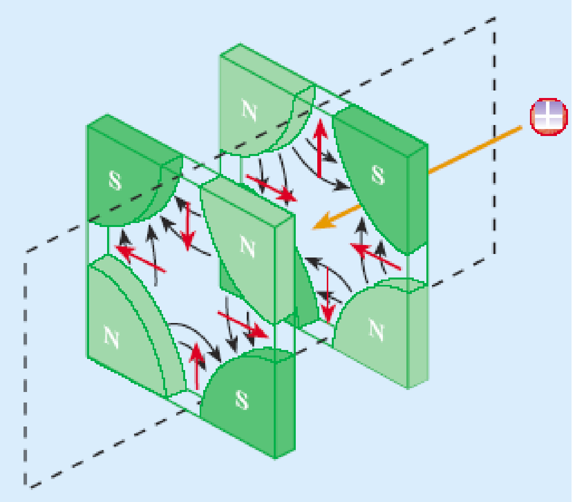

Figure 2.3: The LHC quadrupole (and multipole) magnets are used to adjust the focus of the proton beams. This diagram demonstrates how the magnets control the proton beams when the beam coming from the right. The first quadrupole magnet controls of the width of the beam, and the second magnet controls the height of the beam. The two quadrupoles working together to squeeze the proton beam to increase the proton density and maximize the collision rate at the interaction points.

that cover the beam pipe as shown in Figure 2.4. The inner detector (ID) is the innermost subdetector that provides information of charged particle trajectories. The electromagnetic and hadronic calorimeters are the second layer subdetectors that measure the energy deposits of electrons, photons, and hadrons. The outermost subdetector is the muon spectrometer (MS), which records the trajectories of muons. The ATLAS detector has a magnet system to bend charged particles in the ID and MS detectors for momentum measurement and charge identification. It also has a trigger and data acquisition (TDAQ) system to select and process interesting collision events.

2.2.1 Magnet system

The ATLAS detector has 4 superconducting magnets as shown in Figure 2.5. A solenoid magnet, which surrounds the inner detector, provides an axial magnetic field of 2 T to bend trajectories of charged particles in the inner detector and allows the measurement of the momenta and charges of these particles. Three toroid magnets (one for barrel and two for endcaps), which consist of eight coils each, are installed between the calorimeters and the

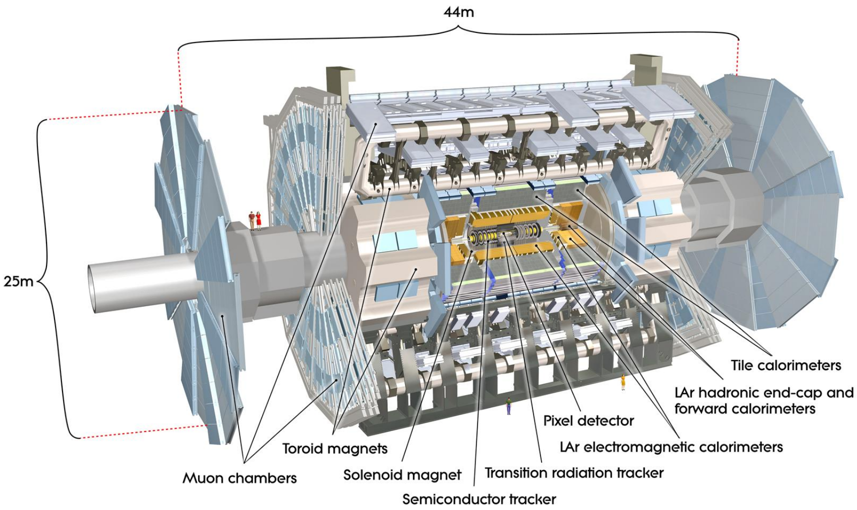

Figure 2.4: The ATLAS detector is composed of an inner detector that records the tracjectories of charged particles, a calorimeter that measures energy deposits of particles, and a muon spectrometer that measures the momenta of muons.

muon spectrometer. These toroids provide toroidal magnetic fields of 0.5 T in the barrel and 1 T in the endcaps to bend the trajectories of muons in the muon spectrometer.

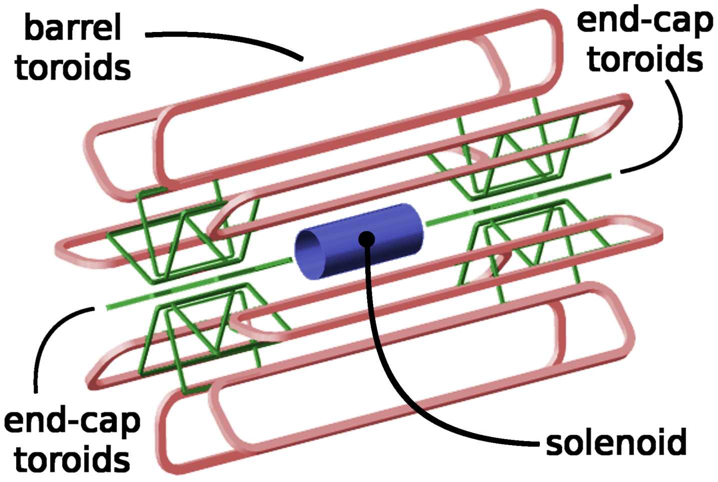

Figure 2.5: The magnet system of the ATLAS detector consists of one solenoid for ID and three toroids for MS.

2.2.2 Inner detector

The inner detector is a subdetector of the ATLAS that is placed closest to the interaction point to provide precise track momentum resolution and vertex reconstruction resolution. The inner detector consists of three subdetectors: a Pixel detector, a Semiconductor Tracker (SCT), and a Transition Radiation Tracker (TRT), as shown in Figure 2.6. A new subdetector, Insertable Barrel Layer (IBL) is installed during the long shutdown in 2012-2015. These subdetectors combined together offer fine detector granularity to resolution charged particle tracks in a high luminosity environment.

Pixel detector

The Pixel detector is a subdetector of ATLAS that is placed most close to the interaction point with only 5 cm away from the beam pipe. The pixel detector has three plus one cylindrical layers of pixels in the barrel region and three disks of pixels in each of the endcaps. The radius of the three cylindrical layers are 50.5 mm, 88.5 mm and 122.5 mm respectively. The fourth cylindrical layer, the Insertable b-layer or IBL, has a radius of 33.3 mm and was installed during LS1 and started operating during Run 2 data taking. The pixel detector provides a coverage of $|\eta| < 2.5$. A total of 1744 rectangular pixel modules, each has an area of $16.4 \times 60.8\text{mm}^2$ and about 47000 pixels, form the pixel layers and disks. These pixel modules are wired to more than 80 million readout channels, and the smallest size of the pixels is $50 \times 400 \mu m^2$ to provide a fine resolution of $14 \times 115 \mu m^2$. When a charged particle traveling through a pixel sensor, the atoms in the silicon are ionized, and the free electrons are collected by the readout channels to form a signal current. The pixel detector is responsible for the precision reconstruction of vertices, including the primary vertices of hard scattering and secondary vertices from heavy flavor meson decays.

Semiconductor Tracker

The semiconductor tracker (SCT) is the second layer detector of ATLAS that uses silicon microstrip sensors to record the trajectories of charged particles with a resolution along the strip length. The SCT detector has 4088 two-sided modules of strip sensors placed at a stereo angle of 40 mrad and arranged in four cylindrical layers in the barrel and nine disks in each endcap. In total SCT has an area of 60m^2 of silicon and 6 million readout channels. The readout strips are placed every 80 μm on the silicon, which allow a resolution of charged particle position of 17 μm in $R-\phi$ and 580 μm in z direction per layer.

Transition Radiation Tracker

The Transition Radiation Tracker (TRT) is the outermost layer of the inner detector. The TRT is composed of 250000 straw tubes (4 mm in diameter, 144 cm in length) filled with a gas mixture of 70% Xe, 27% CO2 and 3% O2. When a charged particle traveling through these gas tubes, transition radiation photons will be created along the path of the charged particle and excite more electrons from the gas molecules, which are then collected by readout channels to form a signal current. The amount of transition radiation photons is determined by the mass of the charged particle, which means the TRT has the ability to discriminate electrons and charged pions. Because of the size of the gas tubes, the TRT has an intrinsic accuracy of 130 μm per straw. Although the TRT does not provide high accuracy, the TRT has a large volume with larger numbers of measurements and longer radial baseline (563 mm to 1066 mm) compared to the silicon detectors, which allows the TRT to provide a significant contribution to the charged particle momentum measurement.

2.2.3 Calorimeters

The ATLAS calorimeter system consists of several electromagnetic and hadronic detectors. These calorimeters surround the inner detector and the solenoid magnet as shown in Figure 2.7. A barrel EM calorimeter (EMB), an end-cap EM calorimeter (EMEC), and a hadronic calorimeter (HEC) form the innermost layer of the calorimeter system. A forward calorimeter (FCal) covers the forward region that is closest to the beam pipe. The out layer of the calorimeter system is the TileCal hadronic calorimeter with one central barrel and two extended barrels on each side.

The ATLAS calorimeters provide both energy and topology measurements of electrons, photons, charged and neutral pions, and other hadrons, over a range of $|\eta| < 4.9$. In the $|\eta|$ range that is covered by the inner detector, the EM calorimeters are designed with higher granularity to provide precision position measurements of electron and photons. In the rest of region the calorimeters are designed with lower granularity but sufficient performance for jet energy reconstruction and missing transverse energy measurement.

The ATLAS calorimeters are composed of alternating layers of sensitive medium and layers of dense absorber medium. The ATLAS EM calorimeters use liquid argon (LAr) as the sensitive medium and lead plates as the absorber, and the TileCal uses scintillator tiles as sensitive medium and steel plates as the absorber. Particles passing through the absorber material lose their energy by interacting with the nucleons in the absorber and developing particle cascades (showers). These energy deposits then generate a signal whose strength is proportional to the energy deposits in the sensitive medium via ionization or scintillation.

Electromagnetic calorimeters

The EM calorimeters use liquid argon as the sensitive medium and lead plates as the absorber and are designed using accordion-shaped geometry. The EM calorimeter system is divided into a central barrel (EMB) and two end-caps (EMEC) to provide a $|\eta|$ coverage up to 3.2. The EMB provides a coverage of $|\eta| < 1.475$, and the EMEC has an outer wheel covering $1.375 < |\eta| < 2.5$ and an inner wheel covering $2.5 < |\eta| < 3.2$. The active depth of the EMB is ≥ 22 radiation length (X_0), and the depth of the EMEC is $> 24X_0$. A presampler is installed in the region of $|\eta| < 1.8$ in between inner detector and the EM calorimeters to measure the energy lost in the upstream material (superconducting coil, inner detector, etc.). The active depth of the presampler is $0.08X_0$ in the region of $|\eta| < 1.475$ and $0.03X_0$ in the region of $1.5 < |\eta| < 1.8$.

The EM calorimeter is segmented into individual readout elements (cells) laterally and longitudinally as shown in Figure 2.8. The central region ($|\eta < 2.5|$) of the calorimeter is designed for precision measurements, and the calorimeter is segmented longitudinally into three layers. The first layer (closest to the beam pipe) is finely segmented into cells of the size of $0.003 \times$

$0.1(\Delta\eta \times \Delta\phi)$ to achieve high granularity and has an active depth of $6X_0$. The second layer is segmented into cell size of $0.025 \times 0.025(\Delta\eta \times \Delta\phi)$ and has the longest active depth of $16X_0$ to collect the majority of the energy of EM showers. The third layer is designed only to collect the tail of the EM shower energy and is only segmented into cell size of $0.05 \times 0.025(\Delta\eta \times \Delta\phi)$ and with an active depth of $3X_0$. The forward region $(2.5 < |\eta < 3.2|)$ of the calorimeter is only segmented into two layers and has lower granularity.

Hadronic calorimeters

The TileCal is the ATLAS hadronic calorimeter system placed around the LAr calorimeters and provides a coverage of $|\eta| < 1.7$ and full azimuthal coverage. The central barrel of the TileCal has the coverage of $|\eta| < 1.0$ and two extended forward barrels cover the $0.8 < |\eta| < 1.7$ range. The TileCal is segmented longitudinally into three layers and has an active depth of 7.4λ ($\lambda = 20.7$ cm is nuclear interaction length) at $\eta = 0$ to provide a maximum containment of the hadronic shower energies. The TileCal is segmented into cells of projective geometry for triggering and energy reconstruction as shown in Figure 2.9. The TileCal has a granularity of 0.1×0.1 $(\Delta\eta \times \Delta\phi)$ in the first two layers and 0.2×0.1 in the third layer.

The TileCal is also segmented azimuthally into 64 modules, each has an angular coverage of $\Delta\phi$ 0.1. Figure 2.10 shows the geometry of a TileCal module. The TileCal uses scintillator as the sensitive medium and steel plates as the absorber. The scintillating tiles are placed in the plane perpendicular to the colliding beams and are radially staggered in depth with a ratio to steel plates of 1 to 4.7. When a hadron enters the steel and interacts with a nucleus in the medium through strong force, it creates a hadronic show which contains pions that would start an EM shower. The charged particles in the EM shower create scintillating photons, which will be collected by the wavelength-shifting fibers into the photomultiplier tubes to magnify the signal strength. However, some of the energy in a hadronic shower could not be captured by the detector because of the neutrinos in the shower or the energy is lost to nuclear recoils or absorbed as binding energies of nucleons. These missing energies during the shower development will be corrected by applying a calibration to hadronic showers.

The hadronic calorimeter system is extended by HEC to forward region of $1.5 < |\eta| < 3.2$. The HEC calorimeter uses liquid argon as the sensitive medium and copper plates as the absorber, segmented into 32 modules azimuthally and two layers longitudinally, providing a granularity of 0.1×0.1 ($\Delta\eta \times \Delta\phi$) in $|\eta| < 2.5$ and 0.2×0.2 in $|\eta| > 2.5$ region.

Forward calorimeters

The ATLAS forward calorimeters (FCal) extend the coverage to $3.1 < |\eta| < 4.9$ for shower energy measurements. It has an active length of 10λ with three modules using liquid argon as sensitive medium at each endcap. The first module is composed of copper absorber for EM shower measurements, and the two other modules are made of tungsten for hadronic shower measurements.

2.2.4 Muon spectrometer

The ATLAS Muon Spectrometer (MS) is designed to detect muons that can penetrate the calorimeter systems without significant energy loss. The MS is composed of a set of large superconducting toroid magnets and several gas chamber detectors. The MS provides a coverage for muon momentum measurements in the region of $|\eta| < 2.7$ and for trigger decision information in the region of $|\eta| < 2.4$. The MS has a barrel section with three cylindrical layers of chambers and two end-cap sections with three disk layers of chambers. The magnet system of MS has a central barrel toroid array and two end-cap toroids. The geometry of the MS is shown in Figure 2.11.

Tracking detector

The MS has two precision tracking chambers, Monitored Drift Tube (MDT) and Cathode Strip Chambers (CSC), to cover the region of $|\eta| < 2.7$ for momentum measurements of muons. The tracking chambers can perform a stand-alone measurement, or a combined measurement with the inner detector. The MDT consists of two layers of drift tubes, each layer has three or four tubes thick. Between the two MDT layers, readout electronics and a laser alignment monitoring system are installed. The drift tubes are filled with a gas mixture of 93% argon, 7% CO2 and a small amount of water vapor. When a charged particle traveling through a tube, the particle ionizes the gas and creates ions and electrons, which are then collected by a tungsten-rhenium anode wire mounted at the center of the tube. The CSC chambers are multiwire proportional chambers with wires oriented in the radial direction, which are designed for the forward region, and the ionization charges are collected and read out with cathode strips.

Trigger detector

The ATLAS Muon system has two trigger detectors designed to provide fast determinations of muon positions, the information of which can be used in hardware level trigger decisions. The muon trigger detectors include Resistive Plate Chambers (RPC) in the barrel region and Thin Gap Chambers (TGC) in the end-cap regions. The RPC has two parallel electrode plates separated by a gap of 2 mm, and the gap is filled with a gas mixture of $C_2H_2F_4$. Across the gap, an electric field of 4.9 kV/mm is applied between the two plates. The ionization charges produced by a muon traveling through the gas will be drifted by the field toward the anode. The TGC has multi-wire proportional chambers filled with CO2 and n-pentane gas mixture.

2.2.5 ATLAS trigger system

The LHC delivers and accelerates protons in bunches. The rate of bunch crossings at the interaction points is 40 MHz in 2016. This rate exceeds the limit of the ATLAS readout system and the storage system. A real-time selection system is thus needed to select events that are interesting to the physics program of the experiment at each bunch crossing, in order to reduce the readout rate.

The first stage selection is the level 1 trigger (L1), which is a hardware-based trigger system. The L1 trigger uses low granularity information from the calorimeter and muon spectrometer to decide interesting events per bunch crossing. The input rate is 40 MHz from the collisions, and the L1 trigger reduces this rate down to a peak rate of 100 kHz, which will then be processed subsequentially by a software high-level trigger. The L1 trigger system also generates Regions of Interest (RoIs) information, which will be used to guide the next level trigger decision.

The next level trigger is High-Level Trigger (HLT), which is a software decision system. The software of HLT runs on a commercially available computer cluster and processes data at the full detector granularity using the RoIs from L1. The HLT performs calorimeter reconstruction, fast tracking, and track-cluster matching within RoIs. The HLT outputs a rate at a maximum of 1 kHz.

In addition, a new trigger upgrade, the Fast TracKer (FTK), will be integrated into ATLAS in 2018. The FTK uses fast track pattern recognition to perform track reconstructions after L1 trigger. The FTK will pass global track information to HLT, which could be used to form primary vertices and to reduce pileup contamination, to guide the software level trigger decisions. A diagram showing the ATLAS trigger system dataflow is shown in Figure 2.12.

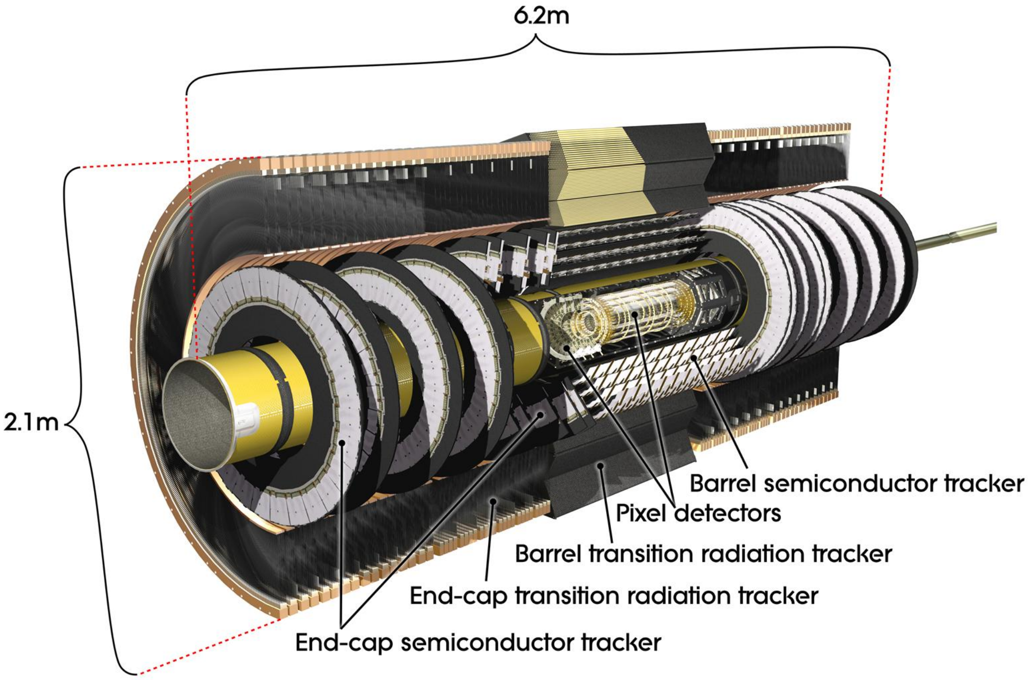

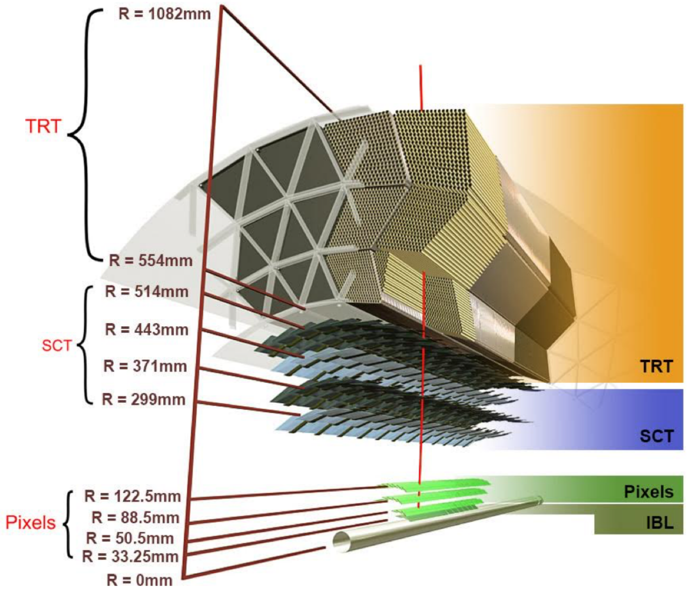

Figure 2.6: (Top) The ATLAS inner detector includes pixels, SCT, and TRT subdetectors. (Bottom) The radial locations of the inner detector layers. The pixel detector (including IBL) is the closest detector to the beam pipe to provide precise tracking and vertexing measurements. The SCT and TRT provide contributions to high momentum track measurement with larger volume and longer radial baseline.

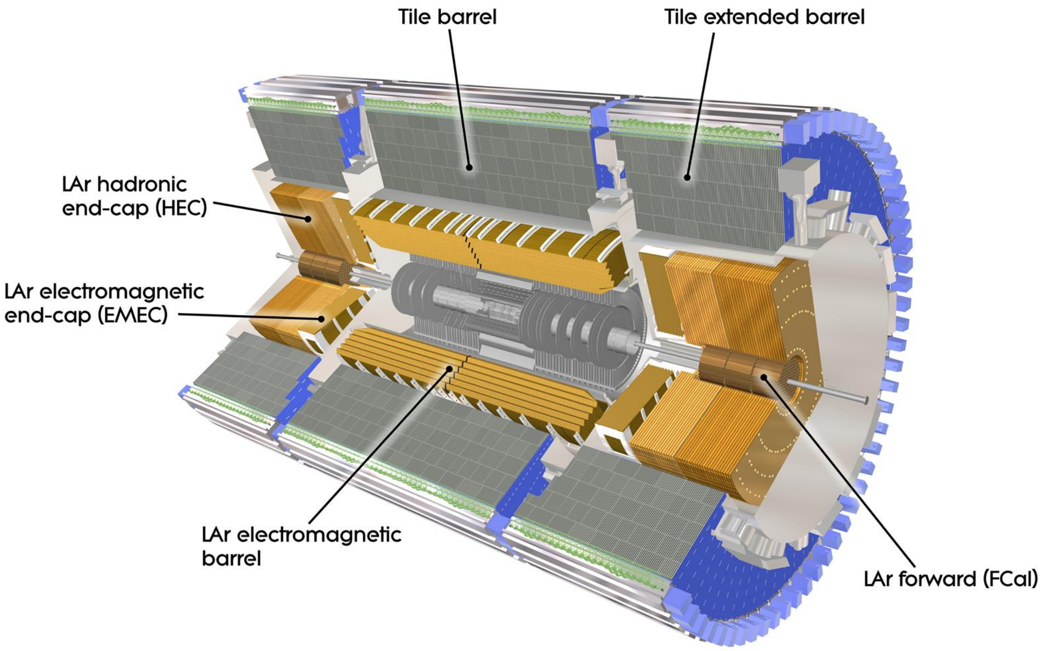

Figure 2.7: The ATLAS calorimeter system consists of a LAr calorimeter system and a tile calorimter system, which surround the inner detector and the solenoid magnet and provide measurements of particle shower energies.

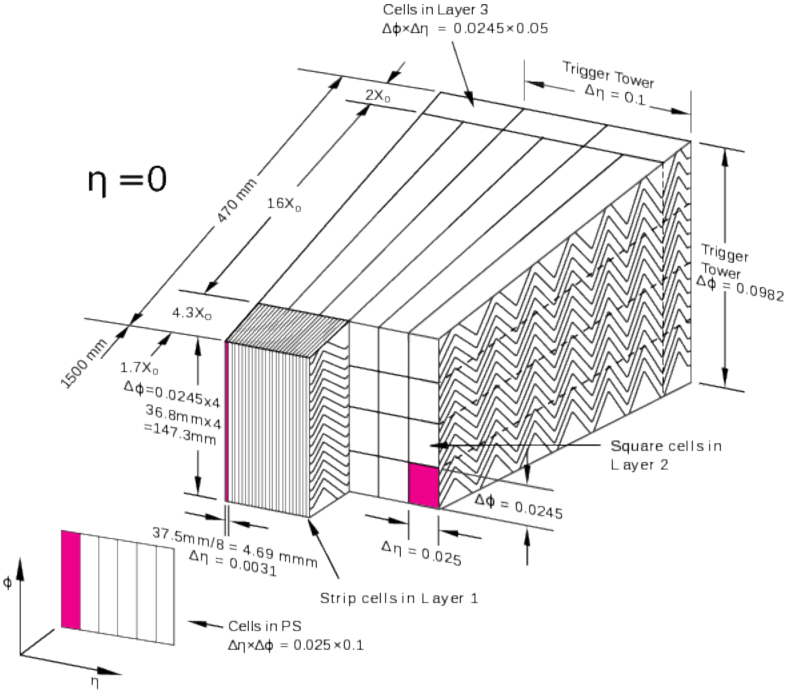

Figure 2.8: The cross-section of the EM barrel calorimeter. The first layer of a depth of $6X_0$ provides measurements of shower directions with the finest granularity. The second layer of a depth of $16X_0$ measures the energy deposits of particle showers. The third layer collects the energies of the tails of showers.

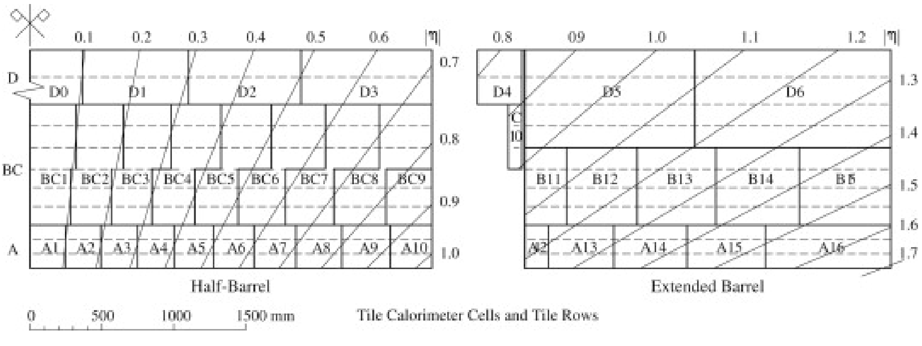

Figure 2.9: The cells of TileCal is segmented into projective geometry to optimize shower reconstruction and triggering.

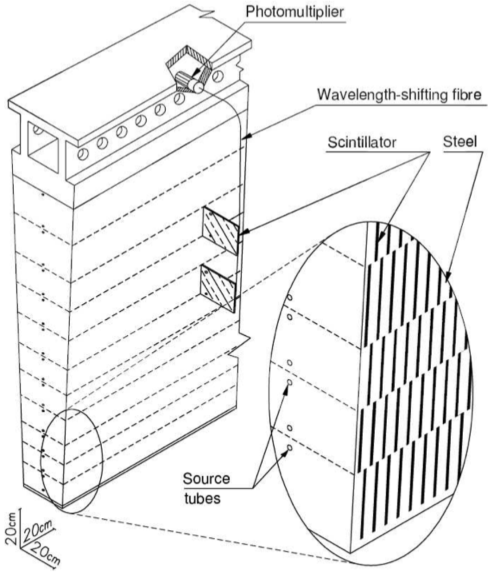

Figure 2.10: The scintillator tiles, the steel plates, the fibers, and photomultipliers in a TileCal module.

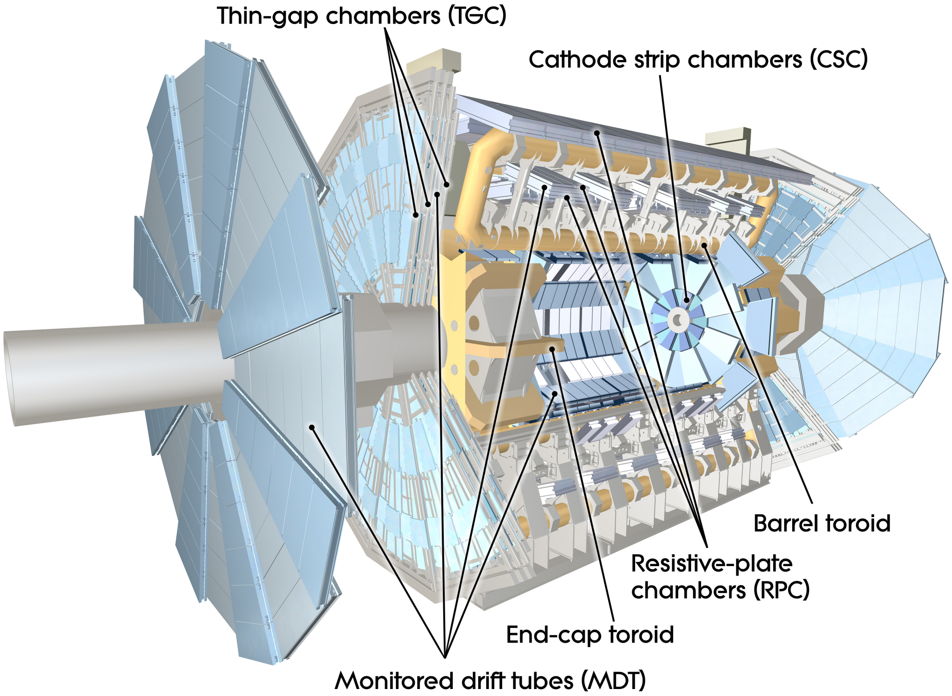

Figure 2.11: The ATLAS Muon Spectrometer is composed of two tracking chambers and two trigger detectors. The tracking chambers (MDT and CSC) perform measurements of muon momenta. The trigger detectors (RPC and TGC) provide fast position determinations and input information to hardware level triggers.

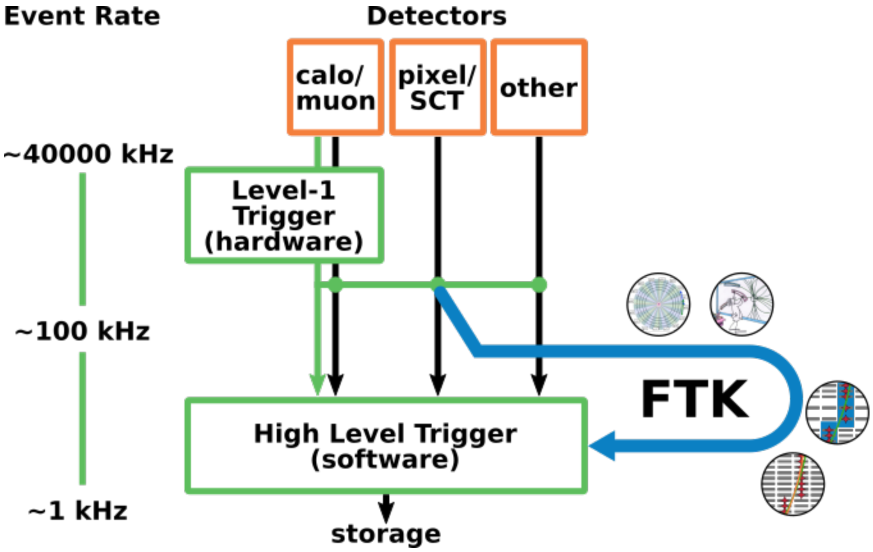

Figure 2.12: The ATLAS trigger system including FTK.

CHAPTER 3

LHC RUN1 RESULTS ON SUPERSYMMETRY

The dilepton final state offers a good sensitivity to search for new physics with a clean background and excellent lepton resolutions. The invariant mass of the two lepton system (m_{ll}) can provide insight into the mass spectrum of the new particle decay chain. In the context of natural SUSY, the masses of gluinos, scalar top quarks, and higgsinos are assumed to be around a few TeV or less.

If gluinos can be produced in LHC proton-proton collisions, they might decay to lighter neutralinos. The neutralinos could further decay to the lightest SUSY particle LSP (could be a lightest neutralino $\tilde{\chi}_1^0$ or a gravitino in models with generalised gauge mediated (GGM) supersymmetry breaking) and radiate a Z boson as illustrated in Figure 3.1 (left). This signal will result in an excess around 91 GeV in the m_{ll} spectrum if the mass difference between the LSP and the next-lightest particle is larger than the mass of Z boson (m_Z). If this mass difference is smaller than m_Z, the signal will give a m_{ll} distribution that is truncated at the mass difference.

Another possible decay scenario is that neutralinos decay to LSP through an intermediate particle (scalar lepton) as it is shown in Figure 3.1 (right). The slepton decay scenario gives a triangle shape in the m_{ll} spectrum with a cut-off edge located around the mass difference between the neutralino and LSP. Thus, the shape of m_{ll} distribution could give an unambiguous evidence of new physics and information of the mass hierarchy of the new particles.

In 2015, an ATLAS analysis team presented results of searches for both Z-decay and slepton-decay scenarios in events with two same-flavor opposite-sign leptons, jets, and $E_{\mathrm{T}}^{\mathrm{miss}}$, using 20.3 fb^{-1} of 8 TeV pp collision data. In an on-shell Z signal region ($m_{ll} \in [81, 101]$, $H_T > 600$ GeV, $E_{\mathrm{T}}^{\mathrm{miss}} > 225$ GeV), they found 29 data events while the SM background is expected to be 10.6 ± 3.2. This corresponds to a significance of 3.0σ. The distribution of m_{ll} in this signal region is shown in Figure 3.2 (top).

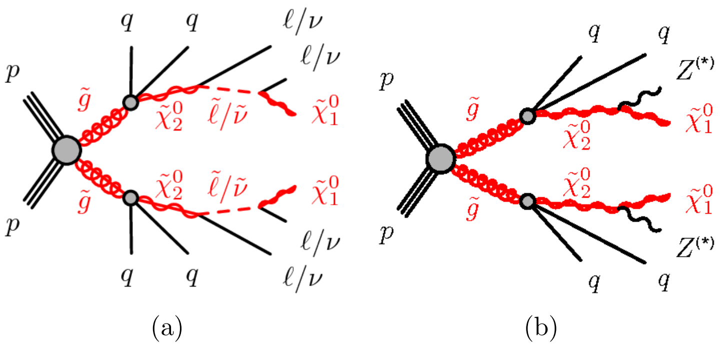

Figure 3.1: Two possible gluino-decay scenarios resulting in two lepton final states: (a) Gluinos decay via neutralinos to gravitino LSPs. (b) Gluinos following two-step decays via sleptons to neutralino LSPs.

Another team on CMS side also made similar searches for the Z-decay and slepton-decay scenarios in the dilepton channel. The CMS team did not find a significant excess in the on-shell region. Instead, they found an off-shell excess with a cut-off edge that would match the predicted m_{ll} shape from the slepton-decay scenario. The signal region of this interesting excess requires at least two jets and $E_{\mathrm{T}}^{\mathrm{miss}} > 150$ GeV (or three jets with $E_{\mathrm{T}}^{\mathrm{miss}} > 100$ GeV) and two central leptons. The excess has a cut-off edge located at 78.7 ± 1.4 GeV and corresponds to a significance of 2.4σ. The distribution of m_{ll} of this off-shell excess is shown in Figure 3.2 (bottom).

The excesses of ATLAS and CMS Run-1 results drew a huge attention from the theory community. A careful investigation using Run-2 13 TeV data is thus demanded and motivates the study of this thesis work. The result of the investigation using 13 TeV data is presented in the following sections.

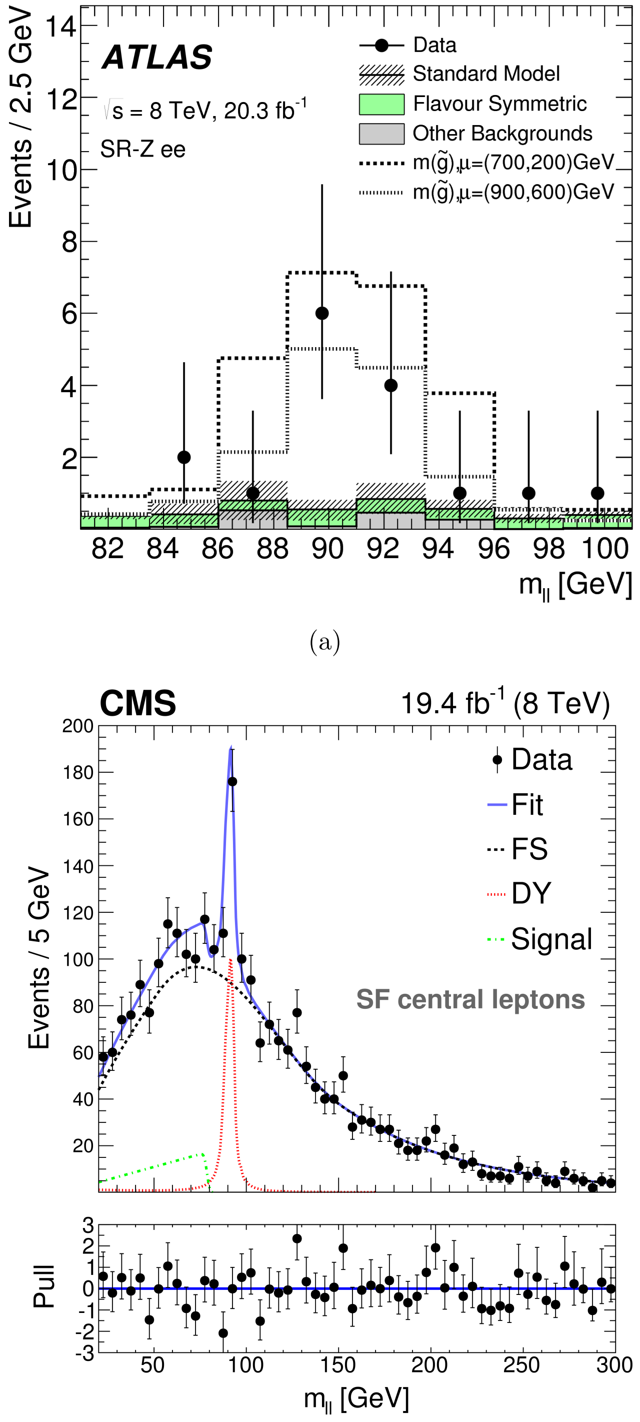

(a)

(b)

Figure 3.2: (a) An ATLAS Run-1 dilepton analysis result shows an excess in the Z mass window that would fit the description of the model shown in Fig. 3.1(a). (b) A CMS Run-1 dilepton analysis result shows an excess in the off-shell region that would fit the description of the model shown in Fig. 3.1(b).

CHAPTER 4

MISSING TRANSVERSE MOMENTUM RECONSTRUCTION AND PERFORMANCE

4.1 Introduction

The content of this chapter describes the work of ATLAS $E_{\mathrm{T}}^{\mathrm{miss}}$ performance study detailed in [8]. When a pp collision takes place in the detector, the sum of momenta of the final state particles is expected to be zero in the plane transverse to the beam axis, because the two incoming protons have no initial transverse momenta. The final state transverse momentum imbalance is observed if one or more final state particles are stable and not participating in electromagnetic and hadronic interactions. For a standard model process, this invisible particle is neutrino, which could arise from $W \to \ell\nu$ or $Z \to \nu\nu$ decays. In the theory of supersymmetry, the lightest supersymmetric particle (LSP) is expected to be stable and only interacts via the weak force, and thus the $E_{\mathrm{T}}^{\mathrm{miss}}$ is a sensitive variable to probe SUSY in collider experiments. However, fake $E_{\mathrm{T}}^{\mathrm{miss}}$ could also be a result of instrumental effects, such as leptons or jets escaping detector acceptance or badly reconstructed objects. Therefore, understanding the sources of $E_{\mathrm{T}}^{\mathrm{miss}}$ is crucial in supersymmetry searches.

4.2 $E_{\mathrm{T}}^{\mathrm{miss}}$ reconstruction

The $E_{\mathrm{T}}^{\mathrm{miss}}$ of an event is the negative sum of momenta of the selected objects (electrons, photons, τ-leptons, jets, and muons) reconstructed by the ATLAS detector. The $E_{\mathrm{T}}^{\mathrm{miss}}$ includes these components:

$$E_{x/y}^{\mathrm{miss}} = -\sum_{e} p_{x/y} - \sum_{\gamma} p_{x/y} - \sum_{\tau} p_{x/y} - \sum_{\mathrm{jet}} p_{x/y} - \sum_{\mu} p_{x/y} - \sum_{\mathrm{soft}} p_{x/y} \quad (4.1)$$

, where $E_{\mathrm{T}}^{\mathrm{miss}} = \sqrt{(E_x^{\mathrm{miss}})^2 + (E_y^{\mathrm{miss}})^2}$. $\sum_{\mathrm{soft}} p_{x/y}$ is the sum of "soft-term", which is reconstructed from detector signals not associated with other selected objects. The soft-term can be inner detector tracks or calorimeter signals. For the analyses presented in this thesis, soft $E_{\mathrm{T}}^{\mathrm{miss}}$ reconstruction only considers the track-based soft term. The objects used in $E_{\mathrm{T}}^{\mathrm{miss}}$ reconstruction are discussed in the following sections.

4.3 Selections and resolutions of objects in $E_{\mathrm{T}}^{\mathrm{miss}}$ reconstruction

4.3.1 Tracks and vertices

Tracks are formed using the hits in the inner detector. The tracks are required to satisfy $p_{\mathrm{T}} > 0.4$ GeV and $|\eta| < 2.5$, and reconstruction quality requirements such as number of hits in the inner detector. Collision vertices are formed using the selected tracks. The reconstructed vertices are required to pass the cuts on the transverse impact parameter $d_0 < 1.5$ cm and longitudinal impact parameter $z_0 < 1.5$ cm. The primary vertex in an event is selected with highest $\sum p_{\mathrm{T}}^2$ using the tracks associated with this vertex. The primary vertex is treated as the hard-scatter vertex in analyses.

4.3.2 Muons

The selected muons are required to pass $p_{\mathrm{T}} > 10$ GeV. In the central region with $|\eta| < 2.5$, the muons are reconstructed using a combined fit with the hits in the inner detector and the hits in the Muon Spectrometer. In the region with $2.5 < |\eta| < 2.7$, the muons are only reconstructed with the hits in the Muon Spectrometer. In addition, muons are also required to pass "Medium" quality recommendation [9]. The reconstruction efficiency of the Medium selection is $95\% - 96\%$ in the case of $t\bar{t} \rightarrow l^+ l^-$ events. On top of the Medium selection, a high-p_{T} muon recommendation aims for reconstructing tracks with $p_{\mathrm{T}} > 100$ GeV with better momentum resolution. The mismeasurement on the muon momentum contributes to the $E_{\mathrm{T}}^{\mathrm{miss}}$ calculation, and the resolution of the muon momentum is parametrized as

$$\frac{\sigma(p_{\mathrm{T}})}{p_{\mathrm{T}}} = \frac{r_0}{p_{\mathrm{T}}} \oplus r_1 \oplus r_2 p_{\mathrm{T}}$$

with $\oplus$ denoting a sum in quadrature. The first term with r_0 accounts for the energy loss in the detector material, which is negligible for muons for their small cross section of Bremsstrahlung radiation. The second term with r_1 accounts for multiple scattering, inhomogeneous magnetic field distribution, and radial displacements of the hits (curvature of muon path). The third term with r_2 arises from the sizes of the detector sensors and the residual misalignment of detectors. With r_0 set to zero and r_2 predetermined in alignment study using special runs data with the toroidal magnetic field off, the remaining r_1 factor is measured by performing a likelihood fit that compares the di-muon invariant mass shapes in $J/\psi \to \mu\mu$ and $Z \to \mu\mu$ decays in simulation and in data.

4.3.3 Electrons and photons

Electrons are reconstructed using the correlations between calorimeter clusters and inner detector tracks [10]. The selected electrons are required to pass $p_{\mathrm{T}} > 10$ GeV and $|\eta| < 2.47$. The region with $1.37 < |\eta| < 1.52$ is vetoed for the electron selection to avoid the "crack" between barrel and end-cap EM calorimeters. In addition, electrons are also required to pass "Medium" quality recommendation. Photons are built using the energy deposits of the electromagnetic showers in the EM calorimeter cells. Photons are selected with $p_{\mathrm{T}} > 25$ GeV and $|\eta| < 2.37$ [11]. The region with $1.37 < |\eta| < 1.52$ is vetoed for the photon selection to avoid the "crack" between barrel and end-cap EM calorimeters. In addition, photons are also required to pass "Tight" quality recommendation. The energy resolution of an EM object comes from three effects. The largest contribution is from the sampling fluctuations of the number of interactions in the calorimeter material, which gives the scale of energy resolution as $\sigma \propto \sqrt{E}$. Secondly, imperfect corrections to longitudinal leakage along the shower direction could give a linear term $\sigma \propto E$. Finally, there is also a constant electronic noise term. Combine all these effects together, the EM energy resolution scales as

$$\frac{\sigma(E)}{E} = \frac{a}{\sqrt{E}} \oplus b \oplus \frac{c}{E}$$

The designed values for these parameters are $a = 9\%\sqrt{E[\text{GeV}]}$ and $b = 0.7\%$ [12].

4.3.4 Jets

Jets are reconstructed based on the clusters of cells that are topologically connected in the hadronic calorimeter. These clusters are calibrated at the electromagnetic energy scale (the relation between the true energy of the hadron and the measured signal), which provides a good energy estimation of the EM component in the calorimeter but does not account for the energy loss in the nuclear recoil and binding energy. The anti-k_t algorithm (cite) is applied for the reconstruction of jets, and the EM+JES scheme (cite) is used to calibrate the jet energy and a correction for pileup contamination (cite). The selected jets have $p_{\text{T}} > 20$ GeV, $|\eta| < 2.4$ and JVT> 0.64 (jet vertex tagger variable) (cite) for the jets with $p_{\text{T}} < 50$ GeV to remove pileup jets. If the jet is associated with the primary vertex but fails these quality requirements, it will be included in the track soft-term for the $E_{\text{T}}^{\text{miss}}$ calculation. The hadronic calorimeter resolution is parametrized as

$$\frac{\sigma(E)}{E} = \frac{a}{\sqrt{E}} \oplus b \oplus \frac{c}{E}$$

, where the first term arises from the sampling fluctuations of the number of interactions in the calorimeter material (which dominates the range of $p_{\text{T}} < 400$ GeV), the second term comes from the energy loss during the shower development in the passive material (e.g. cryostats and solenoid coil), and the third term comes from electronic noise [13].

4.4 $E_{\text{T}}^{\text{miss}}$ soft term

The $E_{\text{T}}^{\text{miss}}$ soft term refers to the detector signals that are included in the $E_{\text{T}}^{\text{miss}}$ calculation but not associated with any selected object in the event. Here the track-based soft term (TST) is described. The track soft term is built from the tracks described in Sec. 4.3.1 but not matched to any hard object, such as muons, electrons, photons, and jets. To suppress the contamination from pile-up interactions, only tracks that match the primary vertex (within a threshold on impact parameters d_0 and z_0) are used in TST $E_{\mathrm{T}}^{\mathrm{miss}}$ calculation. To remove tracks associated with hard objects, an overlap removal procedure is employed to determine the association and remove tracks.

4.5 Components of $E_{\mathrm{T}}^{\mathrm{miss}}$ in $Z+$jets (two leptons) events

The contributions of different object resolutions to the $E_{\mathrm{T}}^{\mathrm{miss}}$ are shown in Figure 4.1. The resolution is interpreted as the mean of absolute deviation of $p_{\mathrm{T}}^{\mathrm{reco.}} - p_{\mathrm{T}}^{\mathrm{truth}}$ of objects in a SHERPA2.2.1 $Z+$jets simulation sample. The mean absolute deviation (MAD) corresponds to the root-mean-square (RMS) of a Gaussian distribution as $MAD = \sqrt{2/\pi} RMS$. Figure 4.1(a) shows the resolutions of different objects in a Z+mono jet region. Because it is difficult to define the truth information of initial-state-radiation jets, the $p_{\mathrm{T}}^{\mathrm{reco.}} - p_{\mathrm{T}}^{\mathrm{truth}}$ of a jet is derived using $E_{\mathrm{T}}^{\mathrm{miss}}$ in this 1-jet region after removing $p_{\mathrm{T}}^{\mathrm{reco.}} - p_{\mathrm{T}}^{\mathrm{truth}}$ of leptons and track soft-terms (TST).

As we see in Figure 4.1(a), the resolutions of calorimeter based objects, jets and electrons, scale as $\sqrt{E}$ and grow very slowly with p_{T} of the object due to the sampling fluctuation of calorimeter cells. At low p_{T} region, jets are the objects with largest uncertainties. However, in the region with $p_{\mathrm{T}} > 500$ GeV, the resolution of muon becomes worse than the resolution of jet and increases linearly with the p_{T} of dimuon system. The behavior of dimuon system resolution changes dramatically at 400 GeV.

A highly boosted Z boson with $p_{\mathrm{T}} > 400$ GeV is formed by two muons, each with roughly $p_{\mathrm{T}} > 200$ GeV. Muons in this momentum region become radiative in a medium. Figure 4.2 shows the stopping power ($< dE/dx >$) behavior in copper of muon momentum. In the middle momentum range from 10 MeV to 100 GeV, the energy loss of the incident muon is well modeled by the Bethe-Bloch theory, which describes the muon losing energy through the ionization of an isolated atom. In the low momentum region with $p_{\mathrm{T}} <$ 1 MeV, the muon motion is slower than that of valence electrons in the absorber, and the muon no longer sees each atom being isolated from other atoms. In this region, the electrons in the medium are described as a plasma (a Fermi sea), and the muon loses energy by polarizing the plasma as it passes through. Finally, in the ultra-relativistic range with $p_{\mathrm{T}} > 200$ GeV, the bremsstrahlung and e^+e^- pair production start dominating the muon energy loss. In this region, a hard radiation could kick the muon off from its original trajectory and increases the difficulty of the muon reconstruction.

The contributions of mis-measurements of different objects as function of $E_{\mathrm{T}}^{\mathrm{miss}}$ can be found in Figure 4.1(b). Figure 4.1(b) is made in a $Z+\geq 2$ jets region. In the low $E_{\mathrm{T}}^{\mathrm{miss}}$ (< 200 GeV) region, the jet mismeasurement is the dominating source of $E_{\mathrm{T}}^{\mathrm{miss}}$. In the high $E_{\mathrm{T}}^{\mathrm{miss}}$ (> 200 GeV) region, the mismeasurement of muons becomes more important and dominates the tail of $E_{\mathrm{T}}^{\mathrm{miss}}$.

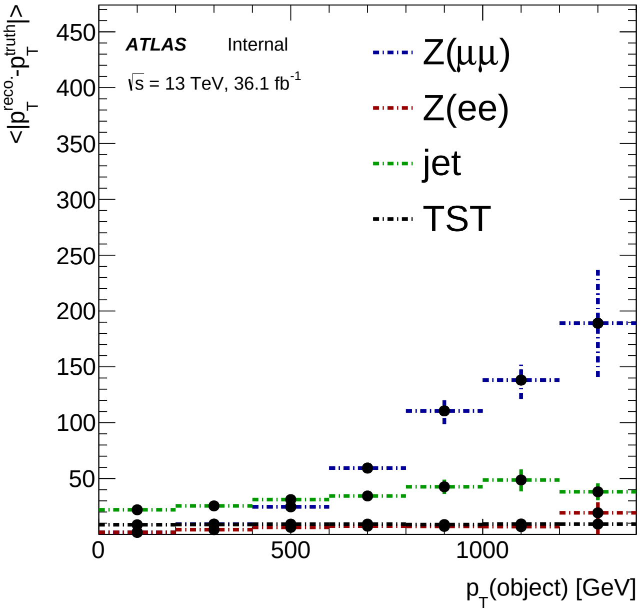

(a)

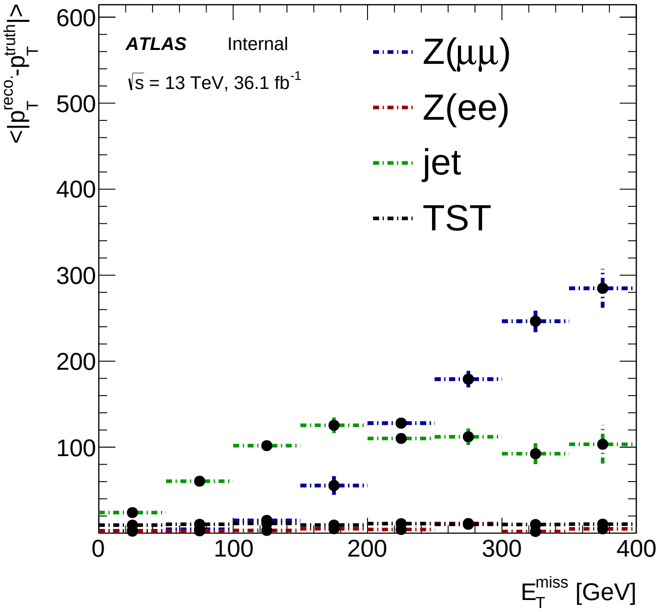

(b)

Figure 4.1: Mean absolute deviation of $p_{\mathrm{T}}^{\text{reco.}} - p_{\mathrm{T}}^{\text{truth}}$ as function of (a) object $p_{\mathrm{T}}^{reco.}$ and (b) $E_{\mathrm{T}}^{\text{miss}}$. The distributions are measured from a SHERPA 2.2.1 $Z +$jets simulation. The truth information of jet p_{T} is derived using $E_{\mathrm{T}}^{\text{miss}}$ in the $Z \to \mu\mu$ events after removing mis-measurements of leptons and track soft-terms (TST).

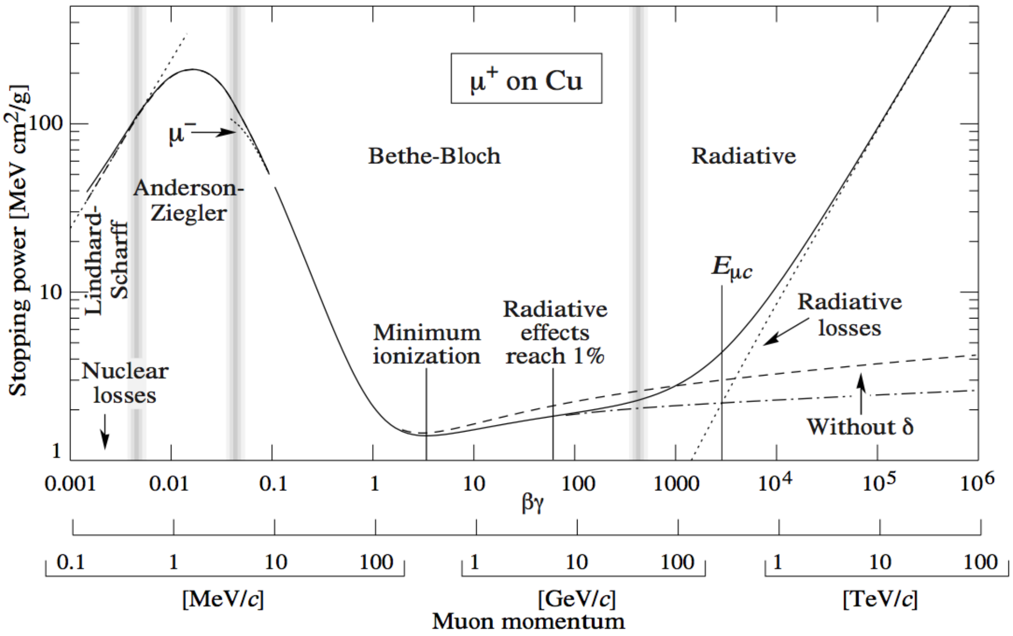

Figure 4.2: Stopping power of ($=< dE/dx >$) for postive muon in copper as function of muon momemtum. This figure is taken from [1].

CHAPTER 5

THE PHOTON TEMPLATE METHOD

This section discusses a photon template method for $Z+\text{jets}$ background estimation in $2\ell + 2jets$ analyses.

5.1 Introduction to the photon template method

In the searches for Supersymmetric processes involving $\tilde{\chi}_2^0/\tilde{\chi}_1^{\pm}$ to $\tilde{\chi}_1^0$ decays, the dilepton final states offer unique sensitivities to probe Supersymmetry. The requirement of two signal leptons largely reduce the overwhelming QCD backgrounds, and the invariant mass of the two leptons will provide an unambiguous information of the SUSY particle mass spectrum if Supersymmetry is discovered.

In the dilepton channel, the expected Standard Model background contributions are from $Z+\text{jets}$, $t\bar{t} \to l^+l^-$ and VV. Among these backgrounds, $t\bar{t}$ and VV are irreducible backgrounds with two prompt leptons and real $E_{\mathrm{T}}^{\mathrm{miss}}$ from neutrinos. These irreducible background processes are usually well modelled in Monte Carlo simulation. On the other hand, modeling $Z+\text{jets}$ (with the Z decays to two leptons) is more challenging for the instrumental $E_{\mathrm{T}}^{\mathrm{miss}}$ in the events with jet energy mismeasurements, which involves complex detector defects and QCD kinematics. Furthermore, $Z+\text{jets}$ events rate is huge ($\sigma(Z)$ is $O(10^2)$ times larger than $\sigma(t\bar{t})$ in the dilepton channel), any small mis-modeling in jet energy resolution could lead to a significant underestimation of $Z+\text{jets}$ background. Large event rate of $Z+\text{jets}$ will also become an issue for Monte Carlo simulations in the era of HL-LHC, when data outruns MC statistics.

To demonstrate the mismodeling of the instrumental $E_{\mathrm{T}}^{\mathrm{miss}}$ and the QCD kinematics that we observed in MC simulations, the $E_{\mathrm{T}}^{\mathrm{miss}}$ distributions of the $Z+\text{jets}$ events in two simulations (Sherpa 2.1 and 2.2.1) are compared in Figure 5.1. In the case of Sherpa 2.1, as shown in Figure 5.1 (a), the $Z+$ jets events are underestimated in the region with $E_{\mathrm{T}}^{\mathrm{miss}} > 50$ GeV. This underestimation is largely improved in Sherpa 2.2.1, which is shown in Figure 5.1 (b). However, when we display these events as function of H_{T} in Figure 5.2 and N_{jets} in Figure 5.3, we still see clear trends of mismodelings of these QCD variables. Furthermore, the $E_{\mathrm{T}}^{\mathrm{miss}}$ shape in the 1-jet channel also seems to be mismodeled in both Sherpa 2.1 and Sherpa 2.2.1 as shown in Figure 5.4, which indicates a mismodeling of the single jet resolution.

To model the jet energy mismeasurement properly, we use $\gamma+$ jets events in data to predict $Z+$ jets events. Both $\gamma+$ jets and $Z+$ jets events share similar topology, i.e. a well measured object (photon or Z boson) recoiling against hadronic system (jets), and no neutrinos present. The information of detector defects and hadronic kinematics will be automatically included in the jets of photon events in data. However, there are some minor corrections needed for the photon method. For example, the event rate of $Z+$ jets is much smaller than the event rate of $\gamma+$ jets process, which needs to be corrected with some reweighting factors. The photon energy resolution is also different from the energy resolutions of $Z \to ee$ and $Z \to \mu\mu$ due to the fact that these objects are reconstructed with different subdetectors. Therefore, to take all these differences into account, a normalization correction will be applied to correct the event rate difference, and a smearing function will be used to adjust photon energy resolution to match Z boson resolutions. In the following sections we will discuss about the procedure of the photon method, the corrections applied in the method, as well as the validation of the method.

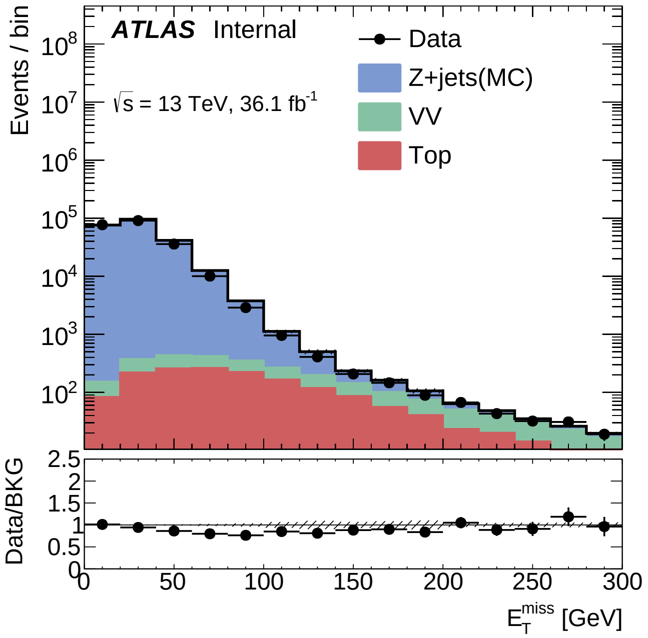

(a) $E_{\mathrm{T}}^{\mathrm{miss}}$ in SHERPA 2.1 $Z+$jets

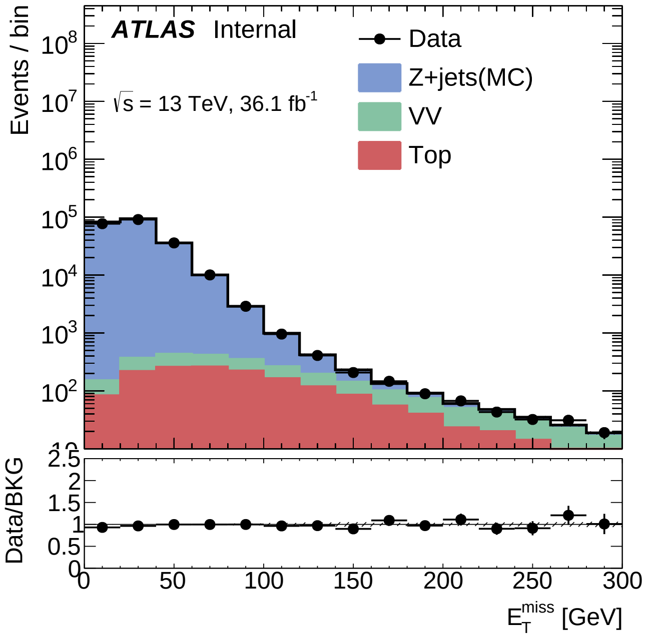

(b) $E_{\mathrm{T}}^{\mathrm{miss}}$ in SHERPA 2.2.1 $Z+$jets

Figure 5.1: Compare the $E_{\mathrm{T}}^{\mathrm{miss}}$ distributions of $Z+$jets events in SHERPA 2.1 (a) v.s. SHERPA 2.2.1 (b). The VV and $t\bar{t}$ are provided by the same simulations in (a) and (b). The selection in this plot requires two OSSF leptons with $m_{ll} \in [61, 121]$ GeV, at least two jets with $p_{\mathrm{T}} > 30$ GeV, and $H_{\mathrm{T}} > 200$ GeV.

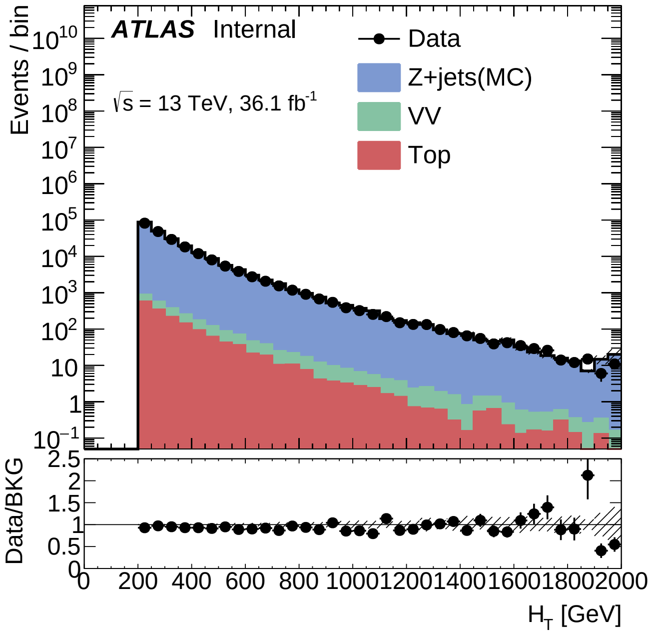

(a) H_{T} in Sherpa 2.1 $Z+$jets

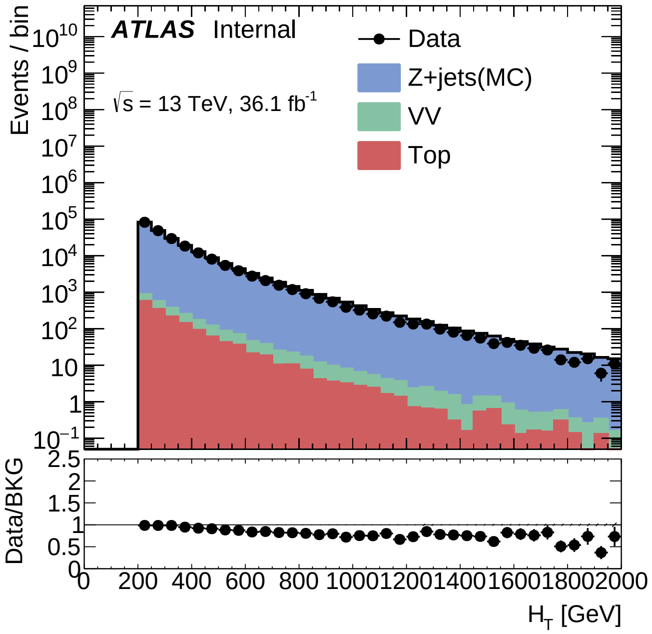

(b) H_{T} in Sherpa 2.2.1 $Z+$jets

Figure 5.2: Compare the H_{T} distributions of $Z+$jets events in Sherpa 2.1 (a) v.s. Sherpa 2.2.1 (b). The VV and $t\bar{t}$ are provided by the same simulations in (a) and (b). The selection in this plot requires two OSSF leptons with $m_{ll} \in [61, 121]$ GeV, at least two jets with $p_{\mathrm{T}} > 30$ GeV, and $H_{\mathrm{T}} > 200$ GeV.

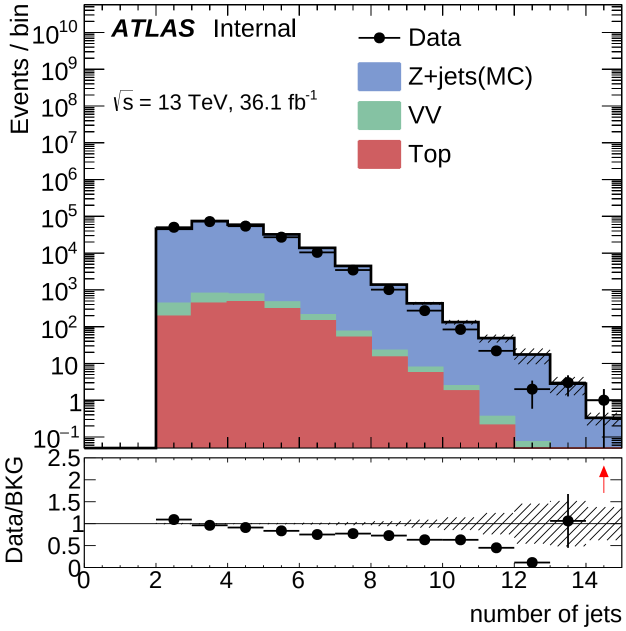

(a) N_{jets} in SHERPA 2.1 $Z+\text{jets}$

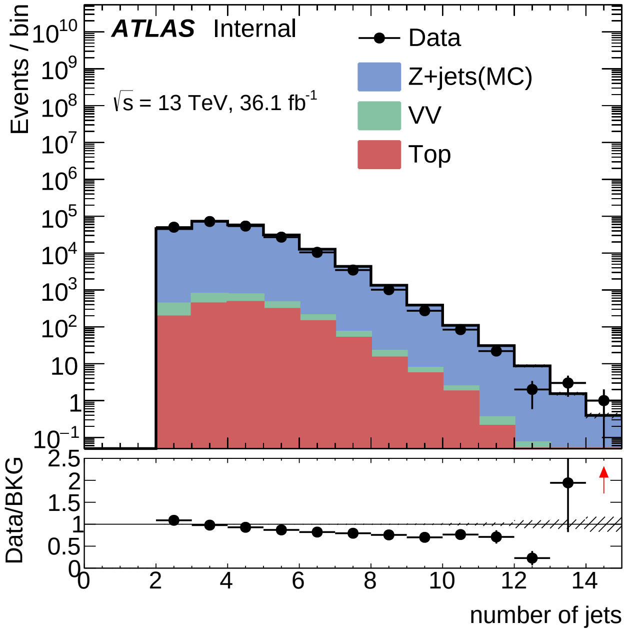

(b) N_{jets} in SHERPA 2.2.1 $Z+\text{jets}$

Figure 5.3: Compare the N_{jets} distributions of $Z+\text{jets}$ events in SHERPA 2.1 (a) v.s. SHERPA 2.2.1 (b). The VV and $t\bar{t}$ are provided by the same simulations in (a) and (b). The selection in this plot requires two OSSF leptons with $m_{ll} \in [61, 121]$ GeV, at least two jets with $p_{\text{T}} > 30$ GeV, and $H_{\text{T}} > 200$ GeV.

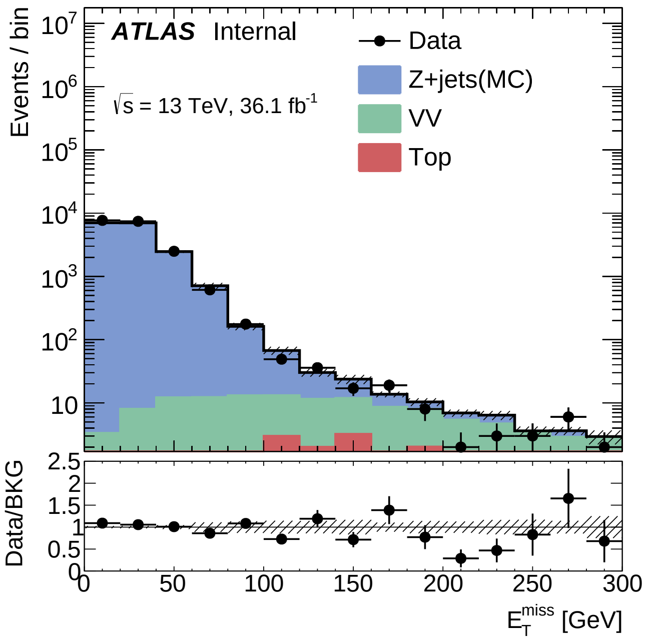

(a) $E_{\mathrm{T}}^{\mathrm{miss}}$ in Sherpa 2.1 $Z+\text{jets}$

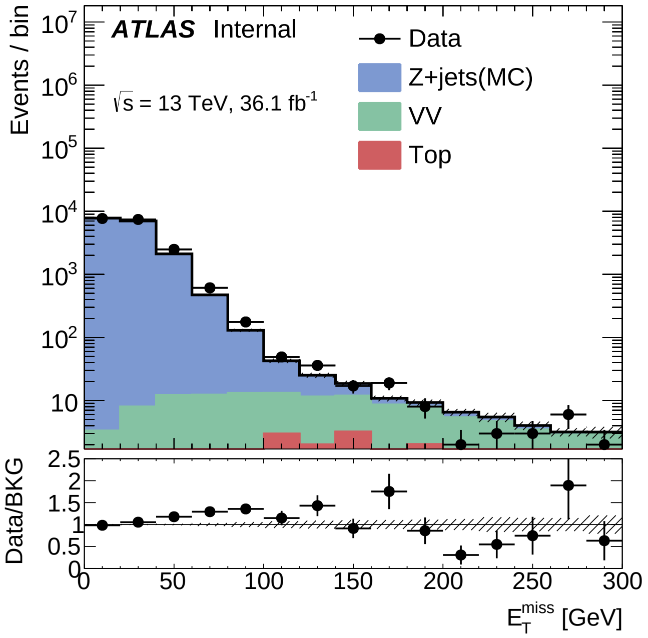

(b) $E_{\mathrm{T}}^{\mathrm{miss}}$ in Sherpa 2.2.1 $Z+\text{jets}$

Figure 5.4: Compare the $E_{\mathrm{T}}^{\mathrm{miss}}$ distributions of $Z+\text{jets}$ events in Sherpa 2.1 (a) v.s. Sherpa 2.2.1 (b). The VV and $t\bar{t}$ are provided by the same simulations in (a) and (b). The selection in this plot requires two OSSF leptons with $m_{ll} \in [61, 121]$ GeV, and exactly one jet with $p_{\mathrm{T}} > 200$ GeV.

5.2 Object definitions and event selections of the photon template method

In this section, all physics objects used in the analysis are introduced, including photon, jets, electrons and muons. In the case of leptons and jets, pre-selection (baseline) cuts are applied before performing overlap removal between objects. In order to satisfy "signal" object selection, the criteria used for pre-selection is subsequently tightened.

For consistency, photons are required to pass the signal selection and included in the $E_{\mathrm{T}}^{\mathrm{miss}}$ calculation for all events in the analysis. Photons are required to pass `tight` selection criteria and fall within $|\eta| < 2.37$. The region $1.37 < |\eta| < 1.52$ is vetoed as a part of the selection criteria of `tight` photons. The `FixedCutTight` isolation criteria are also applied, which require topoetcone40 $< 0.022 p_{\mathrm{T}}$ GeV $+2.45$ and ptcone20/$p_{\mathrm{T}} < 0.05$.

Electrons are reconstructed using the Egamma algorithm and are required to reside within $|\eta| < 2.47$. At baseline level, electrons must have $p_{\mathrm{T}} > 10$ GeV and satisfy the `looseLH` quality criteria. Signal electrons must have $p_{\mathrm{T}} > 25$ GeV and be isolated with respect to other baseline particles, satisfying the `GradientLoose` isolation criteria and additionally passing `mediumLH` quality criteria. Signal electron candidates must also have $d_0/\sigma_{d_0} < 5$ and $z_0 \sin\theta < 0.5$ mm. In MC events, η and E_{T} dependent scale factors are applied to selected electrons in order to account for differences in electron reconstruction, identification, isolation, and trigger efficiency between data and MC. The analysis electron selection is summarised in Table 5.1.

Cut	Value/description
Baseline Electron	
Acceptance	$p_{\mathrm{T}} > 10$ GeV , $\lvert\eta^{\mathrm{clust}}\rvert < 2.47$
Quality	`LHLoose`
Signal Electron	
Acceptance	$p_{\mathrm{T}} > 25$ GeV , $\lvert\eta^{\mathrm{clust}}\rvert < 2.47$
Quality	`LHMedium`
Isolation	`GradientLoose`
Impact parameter	$\lvert z_0 \sin\theta\rvert < 0.5$ mm $\lvert d_0/\sigma_{d_0}\rvert < 5$

Table 5.1: Summary of the electron selection criteria. The signal selection requirements are applied on top of the baseline selection.

Muons used in this analysis must have $p_{\mathrm{T}} > 10$ GeV and reside within $|\eta| < 2.5$. Baseline muons must pass `Medium` quality requirements. Signal muons must have $p_{\mathrm{T}} > 25$ GeV and be isolated with respect to other signal objects, satisfying the `GradientLoose` isolation criteria and additionally having $|d_0/\sigma_{d_0}| < 3$ and $z_0 \sin\theta < 0.5$ mm. Since the muon reconstruction, track-to-vertex association, identification, isolation, and trigger efficiencies differ between data and MC, an η and p_{T} dependent scale factor is applied to each muon passing selection requirements and overlap removal in an MC event. Above 500 GeV, the high-p_{T} working point is used for muons, along with the MCP "bad muon veto." While this bad muon veto is also used at lower momenta with the Medium quality requirement, a much stricter version accompanies the high-p_{T} working point, requiring additional scale factors to be applied to the event. The analysis muon selection is summarised in Table 5.2.

Cut	Value/description
Baseline Muon	
Acceptance	$p_{\mathrm{T}} > 10$ GeV , $\|\eta\| < 2.5$
Quality	`Medium`
Signal Muon	
Acceptance	$p_{\mathrm{T}} > 25$ GeV , $\|\eta\| < 2.5$
Quality	`Medium` (High-p_{T} for $p_{\mathrm{T}} > 500$ GeV
Isolation	`GradientLoose`
Impact parameter	$\|z_0 \sin\theta\| < 0.5$ mm
	$\|d_0/\sigma_{d_0}\| < 3$
isBadMuon	MCP isBadMuon Flag

Table 5.2: Summary of the muon selection criteria. The signal selection requirements are applied on top of the baseline selection.

This analysis used `EMTopo` jets reconstructed using the Anti-kt algorithm with distance parameter $D = 0.4$. At baseline level these jets are required to have $p_{\mathrm{T}} > 20$ GeV and reside within $|\eta| < 2.8$. Signal jets are further required to reside within $|\eta| < 2.5$, have $p_{\mathrm{T}} > 30$ GeV and pass a JVT cut (JVT¿0.59) if the jet p_{T} is less than 60 GeV and it resides within $|\eta| < 2.4$. The analysis jet selection is summarised in Table 5.3.

The missing transverse momentum ($E_{\mathrm{T}}^{\mathrm{miss}}$) definition used in this analysis uses selected analysis objects and tracks. Calibrated (baseline) electrons, muons and jets (the full η range is used for jets in $E_{\mathrm{T}}^{\mathrm{miss}}$) are considered in the $E_{\mathrm{T}}^{\mathrm{miss}}$ calculation, and photons are included and the track-based soft term is used. In order to avoid double-counting in the $E_{\mathrm{T}}^{\mathrm{miss}}$ when a muon deposits significant energy in the calorimeter, the DoMuonJetOR flag is set to TRUE for this analysis.

The photon events are required to pass one of the triggers in Table 5.4 as well as the following selections:

- $n_{\mathrm{jets}} \geq 2$ for analysis region predictions
- $n_{\mathrm{jets}} = 1$ for 1-jet control region, in which the smearing function is derived in data (though in practice, owing to lack of statistics at high boson p_{T} the factors used are derived from MC)
- $\gamma +$ jets event selection

  ≥ 1 photons

  veto photon $1.52 < |\eta| < 1.61$

  No selected leptons

  Leading photon object has to pass electron-photon ambiguity solver.

Cut	Value/description
Baseline jet	
Collection	`AntiKt4EMTopo`
Acceptance	$p_{\mathrm{T}} > 20$ GeV , $|\eta| < 2.8$
Signal jet	
Acceptance	$p_{\mathrm{T}} > 30$ GeV , $|\eta| < 2.5$
JVT	$|\mathrm{JVT}| > 0.59$ for jets with $p_{\mathrm{T}} < 60$ GeV and $|\eta| < 2.4$
Signal b-jet	
b-tagger Algorithm	MV2c20
Efficiency	77 %
Acceptance	$p_{\mathrm{T}} > 30$ GeV , $|\eta| < 2.5$
JVT	$|\mathrm{JVT}| > 0.59$ for jets with $p_{\mathrm{T}} < 60$ GeV and $|\eta| < 2.4$

Table 5.3: Summary of the jet and b-jet selection criteria. The signal selection requirements are applied on top of the baseline requirements.

- $Z +$ jets event selection

  At least two selected leptons

Note that the triggers for the γ + jets events triggered by photons with $p_{\mathrm{T}} < 125$ GeV (2015) or $p_{\mathrm{T}} < 145$ GeV (2016) are prescaled. , i.e. only a fraction of events that fired the triggers were recorded. These events are weighted according to the prescale factors that are provided centrally by ATLAS Data Preparation.

Range	Trigger
2015 triggers	
$37 < p_T < 45$ GeV	HLT_g35_loose_L1EM15
$45 < p_T < 50$ GeV	HLT_g40_loose_L1EM15
$50 < p_T < 55$ GeV	HLT_g45_loose_L1EM15
$55 < p_T < 125$ GeV	HLT_g50_loose_L1EM15
$p_T > 125$ GeV	HLT_g120_loose
2016 triggers	
$37 < p_T < 40$ GeV	HLT_g25_loose_L1EM15
$40 < p_T < 45$ GeV	HLT_g35_loose_L1EM15
$45 < p_T < 50$ GeV	HLT_g40_loose_L1EM15
$50 < p_T < 55$ GeV	HLT_g45_loose_L1EM15
$55 < p_T < 65$ GeV	HLT_g50_loose_L1EM15
$65 < p_T < 75$ GeV	HLT_g60_loose
$75 < p_T < 85$ GeV	HLT_g70_loose
$85 < p_T < 105$ GeV	HLT_g80_loose
$105 < p_T < 145$ GeV	HLT_g100_loose
$p_T > 145$ GeV	HLT_g140_loose

Table 5.4: Single photon triggers used in the phtoon template method.

Reweighting Region Definition	CR $Z+\text{jets}$	CR $\gamma+\text{jets}$
	2 SFOS leptons	≥ 1 photon
	lepton $p_T > 25$ GeV	photon $p_T > 50$ GeV
	b-tagged jet veto	
	≥ 2 jets	
	$H_T > 200$ GeV	

Table 5.5: The definition of the $Z+\text{jets}$ reweighting control region, where the reweighting factor for $\gamma+\text{jets}$ prediction is derived. Note that $H_T > 200$ GeV requirement is made to provide a proper estimate in a signal region with $H_T > 200$ GeV cut. For other signal regions with different H_T cuts (or other kinrematic cuts), this requirement should be changed accordingly.

5.3 Event reweighting of the photon template method

To model $Z+$ jets events, $\gamma+$ jets events have to be rescaled to match $Z+\text{jets}$ normalization. The difference in the normalizations is due to the cross-sections of γ v.s. Z productions and due to the fact that photons are massless particles, while Z bosons have a mass at 91 GeV. Therefore, a correction in $\gamma+$ jets kinematics is needed. The kinematics of $\gamma+$ jets events is corrected by normalizing the $\gamma+\text{jets}$ event yields to match $Z+\text{jets}$ event yields as function of $p_{\mathrm{T}}(Z/\gamma)$. In MC events, the correction factor (reweighting) is measured as

$$f(x) = \frac{N_{Z+\text{jets}}(x)}{N_{\gamma+\text{jets}}(x)}$$

and in data, as

$$f(x) = \frac{N_{\text{data}}(x) - N_{t\bar{t}}(x) - N_{\text{VV}}(x)}{N_{\gamma+\text{jets data}}(x)},$$

where x is the kinematic variable of interest (nominally boson-p_{T}).

The events that are used in deriving the reweighting factors pass the requirements in Tab. 5.5.

Figure 5.5 shows the kinematic distributions of γ+jets events after reweighting compared to that of $Z+\text{jets}$ events. The reweighting is done as function of $p_{\mathrm{T}}(Z)$, and from the plots we can see that the hadronic distributions, such as H_{T} and N_{jets}, are well modeled after reweighting. In Figure 5.6 (a), we also show the jet p_{T} distribution in the 1-jet channel, where a good agreement between γ and Z events are seen after reweighting. However, in Figure 5.6 (b), where the $E_{\mathrm{T}}^{\mathrm{miss}}$ distributions of γ and Z events are compared in the 1-jet channel, we see that reweighting alone cannot fully correct the difference between $Z+$ jets and $\gamma+$ jets in $E_{\mathrm{T}}^{\mathrm{miss}}$ distributions. The remaining difference in $E_{\mathrm{T}}^{\mathrm{miss}}$ distributions is due to the difference in γ v.s. Z boson p_{T} resolutions, which will be discussed in the next section.

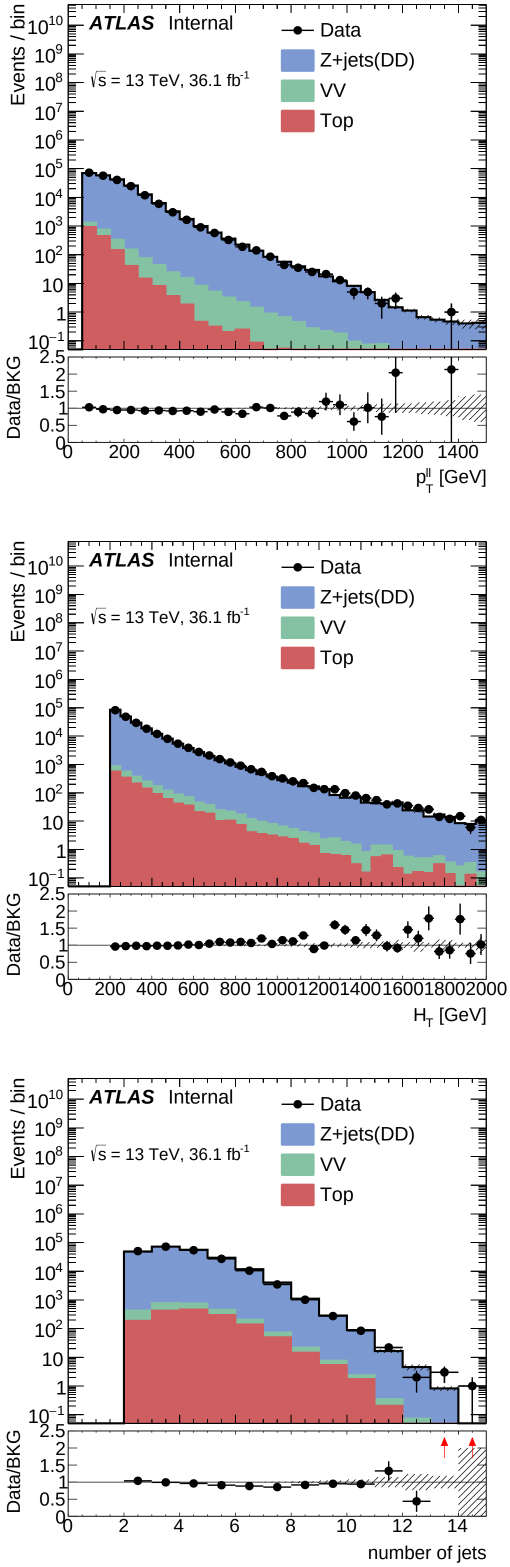

Figure 5.5: Compare $\gamma+$jets event distributions (after reweighting) to the distributions of dilepton data events. The VV and $t\bar{t}$ are provided by MC simulations. The selection in this plot requires two OSSF leptons with $m_{ll} \in [61, 121]$ GeV, at least two jets with $p_{\mathrm{T}} > 30$ GeV, and $H_{\mathrm{T}} > 200$ GeV.

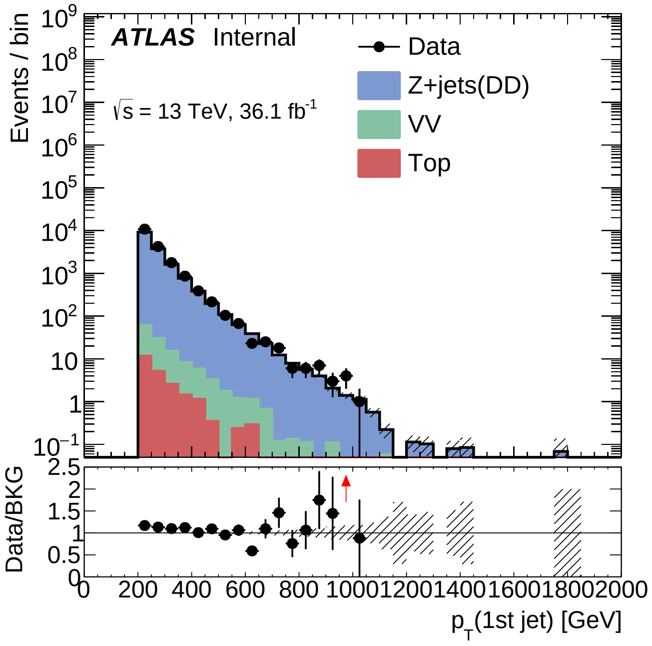

(a) jet p_{T}

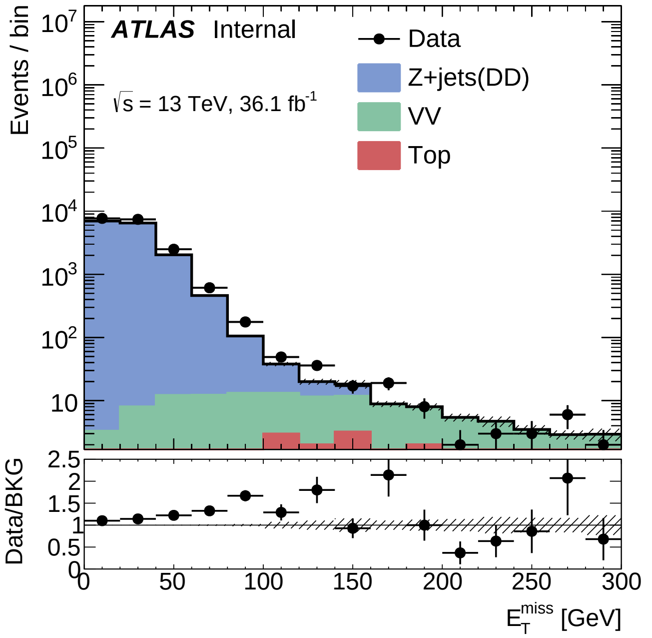

(b) $E_{\mathrm{T}}^{\mathrm{miss}}$

Figure 5.6: Compare $\gamma +$jets event distributions (after reweighting) to the distributions of dilepton data events. The VV and $t\bar{t}$ are provided by MC simulations. The selection in this plot requires two OSSF leptons with $m_{ll} \in [61, 121]$ GeV, exactly one jet with $p_{\mathrm{T}} > 30$ GeV, and $H_{\mathrm{T}} > 200$ GeV. The midmodeling of the $E_{\mathrm{T}}^{\mathrm{miss}}$ distribution is due to the difference between γ v.s. Z resolutions.

5.4 Boson p_{T} smearing of the photon template method

In the previous section we learned that the agreement of $E_{\mathrm{T}}^{\mathrm{miss}}$ shapes between $Z+\text{jets}$ and $\gamma+\text{jets}$ events cannot be fully closed by reweighting $\gamma+\text{jets}$ events alone. Since there is no difference in hadronic kinematics of $Z+\text{jets}$ and $\gamma+\text{jets}$ events (see Figure 5.6 (a)), the difference in $E_{\mathrm{T}}^{\mathrm{miss}}$ shapes must be from the resolutions of the bosons. To investigate the difference in $E_{\mathrm{T}}^{\mathrm{miss}}$ distributions, we separate $E_{\mathrm{T}}^{\mathrm{miss}}$ in $Z \to ee$ and $Z \to \mu\mu$ channels in Fig. 5.7. The simplify the event topology and to reduce the contribution from $t\bar{t}$ events, we use $Z + 1$ jet and $\gamma + 1$ jet to demonstrate the problem and how the smearing method can solve it.

In Figure 5.7, we see that the $E_{\mathrm{T}}^{\mathrm{miss}}$ shapes of $Z+\text{jets}$ and $\gamma+\text{jets}$ events agree well in the ee channel but very poorly in the $\mu\mu$ channel. $Z+\text{jets}$ events and $\gamma+\text{jets}$ events agree well in the ee channel because both photon and electron energies are reconstructed in the EM calorimeter, and their energy resolutions have simliar energy dependence, $\sigma(E) \sim \sqrt{E}$ (resolution scales as the statistical fluctuation of number of interactions in calorimeter material). On the other hand, muon momentum is reconstructed in the muon spectrometer, and the muon resolution depends on the measurement of muon track curvature and is described by Gluckstern formula ($\sigma(p_T)/p_T \sim p_T$).

To see further how boson resolutions affect the shapes of $E_{\mathrm{T}}^{\mathrm{miss}}$, we decompose $E_{\mathrm{T}}^{\mathrm{miss}}$ into $E_{\mathrm{T},\parallel}^{\mathrm{miss}} = E_{\mathrm{T}}^{\mathrm{miss}} \times \cos\phi$ and $E_{\mathrm{T},\perp}^{\mathrm{miss}} = E_{\mathrm{T}}^{\mathrm{miss}} \times \sin\phi$, where ϕ is the azimuthal angle between $E_{\mathrm{T}}^{\mathrm{miss}}$ and the boson momentum. The $E_{\mathrm{T},\parallel}^{\mathrm{miss}}$ component convolves both hadronic and leptonic mismeasurements, while the $E_{\mathrm{T},\perp}^{\mathrm{miss}}$ component only involves hadronic contribution. The distributions of $E_{\mathrm{T},\parallel}^{\mathrm{miss}}$ and $E_{\mathrm{T},\perp}^{\mathrm{miss}}$ are shown in Figure 5.8 for the ee channel and in Figure 5.9 for the $\mu\mu$ channel, separately. The $E_{\mathrm{T},\perp}^{\mathrm{miss}}$ components of $Z+\text{jets}$ and $\gamma+\text{jets}$ agree well in both ee and $\mu\mu$ channels because only hadronic kinematic mismeasurements contribute to $E_{\mathrm{T},\perp}^{\mathrm{miss}}$, and there is no difference in hadronic kinematics in $Z+\text{jets}$ and $\gamma+\text{jets}$ events. The $E_{\mathrm{T},\parallel}^{\mathrm{miss}}$ components of $Z+\text{jets}$ and $\gamma+\text{jets}$ also agree well in ee channel, and this is due to that electron and photon energy resolutions are similar in EM Calorimeter. Finally in the $E_{\mathrm{T},\parallel}^{\mathrm{miss}}$ component in $\mu\mu$ channel, $Z+\text{jets}$ and $\gamma+\text{jets}$ events disagree espectially in the tail of $E_{\mathrm{T},\parallel}^{\mathrm{miss}}$, in contrast to the three other plots. The discrepancy in $\mu\mu$ channel can be understood as the resolution difference between EM Calorimeter v.s. Muon Spectrometer, which leads to the long

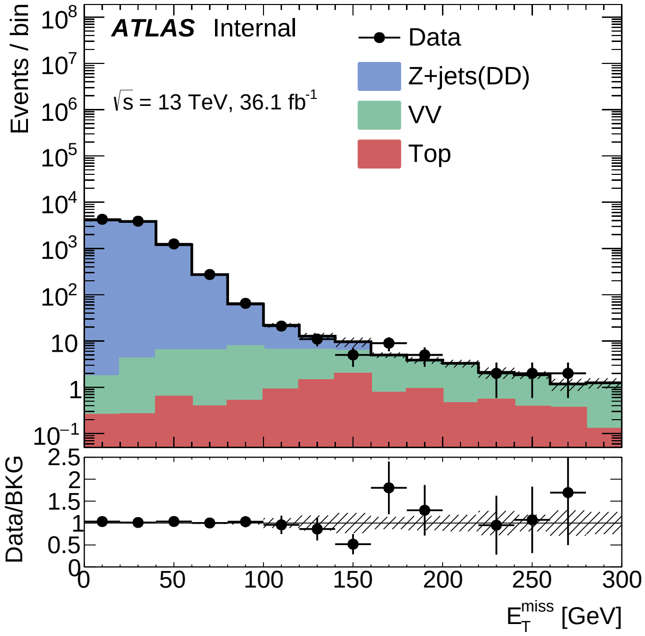

(a) $E_{\mathrm{T}}^{\mathrm{miss}}$ in ee channel

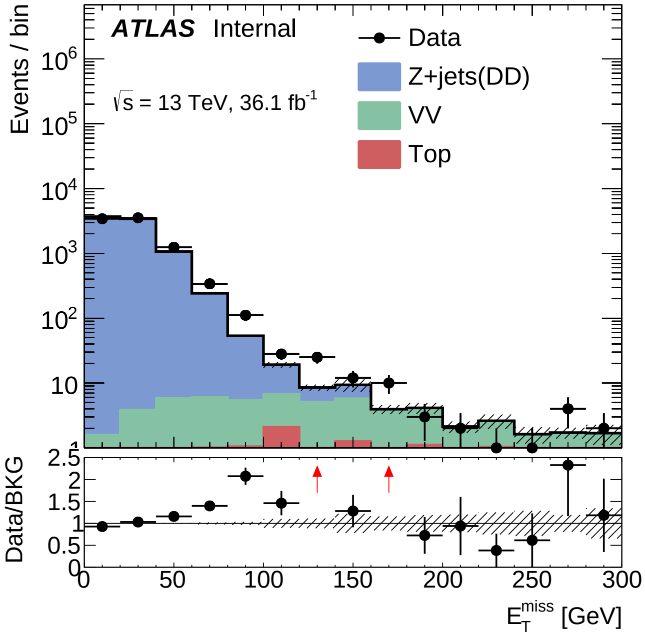

(b) $E_{\mathrm{T}}^{\mathrm{miss}}$ in $\mu\mu$ channel

Figure 5.7: Compare $\gamma +$jets event distributions (after reweighting) to the distributions of dilepton data events. The shapes agree well in ee channel but poorly in $\mu\mu$ channel. The VV and $t\bar{t}$ are provided by MC simulations. The selection in this plot requires two OSSF leptons with $m_{ll} \in [61, 121]$ GeV, exactly one jet with $p_{\mathrm{T}} > 30$ GeV, and $H_{\mathrm{T}} > 200$ GeV.

tail of $E_{\mathrm{T},\parallel}^{\mathrm{miss}}$ in $Z+$jets events.

The most straightforward way to solve the discrepancy in Fig. 5.9 would be taking the $Z \to \mu\mu$ response function $R(p_{\mathrm{T}}^{\mathrm{reco}}(Z) - p_{\mathrm{T}}^{\mathrm{truth}}(Z))$ from MC as a smearing function, and using the smearing function to sample a random number per event to smear the photon resolution. However, this solution is problematic for two reasons. First, the photon resolution isn't perfect, so if we simply take $R(p_{\mathrm{T}}^{\mathrm{reco}}(Z) - p_{\mathrm{T}}^{\mathrm{truth}}(Z))$ as the smearing function, we will overestimate the muon mis-measurement in the photon template method. The photon resolution needs to be taken into account when we smear the photon momentum. Second, muons are charged particles and they can radiate photons (final state radiation, FSR) before entering detector material. Once these FSR photons pass/fail the baseline requirement, they will be included/excluded in $E_{\mathrm{T}}^{\mathrm{miss}}$ computation, which cannot be fully accounted in the response function $R(p_{\mathrm{T}}^{\mathrm{reco}}(Z) - p_{\mathrm{T}}^{\mathrm{truth}}(Z))$. Furthermore, FSR can also make the computation of di-lepton mass tricky when one tries to associate m_{ll} with lepton mis-measurement using the truth information.

To properly model $p_T(Z)$ resolution while taking into account the photon resolution and final-state radiations, we invoke the convolution theorem. Before we can find the seamring function, we need to understand how to interpret the process of smearing function mathematically. Suppose we knew the resolution of photon is as a probability function $R_\gamma(p_\gamma - t)$, where p as the reco value of the momentum, t as the truth value, and $p - t$ as the momentum mis-measuremnt, and the resoluton of Z boson as $R_Z(p_Z - t)$. Then we take a random number Δ from a probability function $S(\Delta - t)$ and add it to p_γ. We perform this process on each photon event, and with enough statistics we wish to reshape $R_\gamma(p_\gamma - t)$ to match $R_Z(p_Z - t)$. This process can be expressed as

$$\int dt_\gamma R_\gamma(p_\gamma - t_\gamma) S(\Delta - t_Z + t_\gamma) = R_Z(p_\gamma + \Delta - t_Z)$$

or in Fourier space, as

$$\hat{R_\gamma} \hat{S} = \hat{R_Z}$$

which means the smearing function that we need is simply

$$\hat{S} = \hat{R_Z} / \hat{R_\gamma}.$$

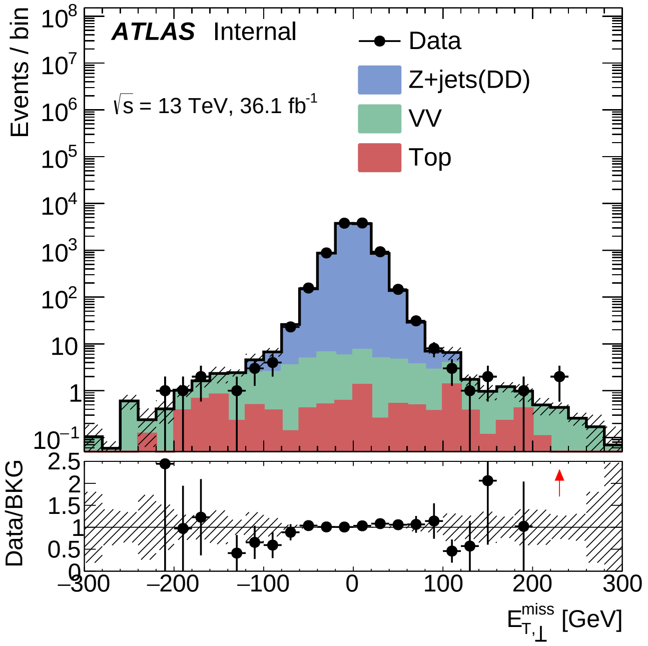

(a) $E_{\mathrm{T},\perp}^{\mathrm{miss}}$ in ee channel

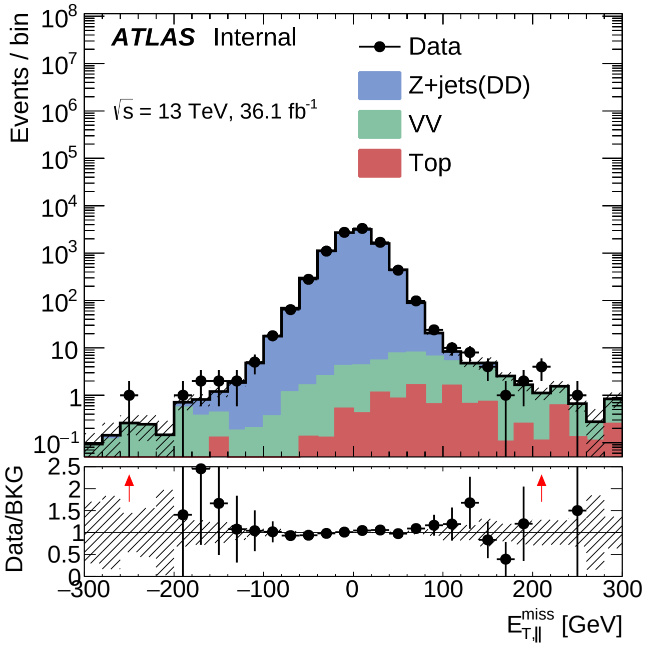

(b) $E_{\mathrm{T},\parallel}^{\mathrm{miss}}$ in ee channel

Figure 5.8: Compare $Z+$jets v.s. $\gamma+$jets (after reweighting) $E_{\mathrm{T},\perp}^{\mathrm{miss}}$ and $E_{\mathrm{T},\parallel}^{\mathrm{miss}}$ shapes in the ee channel. The VV and $t\bar{t}$ are provided by MC simulations. The selection in this plot requires two OSSF leptons with $m_{ll} \in [61, 121]$ GeV, exactly one jet with $p_{\mathrm{T}} > 30$ GeV, and $H_{\mathrm{T}} > 200$ GeV.

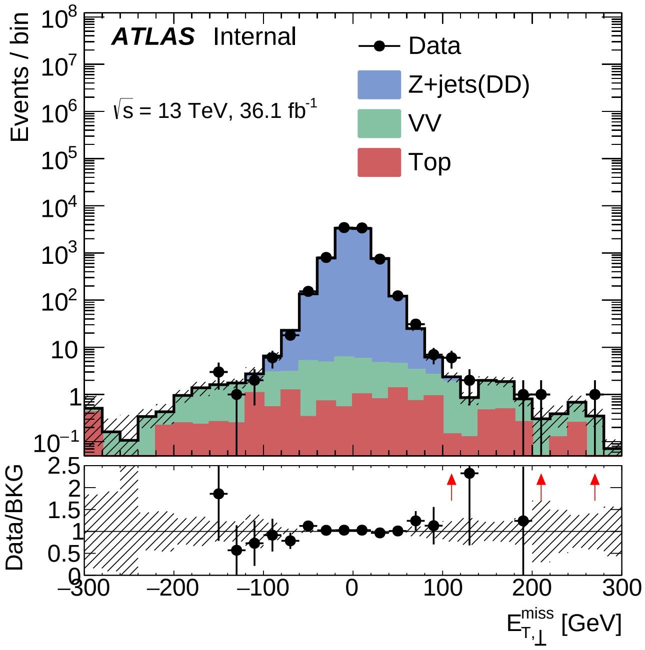

(a) $E_{\mathrm{T},\perp}^{\mathrm{miss}}$ in $\mu\mu$ channel

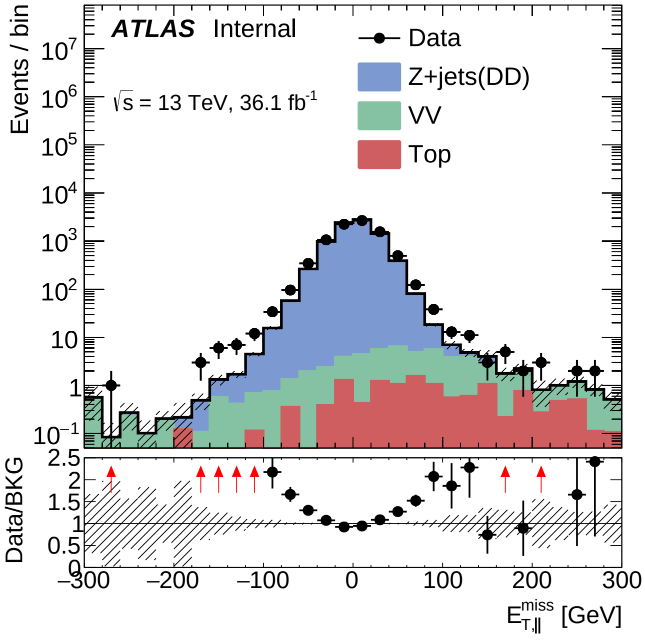

(b) $E_{\mathrm{T},\parallel}^{\mathrm{miss}}$ in $\mu\mu$ channel

Figure 5.9: Compare $Z+$jets v.s. $\gamma+$jets (after reweighting) $E_{\mathrm{T},\perp}^{\mathrm{miss}}$ and $E_{\mathrm{T},\parallel}^{\mathrm{miss}}$ shapes in the $\mu\mu$ channel. The VV and $t\bar{t}$ are provided by MC simulations. The selection in this plot requires two OSSF leptons with $m_{ll} \in [61, 121]$ GeV, exactly one jet with $p_{\mathrm{T}} > 30$ GeV, and $H_{\mathrm{T}} > 200$ GeV. The discrepancy in $E_{\mathrm{T},\parallel}^{\mathrm{miss}}$ in $\mu\mu$ channel can be understood as the resolution difference in EM Calorimeter v.s. Muon Spectrometer.

The resolution $R_\gamma(p_\gamma - t)$ and $R_Z(p_Z - t)$ are encoded in the shape of $E_{\mathrm{T},\parallel}^{\mathrm{miss}}$. In the simplest case of $Z + 1$ jet, $E_{\mathrm{T},\parallel}^{\mathrm{miss}} = p_Z + p_{jet} = \Delta p_Z + \Delta p_{jet}$, where $\Delta p_Z = p_Z - t$ is the Z boson mismeasurement, and $\Delta p_{jet} = t - p_{jet}$ is the jet mismeasurement. Then the spectrum of $E_{\mathrm{T},\parallel}^{\mathrm{miss}}$ is

$$f_Z(E_{\mathrm{T},\parallel}^{\mathrm{miss}}) = \int dt R_Z(p_Z - t) R_{jet}(t - p_{jet})$$

and again in Fourier space

$$\hat{f}_Z(E_{\mathrm{T},\parallel}^{\mathrm{miss}}) = \hat{R}_Z \hat{R_{jet}}$$

where R_{jet} is the resolution function of a signle jet. Similarly in the case of $\gamma + 1$ jet, we have

$$\hat{f}_\gamma(E_{\mathrm{T},\parallel}^{\mathrm{miss}}) = \hat{R}_\gamma \hat{R_{jet}}.$$

Now if we divide these two equations, we get

$$\hat{f}_Z(E_{\mathrm{T},\parallel}^{\mathrm{miss}}) / \hat{f}_\gamma(E_{\mathrm{T},\parallel}^{\mathrm{miss}}) = \hat{R}_Z / \hat{R}_\gamma$$

which is the smearing function we need. Therefore the smearing function in question can be extracted from the deconvolution of the shapes of $E_{\mathrm{T}}^{\mathrm{miss}}$ in Z+jets and γ+jets events in control regions (1-jet regions), without knowing the truth information in MC (which means we can also derive the smearing function from data!). In Fig. 5.10 we can see two examples of the smearing fucntios that we derived from 1-jet regions with the deconvolution method. In the low $p_T(Z/\gamma)$ range, when the photon resolution and the Z resolution are comparable, the smearing function looks like a narrow δ-function because no smearing will be needed. As we move to higher $p_T(Z/\gamma)$ range, the track-based muon resolution becomes worse than the calorimeter-based photon resolution, and thus we need a wide smearing function to modify the photon resoluton. These variations in boson resolutions are encoded in the shapes of $E_{\mathrm{T},\parallel}^{\mathrm{miss}}$, and by deconvolving the $E_{\mathrm{T},\parallel}^{\mathrm{miss}}$ shapes, we are able to extract the difference between photon v.s. Z resolutions, i.e. the smearing functions. The $E_{\mathrm{T}}^{\mathrm{miss}}$ distributions after smearing can be found in Fig. 5.11 and 5.12.

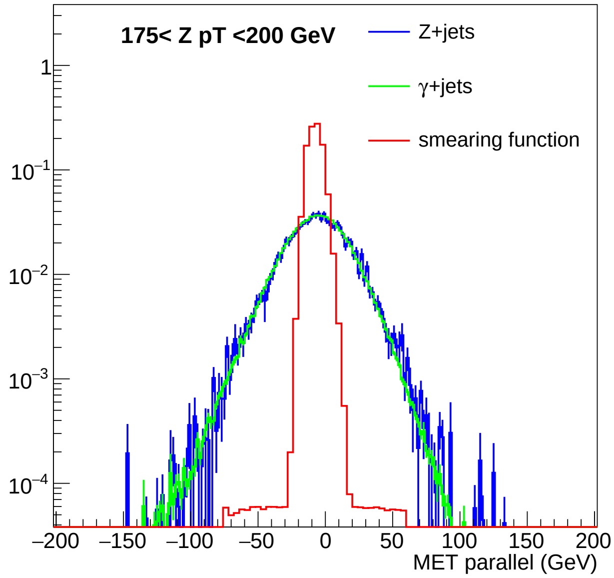

(a) Smearing function in $p_T \in (175, 200)$ GeV range.

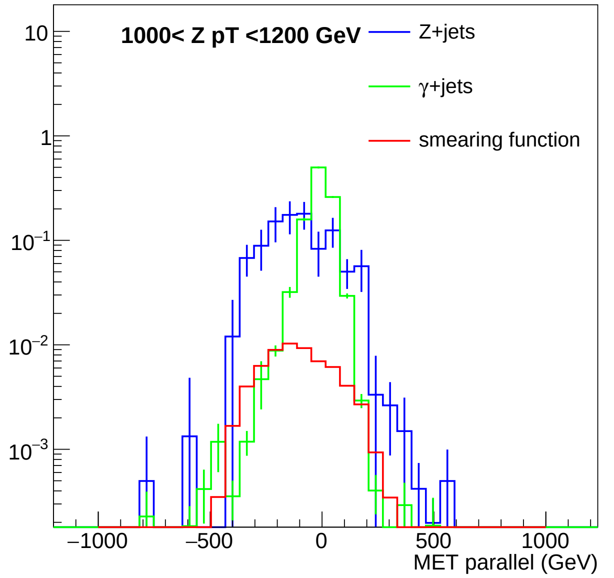

(b) Smearing function in $p_T \in (1000, 1200)$ GeV range.

Figure 5.10: A few examples of the smearing functions in $\mu\mu$ channel that we derived from the 1-jets region. Blue represents the $E_{\mathrm{T},\parallel}^{\mathrm{miss}}$ in $Z+$jets MC, and green represents the $\gamma+$jets MC before applying smearing. When the Z and γ resolutions are similar (figure a), the $E_{\mathrm{T},\parallel}^{\mathrm{miss}}$ distributions of $Z+$jets and $\gamma+$jets are also similar. This results in a narrow smearing function (red), since no smearing is needed to apply to the photon events. However, when the Z and γ resolutions are not similar (figure b), the smearing function becomes wider in order to reshape the $E_{\mathrm{T},\parallel}^{\mathrm{miss}}$ distribution of $\gamma+$jets to match $Z+$jets.

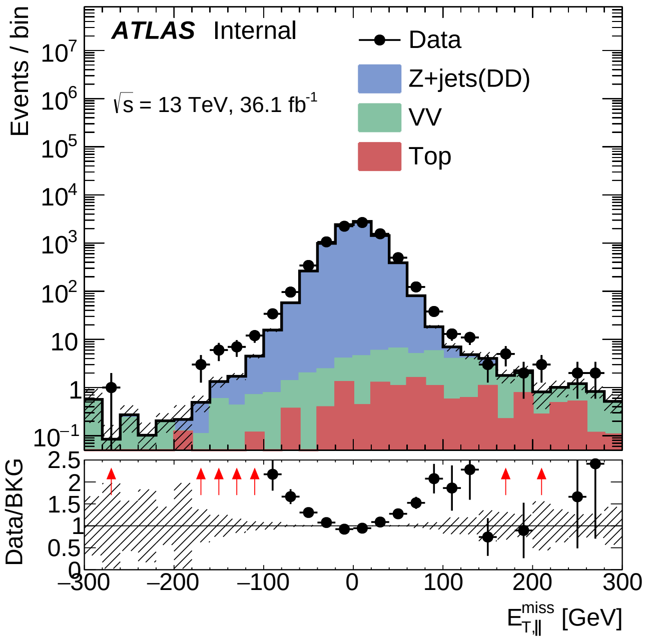

(a) $E_{\mathrm{T},\parallel}^{\mathrm{miss}}$ in $\mu\mu$ channel before smearing

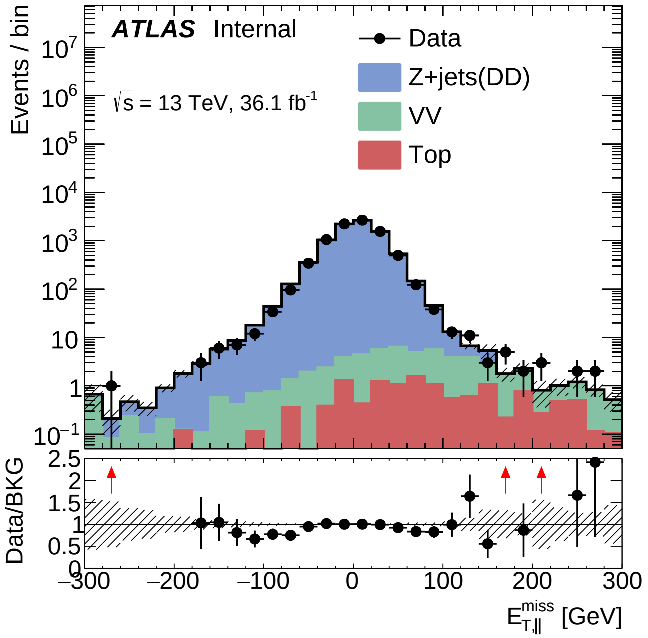

(b) $E_{\mathrm{T},\parallel}^{\mathrm{miss}}$ in $\mu\mu$ channel after smearing

Figure 5.11: Compare $Z+\mathrm{jets}$ v.s. $\gamma+\mathrm{jets}$ (before and after smearing) $E_{\mathrm{T},\parallel}^{\mathrm{miss}}$ shapes in the $\mu\mu$ channel. The VV and $t\bar{t}$ are provided by MC simulations. The selection in this plot requires two OSSF leptons with $m_{ll} \in [61, 121]$ GeV, exactly one jet with $p_{\mathrm{T}} > 30$ GeV, and $H_{\mathrm{T}} > 200$ GeV.

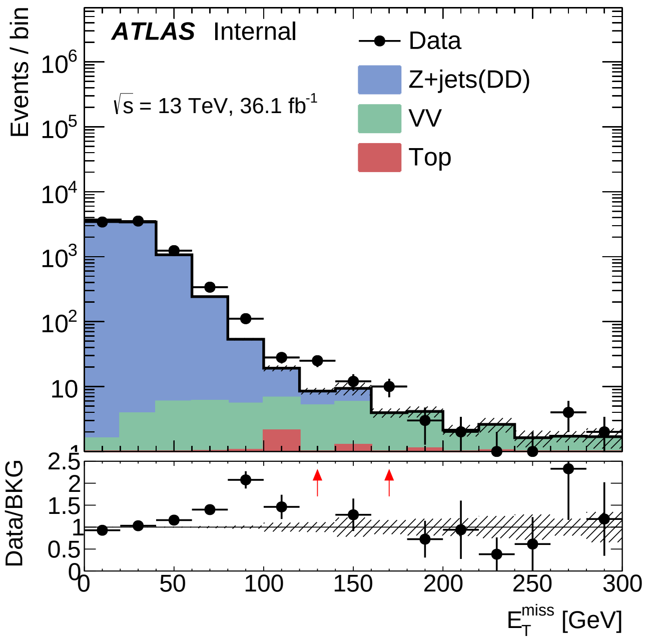

(a) $E_{\mathrm{T}}^{\mathrm{miss}}$ in $\mu\mu$ channel before smearing

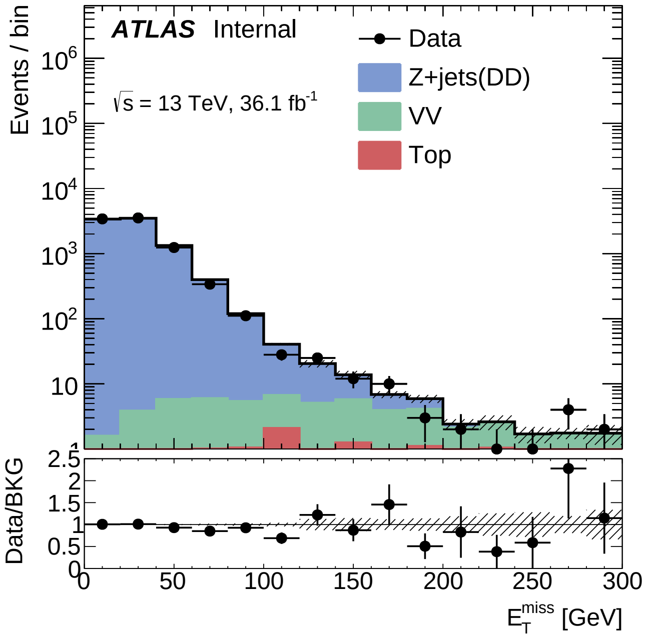

(b) $E_{\mathrm{T}}^{\mathrm{miss}}$ in $\mu\mu$ channel after smearing

Figure 5.12: Compare $Z+\text{jets}$ v.s. $\gamma+\text{jets}$ (before and after smearing) $E_{\mathrm{T}}^{\mathrm{miss}}$ shapes in the $\mu\mu$ channel. The VV and $t\bar{t}$ are provided by MC simulations. The selection in this plot requires two OSSF leptons with $m_{ll} \in [61, 121]$ GeV, exactly one jet with $p_{\mathrm{T}} > 30$ GeV, and $H_{\mathrm{T}} > 200$ GeV.

5.5 Modelling di-lepton mass

Photons are massless particles. To model the $Z+$jets events, we need to assign a fake di-lepton mass (m_{ll}) to each photon event. We use Monte Carlo $Z+$jets events to build m_{ll} template histograms, and then we sample random m_{ll} values from these histograms for photon events. Di-lepton mass is a quantity that is strongly correlated with the mis-measurement of lepton energies. Thus, the m_{ll} templates are made as function of $p_T(ll)$ and $E_{T,\parallel}^{miss}$, which are the two variables telling us the mis-measurement of leptons.

These template histograms are made with MC events that pass the following selection:

- $N_{jets} \geq 1$
- lepton $p_T > 25$ GeV
- $p_T(Z) > 25$ GeV

Then the histograms are parametrized in $p_T(Z)$ and in $E_{T,\parallel}^{miss}$. Remember that $E_{T,\parallel}^{miss}$ is the projection of E_T^{miss} in the direction of Z boson, so the sign and the size of of $E_{T,\parallel}^{miss}$ reflects the lepton mis-measurement. Fig. 5.13 shows the m_{ll} distributions in $p_T \in [300, 400]$ GeV slice, in 3 different $E_{T,\parallel}^{miss}$ ranges. While the m_{ll} shape doesn't change much in ee channel as $E_{T,\parallel}^{miss}$ varies (because $E_{T,\parallel}^{miss}$ is still dominated by jet mis-measurement in ee channel), the m_{ll} shape in $\mu\mu$ channel shows an underestimated Z mass value in $E_{T,\parallel}^{miss} \in [-150, -100]$ GeV slice and an overestimated Z mass value in $E_{T,\parallel}^{miss} \in [100, 150]$ GeV slice. Using the m_{ll} templates (examples shown in Fig. 5.13), we perform a closure test in Fig. 5.14 and Fig. 5.15, where the effect of lepton mismeasurement can be seen in the change of m_{ll} shapes with different $E_{\mathrm{T}}^{\mathrm{miss}}$ selections in the ee v.s. $\mu\mu$ channels.

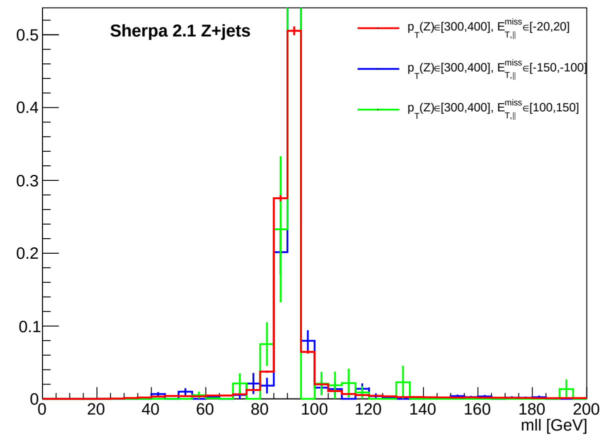

(a) m_{ll} templates in ee channel

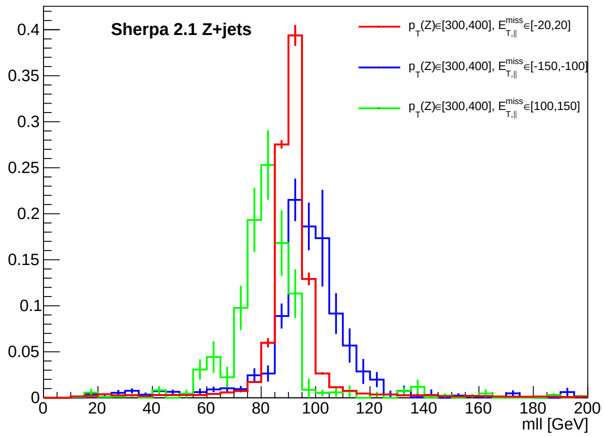

(b) m_{ll} templates in $\mu\mu$ channel

Figure 5.13: Examples of m_{ll} templates of MC $Z+$jets events in ee and $\mu\mu$ channels. The events are selected in $p_T \in [300, 400]$ GeV slice. The distributions are shown in 3 different $E_{T,\parallel}^{miss}$ ranges: $[-150, -100]$ (blue), $[-20, 20]$ (red), $[100, 150]$ (green) GeV.

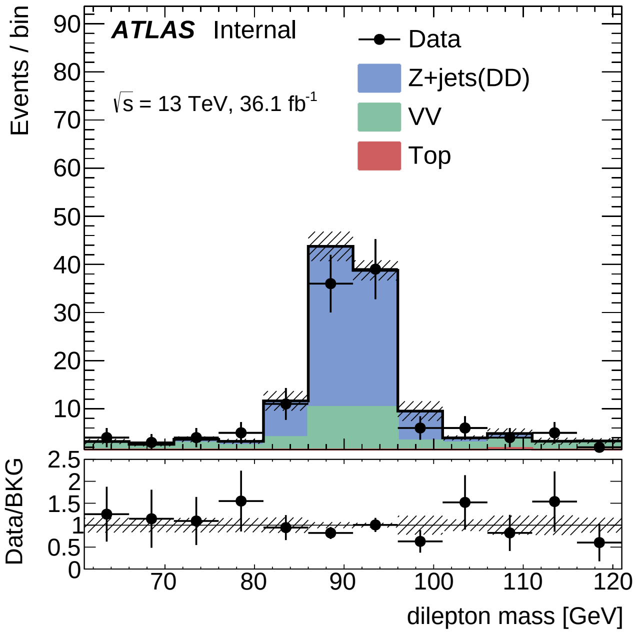

(a) m_{ll} closure test in ee channel with $E_{\mathrm{T}}^{\mathrm{miss}} > 80$ GeV

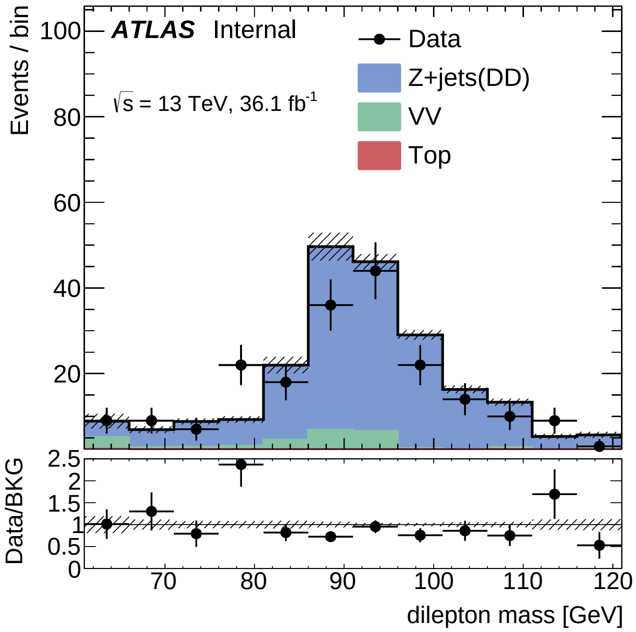

(b) m_{ll} closure test in $\mu\mu$ channel with $E_{\mathrm{T}}^{\mathrm{miss}} > 80$ GeV

Figure 5.14: Closure test of m_{ll} modelling in the 1-jet channel. The VV and $t\bar{t}$ are provided by MC simulations. The selection in this plot requires two OSSF leptons with $m_{ll} \in [61, 121]$ GeV, exactly one jet with $p_{\mathrm{T}} > 200$ GeV, and $E_{\mathrm{T}}^{\mathrm{miss}} > 80$ GeV. The effect of lepton mismeasurement on the shape of m_{ll} can be seen by comparing the shapes in the ee channel (a) and in the $\mu\mu$ channel (b).

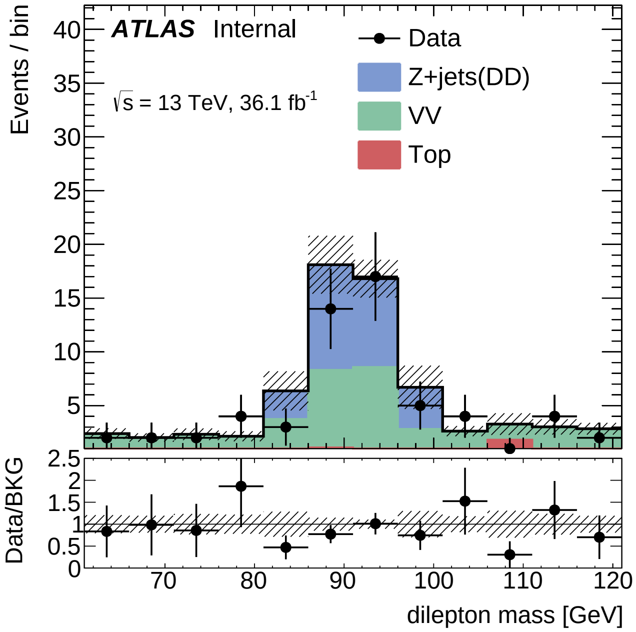

(a) m_{ll} closure test in ee channel with $E_{\mathrm{T}}^{\mathrm{miss}} > 100$ GeV

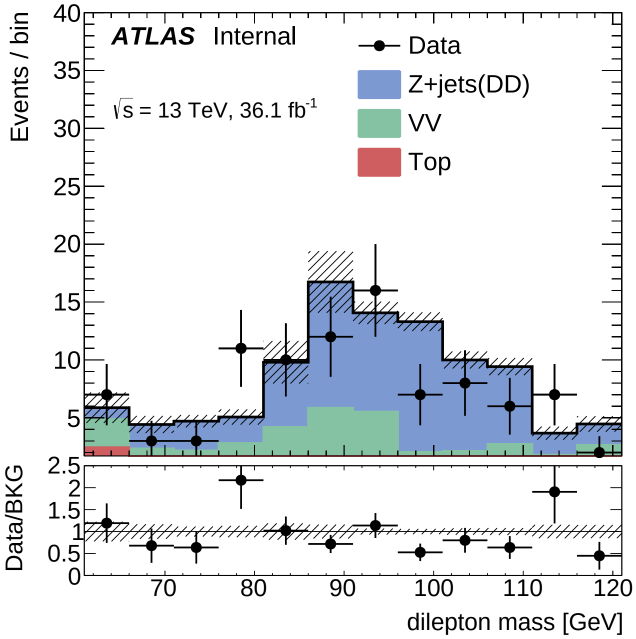

(b) m_{ll} closure test in $\mu\mu$ channel with $E_{\mathrm{T}}^{\mathrm{miss}} > 100$ GeV

Figure 5.15: Closure test of m_{ll} modelling in the 1-jet channel. The VV and $t\bar{t}$ are provided by MC simulations. The selection in this plot requires two OSSF leptons with $m_{ll} \in [61, 121]$ GeV, exactly one jet with $p_{\mathrm{T}} > 200$ GeV, and $E_{\mathrm{T}}^{\mathrm{miss}} > 100$ GeV. The effect of lepton mismeasurement on the shape of m_{ll} can be seen by comparing the shapes in the ee channel (a) and in the $\mu\mu$ channel (b).

5.6 Splitting photon to two leptons

Through the previous sections, we have discussed how to correct the kinematics difference and resolution difference between Z v.s. γ. We also discussed how to model the di-lepton mass of $Z+$jets events in the photon method. However, some variables require not only the jets and Z boson information, but also the information of two individual leptons. For example, m_{T2} is a powerful variable to reject backgrounds with a pair of $W \to \ell\nu$ decays, whose definition is given by

$$m_{T2} = \min_{\vec{p}_T^{\nu(1)} + \vec{p}_T^{\nu(2)} = \vec{p}_T^{miss}} \left[\max \left(m_T^{(1)}, m_T^{(2)} \right) \right]$$

, where

$$(m_T^{(i)})^2 = (m_\ell^{(i)})^2 + (m_\nu^{(i)})^2 + 2 \left(E_T^{\ell(i)} E_T^{\nu(i)} - \vec{p}_T^{\ell(i)} \cdot \vec{p}_T^{\nu(i)} \right)$$

The fomula requires the 3-vector of each lepton, which is not there in a photon event. To create a pair of imaginary leptons, we use the Z mass that we assigned in the previous section. We boost the system of a phton event to the "rest" frame of the photon with a fake Z mass. In the rest frame, the momentum of each lepton is simply $1/2$ of the Z mass, and the leptons are back-to-back to each other, and we choose the angular distribution of the lepton pair randomly. With the lepton momentum and direction defined in the rest frame, the Lab frame lepton kinematics is determined when we boost the system back to the Lab frame. The modelling of the two imaginary leptons is shown in Fig. 5.16 and m_{T2} in Fig. 5.17.

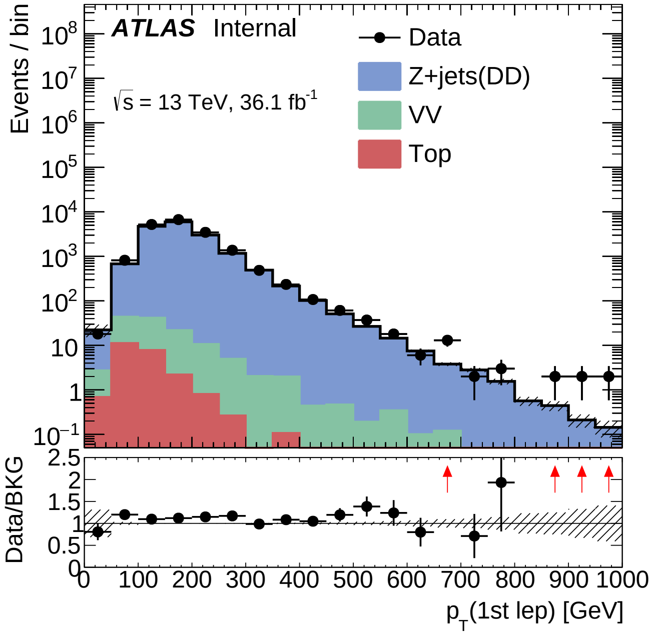

(a) Modelling leading lepton p_T

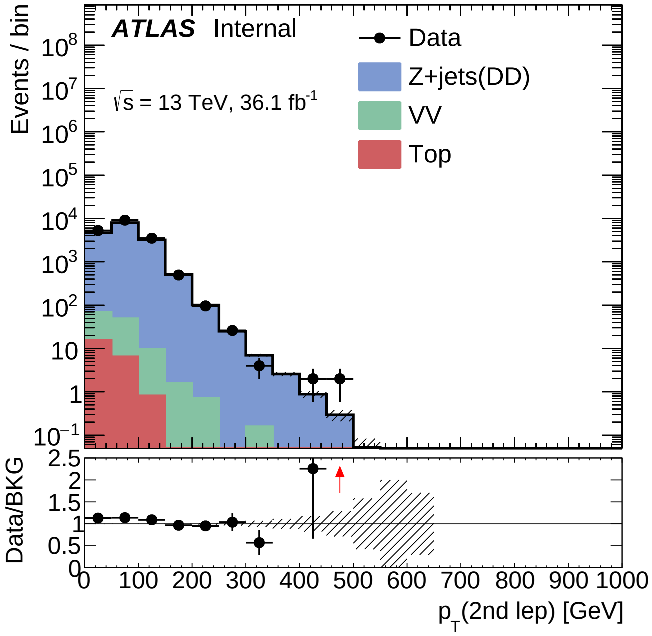

(b) Modelling second lepton p_T

Figure 5.16: Closure test of lepton p_T modellings in the 1-jet channel. The VV and $t\bar{t}$ are provided by MC simulations. The selection in this plot requires two OSSF leptons with $m_{ll} \in [61, 121]$ GeV, exactly one jet with $p_{\mathrm{T}} > 200$ GeV.

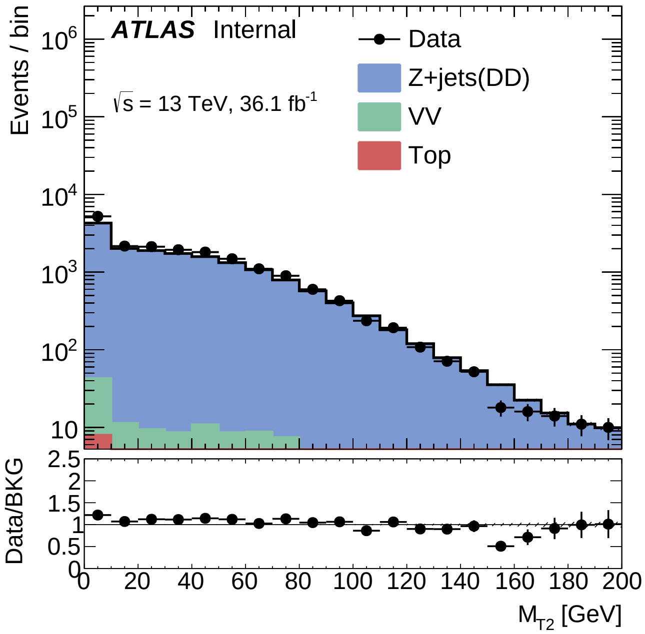

Figure 5.17: Closure test of m_{T2} modelling in the 1-jet channel. The VV and $t\bar{t}$ are provided by MC simulations. The selection in this plot requires two OSSF leptons with $m_{ll} \in [61, 121]$ GeV, exactly one jet with $p_{\mathrm{T}} > 200$ GeV.

5.7 Photon sample contamination

$\gamma+$jets events are selected to model the fake $E_{\mathrm{T}}^{\mathrm{miss}}$ from jet mis-measurement in $Z+$jets events. However, the $\gamma+$jets sample is contaminated with $V+\gamma$ events with real $E_{\mathrm{T}}^{\mathrm{miss}}$ from neutrinos. These contaminations have to be subtracted off from the $\gamma+$jets sample for the final prediction of $Z+$jets events. $V+\gamma$ MC sample is used to estimate the $V+\gamma$ in $\gamma+$jets data, with a scaling factor derived from a $\gamma+1\ell$ region. The definition of the control region for deriving the scaling factor requires:

- $N_{jets} \geq 1$
- $= 1$ signal lepton
- $p_T(\gamma) > 140$ GeV

Fig. 5.18 (a) shows a scaling factor of 1.5 is derived from the $\gamma+1\ell$ control region by comparing the MC-to-data ratio as function of $E_{\mathrm{T}}^{\mathrm{miss}}$. We validate this scaling factor in the $\gamma+0\ell$ region as shown in Fig. 5.18 (b). Note that the scaling factor that we derived from $\gamma+1\ell$ region depends on the selection of the baseline and signal lepton, and overlap removal procedure.

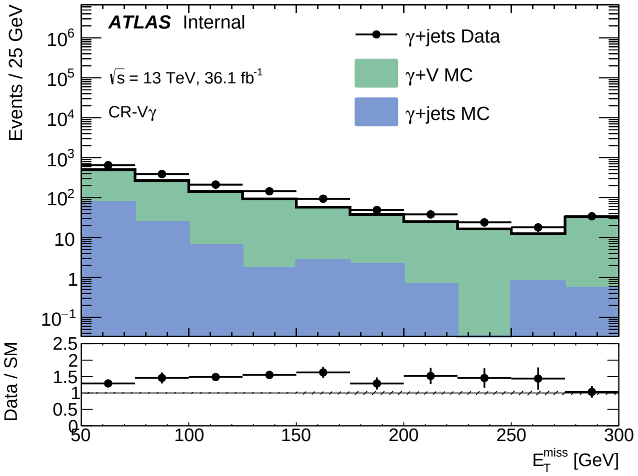

(a) $\gamma + 1\ell$ region.

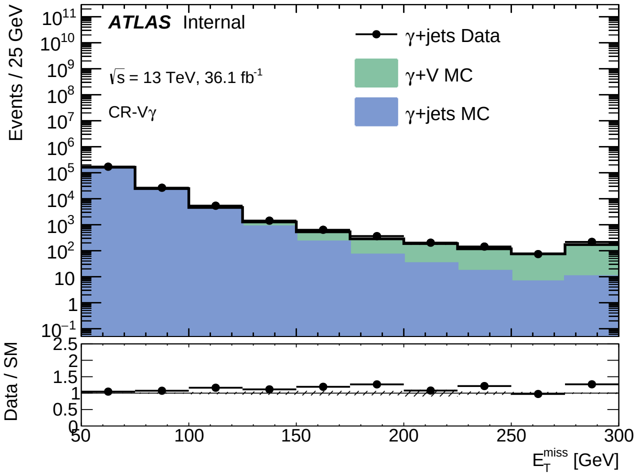

(b) $\gamma + 0\ell$ region.

Figure 5.18: A scaling factor for $V + \gamma$ MC events is derived from a control region containing $\gamma + 1\ell$ events. Then this scaling factor is applied to the $V + \gamma$ MC events and validated in the $\gamma + 0\ell$ region.

5.8 Photon method validation in $\geq$ 2jets channel

In this section, we show the validations of the photon template method in the $\geq$ 2jets channel. For the prediction in the $\geq$ 2jets channel, the smearing function for the lepton resolution correction is derived from the MC events in the 1-jet channel. Note that in Section 5.4, we mention that the output of the deconvolution method does not contain jet information, which allows us to use the smearing functions across different jet multiplicities. We will compare the photon predictions v.s. the dilepton events in data and in SHERPA2.1 MC.

The modeling of $E_{\mathrm{T}}^{\mathrm{miss}}$ distributions is shown in Figure 5.19. In the data closure plot, the $\gamma+$jets data events are used for the $Z+$jets prediction. In the MC closure plot, the $Z+$jets SHERPA2.1 MC events are compared to the prediction from $\gamma+$jets SHERPA2.1 MC events. We also show the validation of the modelings of other variables, such as H_T, N_{jets}, $\Delta\phi(E_{\mathrm{T}}^{\mathrm{miss}}, \mathrm{jet})$, and m_{ll}, in the large $E_{\mathrm{T}}^{\mathrm{miss}}$ region. These validations are shown in Figure 5.20-5.24.

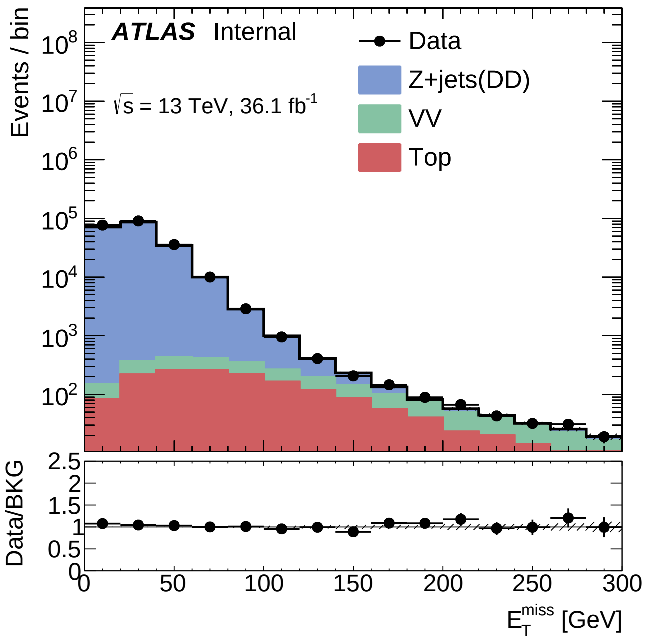

(a) Data closure test of $E_{\mathrm{T}}^{\mathrm{miss}}$ modeling

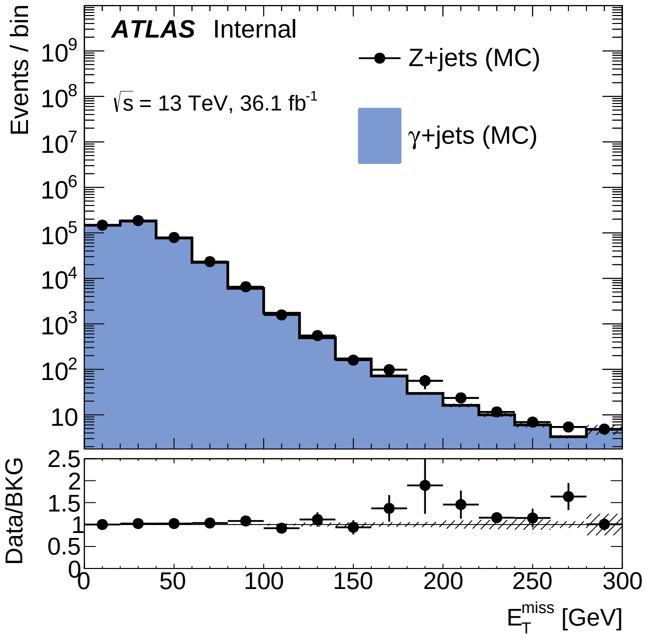

(b) MC closure test of $E_{\mathrm{T}}^{\mathrm{miss}}$ modeling

Figure 5.19: Closure test of $E_{\mathrm{T}}^{\mathrm{miss}}$ modeling in the $\geq$ 2jet channel. The VV and $t\bar{t}$ are provided by MC simulations in the data plot. The selection in this plot requires two OSSF leptons with $m_{ll} \in [61, 121]$ GeV, at least two jet with $p_{\mathrm{T}} > 30$ GeV, and $H_T > 200$ GeV.

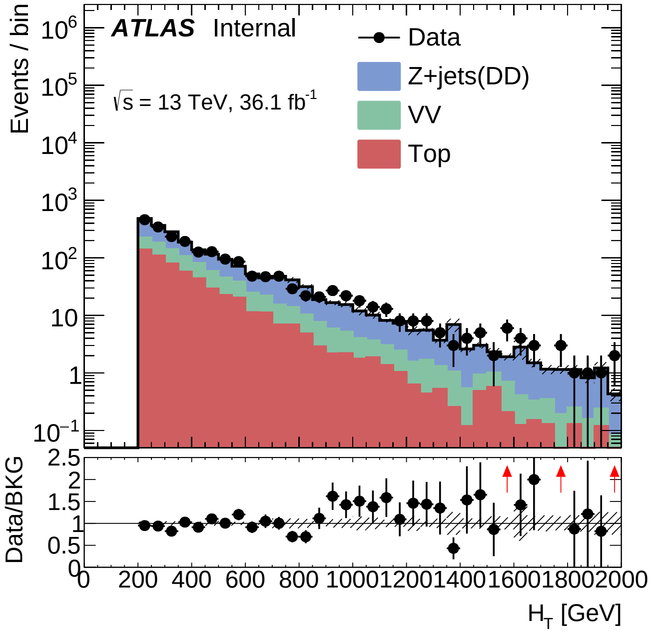

(a) Data closure test of H_T modeling

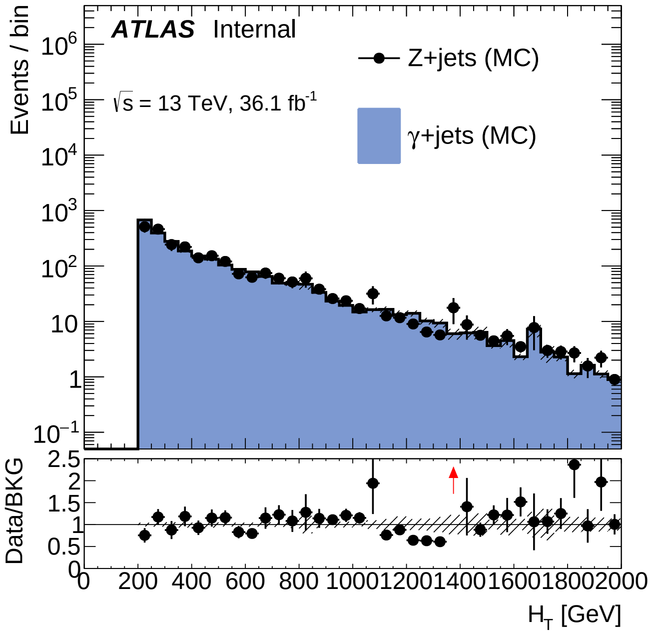

(b) MC closure test of H_T modeling

Figure 5.20: Closure test of $E_{\mathrm{T}}^{\mathrm{miss}}$ modeling in the $\geq$ 2jet channel. The VV and $t\bar{t}$ are provided by MC simulations in the data plot. The selection in this plot requires two OSSF leptons with $m_{ll} \in [61, 121]$ GeV, at least two jet with $p_{\mathrm{T}} > 30$ GeV, $H_T > 200$ GeV, and $E_{\mathrm{T}}^{\mathrm{miss}} > 100$ GeV.

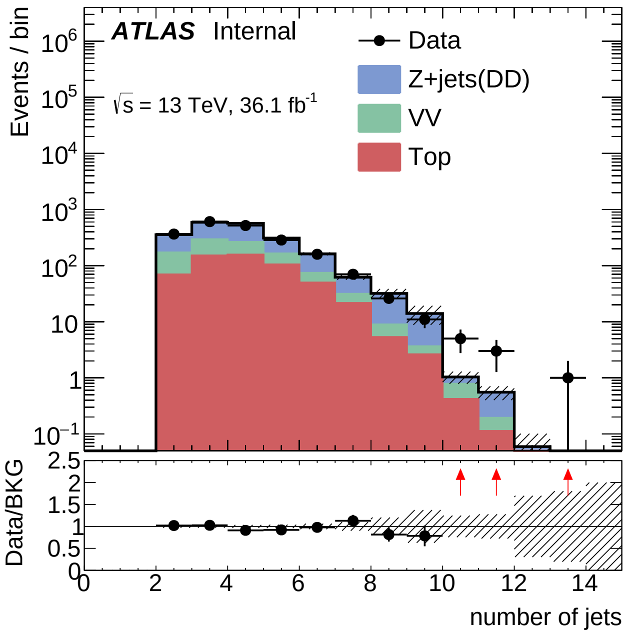

(a) Data closure test of N_{jets} modeling

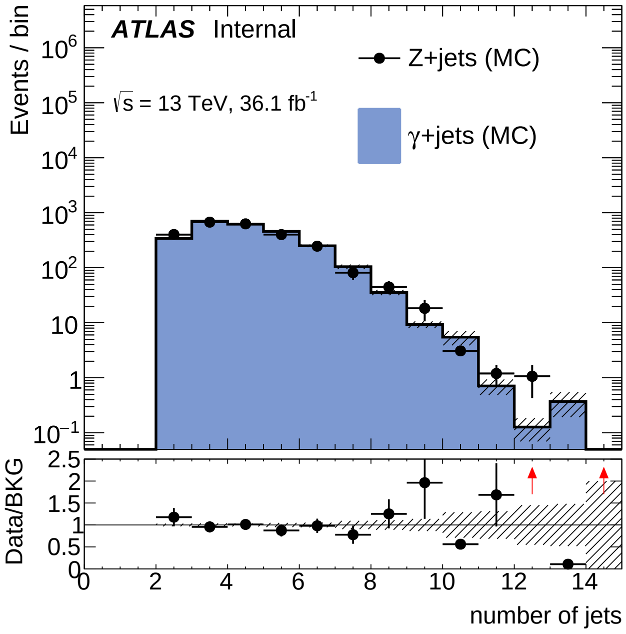

(b) MC closure test of N_{jets} modeling

Figure 5.21: Closure test of N_{jets} modeling in the $\geq$ 2jet channel. The VV and $t\bar{t}$ are provided by MC simulations in the data plot. The selection in this plot requires two OSSF leptons with $m_{ll} \in [61, 121]$ GeV, at least two jet with $p_{\text{T}} > 30$ GeV, $H_T > 200$ GeV, and $E_{\text{T}}^{\text{miss}} > 100$ GeV.

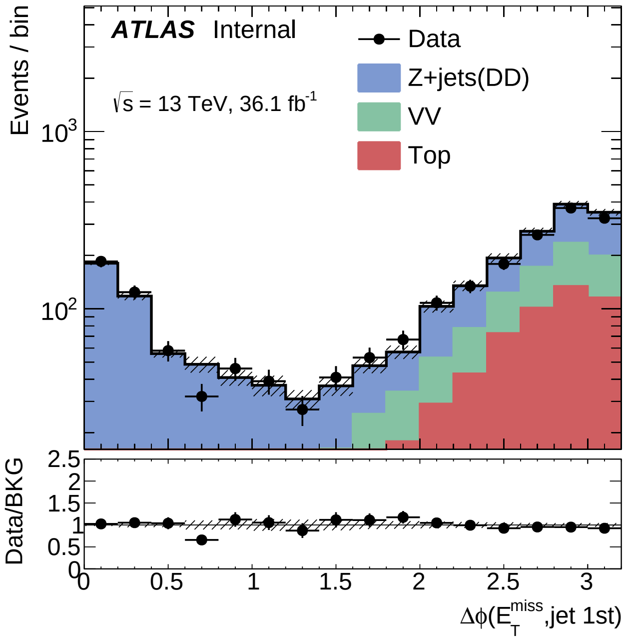

(a) Data closure test of $\Delta\phi(E_{\mathrm{T}}^{\mathrm{miss}}, \mathrm{1stjet})$ modeling

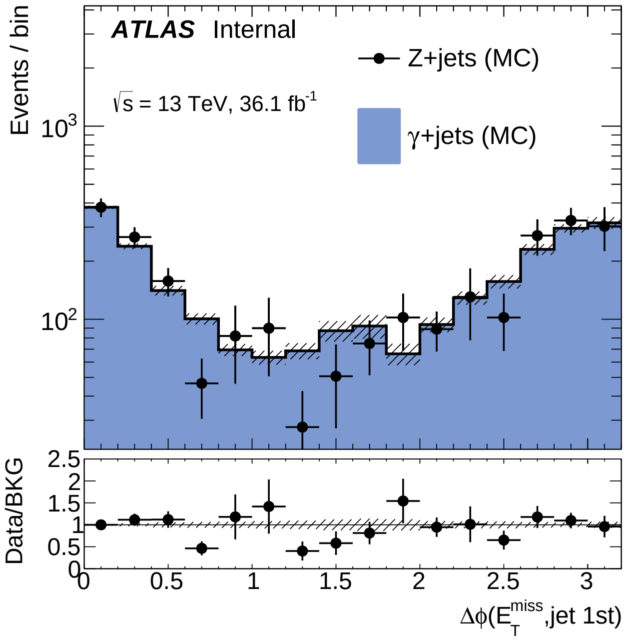

(b) MC closure test of $\Delta\phi(E_{\mathrm{T}}^{\mathrm{miss}}, \mathrm{1stjet})$ modeling

Figure 5.22: Closure test of $\Delta\phi(E_{\mathrm{T}}^{\mathrm{miss}}, \mathrm{1stjet})$ modeling in the $\geq$ 2jet channel. The VV and $t\bar{t}$ are provided by MC simulations in the data plot. The selection in this plot requires two OSSF leptons with $m_{ll} \in [61, 121]$ GeV, at least two jet with $p_{\mathrm{T}} > 30$ GeV, $H_T > 200$ GeV, and $E_{\mathrm{T}}^{\mathrm{miss}} > 100$ GeV.

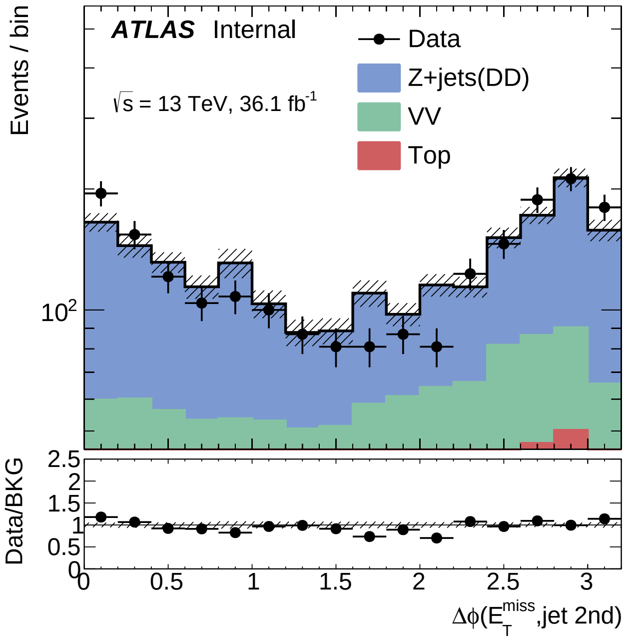

(a) Data closure test of $\Delta\phi(E_{\mathrm{T}}^{\mathrm{miss}}, 2\mathrm{ndjet})$ modeling

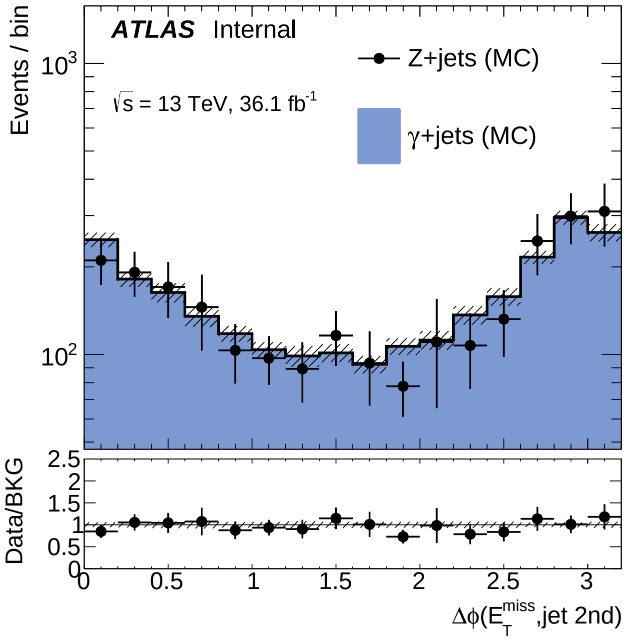

(b) MC closure test of $\Delta\phi(E_{\mathrm{T}}^{\mathrm{miss}}, 2\mathrm{ndjet})$ modeling

Figure 5.23: Closure test of $\Delta\phi(E_{\mathrm{T}}^{\mathrm{miss}}, 2\mathrm{ndjet})$ modeling in the $\geq$ 2jet channel. The VV and $t\bar{t}$ are provided by MC simulations in the data plot. The selection in this plot requires two OSSF leptons with $m_{ll} \in [61, 121]$ GeV, at least two jet with $p_{\mathrm{T}} > 30$ GeV, $H_T > 200$ GeV, and $E_{\mathrm{T}}^{\mathrm{miss}} > 100$ GeV.

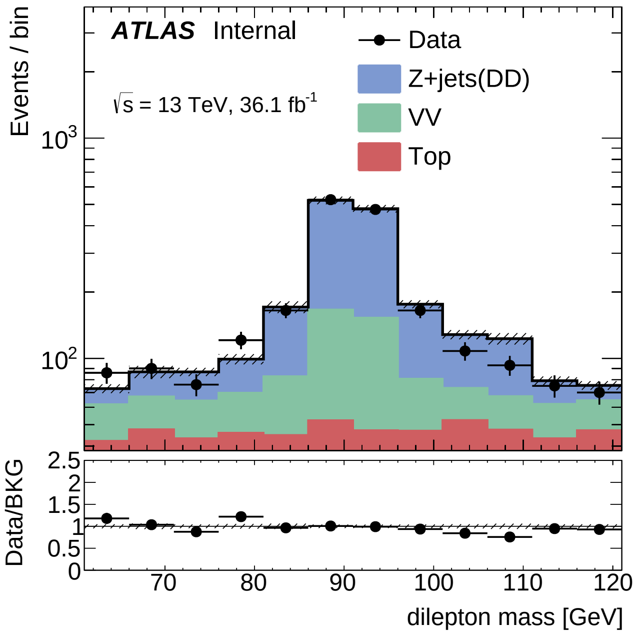

(a) Data closure test of m_{ll} modeling

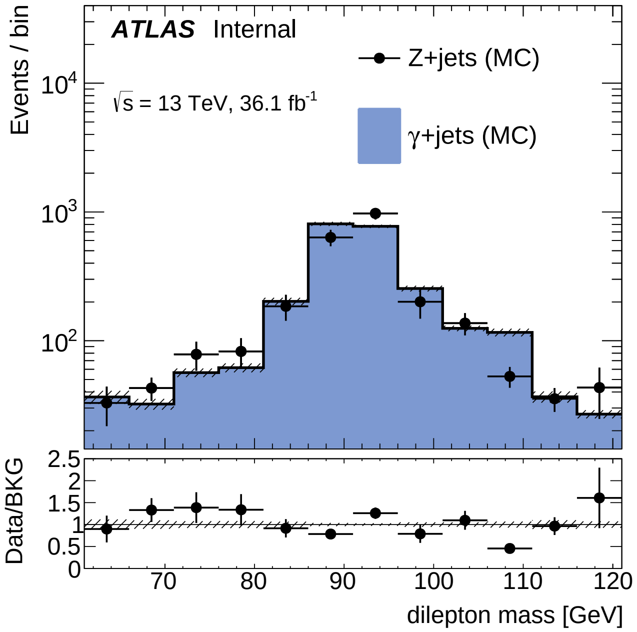

(b) MC closure test of m_{ll} modeling

Figure 5.24: Closure test of m_{ll} modeling in the $\geq$ 2jet channel. The VV and $t\bar{t}$ are provided by MC simulations in the data plot. The selection in this plot requires two OSSF leptons with $m_{ll} \in [61, 121]$ GeV, at least two jet with $p_{\mathrm{T}} > 30$ GeV, $H_T > 200$ GeV, and $E_{\mathrm{T}}^{\mathrm{miss}} > 100$ GeV.

CHAPTER 6

SEARCH FOR GLUINO PAIR PRODUCTION IN $2\ell + JETS + E_{\mathrm{T}}^{\mathrm{MISS}}$ FINAL STATES

6.1 Introduction

In the context of Natural SUSY, the higgsinos are expected to be at the electroweak scale, and the gluinos and squarks are close to the TeV scale. In this case, the strongly interacting sparticles (gluinos and squarks) can be produced with large enough rates to be detected by the LHC experiments with early 13 TeV LHC data. If R-parity is conserved in Supersymmetry, gluinos and squarks could be pair-produced and sequentially decay into jets, or leptons, and the lightest SUSY particles. The lightest SUSY particles are expected to be the lightest neutralinos, which only interact via weak forces and thus would be undetected by the detectors and leave a significant $E_{\mathrm{T}}^{\mathrm{miss}}$.

If the sparticles decay into two leptons, the invariant mass of the two leptons would be a sensitive variable to tell us about the mass difference between sparticles. In this analysis, we consider two search channels with same-flavor opposite-sign lepton pairs. The first channel requires that the invariant mass of a lepton pair (m_{ll}) is consistent with the mass of a Z boson m_Z. This channel is sensitive to the models with the presence of a Z boson in the SUSY decay chain, and the mass difference between neutralinos is larger than m_Z. The second channel allows all possible values of m_{ll} and searches for a cut-off edge in the m_{ll} spectrum. The second channel is sensitive to the models with neutralino decays via sleptons, or with the presence of a Z boson but the mass difference between neutralinos is smaller than m_Z and results in a truncated distribtion of the Z boson mass.

In 2015, using 20.3 fb^{-1} of 8 TeV pp collision data, an ATLAS analysis team presented results of searches in an on-shell Z signal region, where 29 data events were found while the SM background is expected to be 10.6 ± 3.2. This corresponds to a significance of 3.0σ. Another team on CMS side found an off-shell excess with a cut-off edge that would match the predicted m_{ll} shape from the slepton-decay scenario. The excess has a cut-off edge located at 78.7 ± 1.4 GeV and corresponds to a significance of 2.4σ. This thesis is motivated by these Run-1 excesses. We investigate and report on the result of the search for Supersymmetric particles in the same-flavor opposite-sign dilepton channel with 14.7 fb^{-1} pp collision data at a center mass energy of 13 TeV recorded by the ATLAS detector in 2015 and 2016.

6.2 Signal model

In this analysis, we use simplified models to guide us design signal regions. The models that we consider for this analysis involve strong interactions, where a pair of squarks is directly produced or through the decays of a pair of gluinos. The squark then decays to $\tilde{\chi}_2^0$ (the second lightest neutralino), where $\tilde{\chi}_2^0$ finally decays to $\tilde{\chi}_1^0$ (the lightest neutralino, LSP) and radiates two same-flavor opposite-sign leptons, where LSP is a stable particle under the assumption of R-parity conservation. For the models with gluino-pair production, since there is no flavor correlation between gluino and $q\bar{q}$ couplings and the corresponding flavors of squarks are assumed to be mass degenerate, the branching fractions are equally 25% for $q = u, d, c, s$ (heavy flavors are decoupled). Two decay topologies are considered. One topology considers the scenario where $\tilde{\chi}_2^0$ decays to $\tilde{\chi}_2^0$ and radiates a Z boson, and the Z boson decays to two leptons, as shown in Fig. 6.1 (a). The other topology considers the case where $\tilde{\chi}_2^0$ decays to $\tilde{\chi}_2^0$ through an intermediate slepton, the two leptons are radiated independently from the $\tilde{\chi}_2^0$ decay and the slepton decay, as shown in Fig. 6.1 (b). In the simplified models, all sparticles not involved in the decay chains are effectively decoupled.

Two search strategies are inspired by these models to search for Supersymmetry in strong interaction. On-shell Z search targets the signal models where the two leptons are the decay products of an on-shell Z boson. Edge search targets the signal models where the two leptons are from the decay of an off-shell Z boson or from an intermediate slepton. The signal models of the two search strategies show very different signatures in the shape of the dilepton mass spectrum. The signal models that On-shell Z search considers would result in an excess in the Z mass window, while the signal models

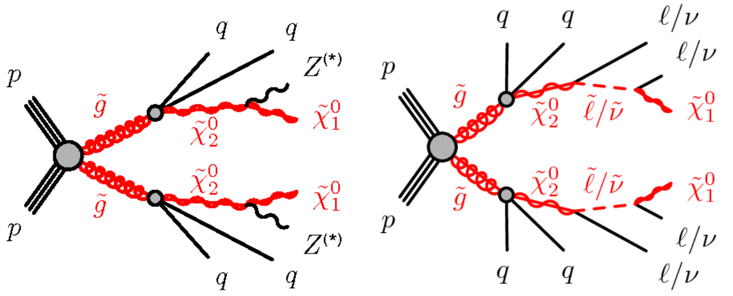

(a) Z model (b) Slepton model

Figure 6.1: Two topologies considered in the strong SUSY analysis. Both topologies involve gluino/squark decaying to $\tilde{\chi}_1^0$ via $\tilde{\chi}_2^0$ and radiating jets and same-flavor opposite-sign lepton pairs. In the Z model, the $\tilde{\chi}_2^0$ decays to $\tilde{\chi}_1^0$ with a Z boson radiation. In the slepton model, the $\tilde{\chi}_2^0$ decays to $\tilde{\chi}_1^0$ through an intermediate slepton.

that Edge search considers would produce a cut-off edge in the dilepton mass spectrum, where the location of the cut-off edge depends on the mass difference between $\tilde{\chi}_2^0$ and $\tilde{\chi}_1^0$. In the simplified models, the mass of gluino (or squark) and the mass of $\tilde{\chi}_2^0$ (or $\tilde{\chi}_1^0$) are the only two parameters. A 2D signal grid is made for each signal model topology by varying the mass parameters. The simplified signal model topologies and mass parametrizations are summarized in Table 6.1.

Model	Production mode	$m(\tilde{g})/m(\tilde{q})$	$m(\tilde{\chi}_2^0)$	$m(\tilde{\chi}_1^0)$
$\tilde{g}$–$\tilde{\chi}_2^0$ on-shell	$\tilde{g}\tilde{g}$	x	y	1 GeV
$\tilde{g}$–$\tilde{\chi}_1^0$ on-shell	$\tilde{g}\tilde{g}$	x	$m(\tilde{\chi}_1^0) + 100$ GeV	y
$\tilde{q}$–$\tilde{\chi}_2^0$ on-shell	$\tilde{q}\tilde{q}$	x	y	1 GeV
$\tilde{g}$–$\tilde{\chi}_2^0$ on(off)-shell	$\tilde{g}\tilde{g}$	x	$[m(\tilde{g}) + m(\tilde{\chi}_1^0)]/2$	y
slepton	$\tilde{g}\tilde{g}$	x	$[m(\tilde{g}) + m(\tilde{\chi}_1^0)]/2$	y

Table 6.1: Summary of the simplified signal model topologies used in this analysis. Here x and y denote the x–y plane across which the signal model masses are varied to construct the signal grid. For the slepton model, the masses of the superpartners of the left-handed leptons are given by $[m(\tilde{\chi}_2^0) + m(\tilde{\chi}_1^0)]/2$, while the superpartners of the right-handed leptons are decoupled.

6.3 Data and Monte Carlo samples

The data sample used in this analysis is collected by the ATLAS detector between year 2015-2016 at a center-of-mass energy of 13 TeV, with an integrated luminosity of 14.7 fb^{-1} (uncertainty $\pm 2.9\%$) and the average number of additional proton-proton interactions per bunch crossing (pile-up) is about 14 in 2015 and 21 in 2016.

The selected data events are required to pass a combination of single-lepton and dilepton triggers. The dilepton triggers (dielectron, dimuon, and electron-muon) have leading lepton p_T thresholds in the range between 12-24 GeV. The single lepton triggers (single-electron and single-muon) require lepton $p_T > 60$ GeV (single-electron) and lepton $p_T > 50$ GeV (single-muon). Events in the analysis are required to have at least two selected leptons passing a p_T threshold at 25 GeV, where the trigger selections are fully efficient.

An additional photon sample is also selected to perform the photon template method for $Z+$jets background estimation. The photon sample events are required to pass a set of single-photon trigger with p_T thresholds in range between 35-140 GeV. All photon triggers are prescaled except the trigger with threshold $p_T = 120$ GeV in 2015 and threshold $p_T = 140$ GeV in 2016. The photon events are further required to at least one photon with $p_T > 37$ GeV, where the trigger selection is efficient.

Monte Carlo samples are used to help signal region optimizations, to provide background estimations, and to validation the data-driven background estimate techniques. The MC samples used in this analysis are listed in Table 6.2.

Physics process	Generator	Parton Shower	Cross section	Tune	PDF set
$t\bar{t}+W$ and $t\bar{t}+Z$ [14, 15]	MG5_aMC@NLO	Pythia 8.186	NLO [16, 17]	A14	NNPDF23LO
$t\bar{t}+WW$ [14]	MG5_aMC@NLO	Pythia 8.186	LO [18]	A14	NNPDF23LO
$t\bar{t}$ [19]	Powheg Box v2 r3026	Pythia 6.428	NNLO+NNLL [20, 21]	Perugia2012	NLO CT10
Single-top (Wt) [19]	Powheg Box v2 r2856	Pythia 6.428	Approx. NNLO [22]	Perugia2012	NLO CT10
WW, WZ and ZZ [23]	Sherpa 2.1.1	Sherpa 2.1.1	NLO [24, 25]	Sherpa default	NLO CT10
$Z/\gamma^{*}(\to \ell\ell)$ + jets [26]	Sherpa 2.1.1	Sherpa 2.1.1	NNLO [27, 28]	Sherpa default	NLO CT10
$\gamma+$jets	Sherpa 2.1.1	Sherpa 2.1.1	LO [29]	Sherpa default	NLO CT10
$V(=W,Z)\gamma$	Sherpa 2.1.1	Sherpa 2.1.1	LO [29]	Sherpa default	NLO CT10

Table 6.2: Simulated background event samples used in this analysis with the corresponding matrix element and parton shower generators, cross-section order in α_S used to normalise the event yield, underlying-event tune and PDF set.

The background MC samples are processed with a full ATLAS detector simulation [30] using GEANT4 [31]. The signal MC samples are processed with a fast simulation, which uses a combination of a parameterisation of the response of the ATLAS electromagnetic and hadronic calorimeters and GEANT4. Minimum-bias interactions are generated with Pythia 8.168 and overlaid on the hard-scattering interactions to model pile-up interactions. The distribution of pile-up interactions in MC samples is simulated to match the pile-up distribution in 2015-2016 data. For more information on the samples, please see [32].

6.4 Analysis object identifications and selections

In this section we will discuss the definitions of the analysis objects, including photons, muons, electrons, and jets. In this analysis, two levels of identifications, baseline and signal, are used to qualify objects (photons, leptons and jets). Objects that pass baseline idetifications (baseline objects) are used in the calculation of missing transverse momentum and to distinguish between objects in the event. Signal object requirements are more strict than the baseline object requirements. Only the objects that pass the signal requirements will be used in defining the analysis region selections. The primary vertex in each event is defined as the reconstructed vertex [33] with the highest $\sum p_T^2$, where the summation includes all tracks with $p_T > 400$ MeV associated with the vertex.

Electron candidates are reconstructed by matching the Inner Detector tracks to the energy clusters in the electromagnetic calorimeter. Electron candidates that pass the baseline selection are required to have transverse energy $E_T > 10$ GeV and satisfy the “loose likelihood” quality selection described in [10] and the candidates’ pseudorapidity $|\eta| < 2.47$. Electron candidates that pass the signal selection are further required to have $p_T > 25$ GeV and satisfy the “medium likelihood” criteria of [10]. In addition to the kinematic and quality requirements, signal electrons must originate from the primary vertex of the event within $|z_0 \sin\theta| = 0.5$ mm and $|d_0/\sigma_{d_0}| < 5$, where z_0 (d_0) is the distance of closest approach between the particle trajectory and the primary vertex in the longitudinal (transverse) plane. Furthermore, the electrons must be isolated from other objects in the event. The isolation is a p_T-dependent requirement and uses calorimeter- and track-based information to obtain 95% efficiency at $p_T = 25$ GeV (99% efficiency at $p_T = 60$ GeV).

Muon candidates are reconstructed by either combining tracks formed from Inner Detector and the muon spectrometer or only using Inner Detector tracks that match hits in a single muon spectrometer layer. Baseline muons are required to have $p_T > 10$ GeV and $|\eta| < 2.5$ and pass "medium" selection criteria in [9]. Signal muons are further required to have $p_T > 25$ GeV and $|z_0 \sin\theta| < 0.5$ mm and $|d_0/\sigma_{d_0}| < 3$ and to be isolated from other objects in the event. The isolation uses calorimeter- and track-based information and reaches 95% efficiency at $p_T = 25$ GeV (99% efficiency at $p_T = 80$ GeV) [9]. For the combined Inner detector and muon spectrometer tracks, the uncertainty in the q/p of each Inner detector track and the uncertainty in the q/p of each muon spectrometer track are required to be less than 80% of the unceraintty in q/p of the combined track to reduce mis-measured muons. The combined isolation and identification efficiency for single leptons is about 70% (80%) for electrons (muons) with $p_T \sim 25$ GeV (90% for $p_T > 200$ GeV), with respect to the trigger requirements.

Jet candidates are reconstructed from energy clusters [34] in the hadronic calorimeter with the anti-k_t algorithm [35, 36], which behaves like an idealised cone algorithm to cluster soft fragmentation with hard particles in a cone of radius of 0.4. MC-based calibration corrections are derived by comparing reconstructed-to-truth jet energies of jets made of stable particles (lifetimes $\tau > 0.3 \times 10^{-10}$ s) in MC simulation. A residual correction is derived and based on studies of the balance of transverse momentum between jets and well-calibrated objects in the MC simulation and data [37, 38]. Jets that pass baseline requirement need to have $p_T > 20$ GeV and with $|\eta| < 4.5$. Jets that further pass signal selection are required to have $p_T > 30$ GeV and only reside within the central region $|\eta| < 2.5$. To reject pile-up originated jets, additional criteria of jet vertex tagger in [39] is made for the jets with $p_T < 60$ GeV and $|\eta| < 2.4$. Events that contain jets being classified as radiations from detector noise and non-collision backgrounds (beam-induced background and cosmic rays) [40, 41] are removed from the analysis. B-hadrons originated jets (b-jets) are identified with a MV2c10 boosted decision tree algorithm [42, 43], based on information of impact parameters of associated tracks and any reconstructed secondary vertices. The efficiency of tagging b-jets (77%) is studied in simulated $t\bar{t}$ events.

Photon candiates are reconstructed from energy clusters in the electromagnetic calorimeter and pass "tight" selection criteria in [12] and with $p_T > 25$ GeV and $|\eta| < 2.37$, except that transition region $1.37 < |\eta| < 1.6$ (where there is a discontinuity in the calorimeter) is excluded. Photon candidates that pass signal requirement need to have $p_T > 37$ GeV and to be isolated from other objects in the event using p_T-dependent requirements on both track- and calorimeter-based isolation.

One particle could be identified as different objects by different reconstruction algorithms. To avoid the duplication of analysis object identifications of a same particle at the baseline selection level, an overlap removal procedure is applied and is described as follows: (1) Electrons v.s. jets overlap removal. All electrons are potentially jets. Electrons are discriminated from jets based on the electromagnetic v.s. hadronic calorimeter energy fraction. Thus, any baseline jet within a cone of $\Delta R = 0.2$ of a baseline electron is removed, unless the jet is b-tagged, in which case the electron is identified as originating from the decay of a heavy-flavor quark, and the electron is removed instead. Remaining electrons residing within a cone of $\Delta R = 0.4$ (the cone size of a jet) of a baseline jet are then removed from the event. (2) Muons v.s. jets overlap removal. Following the electron-jet overlap removal, baseline jet within a cone of $\Delta R = 0.2$ of a baseline muon is removed, unless the jet is b-tagged, in which case the muon is identified as originating from the decay of a heavy-flavor quark, and the muon is removed instead. Any remaining muon found within $\min(0.04 + (10 \text{ GeV})/p_T, 0.4)$ of a jet is also discarded. This p_T-dependent overlap removal procedure improves to preserve muons with final-state radiations in the calorimeter, while still rejecting muons from heavy-flavour decays. (3) Electron v.s. muons overlap removal. Electrons within $\Delta R = 0.01$ of any remaining baseline muon are removed from the event in case of electrons originating from muon bremsstrahlung. (4) Photon v.s. jets and electrons overlap removal. Photons are removed if they reside within a cone of $\Delta R = 0.4$ of a baseline electron, and any jet within $\Delta R = 0.4$ of any remaining photon is removed.

The transverse missing energy $E_{\mathrm{T}}^{\mathrm{miss}}$ is built as the negative magnitude of the vectorial sum of the transverse momenta of all baseline objects (electrons, muons, jets, and photons) [44, 8]. In addition to the baseline objects, the calculation of $E_{\mathrm{T}}^{\mathrm{miss}}$ also includes low momentum particle tracks (soft term) that are associated with the primary vertex but not with baseline objects in an event.

The transverse hadronic energy H_T is defined as the scalar sum of the p_T values of all signal jets. $H_{\mathrm{T}}^{\mathrm{incl}}$ includes both the scalar sum of the p_T values of all signal jets and the two signal leptons with largest p_T.

6.5 Event selections

The selected events must pass at least one lepton trigger. The leptons with the highest p_T (> 25 GeV) in a selected event must match to the objects that triggered the event, and the p_T of these leptons have to pass the threshold of the trigger in question.

There are three types of selections (regions) defined for different purposes. The signal region selections (SR) are designed to target events from specific SUSY signal models. The control regions (CR) are designed to help the background estimations in signal regions, such as the modifications of MC sample normalizations or the resolution corrections. The validation regions (VR) are designed to validate the background estimation methods, to ensure the backgrounds are properly modeled. Both CRs and VRs are designed to minimize the signal event contaminations and to enlarge the portions of the targeted SM process components. SRs, CRs, and VRs should be defined as kinematically close to each other as possible but also mutually orthogonal.

Two sets of signal regions are designed for the on-shell Z search and the edge search, respectively. Both on-shell and edge search regions are summarized in Fig. 6.2, where the on-shell Z search the various regions are shown in the $m_{ll} - E_{\mathrm{T}}^{\mathrm{miss}}$ plane, and the edge search the signal and validation regions are depicted in the $H_{\mathrm{T}} - E_{\mathrm{T}}^{\mathrm{miss}}$ plane.

The on-shell Z search signal region (SRZ) is motivated by SUSY signals with high gluino or squark mass and high jet activity. The SRZ requires the leading-lepton $p_{\mathrm{T}} > 50$ GeV. This enhanced lepton p_T threshold reduces non-prompt leptons from misidentified jets, photon conversions and b-hadron decays while preserves the selection efficiency of signal events with on-shell $Z \to l^+l^-$ decays. The SRZ requires events to have the invariant mass of the dilepton system to be $m_{\ell\ell} \in (81, 101)$ GeV to select events containing a leptonically decaying Z boson. The defining selections of SRZ are $H_{\mathrm{T}}^{\mathrm{incl}} > 600$ GeV and $E_{\mathrm{T}}^{\mathrm{miss}} > 225$ GeV (high gluino or squark mass resulting in large hadronic activity and large transverse momenta of LSP). In SRZ, the

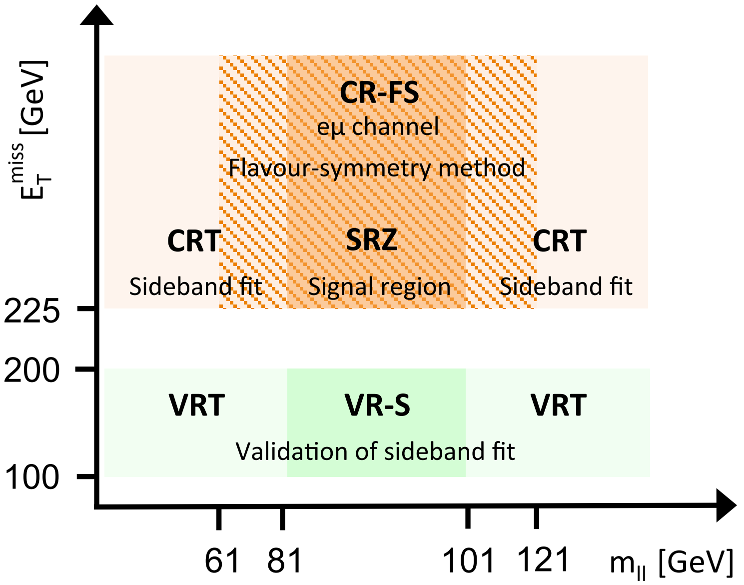

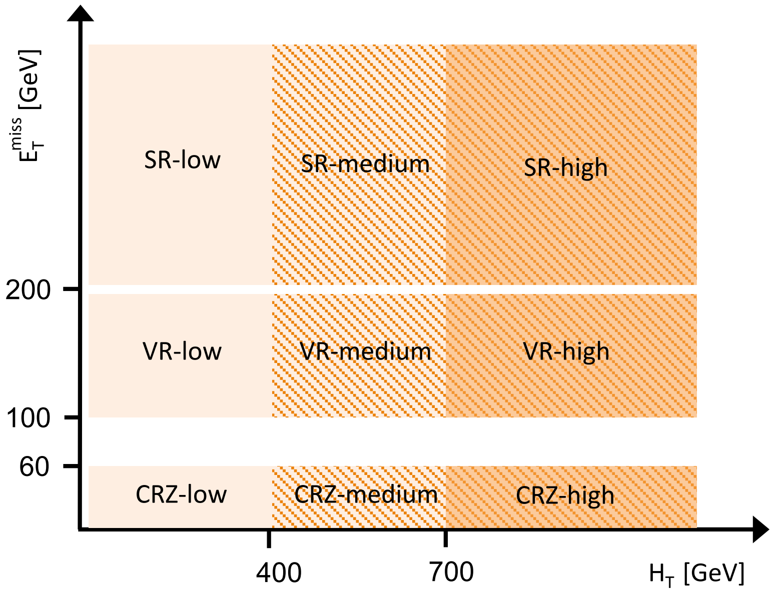

Figure 6.2: Schematic diagrams of the control (CR), validation (VR) and signal regions (SR) for the on-shell Z (top) and edge (bottom) searches. The flavor-symmetry and sideband-fit background estimation methods are described further in Section 6.6.1.

$t\bar{t} \to l^+l^-$ events are the dominant backgrounds (Z+jets process is suppressed for the absence of neutrinos). In the $t\bar{t} \to l^+l^-$ events, the two leptons are uncorrelated (they are decay products of two different W bosons), and thus one can use events with different-flavor lepton pair and $m_{\ell\ell} \notin (81, 101)$ GeV to model and validate $t\bar{t} \to l^+l^-$ background in SRZ. All regions require at least two same-flavor opposite-sign leptons. Except in the case of CRγ and VR-FS, where specific flavor configurations are required, and in VR-WZ, VR-ZZ, VR-3L the number of leptons are different. The details of the on-shell Z search SR, CRs, and VRs can be found in Table 6.3.

On-shell Z regions	$E_{\mathbf{T}}^{\mathbf{miss}}$ **[GeV]**	$H_{\mathbf{T}}^{\mathbf{incl}}$ **[GeV]**	$n_{\mathbf{jets}}$	$m_{\ell\ell}$ **[GeV]**	**SF/DF**	$\Delta\phi(\mathbf{jet}_{12}, \boldsymbol{p}_{\mathrm{T}}^{\mathrm{miss}})$	$m_{\mathbf{T}}(\ell_3, E_{\mathbf{T}}^{\mathbf{miss}})$ [GeV]	$n_{b\text{-}\mathbf{jets}}$
Signal region								
SRZ	> 225	> 600	≥ 2	$81 < m_{\ell\ell} < 101$	SF	> 0.4	–	–
Control regions								
CRZ	$< \mathbf{60}$	> 600	≥ 2	$81 < m_{\ell\ell} < 101$	SF	> 0.4	–	–
CR-FS	> 225	> 600	≥ 2	$\mathbf{61 < m_{\ell\ell} < 121}$	**DF**	> 0.4	–	–
CRT	> 225	> 600	≥ 2	$> \mathbf{45}, \mathbf{m}_{\ell\ell} \notin [\mathbf{81}, \mathbf{101}]$	SF	> 0.4	–	–
CRγ	–	> 600	≥ 2	–	0ℓ, 1γ	–	–	–
Validation regions								
VRZ	$< \mathbf{225}$	> 600	≥ 2	$81 < m_{\ell\ell} < 101$	SF	> 0.4	–	–
VRT	**100–200**	> 600	≥ 2	$> \mathbf{45}, \mathbf{m}_{\ell\ell} \notin [\mathbf{81}, \mathbf{101}]$	SF	> 0.4	–	–
VR-S	**100–200**	> 600	≥ 2	$81 < m_{\ell\ell} < 101$	SF	> 0.4	–	–
VR-FS	**100–200**	> 600	≥ 2	$\mathbf{61 < m_{\ell\ell} < 121}$	**DF**	> 0.4	–	–
VR-WZ	**100–200**	–	–	–	$\mathbf{3\ell}$	–	< 100	0
VR-ZZ	< 100	–	–	–	$\mathbf{4\ell}$	–	–	0
VR-3L	**60–100**	$> \mathbf{200}$	≥ 2	$81 < m_{\ell\ell} < 101$	$\mathbf{3\ell}$	> 0.4	–	–

Table 6.3: Overview of all signal (SR), control (CR) and validation regions (VR) used in the on-shell Z search. The flavor combination of the dilepton pair is denoted as either "SF" for same-flavor or "DF" for different-flavor. The main requirements that distinguish the control and validation regions from the signal region are indicated in bold. The kinematic quantities used to define these regions are discussed in the text. The quantity $m_{\mathrm{T}}(\ell_3, E_{\mathrm{T}}^{\mathrm{miss}})$ indicates the transverse mass formed by the $E_{\mathrm{T}}^{\mathrm{miss}}$ and the lepton which is not assigned to either of the Z-decay leptons.

The edge search signal regions are motivated by SUSY signals with two final-state leptons from either off-shell $Z \to l^+l^-$ decays or $\tilde{\chi}_2^0 \to \tilde{l} \to \tilde{\chi}_1^0$ decays. The edge regions require at least two leptons with $p_{\mathrm{T}} > 25$ GeV, and the search looks for excesses across the full m_{ll} spectrum (except that $m_{ll} < 12$ GeV region is vetoed to reject low-mass DY events and the J/ψ and Υ resonances). Three edge signal regions are designed to target signal models with different $m(\tilde{g}) - m(\tilde{\chi}_1^0)$ splitting. SR-low requires $H_{\mathrm{T}} > 0$ GeV to target small $m(\tilde{g}) - m(\tilde{\chi}_1^0)$ splitting models, while SR-medium and SR-high require $H_\mathrm{T} > 400$ GeV and $H_\mathrm{T} > 700$ GeV, respectively, to target larger $m(\tilde{g}) - m(\tilde{\chi}_1^0)$ splitting models. All these regions require $E_\mathrm{T}^\mathrm{miss} > 200$ GeV for the presence of LSPs with large transverse momenta. Events selected in SR-low, SR-medium and SR-high are further divided into various m_{ll} windows, which represent the search regions used in the edge analysis. The ranges of these m_{ll} windows are chosen to maximize sensitivity to the favored signal models while the statistics of background events is preserved. The windows with $m_{ll} < 80$ GeV target models involving off-shell $Z \to l^+l^-$ decays (in the cases where $m(\tilde{\chi}_2^0) - m(\tilde{\chi}_1^0) < m(Z)$). The windows with $m_{ll} \in (81, 101)$ GeV target models involving on-shell $Z \to l^+l^-$ decays (in the cases where $m(\tilde{\chi}_2^0) - m(\tilde{\chi}_1^0) > m(Z)$). Models with light sleptons ($\tilde{\chi}_2^0 \to \tilde{l} \to \tilde{\chi}_1^0$) are targeted and searched with the full m_{ll} range windows. Please note that the edge selection and on-shell Z selection are not orthogonal. The details of the edge search SRs, CRs, and VRs can be found in Table 6.4.

The signal regions are optimized to target different parameter spaces of the signal models. For the signal models considered in this analysis, the efficiency of SRZ (number of signal events landed in the SR divided by the number of total generated signal events) is about $2 - 8\%$, and the efficiencies are about $8 - 40\%$, $3 - 35\%$, and $1 - 35\%$, for SR-low, SR-medium and SR-high, respectively. The signal region acceptance and efficiency for the signal models with gluino pair production with $\tilde{\chi}_2^0$ decays to $\tilde{\chi}_1^0$ can be found in Fig. 6.3 (Z model) and Fig. 6.4 (slepton model).

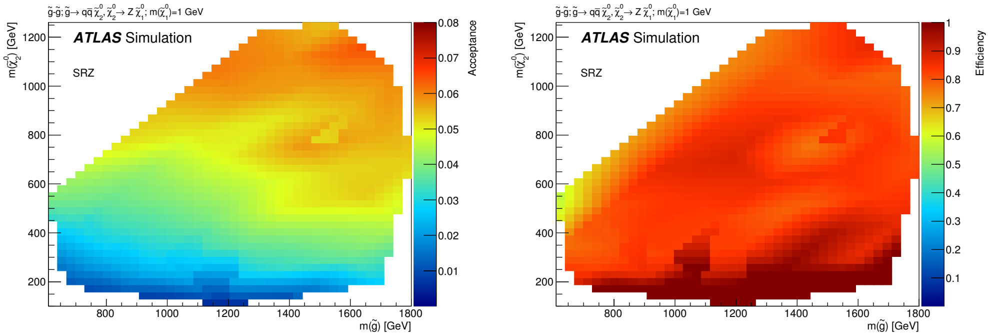

Figure 6.3: Signal region acceptance (left) and efficiency (right) for the simplified model with gluino pair production with $\tilde{\chi}_2^0$ decays to $\tilde{\chi}_1^0$ and an on-shell Z boson. Acceptance is calculated by applying the signal-region kinematic requirements to particle-level objects, which do not suffer from identification inefficiencies or measurement resolutions.

Edge regions	$E_{\mathrm{T}}^{\mathrm{miss}}$ **[GeV]**	H_{T} **[GeV]**	n_{jets}	$m_{\ell\ell}$ **[GeV]**	**SF/DF**	**OS/SS**	$\Delta\phi(\mathbf{jet}_{12}, \boldsymbol{p}_{\mathrm{T}}^{\mathrm{miss}})$	m_{ll} **ranges**
Signal regions								
SR-low	> 200	–	≥ 2	> 12	SF	OS	> 0.4	9
SR-medium	> 200	> 400	≥ 2	> 12	SF	OS	> 0.4	8
SR-high	> 200	> 700	≥ 2	> 12	SF	OS	> 0.4	7
Control regions								
CRZ-low	$\boldsymbol{< 60}$	–	≥ 2	> 12	SF	OS	> 0.4	–
CRZ-medium	$\boldsymbol{< 60}$	> 400	≥ 2	> 12	SF	OS	> 0.4	–
CRZ-high	$\boldsymbol{< 60}$	> 700	≥ 2	> 12	SF	OS	> 0.4	–
CR-FS-low	> 200	–	≥ 2	> 12	**DF**	OS	> 0.4	–
CR-FS-medium	> 200	> 400	≥ 2	> 12	**DF**	OS	> 0.4	–
CR-FS-high	> 200	> 700	≥ 2	> 12	**DF**	OS	> 0.4	–
CRγ-low	–	–	≥ 2	–	0ℓ, 1γ	–	–	–
CRγ-medium	–	> 400	≥ 2	–	0ℓ, 1γ	–	–	–
CRγ-high	–	> 700	≥ 2	–	0ℓ, 1γ	–	–	–
CR-real	–	$\boldsymbol{> 200}$	≥ 2	**81–101**	2ℓ SF	OS	–	–
CR-fake	$\boldsymbol{< 125}$	–	–	$\in [12, \infty)$, $\notin [81, 101]$**(SF)**	2ℓ **SF/DF**	**SS**	–	–
Validation regions								
VR-low	**100–200**	–	≥ 2	> 12	SF	OS	> 0.4	–
VR-medium	**100–200**	> 400	≥ 2	> 12	SF	OS	> 0.4	–
VR-high	**100–200**	> 700	≥ 2	> 12	SF	OS	> 0.4	–
VR-fake	$\boldsymbol{> 50}$	–	≥ 2	$\in [12, \infty)$, $\notin [81, 101]$**(SF)**	**SF/DF**	**SS**	–	–

Table 6.4: Overview of all signal (SR), control (CR) and validation regions (VR) used in the edge search. The flavor combination of the dilepton pair is denoted as either "SF" for same-flavor or "DF" for different-flavor. The charge combination of the leading lepton pairs are given as "SS" for same-sign or "OS" for opposite-sign. All regions require *at least* two leptons, with the exception of CR-real, which requires *exactly* two leptons, and the three γ CRs, which require no leptons and one photon.

However, some signal models can result signal contamination in CRs and VRs too. For example, CRT in Table 6.3 is used to derive a scale factor for $t\bar{t} \to l^+l^-$ MC sample normalization, but some signal models targeted by the edge search can contaminate this region with signal events as many as 80% relative to the expected background. Although the contamination in the CRs could impact on the sensitivity of the SRs to the signal models in question, the signal-to-background ratio of the signal models (which contaminate the SRs the most) in the SRs are very large, and the impact from the contamination is relatively negligible.

6.6 Background estimation

In this section, we discuss the background estimation methods and the validations of the background methods. The dominant background process in the SRs (both on-shell Z and edge searches) is $t\bar{t} \to l^+l^-$. The two leptons in $t\bar{t} \to l^+l^-$ events are from the decays of two separate W bosons, therefore the flavors of the two leptons are uncorrelated. The $t\bar{t} \to l^+l^-$ events and other backgrounds two uncorrelated leptons, such as WW, Wt, and $Z \to \tau\tau$ events, are grouped as "flavor-symmetric" (FS) backgrounds. Since the flavors (as well as kinematics) of the two leptons are uncorrelated, the ratio of ee, $\mu\mu$ and $e\mu$ dileptonic branching fractions is 1:1:2, and we can use events in the $e\mu$ control channel to estimate the yields and kinematic distributions in the same-flavor channels.

The second dominant background process is $Z+$jets (standard model Z bosons produced in association with initial state radiation jets). In a case of an ideal detector, where objects are perfectly reconstructed and measured, the $Z+$jets events would not enter the signal regions for the absence of neutrinos (all SRs have high $E_{\mathrm{T}}^{\mathrm{miss}}$ requirement). However, the $Z+$jets processes still contribute a significant amount of background events in SRs because of the fake $E_{\mathrm{T}}^{\mathrm{miss}}$ originating from instrumental effects or from neutrinos in jet fragments and the large cross sections of $Z+$jets processes. This background is difficult to model with MC simulation and can mimic signal, particularly for the on-shell Z search. To estimate $Z+$jets events in SRs, we use $\gamma+$jets events in data to model the fake $E_{\mathrm{T}}^{\mathrm{miss}}$ resulted from jet mis-measurements. Both $Z+$jets and $\gamma+$jets processes have the similar topology and no neutrino presence, which make a good analogy between the two processes.

The rest of background events in SRs are mostly composed of diboson events (WZ/ZZ). These backgrounds are estimated with MC simulation and validated in dedicated VRs in 3ℓ and 4ℓ channels. Rare top backgrounds such as $t\bar{t}W$, $t\bar{t}Z$ and $t\bar{t}WW$ are also estimated with MC, however no VR is designed for the rare top backgrounds, since their contribution is relatively small ($< 5\%$ of total backgound). The background contribution from fake or misidentified leptons is also small in all SRs ($< 5\%$ of total backgound), except in one m_{ll} window in SR-low where the fake background is about 15%.

6.6.1 Estimation of flavor-symmetric background

The flavor-symmetric (FS) background is dominant in all SRs. The FS background events (mostly $t\bar{t} \to l^+l^-$) enter the signal regions with large hadronic activities and large $E_{\mathrm{T}}^{\mathrm{miss}}$ from neutrinos. The "flavor-symmetry" method, first applied in [45], is used to estimate the FS background contributions in SRs. This method uses events in the different-flavor (DF) control regions to estimate the flavor-symmetric background events in the signal regions (which have same-flavor requirement).

Each DF control region is defined with the same kinematic selections that define the corresponding signal region, except the flavor requirement. The method provides the predictions of the background yields in the Z mass window ($m_{ll} \in (81, 101)$ GeV) for the on-shell Z analysis, and the predictions of the background yields in the full m_{ll} range for the edge analysis. The method for the on-shell Z search has a widened m_{ll} window of $61 - 121$ GeV. This widened window is designed to provide a prediction in the window of $m_{ll} \in (81, 101)$ GeV with a sufficient statistics. All FS control regions (definitions can be seen in Table 6.4) are $88 - 97\%$ pure in flavor-symmetric processes based on MC calculation.

For background processes with two uncorrelated final-state leptons, such as $t\bar{t} \to l^+l^-$ and WW, the ideal relation between yields in SF channel and DF channel is

$$N_{ee}^{\text{est}} = \frac{1}{2} N_{e\mu}^{\text{est}} \tag{6.1}$$

$$N_{\mu\mu}^{\text{est}} = \frac{1}{2} N_{e\mu}^{\text{est}} \tag{6.2}$$

, where N_{SF} and N_{DF} are the event yields in the SF and DF regions of the same selection (except from the flavor requirement). However, this relation needs to be modified for three reasons. First, the trigger efficiency and the object selection efficiency for electrons and muons are not the same. The difference between the SF and DF trigger efficiencies is corrected by the factor

$$\alpha = \frac{\sqrt{\epsilon_{ee}^{\text{trig}} \times \epsilon_{\mu\mu}^{\text{trig}}}}{\epsilon_{e\mu}^{\text{trig}}} \tag{6.3}$$

, where α and ϵ^{trig} (trigger efficiency) are measured as function of (p_{T}, η) of the leading lepton. The difference between the electron and muon selection efficiencies is corrected by the factor

$$k_e(p_{\text{T}}, \eta) = \sqrt{\frac{N_{ee}^{\text{meas}(p_{\text{T}},\eta)}}{N_{\mu\mu}^{\text{meas}(p_{\text{T}},\eta)}}} \tag{6.4}$$

when translating muon to electron, and

$$k_\mu(p_{\text{T}}, \eta) = \sqrt{\frac{N_{\mu\mu}^{\text{meas}(p_{\text{T}},\eta)}}{N_{ee}^{\text{meas}(p_{\text{T}},\eta)}}} \tag{6.5}$$

when translating electron to muon. Here $k_e(p_{\text{T}}, \eta)$ and $k_\mu(p_{\text{T}}, \eta)$ are calculated separately for leading and sub-leading leptons. These correction factor are typically within 10% of unity, except in the region $|\eta| < 0.1$ not covered by the muon spectrometer, where the k-factors are be up to 50%.

Second, the DF regions can contain non-flavor-symmetric contributions from misidentified SF events, such as $Z \to ee$ and $Z \to \mu\mu$, etc. The fraction of non-flavor-symmetric contributions in the DF region is estimated with MC simulation and is defined as

$$f_{\text{non-FS}} = \frac{N_{e\mu} - N_{e\mu}^{\text{MC,non-FS}}}{N_{e\mu}} \tag{6.6}$$

The factor $f_{\text{non-FS}}$ is about 95% in CR-FS.

Third, in the on-shell Z analysis the m_{ll} window is widened to gain statistics, a factor is therefore needed to scale the yield in $m_{ll} \in (61, 121)$ GeV window to $m_{ll} \in (81, 101)$ GeV window as

$$f_{Z-\text{mass}} = \frac{N_{e\mu}^{\text{MC}}(81 - 101 \text{ GeV})}{N_{e\mu}^{\text{MC}}(61 - 121 \text{ GeV})}. \tag{6.7}$$

The factor $f_{Z-\text{mass}}$ is about 38% for the on-shell Z analysis.

Put all these corrections together, we derive the relation between yields in SF channel and DF channel being

$$N_{ee}^{\text{est}} = \frac{1}{2} \cdot f_{\text{non-FS}} \cdot f_{Z-\text{mass}} \cdot \sum_{i}^{N_{e\mu}^{\text{data}}} k_e(p_{\text{T}}^{i,\mu}, \eta^{i,\mu}) \cdot \alpha(p_{\text{T}}^{i,\mu}, \eta^{i,\mu}), \tag{6.8}$$

$$N_{\mu\mu}^{\text{est}} = \frac{1}{2} \cdot f_{\text{non-FS}} \cdot f_{Z-\text{mass}} \cdot \sum_{i}^{N_{e\mu}^{\text{data}}} k_\mu(p_{\text{T}}^{i,e}, \eta^{i,e}) \cdot \alpha(p_{\text{T}}^{i,e}, \eta^{i,e}). \tag{6.9}$$

Since the on-shell Z signal region has a Z-mass window requirement ($m_{ll} \in [81, 101]$ GeV), it is difficult to design a validation region to validate the flavor-symmetry method prediction in the Z-mass window without large contamination from $Z +$ jets events. Thus, a Sideband method is proposed to cross-check the flavor-symmetry method in SRZ by performing a profile likelihood fit [46] of MC yields to data in the Z-mass sidebands ($m_{ll} \notin [81, 101]$ GeV). This result is extrapolated from the Z-mass sidebands to SRZ and gives a prediction of 29 ± 7 events, which is consistent with the nominal flavor-symmetry background estimate of 33 ± 4 in this region. The Sideband method is also performed in VR-S. The flavor-symmetry and the Sideband fit method predictions in both SRZ and VR-S are compared in Table 6.5.

Region	Flavour-symmetry	Sideband fit
SRZ	33 ± 4	29 ± 7
VR-S	99 ± 8	92 ± 25

Table 6.5: Comparison of the predicted yields for the flavor-symmetric backgrounds in SRZ and VR-S as obtained from the nominal data-driven method using CR-FS and the Z-mass sideband method. The quoted uncertainties include statistical and systematic contributions.

In the case of the edge search, the full m_{ll} distribution is validated by applying a flavor-symmetry method to $t\bar{t}$ MC events in VR-low, VR-medium, and VR-high. The difference between the prediction and the observed distribution is used to assign an MC non-closure uncertainty to the estimate. The validations of the flavor-symmetry method in the edge search are shown in Fig. 6.5. The validation regions are chosen to be close to the corresponding signal regions, except that the $E_{\mathrm{T}}^{\mathrm{miss}}$ requirement is relaxed to $100-200$ GeV in order to gain statistics. For the details of the validation region definitions, please see Table 6.4. Fig. 6.5 shows the closure of the method in both MC (left) and data (right), in VR-low (top), VR-medium (middle) and VR-high (bottom). In the MC closure plots, the flavor-symmetry method predictions (from $e\mu$ $t\bar{t}$ MC samples) agree well with the $t\bar{t}$ MC sample in the same-flavor channels in all three VRs. In the data closure plots, the method also provides good predictions across the m_{ll} spectrum within uncertainties, except in the Z-mass bin where $Z+$jets process is the dominant background. The rare top and data-driven fake-lepton backgrounds are grouped under "other" backgrounds.

6.6.2 Estimation of $Z+$jets background

The $Z+$jets background is estimated with a data-driven method, which uses $\gamma+$jets data events to model the jet energy mis-measurement resulting fake $E_{\mathrm{T}}^{\mathrm{miss}}$ in $Z+$jets events. This photon template method is described in Sec. 5.

The $Z+$jets background events enter the signal regions (all require large $E_{\mathrm{T}}^{\mathrm{miss}}$ cuts) because of the fake $E_{\mathrm{T}}^{\mathrm{miss}}$ from jet energy mis-measurements and the large cross section of the $Z+$jets process. To suppress the fake $E_{\mathrm{T}}^{\mathrm{miss}}$ from jet energy mis-measurements, all signal regions have a requirement of $\Delta\phi(\mathrm{jet}_{12}, \boldsymbol{p}_{\mathrm{T}}^{\mathrm{miss}}) > 0.4$ (fake $E_{\mathrm{T}}^{\mathrm{miss}}$ from jet energy mis-measurements are usually aligned with the direction of the leading jets). The fake $E_{\mathrm{T}}^{\mathrm{miss}}$ in the remaining $Z+$jets background events with large $\Delta\phi > 0.4$ are mostly dominated by the lepton mis-measurements. Therefore, the differences between photon v.s. $Z \rightarrow ee/\mu\mu$ p_{T} resolutions are important in the signal regions, especially in the high p_{T} regions where the muon p_{T} resolution becomes significantly worse. Using the method described in Sec. 5.4, we derive a photon resolution smearing function from the 1-jet control regions to correct the photon p_{T} resolution to match $Z \rightarrow ee/\mu\mu$ p_{T} resolutions. The smearing function modifies the photon p_{T} in each photon event, and the $E_{\mathrm{T}}^{\mathrm{miss}}$ of the event is also recalculated accordingly.

The normalization and kinematic differences between $Z+$jets and $\gamma+$jets events are corrected by reweighting the photon sample. The reweighting factors are measured as function of the boson (Z and γ) p_{T} and are derived in the reweighting control regions. The reweighting control regions are chosen to be much looser than the signal region and validation region selections. To properly model the correlation between the boson p_{T} and the hadronic energy H_{T}, the reweighting control region has the same H_{T} cut as the corresponding signal region. The $\gamma+$jets events are then reweighted to match the boson p_{T} distribution of the $Z+$jets events. For each region, an additional normalization factor is derived in the lower $E_{\mathrm{T}}^{\mathrm{miss}}$ ($<$ 60 GeV) region and then applied to the signal region.

The m_{ll} distribution is modeled by parameterizing the m_{ll} in $Z+$jets events as a function of the difference between reconstructed and true Z boson p_{T} in MC simulation. This parameterization ensures that the correlation between lepton momentum mismeasurement and observed m_{ll} values far from the Z boson mass is preserved. The m_{ll} modeling is slightly changed in Sec. 5, where the m_{ll} shape is parametrized as function of $E_{\mathrm{T},\parallel}^{\mathrm{miss}}$ and boson p_{T}. The modified m_{ll} modeling is used in the later analyses. The resulting m_{ll} distribution in $\gamma+$jets MC simulation is compared to that extracted from $Z+$jets MC simulation and the difference is assessed as a systematic uncertainty in the background prediction for each m_{ll} bin. The validations of the m_{ll} modeling in the signal regions are shown in Fig. 6.6.

Fig. 6.7 shows the validation of the photon method in MC (left) and in data (right) closure. The validation regions are chosen to be close to the signal regions, except the $E_{\mathrm{T}}^{\mathrm{miss}}$ requirement is relaxed to $100-200$ GeV range in order to gain statistics. In the MC closure plot, the photon method prediction is derived from the Sherpa $\gamma+$jets MC sample and compared with the Sherpa $Z+$jets MC sample distribution. In the data closure plot, the photon method prediction is derived from the $\gamma+$jets data sample and compared with the dilepton data distribution in VR. Here the flavor-symmetric background is estimated using the data-driven flavor-symmetry method, and the fake-lepton background is estimated using the data-driven method explained in Section **??**. Rare top and diboson backgrounds are taken from MC simulation. The rare top and data-driven fake-lepton backgrounds are grouped under "other" backgrounds.

The Z+jets events enter the signal regions with fake $E_{\mathrm{T}}^{\mathrm{miss}}$ from the jet mis-measurements. The angular separations between the $E_{\mathrm{T}}^{\mathrm{miss}}$ and the leading jets are therefore a powerful discriminator to suppress jet mis-measurements, since the fake $E_{\mathrm{T}}^{\mathrm{miss}}$ is often aligned with the direction of the mis-measured jets. This angular separation is also well-modeled by the photon method. Fig. 6.8 shows the angular separation between $E_{\mathrm{T}}^{\mathrm{miss}}$ and the leading jet in the VR with four different H_{T} cuts. Fig. 6.9 shows the angular separation between $E_{\mathrm{T}}^{\mathrm{miss}}$ and the sub-leading jet. In both Figures, we see that in the regions with larger H_{T} cuts, relatively more Z + jets events appear in the small $\Delta\phi$ bins (where $E_{\mathrm{T}}^{\mathrm{miss}}$ points in the direction of the jet). This is because, in the larger H_{T} cut regions, the jet mis-measurement contributions become more important in the VRs and SRs.

6.6.3 Estimation of fake-lepton background

Semileptonic $t\bar{t}$, $W \to \ell\nu$ and single top events can enter the dilepton channel via fake leptons, which include leptons from heavy-flavor hadron decays, photon-e conversion, and jets being misidentified as leptons. This background has a small contribution in the regions with on-shell Z selections and high p_{T} leptons, but it becomes important in the edge search regions, where low p_{T} leptons are selected. The fake-lepton background is estimated using a matrix method described in [47]. The method correlates the number of fake-lepton events to the number of events passing the signal lepton selection. To illustrate the matrix method, let's consider the case of single-lepton selection. We assume that there is a number of N events in a dataset passing the baseline lepton selection. Among the N events, N_{fake} events are fake-lepton events and N_{real} events are real-lepton events. N_{pass} of the N events pass the signal lepton requirement, and N_{fail} of the N events fail the requirement. These numbers satisfy the relation $N = N_{\mathrm{pass}} + N_{\mathrm{fail}} = N_{\mathrm{real}} + N_{\mathrm{fake}}$. And the relation between the number of passing (failing) events to the real (fake)-lepton events is expressed as

$$\begin{bmatrix} N_{\text{pass}} \\ N_{\text{fail}} \end{bmatrix} = \begin{bmatrix} \epsilon & f \\ \epsilon & 1-f \end{bmatrix} \begin{bmatrix} N_{\text{real}} \\ N_{\text{fake}} \end{bmatrix}$$

, where ϵ is the efficiency of the real-lepton events passing the signal lepton selection and f is the fake rate of the fake-lepton events passing the signal lepton selection. We can invert the matrix and express N_{real} and N_{fake} as

$$\begin{bmatrix} N_{\text{real}} \\ N_{\text{fake}} \end{bmatrix} = \frac{1}{\epsilon - f} \begin{bmatrix} 1-f & -f \\ \epsilon - 1 & \epsilon \end{bmatrix} \begin{bmatrix} N_{\text{pass}} \\ N_{\text{fail}} \end{bmatrix}$$

, and the number of fake-lepton events passing the signal lepton selection is

$$N_{\text{pass}}^{\text{fake}} = f \times N_{\text{fake}} = \frac{(1-1/\epsilon)N_{\text{pass}} + N_{\text{fail}}}{1/f - 1/\epsilon}$$

In the dilepton channel, there are four possible configurations of lepton pairs, i.e. real-real (both leptons are real), real-fake (leading lepton is real and sub-leading lepton is fake), fake-real and fake-fake. The matrix express for the case of dilepton channel is then expand to a 4 × 4 matrix as

$$\begin{bmatrix} N_{\text{pass}-\text{pass}} \\ N_{\text{pass}-\text{fail}} \\ N_{\text{fail}-\text{pass}} \\ N_{\text{fail}-\text{fail}} \end{bmatrix} = \begin{bmatrix} \epsilon^2 & f\epsilon & \epsilon f & f^2 \\ \epsilon(1-\epsilon) & \epsilon(1-f) & (1-f)\epsilon & f(1-f) \\ (1-\epsilon)\epsilon & (1-\epsilon)f & f(1-\epsilon) & (1-f)f \\ (1-\epsilon)^2 & (1-\epsilon)(1-f) & (1-f)(1-\epsilon) & (1-f)^2 \end{bmatrix} \begin{bmatrix} N_{\text{real}-\text{real}} \\ N_{\text{real}-\text{fake}} \\ N_{\text{fake}-\text{real}} \\ N_{\text{fake}-\text{fake}} \end{bmatrix}$$

To estimate $N_{\text{pass}}^{\text{fake}}$, we need to measure the real-efficiency ϵ and the fake-rate f. The real-efficiency ϵ can be measured with $Z \to \ell\ell$ data events using a tag-and-probe method in a Z-rich control region CR-real (see the definition in Table 6.4), where the leading lepton p_{T} is required to be > 40 GeV, and only events with two same-flavor opposite-sign leptons are selected. To measure the fake-rate f, a region enriched with fake leptons is defined by selecting same-sign lepton pairs (see CR-fake in Table 6.4). In CR-fake the leading lepton is assumed to be real, and the fake-rate is evaluated based on the sub-leading lepton. The real-lepton contribution in CR-fake is estimated with MC simulation, which makes up 7% (11%) of the baseline electron (muon) and 10% (61%) of the signal electron (muon) in CR-fake. The measured real-efficiency and fake-rate as functions of lepton p_{T} are shown in Fig. 6.10.

The matrix method is validated in the regions where same-sign lepton pair events are selected (see VR-fake definition in Table 6.4). Fig. 6.11 shows the validation of the fake estimation as function of dilepton mass. The validation is shown in ee, $\mu\mu$, and different-flavor channels. Events in the Z-mass window in the same-flavor channels are removed because of the $Z+$jets contamination.

6.6.4 Estimation of diboson background

The diboson processes considered in this analysis are $WZ/ZZ \rightarrow \ell\ell qq$, $WW/ZZ \rightarrow \ell\ell\nu\nu$, and $WZ \rightarrow \ell\ell\ell\nu$. The $WW \rightarrow \ell\ell\nu\nu$ background is included in the flavor-symmetric method, and the $WZ/ZZ \rightarrow \ell\ell qq$ is included in the photon template method. The only diboson backgrounds that we discuss here are $ZZ \rightarrow \ell\ell\nu\nu$ and $WZ \rightarrow \ell\ell\ell\nu$, and these backgrounds are estimated directly from MC simulation. The $WZ \rightarrow \ell\ell\ell\nu$ background is validated in a 3-lepton region (VR-WZ), and the $ZZ \rightarrow \ell\ell\nu\nu$ background is validated with $ZZ \rightarrow \ell\ell\ell\ell$ sample in a 4-lepton region VR-ZZ ($ZZ \rightarrow \ell\ell\ell\ell$ and $ZZ \rightarrow \ell\ell\nu\nu$ are similar in MC generation). In the 3-lepton VR-WZ region, a same-flavor opposite sign lepton pair with m_{ll} closest to 91 GeV is identified as the Z-boson candidate. VR-WZ also requires the third lepton satisfies $m_T(\ell_3, etmiss) < 100$ GeV ($W \rightarrow \ell\nu$ transverse mass) and requires $E_{\mathrm{T}}^{\mathrm{miss}} > 50$ GeV to suppress $Z+$jets background. In the 4-lepton VR-ZZ region, two same-flavor opposite-sign lepton pairs are selected with the invariant mass combination result being closest to $2M_Z$. $E_{\mathrm{T}}^{\mathrm{miss}} < 100$ GeV is required in VR-ZZ to prevent WZ and $t\bar{t}$ events entering the region. Both VR-WZ and VR-ZZ have b-tagging jet veto requirement to suppress $t\bar{t}$ events. See VR-WZ and VR-ZZ definitions in Table 6.3. The data v.s. MC comparison can be seen in Fig. 6.12 and Table 6.6.

6.6.5 Validation of background estimations

The validations of the background methods are provided by comparing the observed data events v.s. background predictions in the dedicated validation regions. The flavour-symmetric, $Z+$jets, and fake-lepton contributions

	VR-WZ	VR-ZZ	VR-3L
Zee	11.94 ± 3.39	0 ± 0	0.45 ± 0.35
Zmm	14.26 ± 5.23	0 ± 0	0.41 ± 0.24
Ztt	0.07 ± 0.05	0 ± 0	0 ± 0
ttbar	8.81 ± 1.03	0 ± 0	0.40 ± 0.23
Rare Top	13.56 ± 0.17	0.44 ± 0.02	9.15 ± 0.12
VV - llvv	0.28 ± 0.15	0 ± 0	0 ± 0
ZZ - llll	37.51 ± 2.37	138.79 ± 4.95	1.57 ± 0.41
WZ - lllv	535.59 ± 6.01	0.06 ± 0.06	23.23 ± 1.29
MC Total	622.01 ± 9.04	139.29 ± 4.95	35.20 ± 1.44
Data	698	132	32

Table 6.6: Data vs. MC comparisons for the 3l and 4l diboson validation regions and VR-3L using 14.7 fb^{-1} of 2015 and 2016 data. The ttbar category includes Wt processes.

to VR-S are derived using the data-driven estimates described in Section 6.6.1, 6.6.2, and 6.6.3. All remaining backgrounds and all backgrounds in the diboson validation regions are taken from MC simulation. The quoted uncertainties in VR-S include statistical and all systematic contributions. In VR-WZ, VR-ZZ, and VR-3L, the rare top and diboson uncertainties include statistical and all theoretical uncertainties described in Section 6.6.6. The fake-lepton contribution in these three regions is predominantly due to $Z+$jets, and in this case, only the statistical uncertainty is given. The overall background estimations are validated in Table 6.7 and Table 6.8. The validation regions with selections close to SR-Z, SR-low, SR-medium, and SR-high, are also shown in Figure 6.13-6.16. The validations are provided separately in the ee, $\mu\mu$, same-flavor, and different-flavor channels.

6.6.6 Systematic uncertainties of background estimations

The uncertainties on the flavor-symmetry background are assessed based on the statistics in the control regions, the measurement of the efficiency correlation factors, the extrapolation in the m_{ll} shape, and the closure test performed with MC events. The flavor-symmetry background in the on-shell signal region SRZ has the dominant uncertainty (10%) from the low statistics in CR-FS, 3% from the efficiency correlation factors, 3% from the MC closure test, and 1% from the m_{ll} extrapolation. In the edge search, the

	VR-S	VR-WZ	VR-ZZ	VR-3L
Observed events	236	698	132	32
Total expected background events	224 ± 41	622 ± 66	139 ± 25	35 ± 10
Flavour-symmetric events	99 ± 8	-	-	-
WZ/ZZ events	27 ± 13	573 ± 66	139 ± 25	25 ± 10
Rare top events	11 ± 3	14 ± 3	0.44 ± 0.11	9.1 ± 2.3
$Z+$jets events	84 ± 37	-	-	-
Fake-lepton events	4 ± 4	35 ± 6	-	0.6 ± 0.3

Table 6.7: Expected and observed event yields in the four validation regions, VR-S, VR-WZ, VR-ZZ, and VR-3L. The individual uncertainties can be correlated and do not necessarily add up in quadrature to the total systematic uncertainty.

	VR-low	VR-medium	VR-high
Observed events	16253	1917	314
Total expected background events	16500 ± 700	1990 ± 150	340 ± 60
Data-driven flavour-symmetry events	14700 ± 600	1690 ± 120	250 ± 50
WZ/ZZ events	250 ± 80	40 ± 19	9 ± 6
Data-driven $Z+$jets ($\gamma+$jets) events	1100 ± 400	130 ± 70	50 ± 29
Rare top events	87 ± 23	27 ± 7	6.5 ± 1.8
Data-driven fake-lepton events	270 ± 100	98 ± 35	20 ± 11

Table 6.8: Expected and observed event yields in the three validation regions, VR-low, VR-medium and VR-high. The quoted uncertainties include statistical and systematic contributions. The individual uncertainties can be correlated and do not necessarily add up in quadrature to the total systematic uncertainty.

flavor-symmetry background is also dominated by the statistics in CR-FS in the case of SR-high. For SR-low and SR-medium, the statistics becomes larger in the control region, and the systematic uncertainties from MC closure tests and efficiency correlation factors become relatively important.

In the $Z+$jets background estimation, six sources of the systematic uncertainties are considered. The reweighting procedure uncertainty takes into account the difference in the photon method predictions in each region between the nominal reweighting factors using boson p_{T} v.s. the reweighting factors using other kinematic variables, including hadronic energy H_{T}, boson E_T ($\sqrt{m_{ll}^2+p^2}$), and jet multiplicity N_{jets}. The smearing function uncertainty compares the difference in the photon method predictions using the smearing function derived from the $1-$jet control region in MC sample, the $2-$jets region in MC sample, and the $1-$jet control region in data sample. The MC non-closure uncertainty reflects the discrepancy between the $Z+$jets MC prediciton v.s the photon method MC prediction (using photon MC sample) in the signal regoion. A relative uncertainty of 16% is assessed for the $V+\gamma$ contamination in the photon data sample, based on the data-to-MC agreement in a $V+\gamma$ enriched region. The m_{ll} uncertainty is calculated as the relative shape difference of the m_{ll} distributions provided by the MC photon method v.s. the $Z+$jets MC sample. The final uncertainty is the statistics of the photon data sample events that enter the signal region estimation.

The uncertainties in the fake-lepton background include the numbers of events in the regions used to measure the real- and fake-lepton efficiencies, the comparison of the fake-lepton efficiency measurements in b-tagged jet veto region v.s. in b-tagged jet filter region, and the difference in fake-lepton efficiencies by varying Monte Carlo prompt-lepton (real leptons from W decays) subtraction by 20%. The difference in the fake-lepton efficiencies by comparing b-tagged jet veto region v.s. in b-tagged jet filter region gives the largest uncertainty ($50-70\%$ in edge SRs).

Theoretical and experimental uncertainties are taken into account for the signal models and simulation-based background predictions, such as diboson WZ/ZZ and rare top processes. The theoretical uncertainties consider the choice of different PDF sets and factorization and normalization scales, and are assessed by varying these settings and comparing the differences with respect to the nominal values. The theoretical uncertainties for the signal models range from 16% to 30%, and about 20% for the diboson samples, 13% for the rare top samples. The experimental uncertainties consider the modeling of the detector effect in simulation. The jet energy scale concerns the uncertainties associated with the jet flavor composition, pile-up and the jet kinematics. The uncertainty in jet energy resolution is included to account for the differences between data and simulation. Uncertainties in trigger, reconstruction, and identification efficiencies are also considered.

The breakdown of the uncertainties (relative to the total background) in the SR background predictions is provided in Table 6.9.

Source	**Relative systematic uncertainty** [%]			
	SRZ	SR-low	SR-medium	SR-high
Total systematic uncertainty	17	8–30	6–34	10–45
WZ/ZZ generator uncertainty	13	0–7	0–6	0–10
Flavour symmetry (statistical)	7	3–16	5–16	7–28
WZ/ZZ scale uncertainty	6	0–1	0–1	0–2
$Z+$jets (systematic)	4	0–15	0–25	0–15
Flavour symmetry (systematic)	3	2–23	2–15	4–25
$Z+$jets (statistical)	2	0–3	0–5	0–1
Fake leptons	1	0–17	2–18	2–20

Table 6.9: Overview of the dominant sources of systematic uncertainty in the total background estimate in the signal regions. The values shown are relative to the total background estimate, shown in %. The systematic uncertainties for the edge search are quoted as a range across the m_{ll} regions used for statistical interpretations.

6.7 Results

6.7.1 Results in SRZ

Table 6.10 shows the observed data results and the background predictions in SRZ. The flavor-symmetric ($t\bar{t}$, Wt, WW and $Z \to \tau\tau$), $Z+$jets and fake-lepton components are all derived using data-driven estimates described in Section 6.6. All remaining backgrounds are taken from MC simulation. A total of 60 events are observed in data with a background prediction of 53.5 ± 9.3 events. There are 35 events observed in SRZ ee channel, and 25 events are observed in SRZ $\mu\mu$ channel. The observed significance, which is the standard deviation with respect to the background prediction is 0.47σ.

Figure 6.17 shows the summary of the agreements between the data event yields and the background predictions in the on-shell search VRs and SRZ. Figure 6.18 shows the dilepton invariant mass distributions for the $ee + \mu\mu$ and $e\mu$ channels with SRZ requirement but the on-shell Z mass cut ($m_{ll} \in [81, 101]$ GeV), where a good agreement between the data and the background prediction is seen across the full m_{ll} spectrum. With the exception of the $Z+$jets background, MC simulation is used to show the expected shapes of the m_{ll} distributions, with the backgrounds being normalized according to their SRZ prediction. Figure 6.19 shows the dilepton invarint mass, jet and b-tagged jet multiplicity, $E_{\mathrm{T}}^{\mathrm{miss}}$, $H_{\mathrm{T}}^{\mathrm{incl}}$, and dilepton p_{T} in SRZ. Figure 6.20 shows the minimum $\Delta\phi(jet_{1,2}, p_{\mathrm{T}}^{\mathrm{miss}})$ distributions in VR-S and SRZ with the cut on $\Delta\phi(jet_{1,2}, p_{\mathrm{T}}^{\mathrm{miss}})$ removed (VR-S and SRZ require $\Delta\phi(jet_{1,2}, p_{\mathrm{T}}^{\mathrm{miss}}) > 0.4$), and a good agreement between the data events and data-driven photon prediction is observed.

6.7.2 Results in Edge SRs

The integrated yields in the edge signal regions are compared to the background predictions in Table 6.11. To allow for the visualization of a potential signal edge, the full m_{ll} distributions in the three search regions are compared to the background predictions in Figure 6.21. A "sliding window" approach is used in the edge search to look for any excess across the m_{ll} spectrum as signal models may produce kinematic endpoints at any value of m_{ll}. There are 24 m_{ll} windows (9 for SR-low, 8 for SR-medium, 7 for SR-high) chosen based on the sensitivity optimization guided by the signal models. These bins, and sets of neighboring bins, make up the m_{ll} windows used for the interpretation. The results in the sliding window regions are summarized in Figure 6.22 , where the expected and observed yields in the 24 (overlapping) m_{ll} ranges of SR-low, SR-medium, and SR-high are shown. The observed data events, background predictions, model-independent limits, and significances are summarized in Table 6.12 , where the total expected background, with combined statistical and systematic uncertainties, observed data, 95% CL upper limits on the visible cross section ($\langle\epsilon\sigma\rangle_{\mathrm{obs}}^{95}$) and on the number of

	SRZ	SRZ ee	SRZ $\mu\mu$
Observed events	60	35	25
Total expected background events	53.5 ± 9.3	27.1 ± 5.1	26.8 ± 4.4
Flavour-symmetric events	33.2 ± 3.9	16.5 ± 2.1	16.7 ± 2.0
$Z +$ jets events	3.1 ± 2.8	$1.0^{+1.3}_{-1.0}$	2.1 ± 1.4
WZ/ZZ events	14.2 ± 7.7	7.8 ± 4.3	6.4 ± 3.5
Rare top events	2.9 ± 0.8	1.4 ± 0.4	1.5 ± 0.4
Fake-lepton events	$0.1^{+0.8}_{-0.1}$	$0.5^{+0.7}_{-0.5}$	$0^{+0.2}$
$p(s = 0)$	0.32	0.15	0.5
Significance (σ)	0.47	1.02	0
Observed (Expected) S^{95}	28.2 ($24.5^{+8.9}_{-6.7}$)	22.0 ($15.8^{+6.5}_{-4.5}$)	12.9 ($14.0^{+5.7}_{-3.9}$)
$\langle\epsilon\sigma\rangle^{95}_{\text{obs}}$ [fb]	1.9	1.5	0.88

Table 6.10: Expected and observed event yields in SRZ, inclusively, in the ee channel, and in the $\mu\mu$ channel, along with the discovery p-value for zero signal strength ($p(s = 0)$), Gaussian significance, 95% confidence level (CL) observed and expected upper limits on the number of signal events (S^{95}), and the corresponding observed upper limit on the visible cross section ($\langle\epsilon\sigma\rangle^{95}_{\text{obs}}$). For regions in which the data yield is less than expected, the discovery p-value is truncated at 0.5 and the significance is set to zero. The quoted uncertainties include statistical and systematic contributions. The individual uncertainties can be correlated and do not necessarily add up in quadrature to the total systematic uncertainty.

	SR-low	SR-medium	SR-high
Observed events	1394	689	212
Total expected background events	1500 ± 100	700 ± 60	171 ± 18
Flavour-symmetric events	1270 ± 70	584 ± 32	148 ± 14
$Z +$ jets events	90 ± 50	50 ± 40	3^{+7}_{-3}
WZ/ZZ events	68 ± 31	26 ± 11	7 ± 4
Rare top events	19 ± 5	11.3 ± 3.2	4.2 ± 1.4
Fake-lepton events	59 ± 34	32 ± 19	10 ± 8

Table 6.11: Breakdown of the expected background and observed data yields for SR-low, SR-medium and SR-high, integrated over the m_{ll} spectrum. The quoted uncertainties include statistical and systematic contributions.

signal events (S^{95}_{obs}) are provided. Table 6.12 also shows the expected 95% CL upper limit on the number of signal events (S^{95}_{exp}), given the expected number (and $\pm 1\sigma$ excursions) of background events. The last two columns of Table 6.12 indicate the discovery p-value ($p(s = 0)$), and the Gaussian significance ($Z(s = 0)$). In SR-low and SR-medium, the data are consistent with the background prediction across the m_{ll} spectrum. In SR-high, the data shows a small excess at low m_{ll} windows. This excess locates in $m_{ll} \in [12, 101]$ GeV range, where 90 data events are observed and 65 ± 10 background events are predicted. The excess corresponds to a local significance of 1.7σ.

6.8 Interpretation

The observed data results in the search signal regions are interpreted in this section using the SUSY signal models detailed in Sec. 6.2. For the on-shell Z search, the asymptotic CL_S prescription, which is implemented in the HistFitter program [48], is used to determine the cross-section upper limits at 95% confidence level (CL). For the edge search, a set of pseudo-experiments are used to calculate the cross-section upper limits. To compute the significances and the cross-section upper limits, a Gaussian model for nuisance parameters is used for the systematic uncertainties of all signal models and backgrounds, while Poissonian nuisance parameters are used for the statistical uncertainties

Signal Region	Total Bkg.	Data	$\langle\epsilon\sigma\rangle^{95}_{\mathrm{obs}}$[fb]	S^{95}_{obs}	S^{95}_{exp}	$p(s=0)$	$Z(s=0)$
SR-low							
12–61	187 ± 18	175	2.68	39.4	48^{+23}_{-14}	0.50	0.00
12–81	330 ± 24	320	3.88	57.1	64^{+30}_{-19}	0.50	0.00
12–101	617 ± 63	534	4.64	68.2	98^{+36}_{-26}	0.50	0.00
81–101	287 ± 50	214	2.73	40.2	62^{+22}_{-16}	0.50	0.00
101–201	529 ± 34	540	6.80	99.9	91^{+52}_{-29}	0.40	0.26
101–301	741 ± 48	732	7.28	107	113^{+53}_{-33}	0.50	0.00
201–401	295 ± 30	262	3.43	50.5	70^{+37}_{-21}	0.50	0.00
301–501	113 ± 17	99	2.37	34.8	46^{+41}_{-16}	0.50	0.00
> 501	29 ± 10	29	1.88	27.7	27^{+34}_{-10}	0.50	0.01
SR-medium							
12–61	119 ± 15	109	2.38	35.1	43^{+29}_{-14}	0.50	0.00
12–81	190 ± 18	191	3.57	52.5	51^{+31}_{-15}	0.48	0.06
12–101	315 ± 43	299	5.12	75.3	81^{+29}_{-20}	0.50	0.00
81–101	125 ± 35	108	3.18	46.7	51^{+17}_{-12}	0.50	0.00
101–201	235 ± 20	240	4.26	62.6	58^{+37}_{-19}	0.42	0.19
101–301	332 ± 25	336	4.92	72.3	69^{+39}_{-22}	0.45	0.14
201–401	126 ± 13	128	3.27	48.0	46^{+52}_{-16}	0.46	0.11
> 401	28 ± 8	22	1.09	16.1	21^{+19}_{-7}	0.50	0.00
SR-high							
12–61	23 ± 5	27	1.84	27.0	20^{+31}_{-8}	0.27	0.62
12–81	39 ± 7	53	3.32	48.9	26^{+28}_{-10}	0.08	1.40
12–101	65 ± 10	90	4.00	58.8	31^{+17}_{-10}	0.04	1.73
81–101	26 ± 6	37	2.17	31.9	20^{+13}_{-7}	0.12	1.18
101–201	59 ± 9	75	3.68	54.1	31^{+29}_{-11}	0.10	1.27
201–401	39 ± 7	33	1.82	26.7	28^{+14}_{-7}	0.50	0.00
> 401	10 ± 5	14	2.04	30.0	21^{+79}_{-10}	0.27	0.62

Table 6.12: Breakdown of the expected background and observed data yields in the edge signal regions. The results are given for SR-low, SR-medium and SR-high in all 24 m_{ll} ranges. For an observed number of events lower than expected, the discovery p-value is truncated at 0.5 and the significance is set to zero.

of the signal models and backgrounds. The different experimental uncertainties are treated as correlated between signal and MC background samples (the experimental uncertainties are related to the detector effects, such as object resolutions and efficiencies, which affect the background and signal events in the same way).

The expected and the observed limits are set based on the signal model events, observed data events, and the background estimations in the signal regions with all uncertainties included. For example, the limits on $\tilde{g}$–$\tilde{\chi}_2^0$ and $\tilde{q}$–$\tilde{\chi}_2^0$ models from the results in SRZ are shown in Figure 6.23 and 6.24, respectively. The dashed blue line represents the expected limits at 95% CL with all uncertainties in the background estimations and the experimental uncertainties in the signal models. The yellow band shows the 1σ variation ($\pm 1\sigma_{\mathrm{exp}}$) of the expected limits. The observed limits are shown by the solid red line, which includes all background estimation uncertainties and MC experimental uncertainties, except the theoretical uncertainty of the signal cross-section. The impact of the theoretical uncertainty of the signal cross-section is shown by the dotted red lines, which indicate the results of variating the signal cross-section by $\pm 1\sigma_{\mathrm{theory}}^{\mathrm{SUSY}}$.

The signal contamination in the CRs is found to have a negligible impact for the signal points near the exclusion boundaries, and thus the signal contamination in the CRs is neglected. For the signal points far from the boundaries, the signal contamination in CRs is not small, but the expected numbers of signal events in the signal regions are large enough that these points are still excluded.

Figure 6.23 interprets the results of the on-shell Z search with a simplified gluino-pair production model, where each gluino decays as $\tilde{g} \to q\bar{q}\tilde{\chi}_2^0, \tilde{\chi}_2^0 \to Z\tilde{\chi}_1^0$ and the mass of $\tilde{\chi}_1^0$ is set to 1 GeV. The expected and the observed exclusions, based on the background estimations and observed data events, are presented in the plane of $m(\tilde{g})$–$m(\tilde{\chi}_2^0)$ parameters. The expected and the observed highest lower limits on the gluino mass is about 1.35 TeV for $\tilde{\chi}_2^0$ mass ranges from 400 GeV to 1.1 TeV. The uncertainty on the exclusion contour, which arose from the systematic uncertainties in the data-driven background estimations and the experimental uncertainties in the MC samples, is about ±50 GeV on the gluino mass limit. The impact of the uncertainty in the signal cross-section is shown as the dotted red lines and has an uncertainty about 40 GeV on the exclusion contour. The expected and the observed exclusion limits for the $\tilde{q}$–$\tilde{\chi}_2^0$ on-shell model are shown in Figure 6.24. This simplified model has squark-pair production with each squark decays to a quark and a neutralino, and the neutralino subsequently decaying to a Z boson and an LSP, whose mass is set to 1 GeV. The expected and observed exclusion limits for this model are about 1040 GeV (expected) and 980 GeV (observed) for the masses of squarks.

The results of the edge search are interpreted as the slepton model in Figure 6.25 and as the off-shell decay Z model in Figure 6.26. In the slepton model, a pair of gluino is produced and each gluino decays as $\tilde{g} \rightarrow q\bar{q}\tilde{\chi}_2^0, \tilde{\chi}_2^0 \rightarrow \ell^{\pm}\tilde{\ell}^{\mp}, \tilde{\ell}^{\mp} \rightarrow \ell^{\mp}\tilde{\chi}_1^0$. The exclusion contour is presented in the $m(\tilde{g})$–$m(\tilde{\chi}_1^0)$ plane, which shows the largest lower limit on the masses of gluinos about 1.7 TeV with light $\tilde{\chi}_1^0$. The results probe the mass gap between $m(\tilde{\chi}_2^0) - m(\tilde{\chi}_1^0)$ as small as 50 GeV.

In the off-shell decay Z model ($Z^{(*)}$), pair-produced gluinos each decay as $\tilde{g} \rightarrow q\bar{q}\tilde{\chi}_2^0, \tilde{\chi}_2^0 \rightarrow Z^{(*)}\tilde{\chi}_1^0$. The Z boson decays off-shell when the mass splitting between the $\tilde{\chi}_2^0$ and the $\tilde{\chi}_1^0$ is smaller than the mass of the Z boson at 91 GeV. The decay chain of the off-shell decay Z model (edge search) is the same as the decay chain of the on-shell Z model (on-shell search), and the results of the two searches are compared in Figure 6.26. Compared to the on-shell search, the edge search extends the sensitivity to the more compressed region, where the mass splitting between the $\tilde{\chi}_2^0$ and the $\tilde{\chi}_1^0$ is small.

Based only on the observed numbers of data events and the background estimations in the SRs, the model-independent upper limits at 95% CL on the number of beyond-standard-model physics events in the SRs is derived with CL_{S} prescription, and the possibility of signal contamination in the CRs is neglected. The expected and observed upper limits of the on-shell Z search are given in Table 6.10. The same information is given for the 24 m_{ll} ranges of the edge search in Table 6.12.

6.9 Conclusion

Two searches for new physics in the two same-flavor opposite-sign leptons in association with jets and large missing transverse momentum final states are performed using 14.7 fb^{-1} of ATLAS data collected during 2015 and 2016 at the LHC at $\sqrt{s} = 13$ TeV. The on-shell search signal region is motivated by the observed excess in the ATLAS Run-1 results. In addition ot the on-shell search, the edge search considers 24 ranges in the m_{ll} spectrum, with different $E_{\mathrm{T}}^{\mathrm{miss}}$ and H_{T} requirements, to look for possible kinematic endpoint as the result of the mass splitting between the supersymmetric particles. The most difficult background to model in this final-state channel is the standard model Z+jets production, which enters the signal regions with the mismeasurements on the jet and lepton energies. This background is estimated using the data $\gamma +$ jets events to model the jet energy mismeasurements in $Z +$ jets events and performing a deconvolution method in the control region to estimate the lepton energy mismeasurements. The dominant background events are from the $t\bar{t}$ process, which is estimated using $e\mu$ data based on the fact that the flavors of the two leptons from the top quarks decay are uncorrelated. The fake lepton contribution in the signal regions is estimated using a matrix method. The data in both searches are found to be consistent with the background prediction. Based on the observation, the masses of gluinos (sqaurks) are excluded up to 1.7 TeV (980 GeV) in the simplified models of gluino-pair (squark-pair) productions used in this analysis.

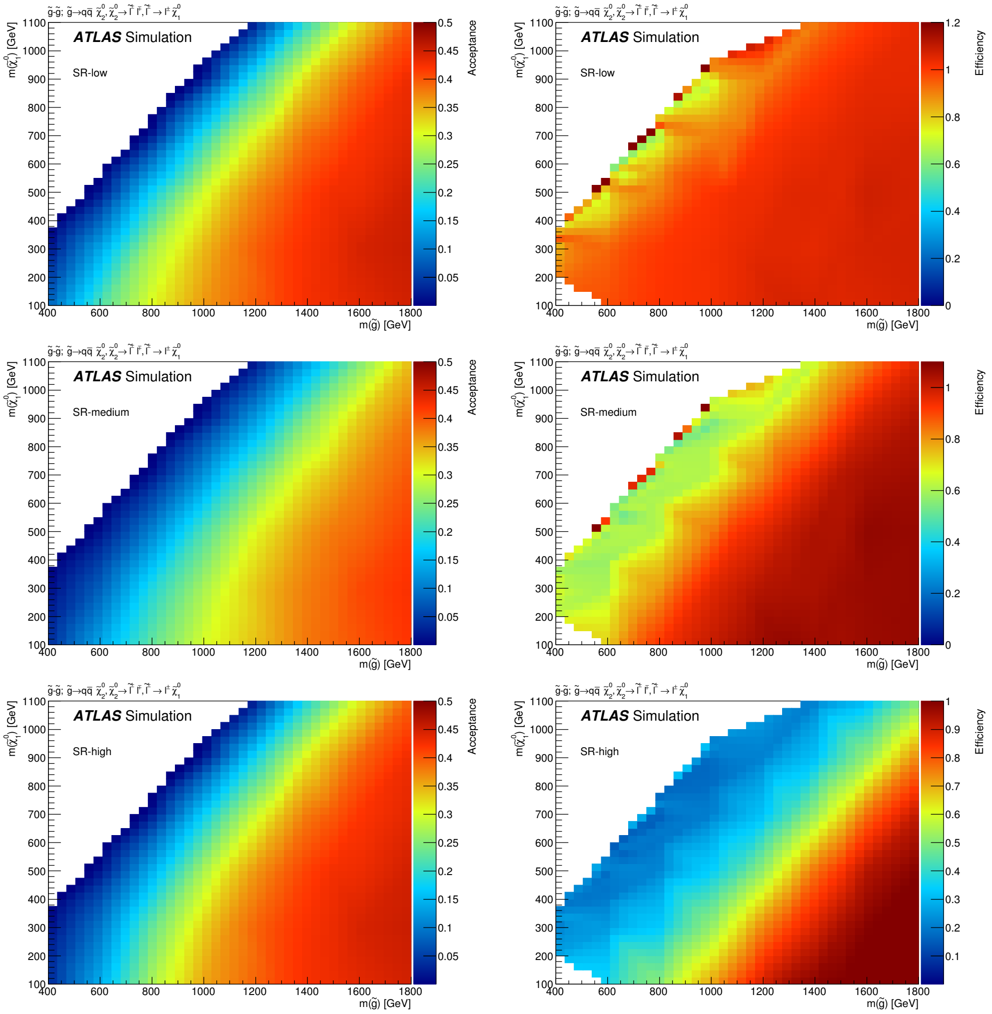

Figure 6.4: Signal region acceptance (left) and efficiency (right) over the full m_{ll} range for SR-low (top), SR-medium (middle) and SR-high (bottom) for the slepton model. Acceptance is calculated by applying the signal-region kinematic requirements to particle-level objects, which do not suffer from identification inefficiencies or measurement resolutions. A particle-level filter requiring at least two leptons (electrons or muons) with $p_{\mathrm{T}} > 5$ GeV and $|\eta| < 2.8$ is applied during event generation, and the acceptance is provided relative to that filter.

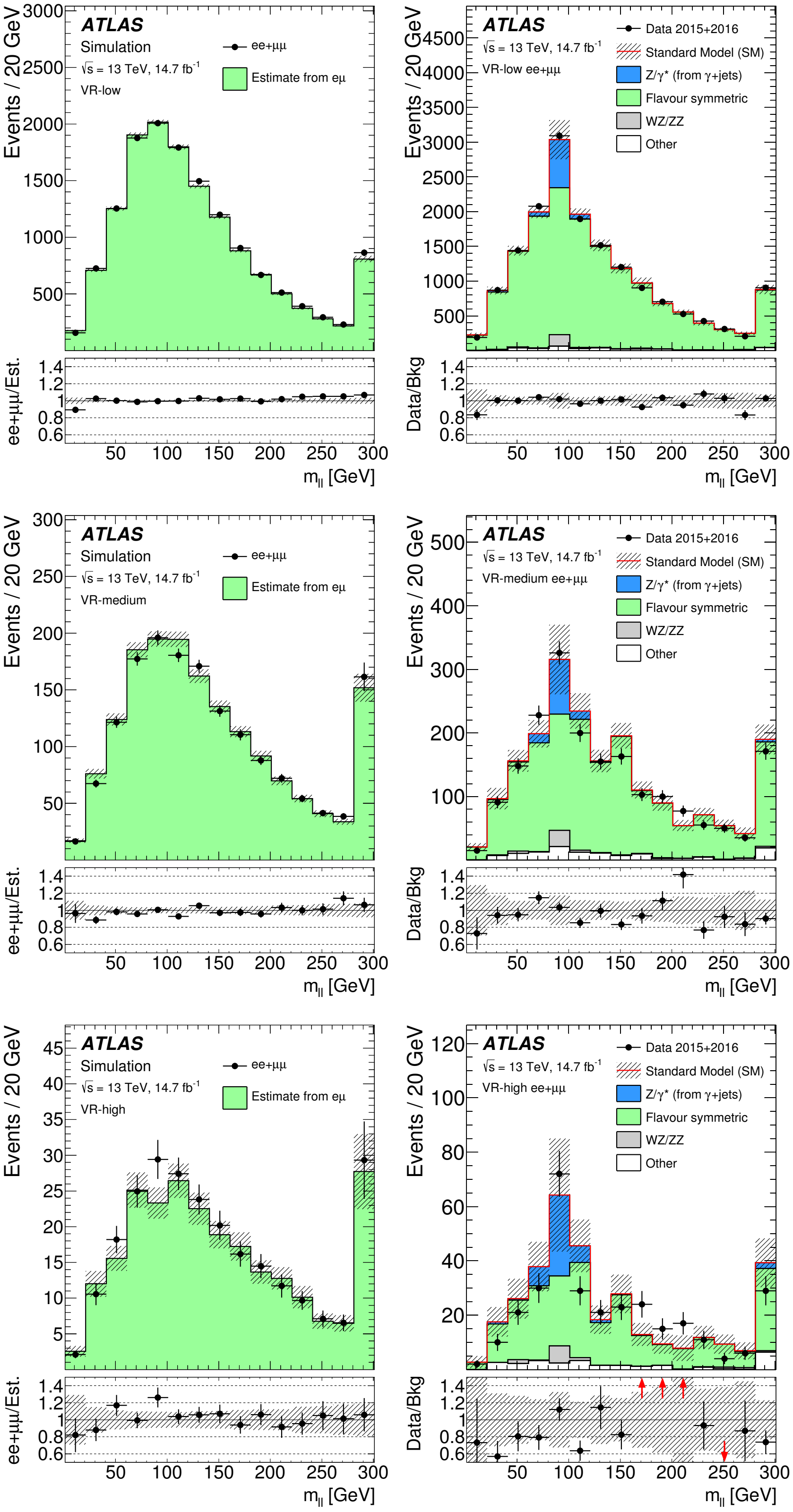

Figure 6.5: Validation of the flavor-symmetry method for the edge search using MC events (left) and data (right), in the VR-low (top), VR-medium (middle), and VR-high (bottom) regions.

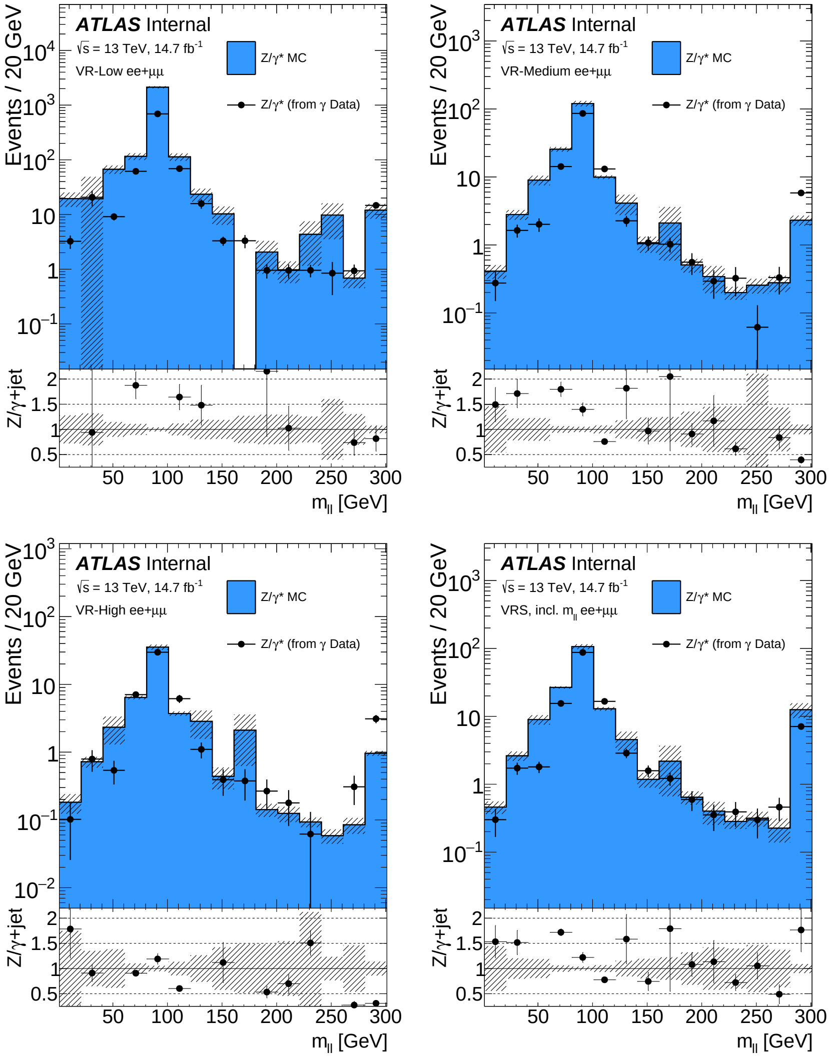

Figure 6.6: The m_{ll} distributions in $Z+$jets MC compared with the $\gamma+$jets prediction in the region with inclusive H_{T} (top left), $H_{\mathrm{T}} > 400$ GeV (top right), $H_{\mathrm{T}} > 700$ GeV (bottom left) and $H_{\mathrm{T}}^{\mathrm{incl}} > 600$ GeV (bottom right) in the $ee+\mu\mu$ channel. The hashed band includes the statistical uncertainty only.

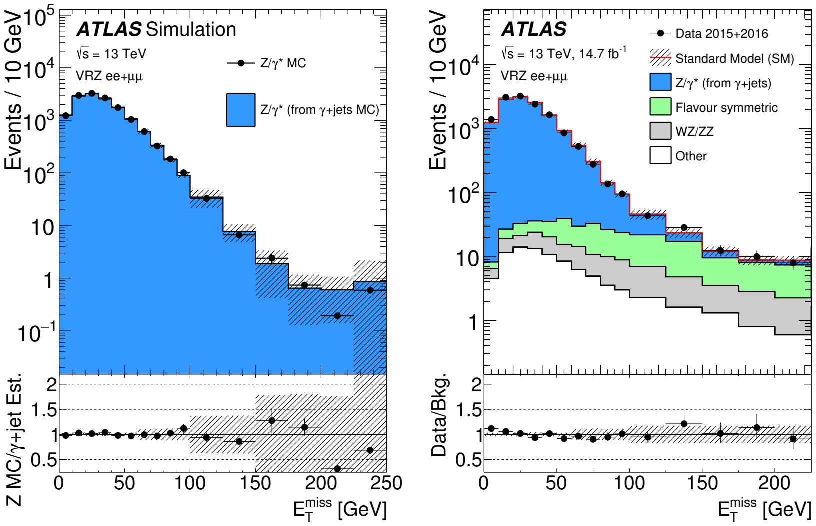

Figure 6.7: Left, the $E_{\mathrm{T}}^{\mathrm{miss}}$ spectrum in Sherpa $Z + \text{jets}$ MC simulation compared to that of the $\gamma + \text{jets}$ background estimation technique applied to Sherpa $\gamma + \text{jets}$ MC simulation in VRZ. The hashed uncertainty bands indicate the statistical and reweighting systematic uncertainties of the $\gamma + \text{jets}$ background method. Right, the $E_{\mathrm{T}}^{\mathrm{miss}}$ spectrum when the method is applied to data in VRZ. The hashed bands indicate the systematic uncertainty of only the $\gamma + \text{jets}$ and flavor-symmetric backgrounds below 100 GeV and the full uncertainty of the VR-S prediction above 100 GeV.

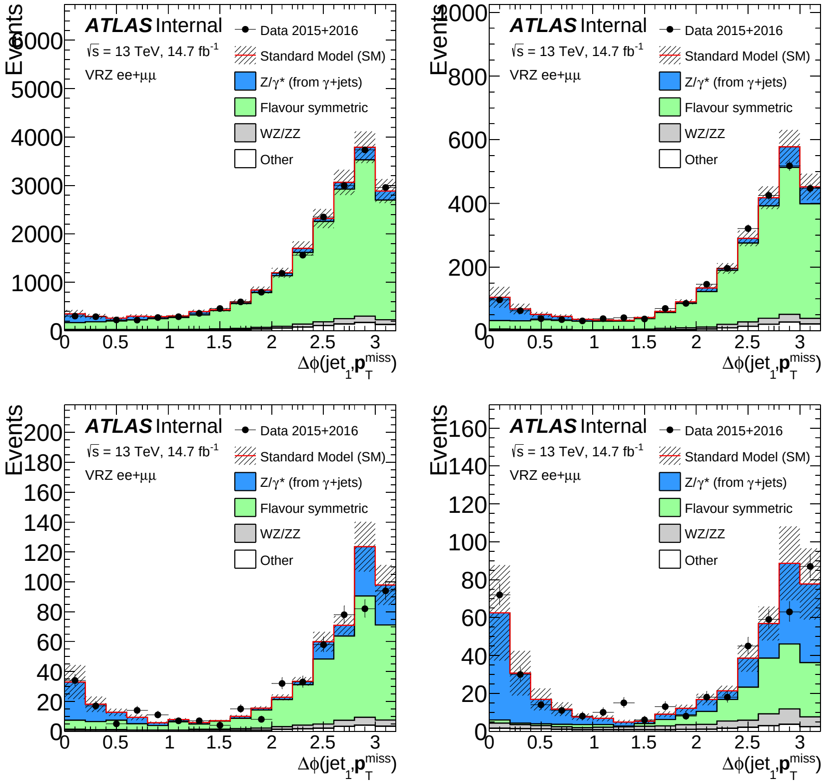

Figure 6.8: The $\Delta\phi(\text{jet}_1, E_{\text{T}}^{\text{miss}})$ distributions in data compared with the full $\gamma + \text{jets}$ prediction in the region with inclusive H_{T} (top), $H_{\text{T}} > 400$ GeV (middle), $H_{\text{T}} > 700$ GeV (bottom left) and $H_{\text{T}}^{\text{incl}} > 600$ GeV with $m_{ll} \in [81, 101]$ GeV (bottom right) in the $ee + \mu\mu$ channel. In these distributions the flavor-symmetric background is taken from the flavor-symmetry method. The uncertainty band includes the total systematic uncertainty on each background applied as a flat uncertainty in $\Delta\phi(\text{jet}_1, E_{\text{T}}^{\text{miss}})$.

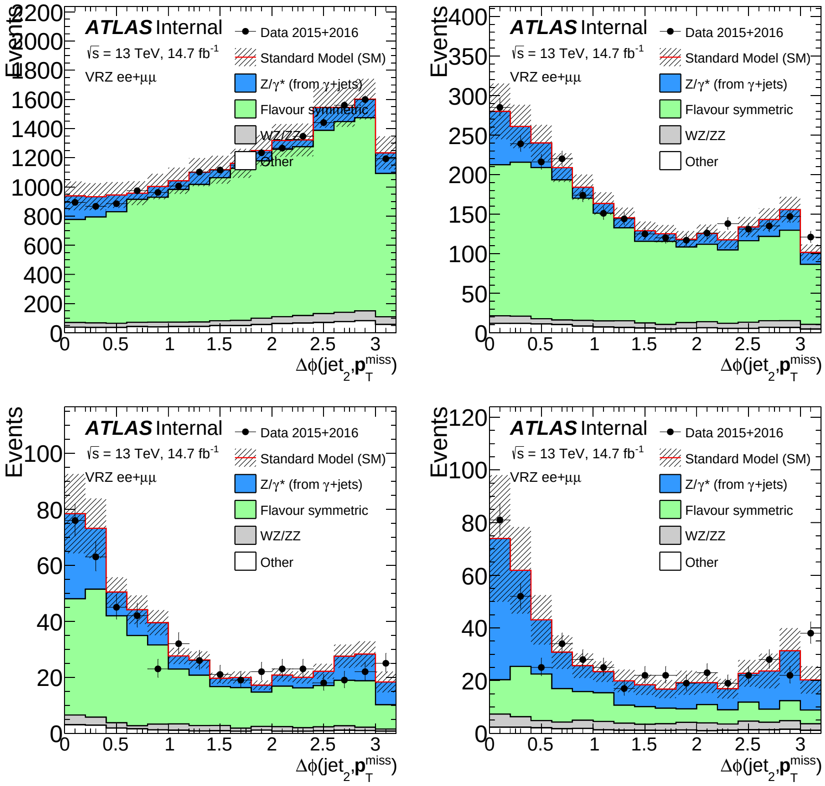

Figure 6.9: The $\Delta\phi(\mathrm{jet}_2, E_{\mathrm{T}}^{\mathrm{miss}})$ distributions in data compared with the full $\gamma + \mathrm{jets}$ prediction in the region with inclusive H_{T} (top), $H_{\mathrm{T}} > 400$ GeV (middle), $H_{\mathrm{T}} > 700$ GeV (bottom left) and $H_{\mathrm{T}}^{\mathrm{incl}} > 600$ GeV with $m_{ll} \in [81, 101]$ GeV (bottom right) in the $ee + \mu\mu$ channel. In these distributions the flavor-symmetric background is taken from the flavor-symmetry method. The uncertainty band includes the total systematic uncertainty on each background applied as a flat uncertainty in $\Delta\phi(\mathrm{jet}_2, E_{\mathrm{T}}^{\mathrm{miss}})$.

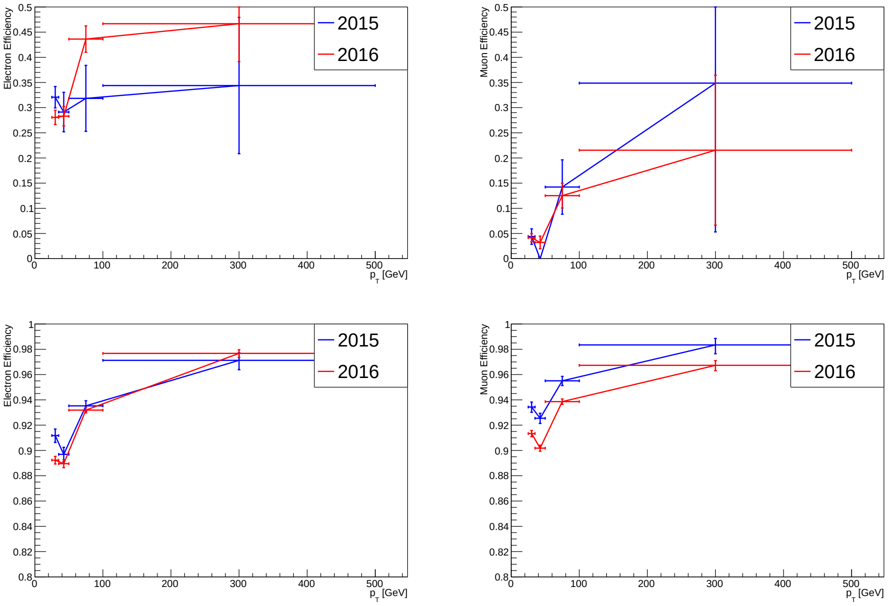

Figure 6.10: Electron (left) and muon (right) fake efficiency (top) and real efficiency (bottom) as measured with the 2015 and 2016 datasets. Errors are statistical only.

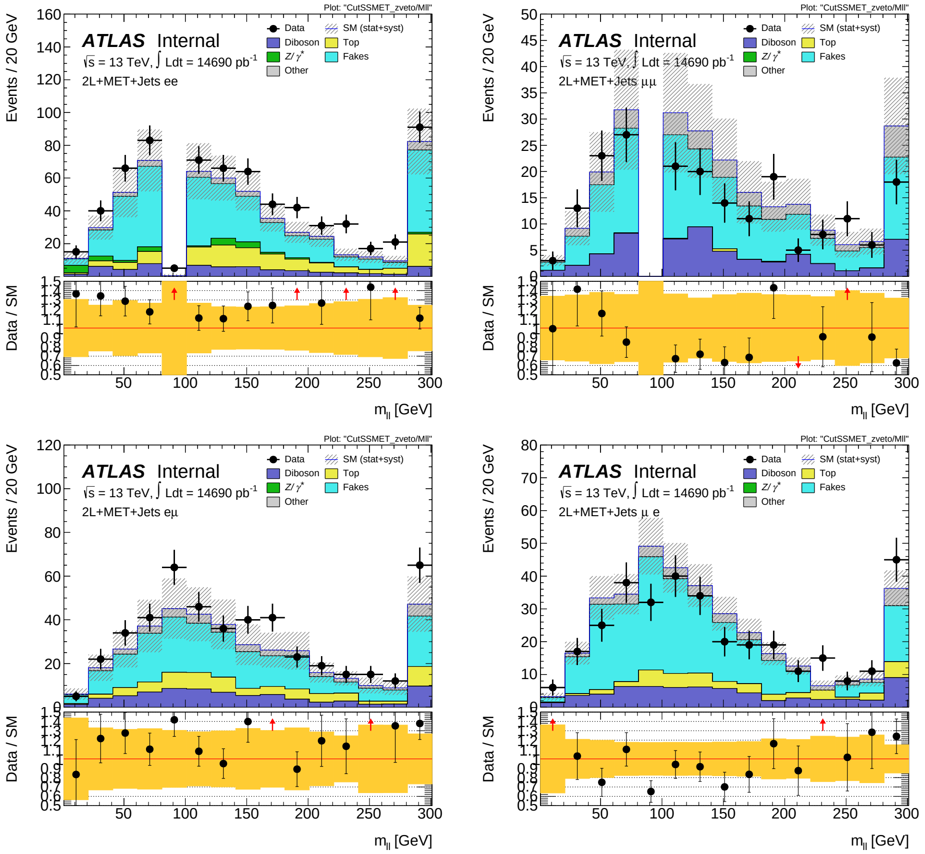

Figure 6.11: Same sign validation regions in the ee (top left), $\mu\mu$ (top right), $e\mu$ (bottom left) and μe (bottom right) channels combining 2015+2016 data.

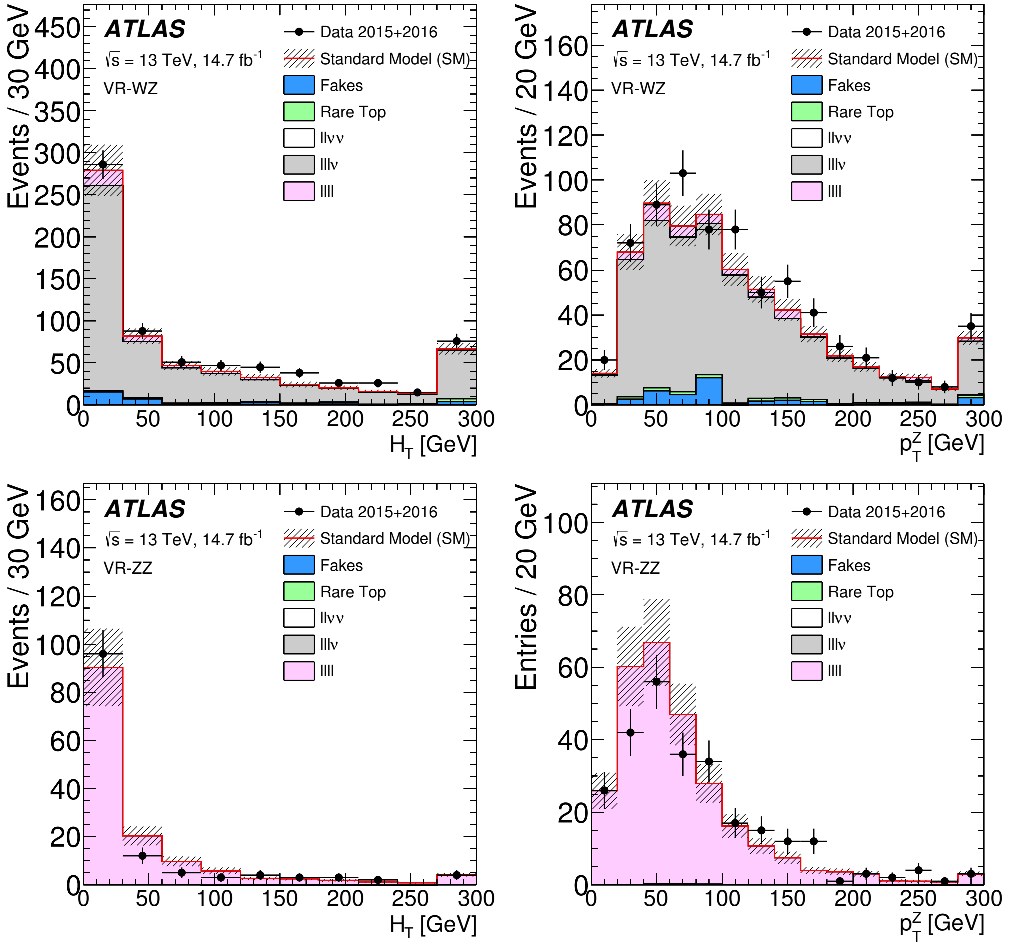

Figure 6.12: H_{T} (left) and boson p_{T} (right) distributions in VR-WZ (top) and VR-ZZ (bottom). All backgrounds are taken from MC. The hashed bands include the MC statistical uncertainties and theoretical uncertainties on the diboson background. The last bin contains the overflow.

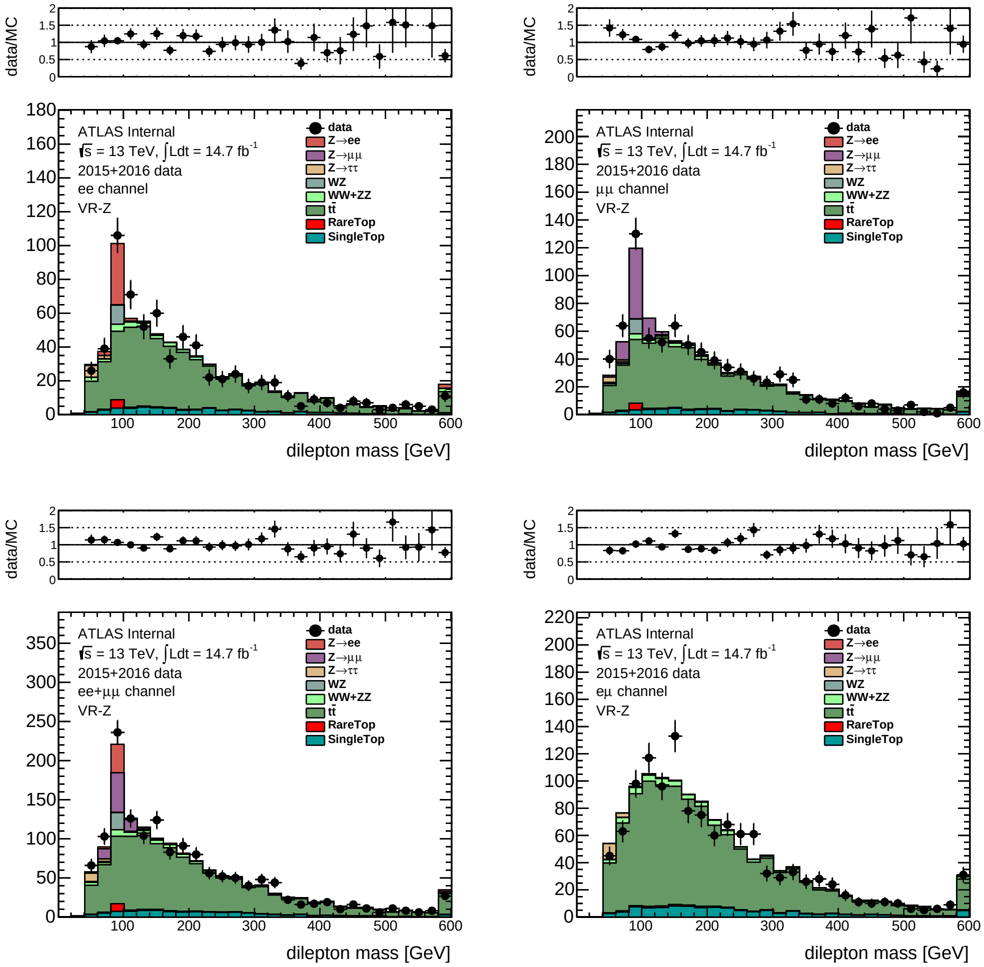

Figure 6.13: Data/MC comparison of m_{ll} in the VR-Z region, in the (top left) ee, (top right) $\mu\mu$, (bottom left) $ee + \mu\mu$, and (bottom right) $e\mu$ channels, using 2015+2016 data. The $t\bar{t}$MC is normalized by $\mu_{t\bar{t}} = 0.89$ such that the total MC matches data in the $e\mu$ channel. The $Z +$jets background is normalized to match the prediction from the $\gamma +$jets method.

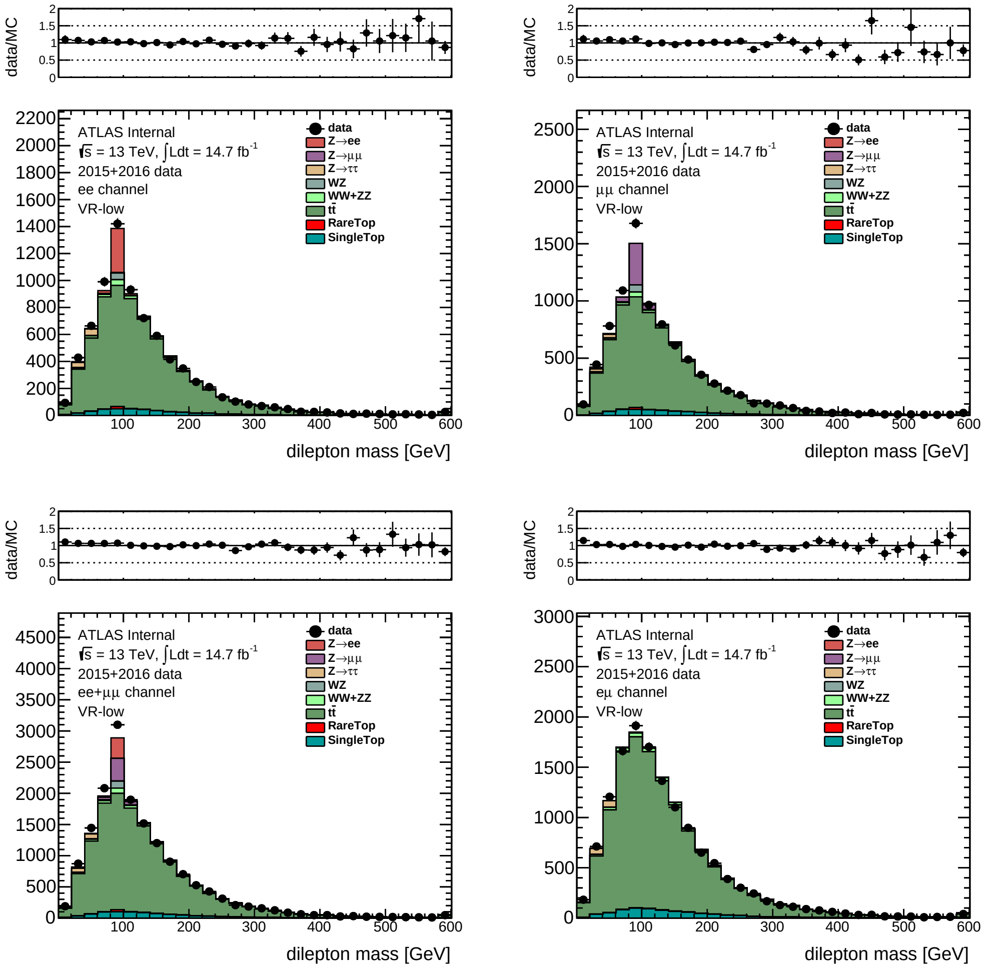

Figure 6.14: Data/MC comparison of m_{ll} in the VR-low region, for 2015+2016 data. The $Z+$jets background is modelled using the $\gamma+$jets method. Here $\mu_{t\bar{t}} = 0.95$.

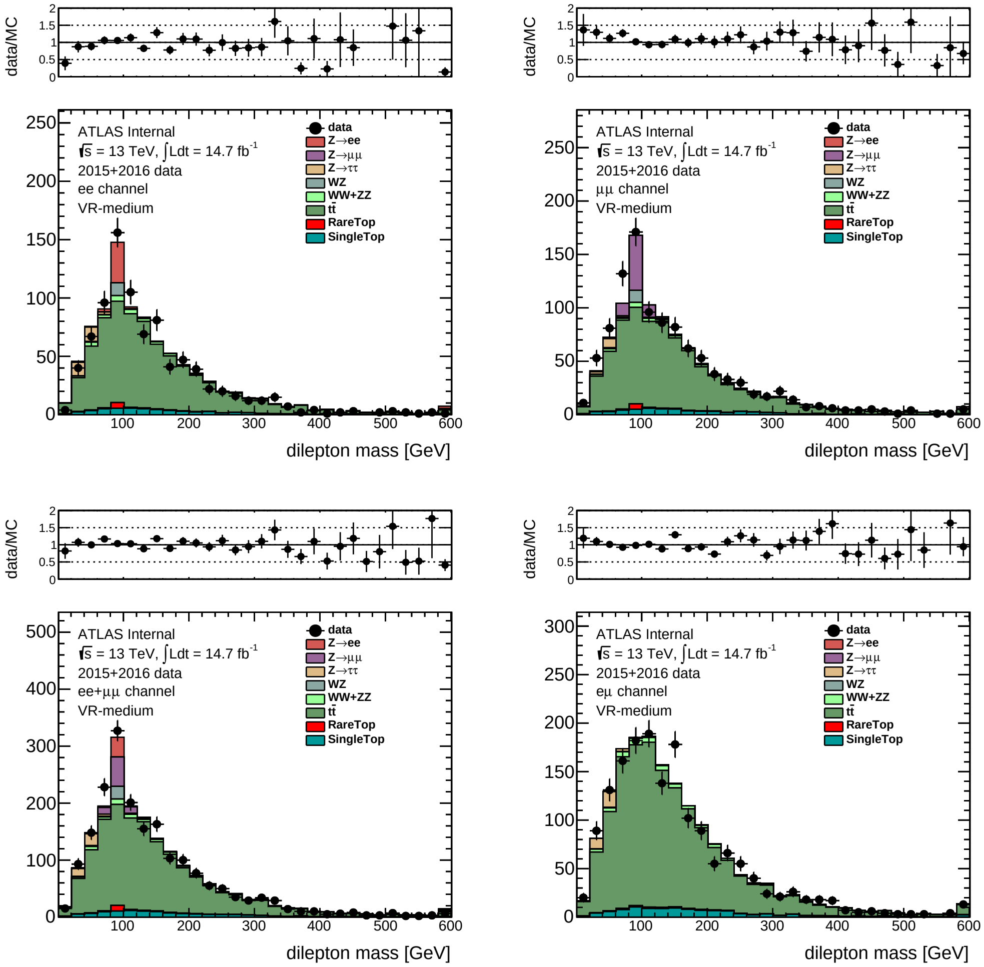

Figure 6.15: Data/MC comparison of m_{ll} in the VR-medium region, for 2015+2016 data. Details are the same as in Figure 6.14. The $Z+$jets background is modelled using the $\gamma+$jets method. Here $\mu_{t\bar{t}} = 0.94$.

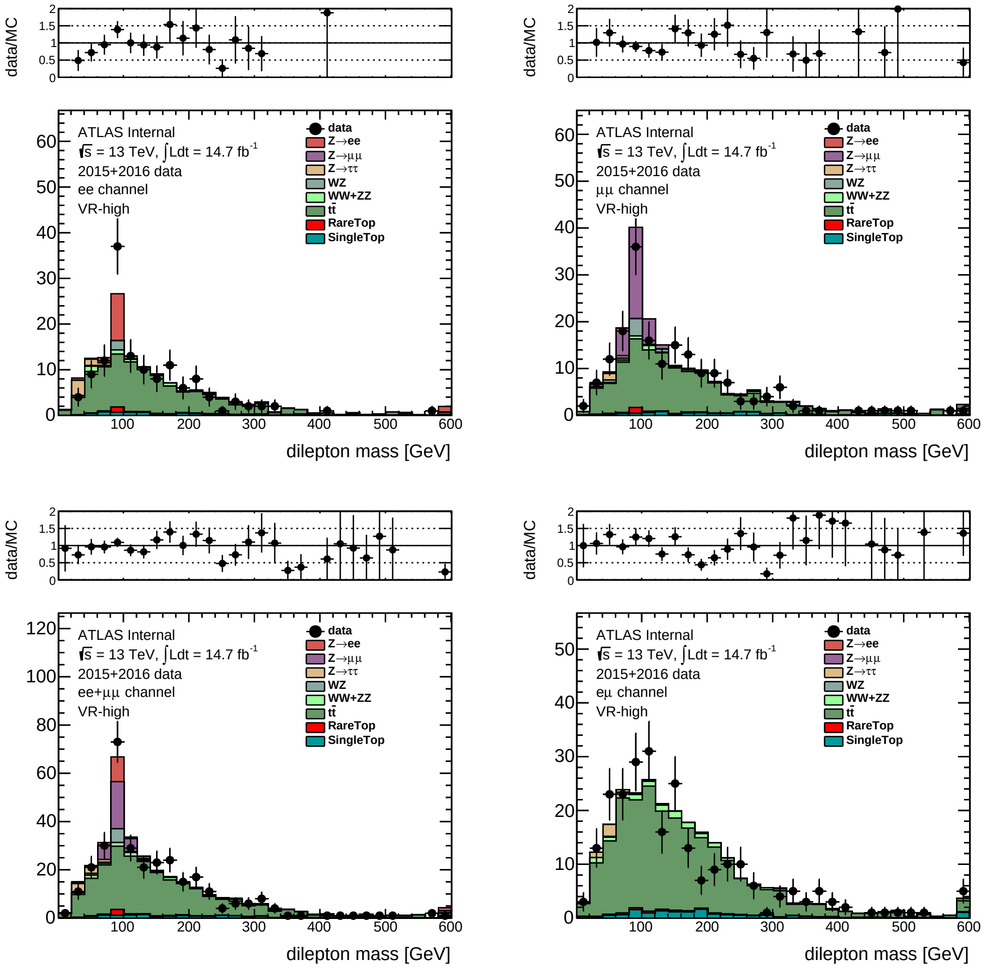

Figure 6.16: Data/MC comparison of m_{ll} in the VR-high region, for 2015+2016 data. Details are the same as in Figure 6.14. The $Z+$jets background is modelled using the $\gamma+$jets method. Here $\mu_{t\bar{t}} = 0.93$.

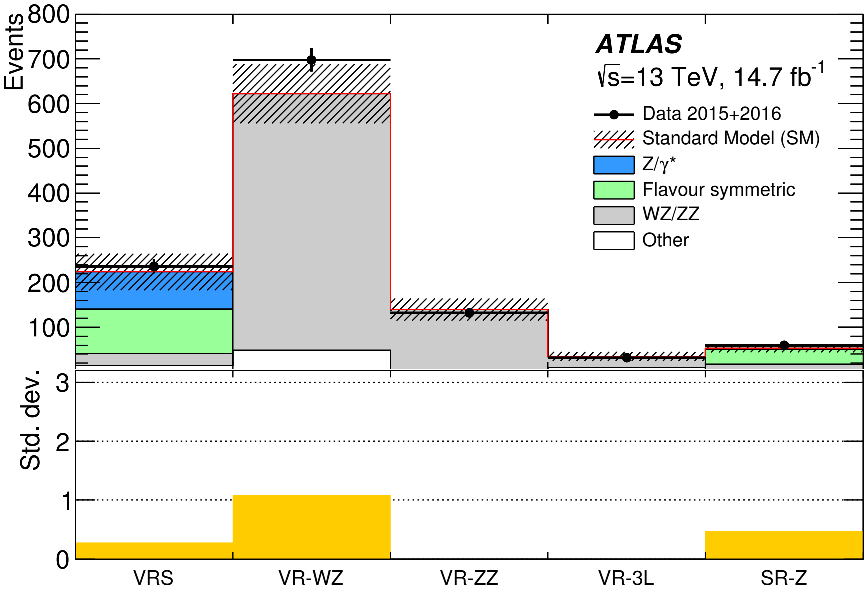

Figure 6.17: The expected and observed yields in the validation regions and signal region of the on-shell Z search. The rare top and data-driven fake-lepton backgrounds are grouped under “other” backgrounds. The significance of the difference between the data and the expected background (see text for details) is shown in the bottom plot; for regions in which the data yield is less than expected, the significance is set to zero. The hashed uncertainty bands include the statistical and systematic uncertainties in the background prediction.

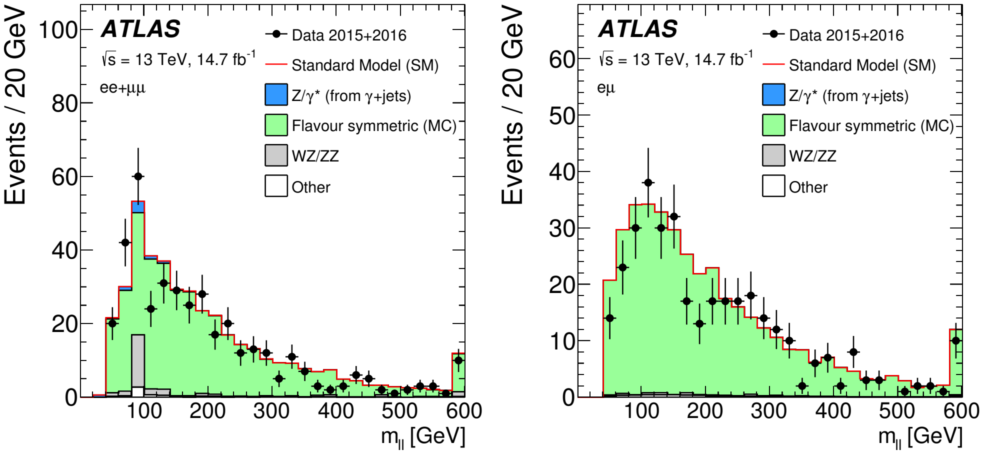

Figure 6.18: The dilepton invariant-mass distribution for an SRZ-like selection, but with the Z mass requirement removed, in the same-flavor (left) and different-flavor (right) channels. The rare top and data-driven fake-lepton backgrounds are grouped under “other” backgrounds. The last bin includes the overflow.

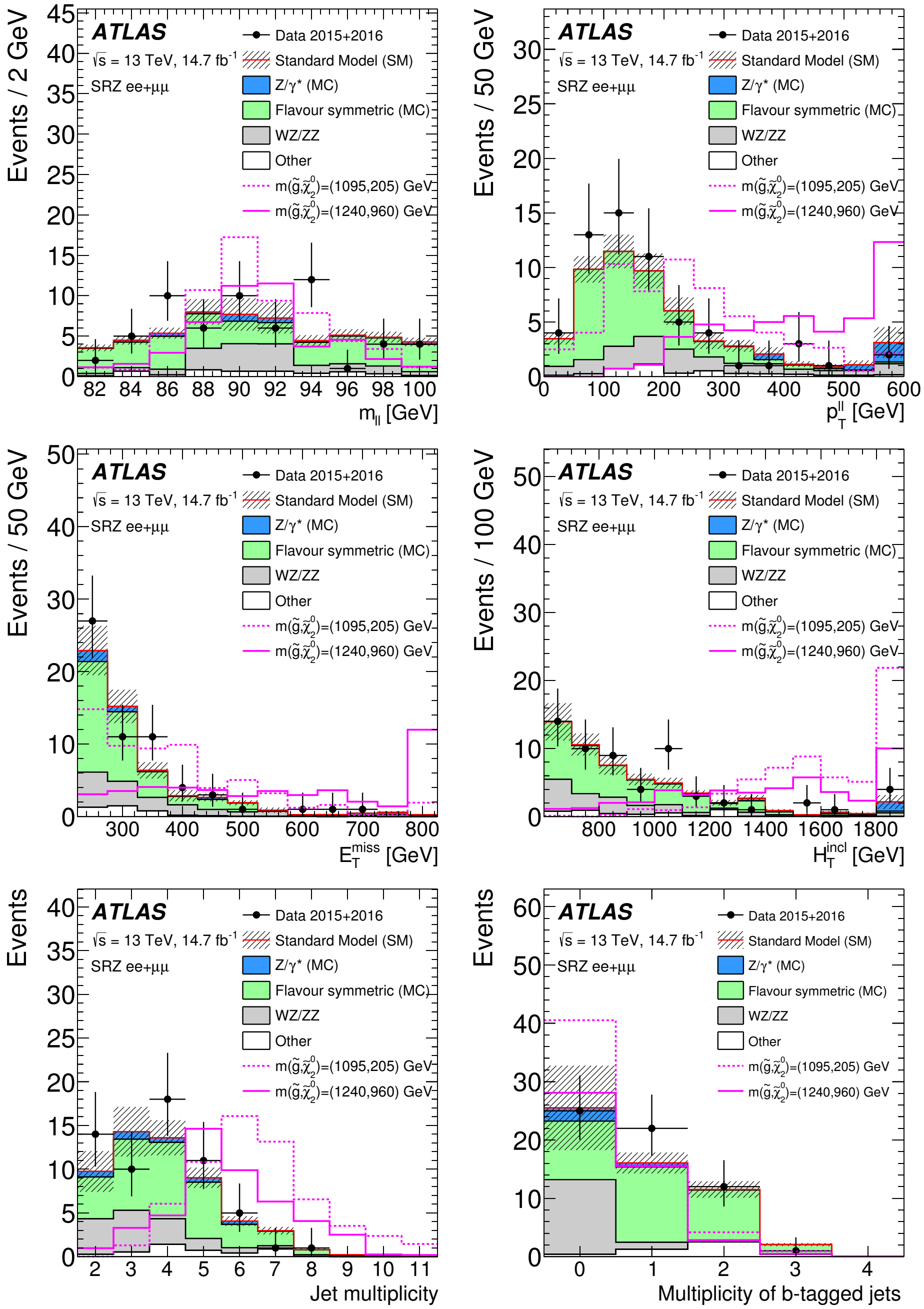

Figure 6.19: The m_{ll} (top left), $p_{\mathrm{T}}^{\ell\ell}$ (top right), $E_{\mathrm{T}}^{\mathrm{miss}}$ (middle left), $H_{\mathrm{T}}^{\mathrm{incl}}$ (middle right), jet multiplicity (bottom left) and b-tagged jet multiplicity (bottom right) distributions in SRZ. Two examples of signal models from the $\tilde{g}$–$\tilde{\chi}_2^0$ on-shell grid, described in Section **??**, with $(m(\tilde{g}), m(\tilde{\chi}_2^0)) = (1095, 205)$ GeV and $(m(\tilde{g}), m(\tilde{\chi}_2^0)) = (1240, 960)$ GeV, are overlaid. In the case of the $E_{\mathrm{T}}^{\mathrm{miss}}$, $H_{\mathrm{T}}^{\mathrm{incl}}$ and $p_{\mathrm{T}}^{\ell\ell}$ distributions, the last bin contains the overflow. The rare top and data-driven fake-lepton backgrounds are grouped under “other” backgrounds. The hashed uncertainty bands include the statistical and systematic uncertainties in the background prediction.

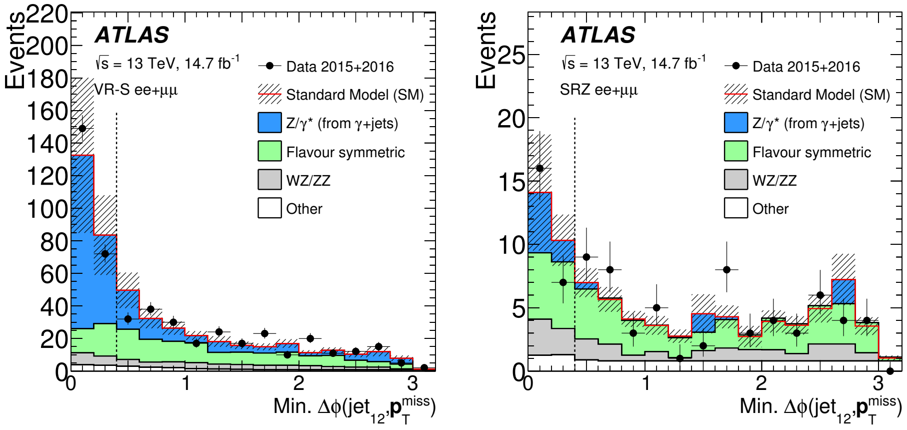

Figure 6.20: The min. $\Delta\phi(\text{jet}_{12}, \boldsymbol{p}_{\mathrm{T}}^{\text{miss}})$ distribution in (left) VR-S and (right) SRZ, where the min. $\Delta\phi(\text{jet}_{12}, \boldsymbol{p}_{\mathrm{T}}^{\text{miss}}) > 0.4$ requirement has been lifted. The vertical dashed lines indicate the requirement in each region. The rare top and data-driven fake-lepton backgrounds are grouped under "other" backgrounds. The hashed uncertainty bands include the statistical and systematic uncertainties in the background prediction.

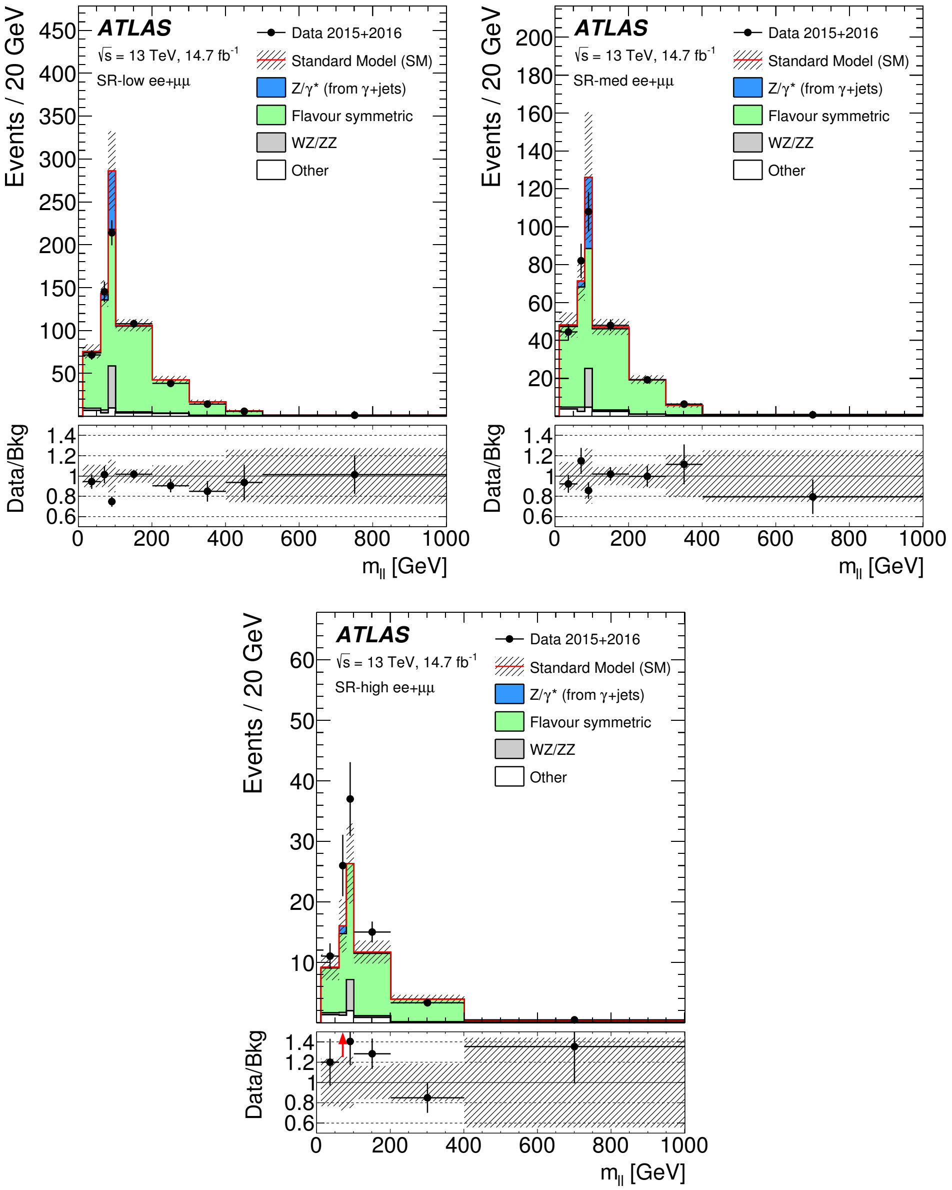

Figure 6.21: Expected and observed dilepton mass distributions, with the bin boundaries considered for the interpretation, in (top left) SR-low, (top-right) SR-medium, and (bottom) SR-high of the edge search. The flavor-symmetric and $Z+$jets distributions are taken completely from the data-driven estimate. The rare top and data-driven fake-lepton backgrounds are grouped under "other" backgrounds. All statistical and systematic uncertainties are included in the hashed bands. The ratio of data to predicted background is shown in the bottom panels. In cases where the data point is not accommodated by the scale of this panel, a red arrow indicates the direction in which the point is out of range.

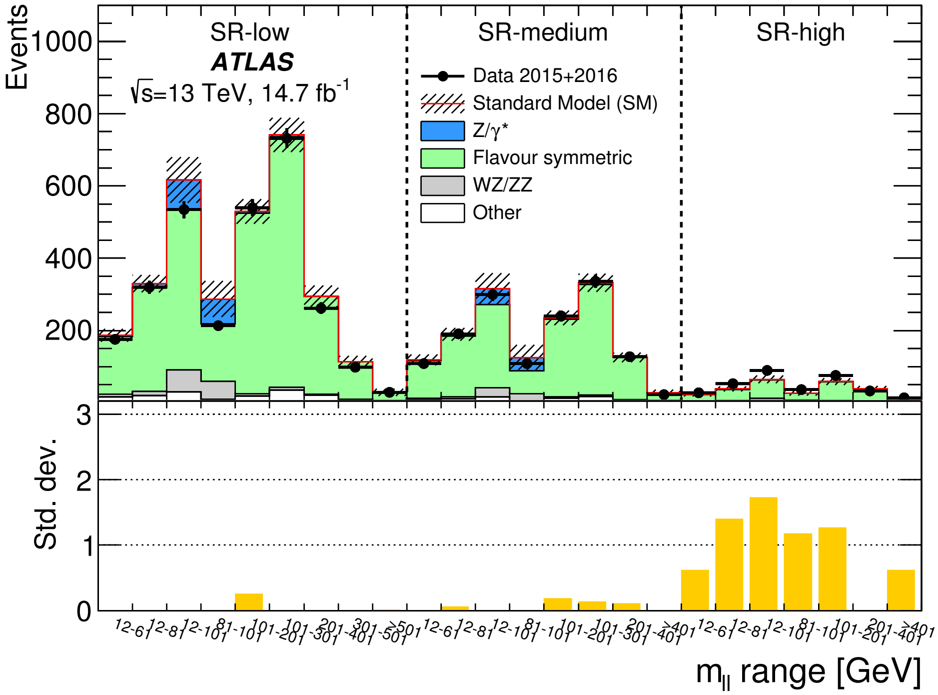

Figure 6.22: The expected and observed yields in the 24 (overlapping) m_{ll}ranges of SR-low, SR-medium, and SR-high. The data are compared to the sum of the expected backgrounds. The rare top and data-driven fake-lepton backgrounds are grouped under “other” backgrounds. The significance of the difference between the data and the expected background (see text for details) is shown in the bottom plots; for regions in which the data yield is less than expected, the significance is set to zero. The hashed uncertainty bands include the statistical and systematic uncertainties in the background prediction.

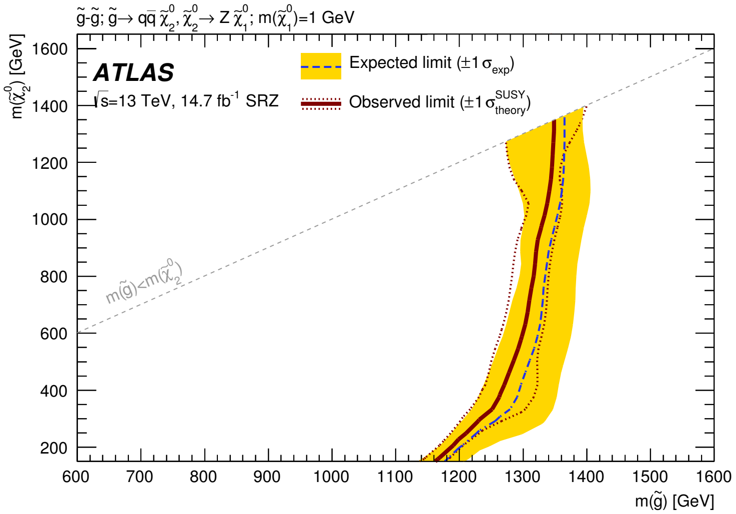

Figure 6.23: Expected and observed exclusion contours derived from the results in SRZ for the $\tilde{g}$–$\tilde{\chi}_2^0$ on-shell grid. The dashed blue line indicates the expected limits at 95% CL and the yellow band shows the 1σ variation of the expected limit as a consequence of the uncertainties in the background prediction and the experimental uncertainties in the signal ($\pm1\sigma_{\mathrm{exp}}$). The observed limits are shown by the solid red line, with the dotted red lines indicating the variation resulting from changing the signal cross-section within its uncertainty ($\pm1\sigma^{\mathrm{SUSY}}_{\mathrm{theory}}$).

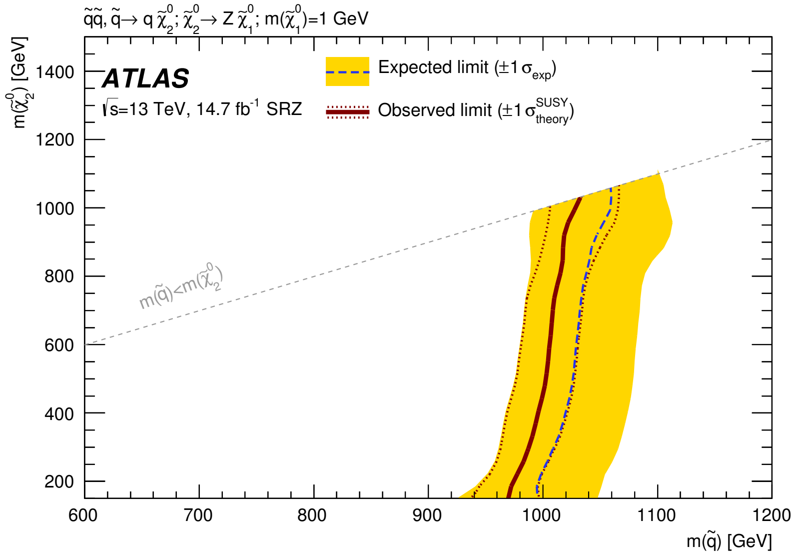

Figure 6.24: Expected and observed exclusion contours derived from the results in SRZ for the $\tilde{q}$–$\tilde{\chi}_2^0$ on-shell grid. The dashed blue line indicates the expected limits at 95% CL and the yellow band shows the 1σ variation of the expected limit as a consequence of the uncertainties in the background prediction and the experimental uncertainties in the signal ($\pm1\sigma_{\mathrm{exp}}$). The observed limits are shown by the solid red line, with the dotted red lines indicating the variation resulting from changing the signal cross-section within its uncertainty ($\pm1\sigma^{\mathrm{SUSY}}_{\mathrm{theory}}$).

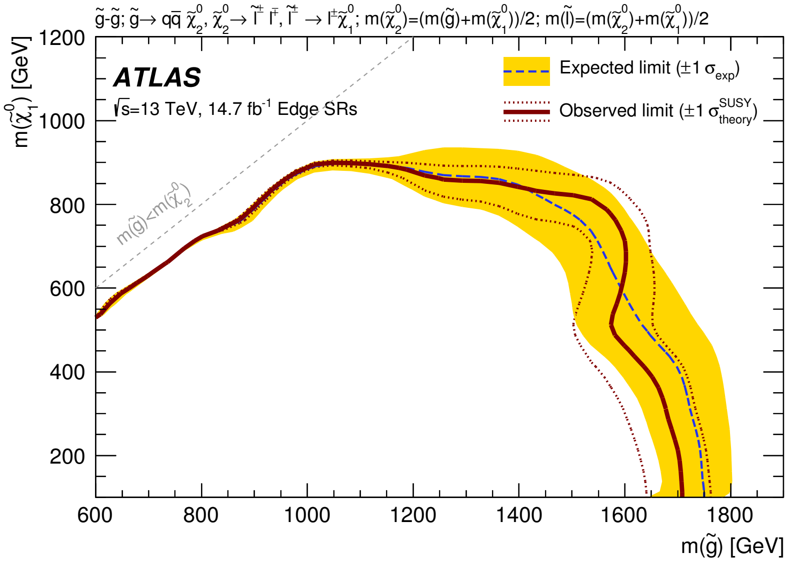

Figure 6.25: Expected and observed exclusion contours derived from the results in the edge search SRs for the slepton signal model. The dashed blue line indicates the expected limits at 95% CL and the yellow band shows the 1σ variation of the expected limit as a consequence of the uncertainties in the background prediction and the experimental uncertainties in the signal ($\pm1\sigma_{\mathrm{exp}}$). The observed limits are shown by the solid red lines, with the dotted red lines indicating the variation resulting from changing the signal cross-section within its uncertainty ($\pm1\sigma^{\mathrm{SUSY}}_{\mathrm{theory}}$).

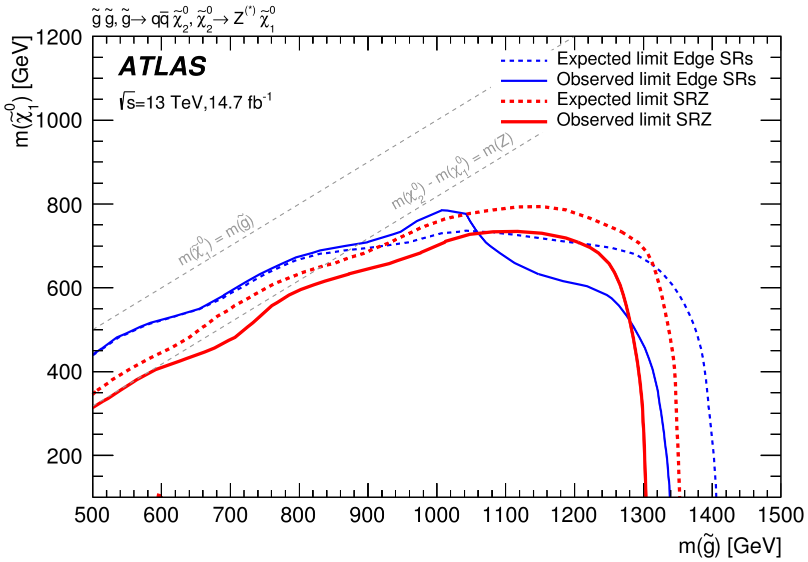

Figure 6.26: Expected and observed exclusion contours derived from the results in the edge search SRs and SRZ for the $Z^{(*)}$ model. The dashed and solid blue lines indicate the expected and observed limits at 95% CL from the results in the edge SRs, while the thick dashed and solid red lines indicate the expected and observed limits at 95% CL from the results in SRZ.

CHAPTER 7

SEARCH FOR ELECTROWEAK GAUGINO-PAIR PRODUCTION IN $2\ell + JETS + E_{\mathrm{T}}^{\mathrm{MISS}}$ FINAL STATES

7.1 Introduction

The cross-sections of the SUSY particle productions depend on two factors, i.e. the masses of the particles and the type of interaction involved. The colored SUSY particles (gluinos and squarks) participate in the strong interactions, which has significantly larger production cross-sections than the non-colored SUSY particles if the masses were equal. Searching for the strong interaction SUSY particles was thus the main focus in the year 2015-2016 because the colored SUSY particles could be largely produced with the increased LHC center-mass energy if the masses of the gluinos and squarks were not too high. However, with early 13 TeV LHC data, the exclusion limits on the gluinos and squarks have been extensively set to 2 TeV scale by dozens of LHC papers [49, 50, 51]. Doubling the data statistics will not improve much on the analysis sensitivity on the high mass gluino or squark limits, therefore we switch our focus to the search for non-colored SUSY particles, such as neutralinos, charginos, and sleptons, which might still live in a few hundred GeV range, but large statistics is required for analyses to be sensitive to these particles.

This chapter presents the search for the electroweak production of chargino-neutralino ($\tilde{\chi}_2^0\tilde{\chi}_1^{\pm}$) pair in the final states with two leptons (electron or muon-pair), using 36.1 fb^{-1} of proton-proton collision data delivered by the LHC at a center-of-mass energy of $\sqrt{s}$=13 TeV. This study is based on the results performed by the ATLAS Run I analyses [2, 52, 6] that targeted the same signal models. The results in the dilepton final states are combined with the results in 3-lepton final states to provide the final exclusion limits on the masses of charginos and neutralinos. Analogous studies by the CMS collaboration are presented in Refs. [53, 7, 54].

7.2 Signal model

This analysis uses a simplified model [55] to guide the signal region optimizations and to explore the direct production of $\tilde{\chi}_2^0\tilde{\chi}_1^{\pm}$, where $\tilde{\chi}_2^0$ decays to $\tilde{\chi}_1^0$ (the lightest SUSY particle, LSP) and a SM Z boson, $\tilde{\chi}_1^{\pm}$ decays to $\tilde{\chi}_1^0$ and a SM W boson. This analysis focuses on the decay branch where the SM Z boson decays leptonically and the W boson decays hadronically, which results in two leptons plus two jets final states. In this simplified model, the masses of the $\tilde{\chi}_2^0$ and the $\tilde{\chi}_1^0$ are the only parameters (other heavier SUSY particles are assumed highly decoupled), and the $\tilde{\chi}_2^0$ and the $\tilde{\chi}_1^{\pm}$ are mass-degenerate. A 2D signal grid is made for the signal model topology by varying the mass parameters. The result of this analysis is combined with the analysis that looks at the decay branch where W boson decays leptonically (3-lepton final states) to provide the final exclusion limits on the masses of $\tilde{\chi}_2^0\tilde{\chi}_1^{\pm}$ in (cite). The model of $\tilde{\chi}_2^0\tilde{\chi}_1^{\pm}$ production to WZ decay is shown in Figure 7.1 for both 2ℓ2jets and 3ℓ final states. Other simplified electroweak models, such as slepton-pair and $\tilde{\chi}_1^{+}\tilde{\chi}_1^{-}$ productions, are also explored in (cite).

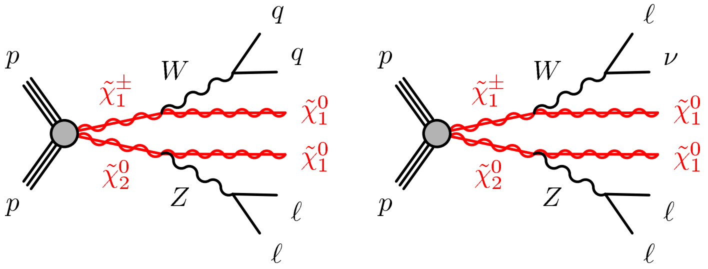

(a) 2ℓ2jets final state (b) 3ℓ final state

Figure 7.1: Diagrams of the physics scenarios studied in this paper: (a) $\tilde{\chi}_1^{\pm}\tilde{\chi}_2^0$ production with decays via leptonically decaying W and Z bosons to final states with three leptons, (b) $\tilde{\chi}_1^{\pm}\tilde{\chi}_2^0$ production with decays via a hadronically decaying W boson and a leptonically decaying Z boson to final states with two leptons and two jets.

7.3 Data and Monte Carlo samples

This analysis uses data delivered by the LHC at $\sqrt{s} = 13$ TeV in 2015 and 2016, an integrated luminosity of 36.1 fb^{-1} of which passes the data-quality requirements. The integrated luminosity of 36.1 fb^{-1} with an uncertainty of $\pm 3.2\%$ is derived using a methodology similar to that detailed in [56, 57].

Monte Carlo (MC) simulations are used to model SUSY signal events and in some cases to help the SM background estimations. These MC samples are processed with an ATLAS detector simulation [58], either based on GEANT4 [31], or a fast simulation that uses a parametrisation of the calorimeter response [59]. More detailed information about the MC background samples can be found in Section 6.3.

7.4 Event selections

This analysis targets $\tilde{\chi}_2^0\tilde{\chi}_1^\pm$ production. The $\tilde{\chi}_2^0$ decays to a SM Z boson and a $\tilde{\chi}_1^0$, and the $\tilde{\chi}_1^\pm$ decays to a SM W boson and a $\tilde{\chi}_1^0$. The Z boson further decays to a pair of leptons, and the W boson decays to a pair of jets. The general strategy of this analysis is to select the final state Z boson with m_{ll} in the Z mass window $(81 - 101$ GeV), and to select the final state W boson with m_{jj} in the W mass window $(70 - 100$ GeV), with a large $E_{\mathrm{T}}^{\mathrm{miss}}$ cut for the presence of $\tilde{\chi}_1^0$, which is assumed to be massive and invisible to the detector.

There are two sets of signal regions designed; one (SR2-int and SR2-high) targets intermediate/high $\tilde{\chi}_2^0\tilde{\chi}_1^\pm$ mass limit with large $\tilde{\chi}_2^0 - \tilde{\chi}_1^0$ mass splitting, the other (SR2-low) targets lower $\tilde{\chi}_2^0\tilde{\chi}_1^\pm$ mass with $\tilde{\chi}_2^0 - \tilde{\chi}_1^0$ mass splitting close to the $m(Z) = 91$ GeV. SR2-int/high is designed to search for boosted final state objects as a result of large $\tilde{\chi}_2^0 - \tilde{\chi}_1^0$ mass splitting. In SR2-int/high, the two leptons are used to form the Z boson, and the two leading jets are used to reconstruct the W boson in the events. The boosted objects are selected by requiring $p_{\mathrm{T}}^{Z} > 80$ GeV and $p_{\mathrm{T}}^{W} > 100$ GeV. The small angular separations ($\Delta R_{(\ell\ell)}$ and $\Delta R_{(jj)}$) are also made to ensure the boosted topology. To reduce the possible artificial $E_{\mathrm{T}}^{\mathrm{miss}}$ introduced by jet or lepton energy mismeasurements, the $E_{\mathrm{T}}^{\mathrm{miss}}$ is required not to overlap the (opposite-)directions of two-lepton and two-jet systems ($\Delta\phi_{(E_{\mathrm{T}}^{\mathrm{miss}},Z)} \in (0.5, 3.0)$ and $\Delta\phi_{(E_{\mathrm{T}}^{\mathrm{miss}},W)} \in (0.5, 3.0)$). In addition to these topological selections, a $m_{\mathrm{T2}} >$ 100 GeV selection is made to reject SM backgrounds with a pair of $W \to \ell\nu$ decay, such as $t\bar{t}$ and WW.

SR2-low is designed to search for signal events with small mass splitting

($\leq$ 100 GeV) between $\tilde{\chi}_2^0$ and $\tilde{\chi}_1^0$, as well as low mass $\tilde{\chi}_2^0$ ($\leq$ 200 GeV). Two channels of different jet multiplicities are considered in SR2-low. The exact two-jet channel assumes that there is no initial-state radiation (ISR) jet present. The two jets are used to form the W boson (m_{jj} window is tightened to reduce $Z+$jets background). The $E_{\mathrm{T}}^{\mathrm{miss}}$ is required not to overlap with the two-jets ($\Delta\phi_{(E_{\mathrm{T}}^{\mathrm{miss}},W)} > 1.5$) to reduce jet energy mismeasurement, and to point to the direction of the two-leptons instead (less lepton mismeasurement is expected for low p_{T}leptons that populate SR2-low). The mass of $\tilde{\chi}_1^0$ is expected to be similar to the masses of W and Z boson in the parameter space that SR2-low is targeting, thus the kinematic energy is expected to be distributed equally among Z, and $\tilde{\chi}_1^0$s. The assumption of the equal-energy distribution among W, Z, and $\tilde{\chi}_1^0$s motivates the selection $E_{\mathrm{T}}^{\mathrm{miss}}/p_{\mathrm{T}}^{Z} \in (0.6, 1.6)$.

The three-or-four-jets channel assumes that there is at least one ISR jet in the final state. The leading jet in the event is assumed to be one of the ISR jets. The W boson is formed with the two jets that have the smallest angular separation from the $Z+E_{\mathrm{T}}^{\mathrm{miss}}$ system. The topology of the event is assumed to have one strong ISR jet recoiling against the $W+Z+2\tilde{\chi}_1^0$ system. The angular selections are made to shape the topology ($\Delta\phi_{(E_{\mathrm{T}}^{\mathrm{miss}},\mathrm{ISR})} > 2.4$, $\Delta\phi_{(E_{\mathrm{T}}^{\mathrm{miss}},W)} < 2.2$). Finally, $E_{\mathrm{T}}^{\mathrm{miss}}$/ISR is a useful variable, because it indicates the $\tilde{\chi}_1^0$-to-$\tilde{\chi}_2^0$ mass ratio in a compressed (small mass splitting) signal model as

$$E_{\mathrm{T}}^{\mathrm{miss}} \simeq p_{\mathrm{T}}^{\mathrm{ISR}} \times \frac{m(\tilde{\chi}_1^0)}{m(\tilde{\chi}_2^0)}.$$

The cut on $E_{\mathrm{T}}^{\mathrm{miss}}$/ISR is set to be in $0.4-0.8$ range to target the parameter space around $m(\tilde{\chi}_2^0, \tilde{\chi}_1^0) = (200, 100)$ GeV. The detailed selections can be found in Table 7.1.

The signal regions are optimized to target different parameter spaces of the signal models. For the signal models considered in this analysis, the SR2-low acceptance (number of signal events landed in the SR divided by the number of total generated signal events) is about 0.014% at $m(\tilde{\chi}_2^0, \tilde{\chi}_1^0) = (200, 100)$ GeV, and the acceptances of SR2-int and SR2-high are about 0.6% at $m(\tilde{\chi}_2^0, \tilde{\chi}_1^0) = (600, 0)$ GeV. The signal region efficiencies (number of signal events at detector level divided by the number of signal events at particle level in the SR) are above 60% for all signal regions. The signal region acceptance and efficiency can be found in Fig. 7.2 (SR2-low), Fig. 7.3 (SR2-int), and

2ℓ+jets signal region definitions				
	SR2-int	SR2-high	SR2-low-2J	SR2-low-3J
$n_{\mathrm{non-b-tagged\ jets}}$	≥ 2		2	3-5
$m_{\ell\ell}$ [GeV]	81-101		81-101	86-96
m_{jj} [GeV]	70-100		70-90	70-90
$E_{\mathrm{T}}^{\mathrm{miss}}$[GeV]	>150	> 250	>100	>100
p_{T}^{Z} [GeV]	>80		> 60	> 40
p_{T}^{W} [GeV]	>100			
m_{T2} [GeV]	>100			
$\Delta R_{(jj)}$	<1.5			<2.2
$\Delta R_{(\ell\ell)}$	<1.8			
$\Delta\phi_{(E_{\mathrm{T}}^{\mathrm{miss}},Z)}$			< 0.8	
$\Delta\phi_{(E_{\mathrm{T}}^{\mathrm{miss}},W)}$	0.5-3.0		> 1.5	< 2.2
$E_{\mathrm{T}}^{\mathrm{miss}}/p_{\mathrm{T}}^{Z}$			$0.6 - 1.6$	
$E_{\mathrm{T}}^{\mathrm{miss}}/p_{\mathrm{T}}^{W}$			< 0.8	
$\Delta\phi_{(E_{\mathrm{T}}^{\mathrm{miss}},\mathrm{ISR})}$				> 2.4
$\Delta\phi_{(E_{\mathrm{T}}^{\mathrm{miss}},\mathrm{jet1})}$				> 2.6
$E_{\mathrm{T}}^{\mathrm{miss}}/\mathrm{ISR}$				0.4-0.8
$\lvert\eta(Z)\rvert$				< 1.6
$p_{\mathrm{T}}^{\mathrm{jet3}}$ [GeV]				> 30

Table 7.1: Signal region definitions used for the 2ℓ+jets channel. The abbreviations W and Z correspond to the reconstructed W and Z bosons in the final state. The Z boson is always reconstructed from the two leptons, whereas the W boson is reconstructed from the two jets leading in p_{T} for SR2-int, SR2-high and the 2-jets channel of SR2-low, whilst for the 3-5 jets channel of SR2-low it is reconstructed from the two jets which combine to be closest in ΔR to the Z ($\rightarrow \ell\ell$) + $E_{\mathrm{T}}^{\mathrm{miss}}$system. ISR refers to the vectorial sum of the initial-state-radiation jets in the event (i.e. those not used in the reconstruction of the W boson) and jet1 and jet3 refer to the leading and third leading jet respectively.

Fig. 7.4 (SR2-high).

7.5 Background estimation

In this section, we discuss the background estimation methods and the validations. The dominant background process in the SRs (both SR2-int/high and SR2-low) is diboson. The diboson events (WZ/ZZ) enter the signal regions with two real leptons from Z decays and real $E_{\mathrm{T}}^{\mathrm{miss}}$ from neutrinos. The diboson events are estimated with MC simulation and validated in monojet

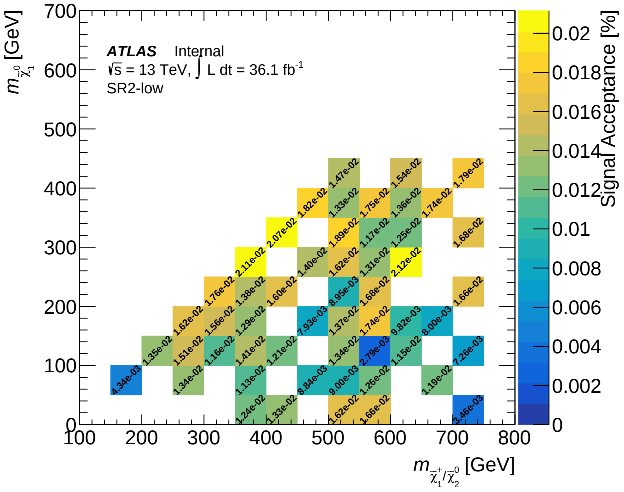

(a) Acceptance for $\tilde{\chi}_2^0\tilde{\chi}_1^\pm$ pair production in SR2-low

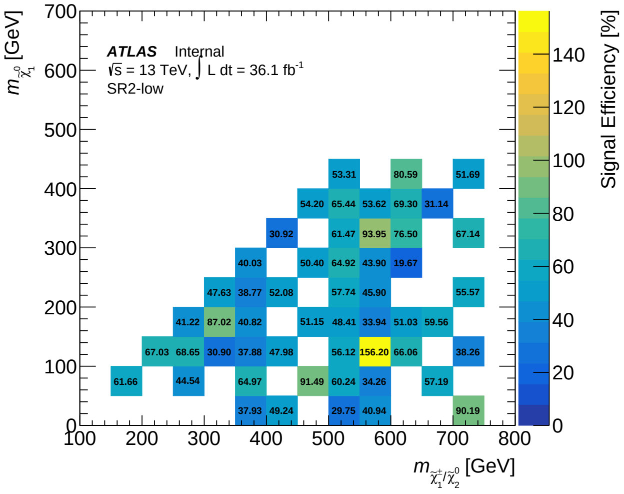

(b) Efficiency for $\tilde{\chi}_2^0\tilde{\chi}_1^\pm$ pair production in SR2-low

Figure 7.2: Signal acceptances (left) and efficiencies (right) for direct $\tilde{\chi}_2^0\tilde{\chi}_1^\pm$ pair production with WZ-mediated decays in SR2-low.

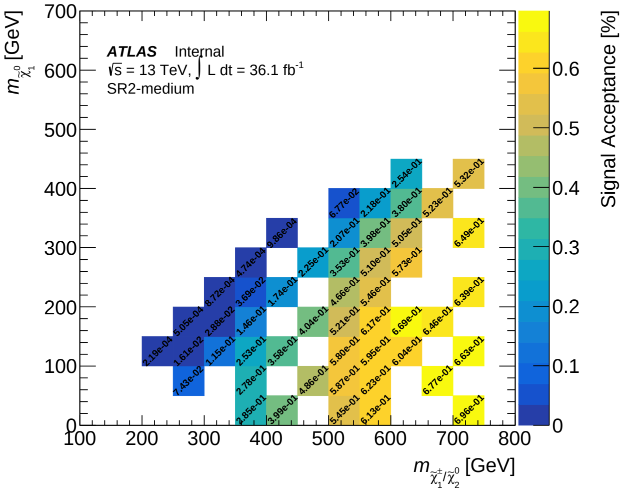

(a) Acceptance for $\tilde{\chi}_2^0\tilde{\chi}_1^\pm$ pair production in SR2-int

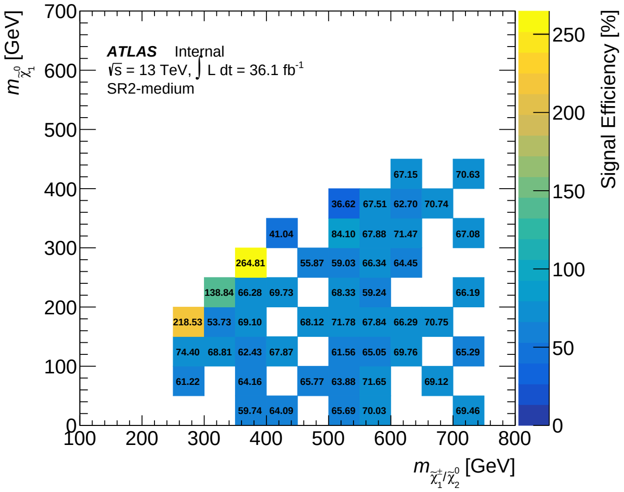

(b) Efficiency for $\tilde{\chi}_2^0\tilde{\chi}_1^\pm$ pair production in SR2-int

Figure 7.3: Signal acceptances (left) and efficiencies (right) for direct $\tilde{\chi}_2^0\tilde{\chi}_1^\pm$ pair production with WZ-mediated decays in SR2-int.

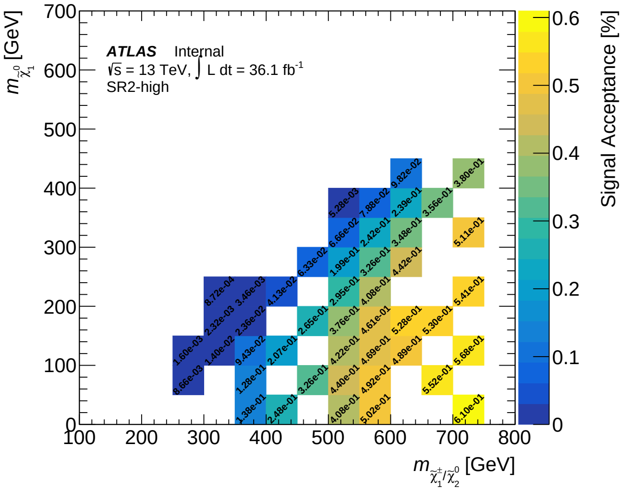

(a) Acceptance for $\tilde{\chi}_2^0\tilde{\chi}_1^\pm$ pair production in SR2-high

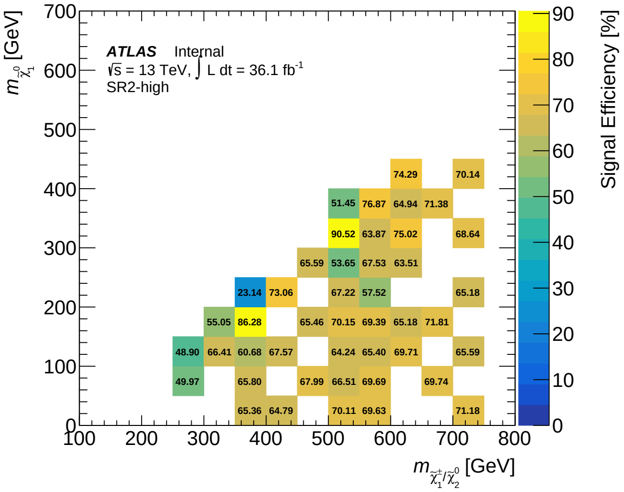

(b) Efficiency for $\tilde{\chi}_2^0\tilde{\chi}_1^\pm$ pair production in SR2-high

Figure 7.4: Signal acceptances (left) and efficiencies (right) for direct $\tilde{\chi}_2^0\tilde{\chi}_1^\pm$ pair production with WZ-mediated decays in SR2-high.

regions. The second dominant background in SR2-int/high is $t\bar{t} \to l^+l^-$. The two leptons in $t\bar{t} \to l^+l^-$ events are from the decays of two separate W bosons, therefore the flavors of the two leptons are uncorrelated. The $t\bar{t} \to l^+l^-$ events are also estimated with MC simulation.

The second dominant background process in SR2-low is $Z+$jets (standard model Z bosons produced in association with initial state radiation jets). In a case of an ideal detector, where objects are perfectly reconstructed and measured, the $Z+$ jets events would not enter the signal regions for the absence of neutrinos (all SRs have high $E_{\mathrm{T}}^{\mathrm{miss}}$ requirement). However, the $Z+$jets processes still contribute a significant amount of background events in SRs because of the fake $E_{\mathrm{T}}^{\mathrm{miss}}$ originating from instrumental effects or from neutrinos in jet fragments and the large cross sections of $Z+$jets processes. To estimate $Z+$jets events in SRs, we use $\gamma+$jets events in data to model the fake $E_{\mathrm{T}}^{\mathrm{miss}}$ resulted from jet mismeasurements.

Rare backgrounds such as Higgs, $t\bar{t}W$, $t\bar{t}Z$ and $t\bar{t}WW$ are also estimated with MC, however no VR is designed for the rare backgrounds, since their contribution is relatively small ($< 5\%$ of total backgound). The background contribution from fake or misidentified or non-prompt leptons (FNP) is also small in all SRs, and FNP leptons are estimated using a data-driven matrix method following the similar technique detailed in Section 6.6.3.

The details of the photon method can be found in Section 5. Similar methods have been employed in searches for SUSY in events with two leptons, jets, and large $E_{\mathrm{T}}^{\mathrm{miss}}$ in ATLAS [60] and CMS [61, 62]. The jet mismeasurement contribution to the $E_{\mathrm{T}}^{\mathrm{miss}}$ in the $Z+$jets events is modeled with the $\gamma+$jets events. The lepton mismeasurement contribution to the $E_{\mathrm{T}}^{\mathrm{miss}}$ in the $Z+$jets events is estimated using Z+monojet and γ+monojet MC control regions. The correction for the difference in γ vs. lepton resolutions is derived by deconvolving the $E_{\mathrm{T}}^{\mathrm{miss}}$ shape in the monojet MC control regions, and the correction is applied to the multi-jet regions. Backgrounds of $W\gamma$ and $Z\gamma$ production, which contain a photon and genuine $E_{\mathrm{T}}^{\mathrm{miss}}$ from neutrinos, are subtracted using MC that is normalized to data in a $V\gamma$ control region containing a selected lepton and photon. For each SR separately, the $E_{\mathrm{T}}^{\mathrm{miss}}$ shape is then normalized to dilepton data in a region with $E_{\mathrm{T}}^{\mathrm{miss}} < 100$ GeV and with all other SR requirements.

7.5.1 Background validation

To test the photon template estimation and diboson MC simulation, a set of validation regions are defined in Table 7.2. The The validation regions for the $Z+$jets background (VR2-int/high and VR2-low) have a $W-$veto, which requires the invariant mass of the two candidate jets from the W boson decay does not locate in 60-100 GeV range. The $W-$veto requirement makes sure the $Z+$ jets VRs are orthogonal to the signal regions.

There are two sets definitions of $Z+$ jets VR, tight and loose. The loose VRs have basic energy requirements, such as the cuts on p_{T}^{Z} and p_{T}^{W}, and these cuts are the same as the SR requirements. The angular cuts, ratio cuts (such as $E_{\mathrm{T}}^{\mathrm{miss}}$/ISR) are not applied in the loose VRs. The loose VRs have enough statistics and are used to validate the modeling of kinematic distributions, such as $E_{\mathrm{T}}^{\mathrm{miss}}$, m_{T2}, and the angular distributions between $E_{\mathrm{T}}^{\mathrm{miss}}$ and other objects. The loose VRs are also used to access the systematics of the $Z+$jets estimations in SRs. The tight VRs have all SR requirements applied except the $W-$veto to make the VRs be orthogonal from SRs. The tight VRs are used to verify that the $Z+$ jets backgrounds in the corresponding SRs are indeed very small.

The diboson validation regions (VR2-VV-int and VR2-VV-low) are defined in mono-jet regions, which strongly suppress the $t\bar{t} \to l^{+}l^{-}$ contributions and are orthogonal to the signal regions, which have at least two jets. The diboson VRs also have $E_{\mathrm{T}}^{\mathrm{miss}} > 150$ GeV and $\Delta\phi(E_{\mathrm{T}}^{\mathrm{miss}}, jets) > 0.4$ cuts applied to suppress $Z+$jets.

The validations of the photon template method modeling the $E_{\mathrm{T}}^{\mathrm{miss}}$ shapes in the loose VRs are shown in Figure 7.5. The loose VRs have the angular requirements removed to allow us to see the $Z+$jets distribution in the region with $E_{\mathrm{T}}^{\mathrm{miss}} > 100$ GeV with large statistics. In Figure 7.5, we can see the data v.s. background prediction agreement is good in both VR2-int/high-loose (left) and in VR2-low-loose (right) across the $E_{\mathrm{T}}^{\mathrm{miss}}$ spectrum until 150 GeV where the top and diboson events become important. The $E_{\mathrm{T}}^{\mathrm{miss}}$ in the $Z+$ jets events is mainly due to jet energy mismeasurements. This effect can be illustrated by the angular correlation between the direction of $E_{\mathrm{T}}^{\mathrm{miss}}$ and the directions of the jets with the largest momenta. Figure 7.6 shows the min. $\Delta\phi(E_{\mathrm{T}}^{\mathrm{miss}},\mathrm{jet})$ distribution in the loose VRs with $E_{\mathrm{T}}^{\mathrm{miss}} > 100$ GeV requirement, where we can see this angular correlation is well modeled by the

2ℓ+jets validation region definitions

	VR2-int(high)	VR2-low-2J(3J)	VR2-VV-int	VR2-VV-low
loose selection				
$n_{\mathrm{non-b-tagged\ jets}}$	≥ 2	2 (3-5)	1	1
$E_{\mathrm{T}}^{\mathrm{miss}}$[GeV]	>150 (250)	>100	>150	>150
$m_{\ell\ell}$ [GeV]	81-101	81-101 (86-96)		81-101
m_{jj} [GeV]	<60,>100	<60,>100		
p_{T}^{Z} [GeV]	>80	$> 60(40)$		
p_{T}^{W} [GeV]	>100			
$\lvert\eta(Z)\rvert$		(< 1.6)		
$p_{\mathrm{T}}^{\mathrm{jet3}}$ [GeV]		(> 30)		
$\Delta\phi_{(E_{\mathrm{T}}^{\mathrm{miss}},\mathrm{jet})}$			>0.4	>0.4
m_{T2} [GeV]			>100	
$\Delta R_{(\ell\ell)}$				<0.2
tight selection				
$\Delta R_{(jj)}$	<1.5	(<2.2)		
$\Delta\phi_{(E_{\mathrm{T}}^{\mathrm{miss}},W)}$	0.5-3.0	$> 1.5(< 2.2)$		
$\Delta\phi_{(E_{\mathrm{T}}^{\mathrm{miss}},Z)}$		$< 0.8(-)$		
$E_{\mathrm{T}}^{\mathrm{miss}}/p_{\mathrm{T}}^{W}$		$< 0.8(-)$		
$E_{\mathrm{T}}^{\mathrm{miss}}/p_{\mathrm{T}}^{Z}$		$0.6 - 1.6(-)$		
$E_{\mathrm{T}}^{\mathrm{miss}}$/ISR		$(0.4 - 0.8)$		
$\Delta\phi_{(E_{\mathrm{T}}^{\mathrm{miss}},\mathrm{ISR})}$		(> 2.4)		
$\Delta\phi_{(E_{\mathrm{T}}^{\mathrm{miss}},\mathrm{jet1})}$		(> 2.6)		
m_{T2} [GeV]	>100			
$\Delta R_{(\ell\ell)}$	<1.8			

Table 7.2: Validation region definitions used for the 2ℓ+jets channel. Symbols and abbreviations are analogous to those in Table 7.1.

photon method. The discrepancies in data v.s. background comparisons in loose VRs will be quoted as a systematic uncertainty on the SR estimation of $Z+$jets.

The validation of the diboson background modeling is shown in Figure 7.7 as function of m_{T2} of the events in VR2-VV-int and VR2-VV-low. These diboson VRs have $E_{\mathrm{T}}^{\mathrm{miss}} > 150$ GeV cut to suppress $Z+$jets events and require exact one light-flavor jet to suppress $t\bar{t} \to l^{+}l^{-}$ events. The diboson background is estimated using MC simulation, and the measured data v.s. MC ratios in these VRs are used as scale factors (about 1.1) to correct the normalizations of the diboson MC predictions in SRs.

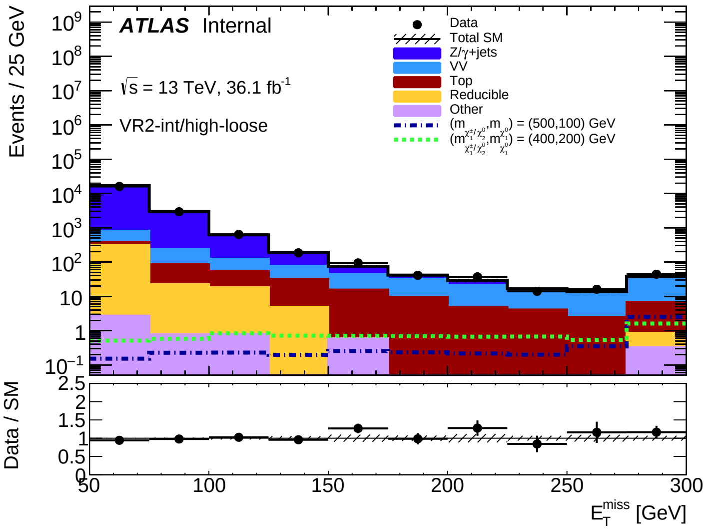

(a) VR2-int/high-loose

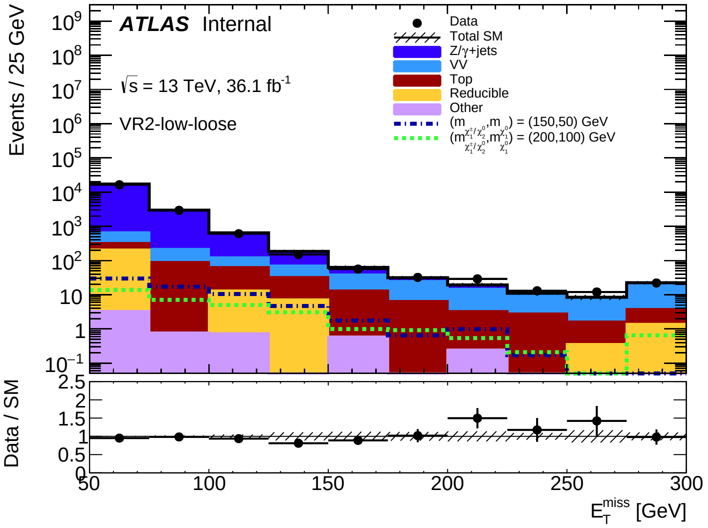

(b) VR2-low-loose

Figure 7.5: Distributions for data and the expected SM backgrounds in the loose validation regions in the 2ℓ+jets channel. The distributions of $E_{\mathrm{T}}^{\mathrm{miss}}$ are shown for (left) VR2-int/high-loose and (right) VR2-low-loose. The Z/γ+jets contribution is evaluated using the data-driven photon method and the "Reducible" category corresponds to the data-driven matrix method estimate. The "top" background includes $t\bar{t}$ Wt and $t\bar{t}$V and the "other" backgrounds include Higgs, V+γ and VVV .The statistical uncertainties on the background prediction are included in the uncertainty band, as well as the experimental and theoretical uncertainties.

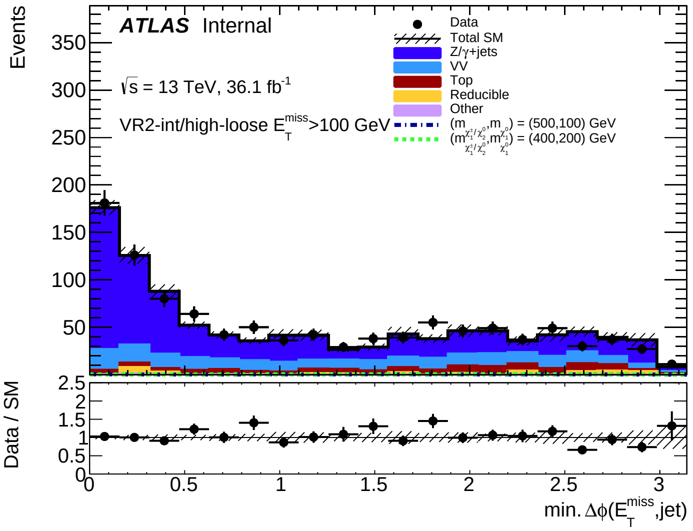

(a) VR2-int/high-loose

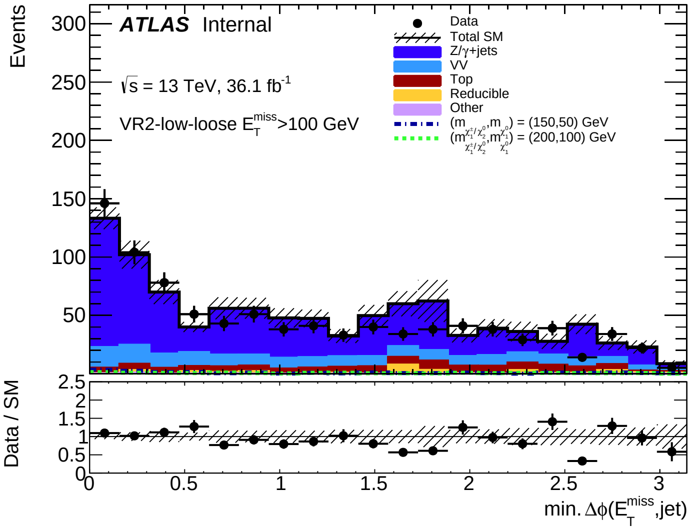

(b) VR2-low-loose

Figure 7.6: Distributions for data and the expected SM backgrounds in the loose validation regions in the 2ℓ+jets channel. The distributions of the minimum difference in azimuthal angle between the $E_{\mathrm{T}}^{\mathrm{miss}}$ vector and either of the two highest p_{T} jets, min. $\Delta\phi(E_{\mathrm{T}}^{\mathrm{miss}}, \mathrm{jet})$ are shown for (left) VR2-int/high-loose and (right) VR2-low-loose. The requirement $E_{\mathrm{T}}^{\mathrm{miss}} > 100$ GeV is included. The Z/γ+jets contribution is evaluated using the data-driven photon method and the ”Reducible” category corresponds to the data-driven matrix method estimate. The “top” background includes $t\bar{t}$ Wt and $t\bar{t}$V and the “other” backgrounds include Higgs, V+γ and VVV .The statistical uncertainties on the background prediction are included in the uncertainty band, as well as the experimental and theoretical uncertainties.

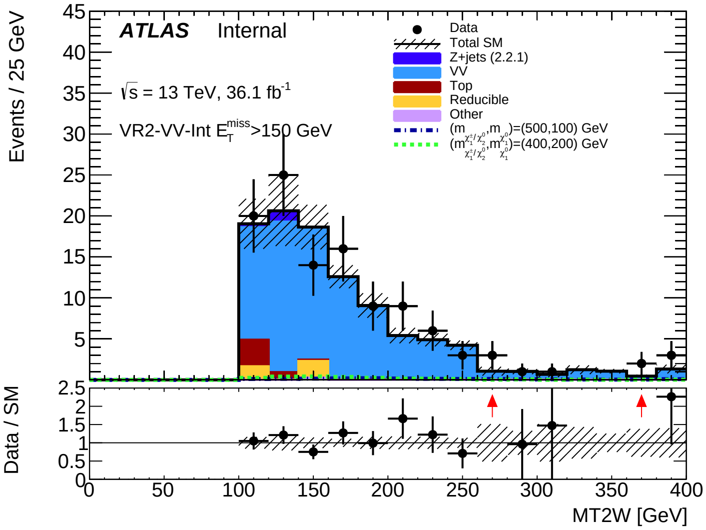

(a) VR2-VV-int

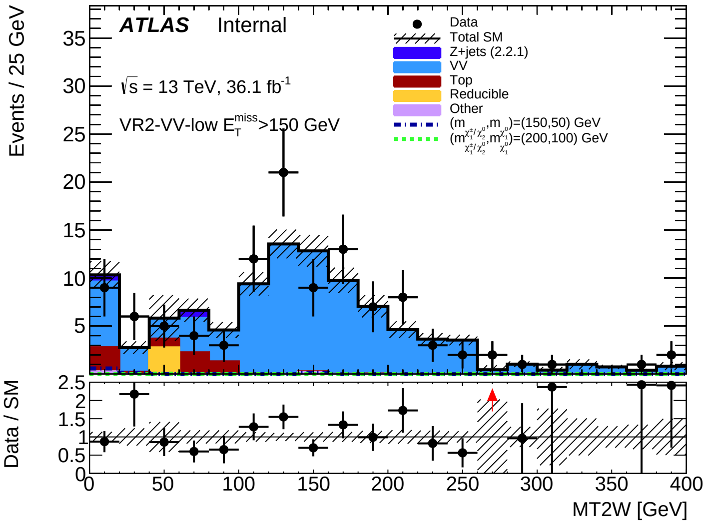

(b) VR2-VV-low

Figure 7.7: Distributions of m_{T2} for data and the expected SM backgrounds in the diboson validation regions (a) VR2-VV-int and (b) VR2-VV-low in the 2ℓ+jets channel. The Z/γ+jets contribution is evaluated using the data-driven photon method and the ”Reducible” category corresponds to the data-driven matrix method estimate. The “top” background includes $t\bar{t}$ Wt and $t\bar{t}$V and the “other” backgrounds include Higgs, V+γ and VVV . The statistical uncertainties on the background prediction are included in the uncertainty band, as well as the experimental and theoretical uncertainties.

7.5.2 Systematic uncertainty of $Z+$jets estimation

The systematic uncertainties for the photon method prediction are summarized in Table 7.3 and 7.4, for SR2-int/high and SR2-low, respectively. The systematic uncertainties are assessed using events that pass Loose VR selections (see Table 7.2), in order to gain enough statistics and to reduce contaminations from other backgrounds. The $E_{\mathrm{T}}^{\mathrm{miss}}$ distributions in Loose VRs are shown in Figure 7.5 and $\Delta\phi(E_{\mathrm{T}}^{\mathrm{miss}}, jets)$ distribution in Figure 7.6. The method to compute photon prediction systematics is listed following.

- Reweighting uncertainty compares the boson p_T-reweighting (nominal) prediction v.s. H_T-reweighting prediction.
- Smearing uncertainty compares the prediction using smearing function nominally derived from MC v.s. the prediction using smearing function from data monojet control region.
- MC closure uncertainty takes the difference between Z+jets v.s. γ+jets prediction in MC VR.
- Data closure uncertainty take the difference between Z+jets v.s. γ+jets prediction in data VR.
- $V+\gamma$ contamination uncertainty. $V+\gamma$ events contribute real $E_{\mathrm{T}}^{\mathrm{miss}}$ in photon data. Variation prediction assumes zero $V+\gamma$ contamination in SR.
- Sideband uncertainty extrapolate m_{jj} shapes from Loose VRs and use Tight VR predictions to estimate SR yields.
- Photon event statistics reflects the raw number of photon events in SR.

The definition of VR and SR can be found in Table 7.2 and 7.1.

The methodology is the same as the strong 2L analysis, except here we have an additional sideband estimation uncertainties. The sideband estimation is proposed to use the observed photon events in the W mass sidebands ($m_{jj} < 60$ GeV and $m_{jj} > 100$ GeV) to estimate the $Z+$jets yield in the W mass window. The sideband prediction is given as

$$N_{\gamma\text{+jets}}(SR) = N_{\gamma\text{+jets}}(\mathrm{VR_{tight},\ m_{jj}\ cut\ removed}) \times \frac{\mathrm{N_{\gamma+jets}(SR_{loose})}}{\mathrm{N_{\gamma+jets}(VR_{loose},\ m_{jj}\ cut\ removed)}} \tag{7.1}$$

, where we assume the m_{jj} shape remains the same in Loose v.s. Tight regions (see Table 7.2 for Tigth and Loose VR definition). With sideband method, we have more statistics to provide predictions in SR, and both photon method and Sherpa 2.2.1 give very consistent sideband predictions. The sideband prediction is included as a systematic uncertainty in the final result.

7.6 Results

The observed results in the signal regions are summarized in Table 7.5. In SR2-int/high, 2/0 data events are observed and are consistent with the expected backgrounds of $4.1^{+2.6}_{-1.8}/1.6^{+1.6}_{-1.1}$. In SR2-low, 11 events are observed with an expected background of $4.2^{+3.4}_{-1.6}$. The data in the SR2-int/high is in good agreement with the expected background, while the SR2-low has a modest excess, which corresponds to a local significance of 1.58σ.

The numbers of observed data events and the composition of expected SM backgrounds in the signal regions are summarized in Table 7.5. In all signal regions, diboson ($WZ \rightarrow 3\ell1\nu$ and $ZZ \rightarrow 2\ell2\nu$) is the dominating background. However, the largest uncertainty contribution is from $Z+$jets in all 3 SRs. In SR2-int/high, the largest $Z+$jets systematic uncertainty arises from the $V+\gamma$ contamination in the photon data sample, which contributes to high $E_{\mathrm{T}}^{\mathrm{miss}}$ region with neutrinos. In SR2-low, the uncertainty from $V+\gamma$ contamination is less important since the $E_{\mathrm{T}}^{\mathrm{miss}}$ requirement in SR2-low is relatively low. The largest $Z+$jets uncertainty in SR2-low is due to the lack of photon statistics in the signal region with $m_{jj} \in (60, 100)$ GeV. The sideband of the signal region ($m_{jj} < 60$ GeV and $m_{jj} > 100$ GeV) provides a cross-check of the $Z+$jets yields in SR. The difference between the nominal prediction and the sideband prediction gives the largest uncertainty in SR2-low. The $E_{\mathrm{T}}^{\mathrm{miss}}$ distributions in SR2-int/high and SR2-low are shown in Figure 7.8.

The model-independent limits on the visible signal cross-section ($\langle\epsilon\sigma\rangle^{95}$)

SR medium/high Systematics	Nominal prediction	Variation method	Relative uncertainty (%)
Reweighting uncertainty	p_T-reweighting	H_T-reweighting	
	48.7	50.3	3
Smearing uncertainty	MC smearing function	data smearing function	
	48.7	68.7	41
MC-closure uncertainty	$\gamma+$jets MC prediction	$Z+$jets Sherpa MC	
	50.1	60.1	20
Data-closure uncertainty	$\gamma+$jets data prediction	dilepton data-$t\bar{t}$-VV	
	48.7	81.8	68
$V+\gamma$ uncertainty	$V+\gamma$ subtracted	no subtraction	
	0.0 (SR medium)	1.6	
	0.0 (SR high)	0.8	
Sideband uncertainty	nominal	sideband extrapolation	
($\gamma+$jets method)	0.0 (SR medium)	0.1	
	0.0 (SR high)	0.0	
(Sherpa 2.2.1)	0.1 (SR medium)	0.1	
	0.0 (SR high)	0.0	
$Z+$jets prediction	nominal	statistical uncertainty	absolute systematic uncertainty
	0.0 (SR medium)	0.9	1.6
	0.0 (SR high)	0.9	0.8

Table 7.3: Photon method systematic uncertainties in 2L2J Conventional medium/high mass SRs. The relative uncertainties (reweighting, smearing, MC-closure and data-closure) are derived in Loose VRs. The absolute uncertainties ($V+\gamma$ subtraction and sideband) are quoted in SRs. In medium/high mass regions, the largest uncertainty comes from the $V+\gamma$ subtraction because of the fact that the photon sample is contaminated by $V+\gamma$ in the region of $E_{\mathrm{T}}^{\mathrm{miss}} > 150$ GeV. SR/VR definition can be found in Table 7.1 and 7.2.

SR low Systematics	Nominal prediction	Variation method	Relative uncertainty (%)
Reweighting uncertainty	p_T-reweighting	H_T-reweighting	
	641.4	567.2	12
Smearing uncertainty	MC smearing function	data smearing function	
	641.4	650.9	1
MC-closure uncertainty	$\gamma+$jets MC prediction	$Z+$jets Sherpa MC	
	678.2	656	3
Data-closure uncertainty	$\gamma+$jets data prediction	dilepton data-$t\bar{t}$-VV	
	641.4	624.3	3
$V+\gamma$ uncertainty	$V+\gamma$ subtracted	no subtraction	
	1.0	1.6	
Sideband uncertainty	nominal	sideband extrapolation	
($\gamma+$jets method)	1.0 ± 0.6	3.5 ± 0.9	
(Sherpa 2.2.1)	7.1 ± 3.1	3.9 ± 1.3	
$Z+$jets prediction	nominal	statistical uncertainty	absolute systematic uncertainty
	1.0	0.6	2.6

Table 7.4: Photon method systematic uncertainties in 2L2J Conventional low mass SRs. The relative uncertainties (reweighting, smearing, MC-closure and data-closure) are derived in Loose VRs. The absolute uncertainties ($V+\gamma$ subtraction and sideband) are quoted in SRs. In low mass regions, the largest uncertainty comes from the sideband v.s. nominal difference. This is due to the statistical fluctuation in the W mass window in SR. Sherpa 2.2.1 $Z+$jets prediction is provided as a cross check, where a consistent sideband prediction is seen. SR/VR definition can be found in Table 7.1 and 7.2.

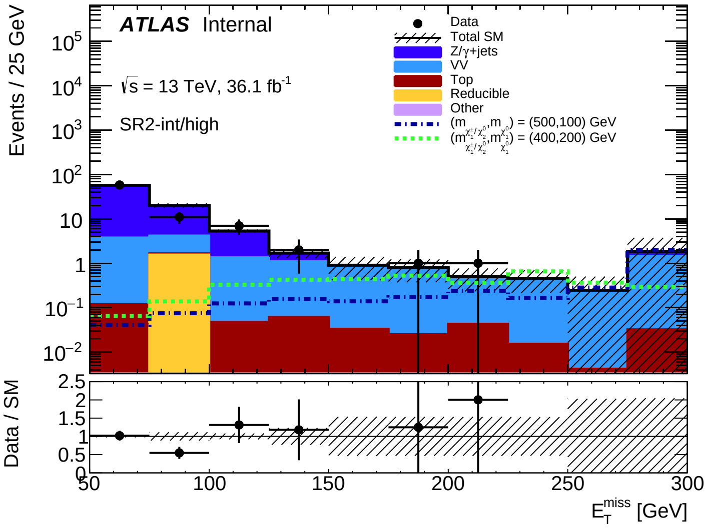

(a) SR2-int/high

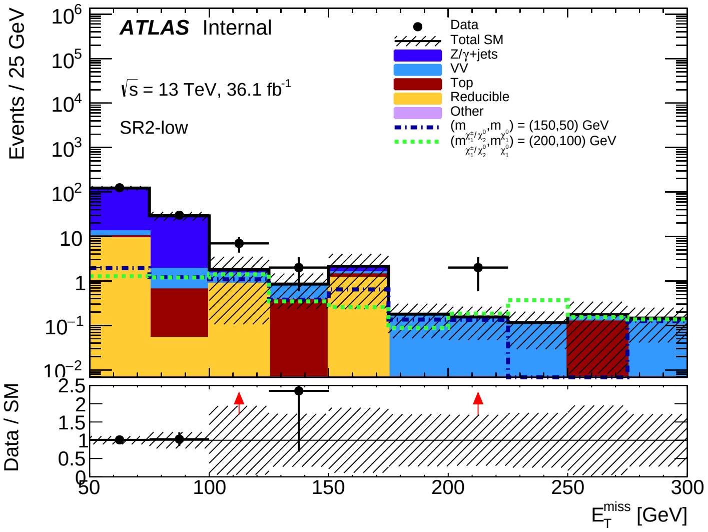

(b) SR2-low

Figure 7.8: $E_{\mathrm{T}}^{\mathrm{miss}}$ distributions of data and the expected SM backgrounds in the 2ℓ+jets channel for SR2-int/high (a) and SR2-low (b), without the final $E_{\mathrm{T}}^{\mathrm{miss}}$ requirement applied. The Z/γ+jets contribution is evaluated using the data-driven photon method and the "Reducible" category corresponds to the data-driven matrix method estimate. The "top" background includes $t\bar{t}$ Wt and $t\bar{t}$V and the "other" backgrounds include Higgs, V+γ and VVV . The statistical uncertainties on the background prediction are included in the uncertainty band, as well as the experimental and theoretical uncertainties.

SR2-	int	high	low (combined)
Observed	2	0	11
Expected events			
Total SM	$4.1^{+2.6}_{-1.8}$	$1.6^{+1.6}_{-1.1}$	$4.2^{+3.4}_{-1.6}$
VV	4.0 ± 1.8	1.6 ± 1.1	1.7 ± 1.0
Top	0.15 ± 0.11	0.04 ± 0.03	0.8 ± 0.4
FNP	$0.0^{+0.2}_{-0.0}$	$0.0^{+0.1}_{-0.0}$	$0.7^{+1.8}_{-0.7}$
$Z+$jets	$0.0^{+1.8}_{-0.0}$	$0.0^{+1.2}_{-0.0}$	$1.0^{+2.7}_{-1.0}$
others	-	-	-

Table 7.5: SM background results in the 2ℓ+jets SRs. All systematic and statistical uncertainties are included. The "Top" background includes all processes containing one or more top quarks and the "other" backgrounds include all processing containing a Higgs boson, VVV and $V\gamma$. A "–" symbol indicates that the background contribution is negligible.

and the number of BSM events (S^{95}) are presented in Table 7.6. The limits are given at 95% confidence level. The p-value and the significance for the background-only hypothesis are also presented.

Signal channel	Region	N_{obs}	N_{exp}	$\langle\epsilon\sigma\rangle^{95}_{\text{obs}}$[fb]	S^{95}_{obs}	S^{95}_{exp}	$p(s=0)$	Z
2ℓ+jets	SR2-int	2	$4.1^{+2.6}_{-1.8}$	0.13	4.5	$5.6^{+2.2}_{-1.4}$	0.5	0
	SR2-high	0	$1.6^{+1.6}_{-1.1}$	0.09	3.1	$3.1^{+1.4}_{-0.1}$	0.5	0
	SR2-low	11	$4.2^{+3.4}_{1.6}$	0.43	15.7	$11.8^{+3.8}_{-1.5}$	0.06	1.58

Table 7.6: Summary of results and model-independent limits in the inclusive 2ℓ+jets SRs. The observed yields (N_{obs}) and expected backgrounds (N_{exp}) in the signal regions are indicated. Signal model-independent upper limits at 95% C.L. on the the visible signal cross-section ($\langle\epsilon\sigma\rangle^{95}_{\text{obs}}$), and the observed and expected upper limit on the number of BSM events (S^{95}_{obs} and S^{95}_{exp}, respectively) are also shown. The $\pm1\sigma$ variations on the expected limit are due to the statistical and systematic uncertainties in the background prediction. The last two columns show the p-value and the corresponding significance for the background-only hypothesis.

7.7 Interpretation

The observed data results in the search signal regions are interpreted in this section using the SUSY signal models detailed in Sec. 7.2. The exclusion limits are set on the masses of charginos and neutralinos for the simplified models shown in Figure 7.9. The limits are calculated by statistically combining the mutually orthogonal signal regions. The expected and the observed limits are set based on the signal model events, observed data events, and the background estimations in the signal regions with all uncertainties included. The dashed blue line represents the expected limits at 95% CL with all uncertainties in the background estimations and the experimental uncertainties in the signal models. The yellow band shows the 1σ variation ($\pm 1\sigma_{\rm exp}$) of the expected limits. The observed limits are shown by the solid red line, which includes all background estimation uncertainties and MC experimental uncertainties, except the theoretical uncertainty of the signal cross section. The impact of the theoretical uncertainty of the signal cross section is shown by the dotted red lines, which indicate the results of variating the signal cross section by $\pm 1\sigma^{\rm SUSY}_{\rm theory}$. The grey area in Figure 7.9 represents the limits set by the ATLAS Run-1 result. Figure 7.9(a) interprets the results of the 2ℓ+jets signal regions, where the limit on $\tilde{\chi}^0_2$ and $\tilde{\chi}^\pm_1$ masses is set as large as 580 GeV. Figure 7.9(b) interprets the results of the combined 2ℓ+jets and 3ℓ (where both Z and W decay leptonically) signal regions, which provide a better sensitivity in the small mass splitting region near the diagonal line. However, the low mass $m(\tilde{\chi}^0_2) < 200$ GeV and small mass splitting $\Delta m < 100$ GeV parameter space, which favors the higgsino-like LSP, remains unprobed by this analysis.

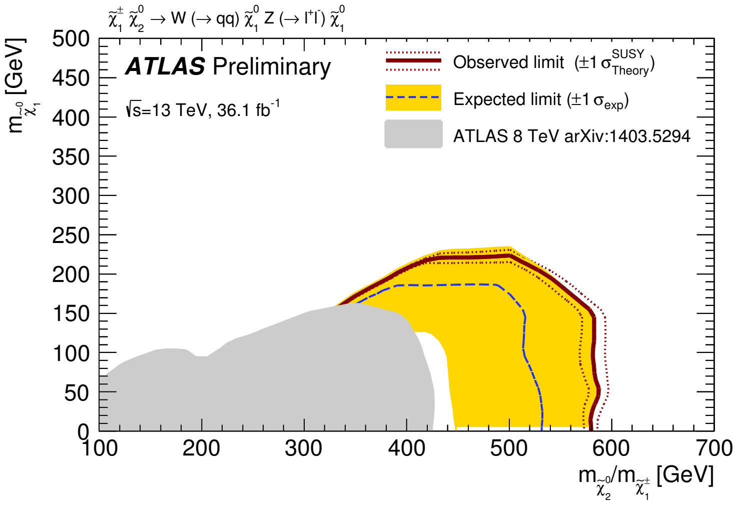

(a) 2ℓ+jets channel only

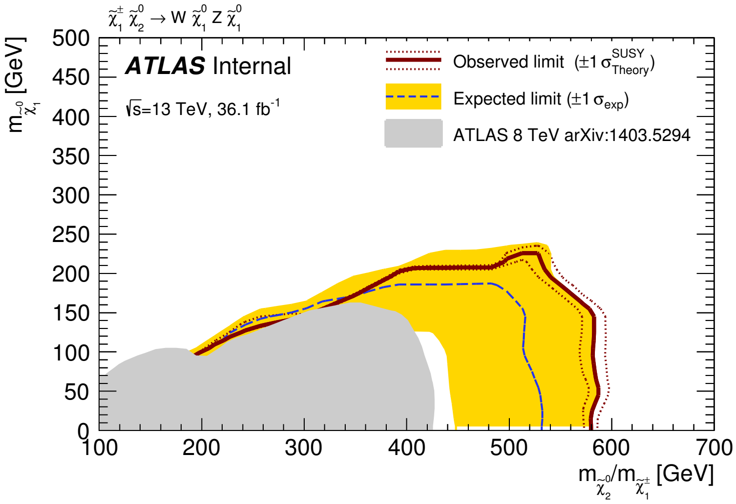

(b) 2ℓ+jets and 3ℓ channels

Figure 7.9: Expected exclusion limits on SUSY simplified models for chargino-neutralino production with decays via W/Z bosons. The observed (solid thick red line) and expected (thin dashed blue line) exclusion contours are indicated. The contours of the band around the expected limit are the $\pm 1\sigma$ results, including all uncertainties except theoretical uncertainties on the signal cross-section. The dotted lines around the observed limit illustrate the change in the observed limit as the nominal signal cross-section is scaled up and down by the theoretical uncertainty. All limits are computed at 95% CL. The observed limits obtained from ATLAS in Run I are also shown [2].

CHAPTER 8

IDEAS FOR FUTURE HIGGSINO SEARCHES IN THE DILEPTON CHANNEL

Using 2015 and 2016 ATLAS 13 TeV $p-p$ collision data, we have probed the masses of gluinos and squarks up to 2 TeV scale and the masses of electroweak gauginos up to 600 GeV scale. However, to solve the hierarchy problem, the Naturalness of SUSY requires that gluino masses should not be much larger than the TeV scale, and higgsinos should be light and nearly mass degenerated. Further probing SUSY particles in the higher mass parameter space is no longer favorable. The previous analyses that targeted large mass splittings between SUSY particles by requiring high $E_{\mathrm{T}}^{\mathrm{miss}}$ and high p_{T} objects are not sensitive to the naturalness higgsino models with compressed mass spectrum. As indicated in Figure 8.5, the compressed SUSY spectrum would lead to soft final-state kinematics, whcih will require different probing variables and new background estimation methods for the analyses to be sensitive to these compressed models. In this chapter, we will discuss the new variables and new $Z+$jets estimation method for the higgsino-like searches.

8.1 New variable for future higgsino searches

As it is indicated in Figure 8.5, the compressed SUSY spectrum produces soft objects, and therefore requiring large $E_{\mathrm{T}}^{\mathrm{miss}}$ will not be sensitive to the compressed models without requiring a strong initial-state-radiation (ISR) jet. An example of the $E_{\mathrm{T}}^{\mathrm{miss}}$ distribution of a compressed model is shown in Figure 8.2. In the figure, three SUSY models of the $\tilde{\chi}_2^0\tilde{\chi}_1^{\pm}$ production are presented, each with mass splitting $\Delta m(\tilde{\chi}_2^0/\tilde{\chi}_1^{\pm},\tilde{\chi}_1^0)$ equals to 100, 200, 500 GeV, repectively. While the SUSY models with larger mass splittings tend to have longer $E_{\mathrm{T}}^{\mathrm{miss}}$ tail than the SM backgrounds, the small mass splitting model behaves similar to the backgrounds in the region with $E_{\mathrm{T}}^{\mathrm{miss}} > 150$ GeV.

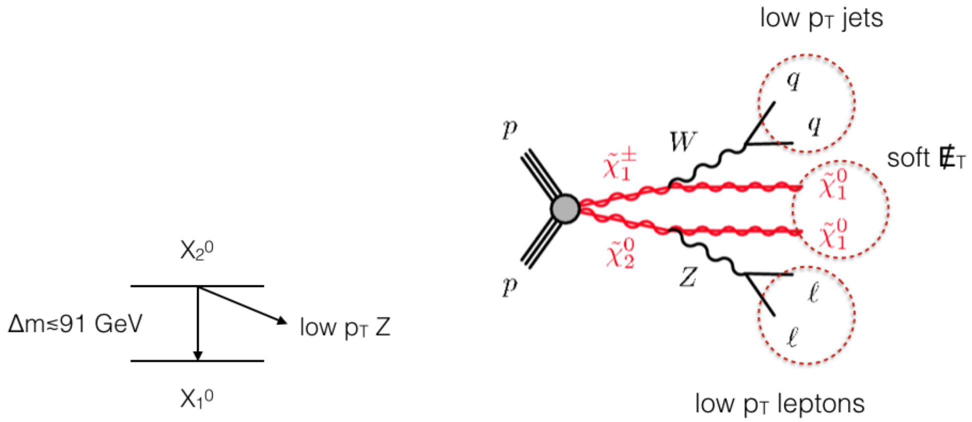

Figure 8.1: (Left) If the mass difference between $\tilde{\chi}_2^0$ and $\tilde{\chi}_1^0$ is similar to or less than the mass of the Z boson, the Z boson would be produced with low p_{T} and even off-shell. (Right) In the case of $\tilde{\chi}_2^0\tilde{\chi}_1^{\pm}$ production, the small mass splitting of $m(\tilde{\chi}_2^0/\tilde{\chi}_1^{\pm}) - m(\tilde{\chi}_1^0)$ would lead to soft final-state kinematics.

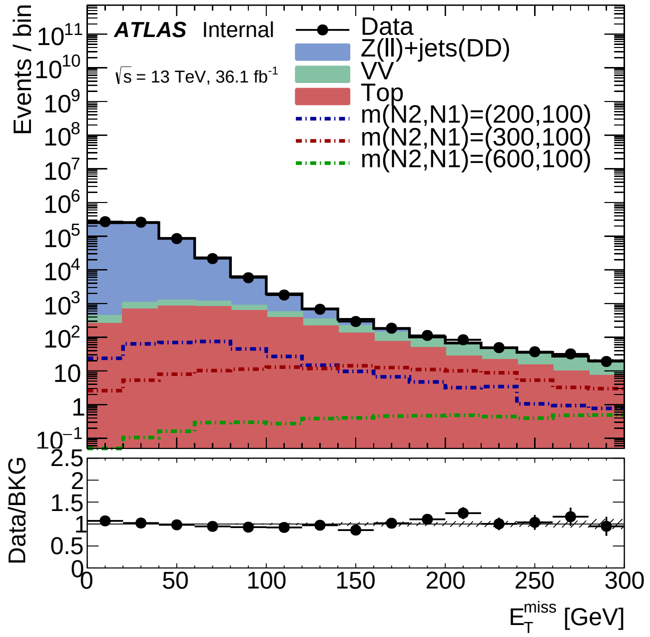

Figure 8.2: The $E_{\mathrm{T}}^{\mathrm{miss}}$ distributions of the SM model backgrounds and three $\tilde{\chi}_2^0\tilde{\chi}_1^{\pm}$ models with different mass splittings. The selection requires two SFOS leptons and at least two jets (p_{T} >20 GeV).

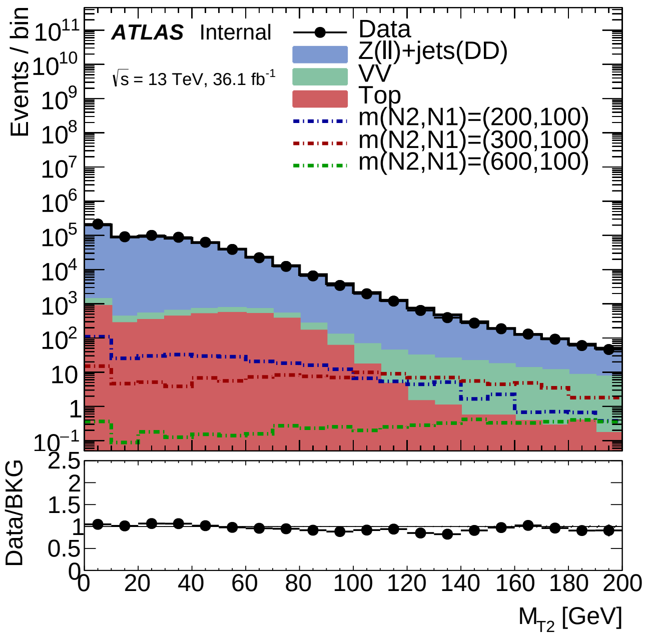

Figure 8.3: The $m_{\mathrm{T2}}(\ell_1, \ell_2, E_{\mathrm{T}}^{\mathrm{miss}})$ distributions of the SM model backgrounds and three $\tilde{\chi}_2^0\tilde{\chi}_1^\pm$ models with different mass splittings. The selection requires two SFOS leptons and at least two jets (p_{T} >20 GeV).

Thus, cutting hard on $E_{\mathrm{T}}^{\mathrm{miss}}$ and individual object kinematics is not sensitive to the ligh and highly mass degenerated higgsino models. A better idea to probe the compressed models could be combining the different object kinematics to form a new variable. m_{T2} is an example that combines the kinematics of visible objects and invisible objects, and it is a powerful variable to reject backgrounds with a pair of $W \to \ell\nu$ decays, whose definition is given by

$$m_{T2} = \min_{\vec{p}_T^{\nu(1)}+\vec{p}_T^{\nu(2)}=\vec{p}_T^{miss}} \left[\max\left(m_T^{(1)}, m_T^{(2)} \right) \right]$$

, where

$$(m_T^{(i)})^2 = (m_\ell^{(i)})^2 + (m_\nu^{(i)})^2 + 2\left(E_T^{\ell(i)} E_T^{\nu(i)} - \vec{p}_T^{\ell(i)} \cdot \vec{p}_T^{\nu(i)} \right)$$

The m_{T2} variable uses two leptons and $E_{\mathrm{T}}^{\mathrm{miss}}$ and constructs an endpoint for the $t\bar{t} \to l^+l^-$ and $WW \to ll\nu\nu$ backgrounds at m_W, as shown in Figure8.3.

Under the assumption of $R-$parity conservation, the SUSY decay topologies are similar to the topology of $WW \to ll\nu\nu$. Thus, we can use the four-vector of W, Z, and $E_{\mathrm{T}}^{\mathrm{miss}}$, to define a new m_{T2} variable as

$$m_{T2}(W, Z, E_{\mathrm{T}}^{\mathrm{miss}}) = \min_{\vec{p}_T^{\tilde{\chi}_1^0(1)} + \vec{p}_T^{\tilde{\chi}_1^0(2)} = \vec{p}_T^{miss}} \left[\max\left(m_T(W, \tilde{\chi}_1^0(1)), m_T(Z, \tilde{\chi}_1^0(2))\right)\right].$$

This new $m_{T2}(W, Z, E_{\mathrm{T}}^{\mathrm{miss}})$ variable constructs an endpoint at the mass difference between the parent and the daughter particles of each signal model.

In Figure 8.2, we have seen that the $E_{\mathrm{T}}^{\mathrm{miss}}$ distribution of the compressed signal model (Δm = 100 GeV) behaves similar to the SM background distribution in the $E_{\mathrm{T}}^{\mathrm{miss}} > 150$ GeV region. Figure 8.4 top plot shows the new variable $m_{T2}(W, Z, E_{\mathrm{T}}^{\mathrm{miss}})$ distributions in the $E_{\mathrm{T}}^{\mathrm{miss}} > 150$ GeV region, where we can see an endpoint corresponding to the mass splitting of each signal model. More interestingly, the bottom plot of Figure 8.4 shows the zoom-in of the top plot, and we can see that, while the background has a wider distribution, the signal model with $\Delta m = 100$ GeV has a distribution that is localized in the region of $m_{T2}(W, Z, E_{\mathrm{T}}^{\mathrm{miss}}) < 150$ GeV. This new variable can be very sensitive to discriminate between signals and backgrounds and between signal models of different mass splittings.

Furthermore, in the cases of searching for compressed models, there is an unique relation between the ISR jet p_{T} and the $E_{\mathrm{T}}^{\mathrm{miss}}$ as

$$\frac{E_{\mathrm{T}}^{\mathrm{miss}}}{p_{\mathrm{T}}^{\mathrm{ISR}}} \sim \frac{m(\text{daughter})}{m(\text{parent})}.$$

Together with the m_{T2} variable, which gives us the information of $m(\text{parent})-$ m(daughter), we will be able to resolve the gaugino mass spectrum in the case of discovery.

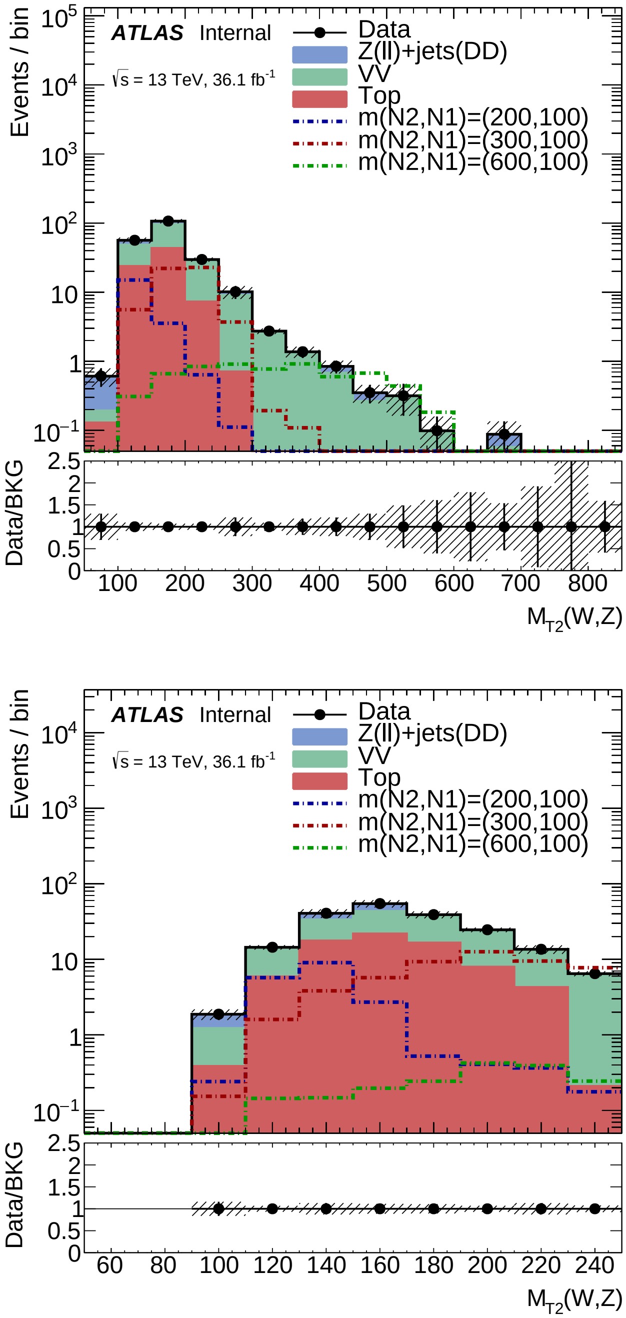

Figure 8.4: The $m_{\mathrm{T2}}(W, Z, E_{\mathrm{T}}^{\mathrm{miss}})$ distributions of the SM model backgrounds and three $\tilde{\chi}_2^0\tilde{\chi}_1^{\pm}$ models with different mass splittings. The selection requires two SFOS leptons and at least two jets (p_{T} >20 GeV) and $E_{\mathrm{T}}^{\mathrm{miss}} > 150$ GeV. The W boson is reconstructed with the two jets of the invariant mass that is closest to 80 GeV. The bottom plot has the same selection as the top plot, only the scale of the x-axis is different. Data points are blinded.

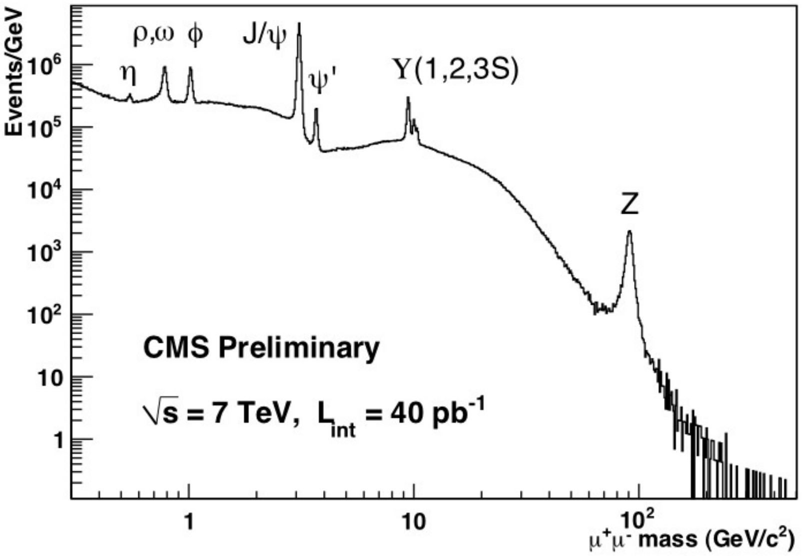

Figure 8.5: The B-physics template method uses J/ψ and Υ+jets events to model $Z+$jets events.

8.2 New $Z+$jets estimation method for future higgsino searches

In the compressed signal models with $\tilde{\chi}_2^0 \to \tilde{\chi}_1^0 + Z$ decay, the Z boson will be produced with low p_{T} or even off-shell if $m(\tilde{\chi}_2^0) - m(\tilde{\chi}_1^0) \lessapprox m_Z$. Thus, the SM low p_{T} $Z+$jets or low mass Drell-Yan processes will become important backgrounds for the higgsino-like searches. However, the photon template method isn't capable to cover the low p_{T} space due to the lack of low p_{T} photon triggers (<35 GeV).

To provide a data-driven estimation in the low p_{T} phase space, we will use J/ψ and Υ+jets events. The ATLAS J/ψ and Υ triggers select dimuon events with the invariant mass $m_{\mu\mu}$ consistent with the J/ψ and Υ masses. The B-physics triggers select events with muon p_{T} as low as 4 GeV. This allows the B-physics template method, which uses 3 GeV J/psi and $9-11$ GeV Υ to model the low p_{T} $Z+$jets events down to roughly 2 GeV.

Following the photon method procedure detailed in Chapter 5, we can modify the B-physics events and transform them into $Z+$jets events. A few closure plots are shown in Figure 8.6, 8.7, and 8.8, to validate the modeling of low p_{T} $Z+$jets events using the B-physics triggers.

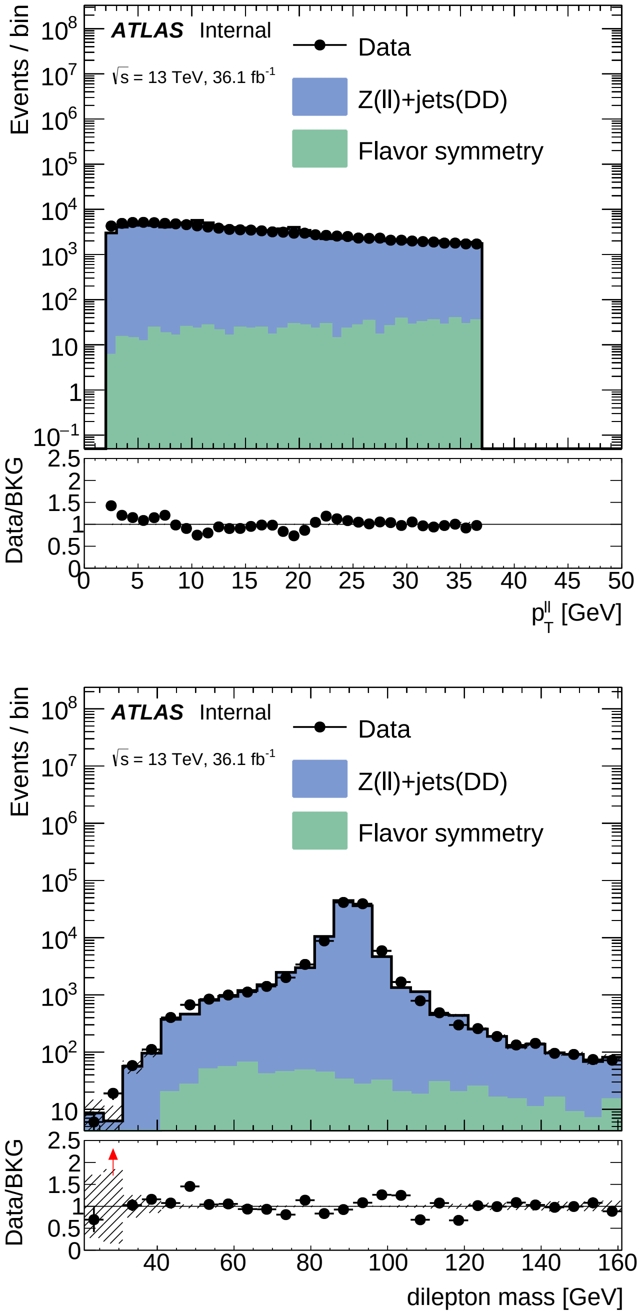

Figure 8.6: Using B-physics low p_T triggers, we are able to model low p_T $Z+$jets and low mass DY events. Z boson p_T can be modeled as low as 2 GeV. m_{ll} can be modeled as low as 12 GeV.

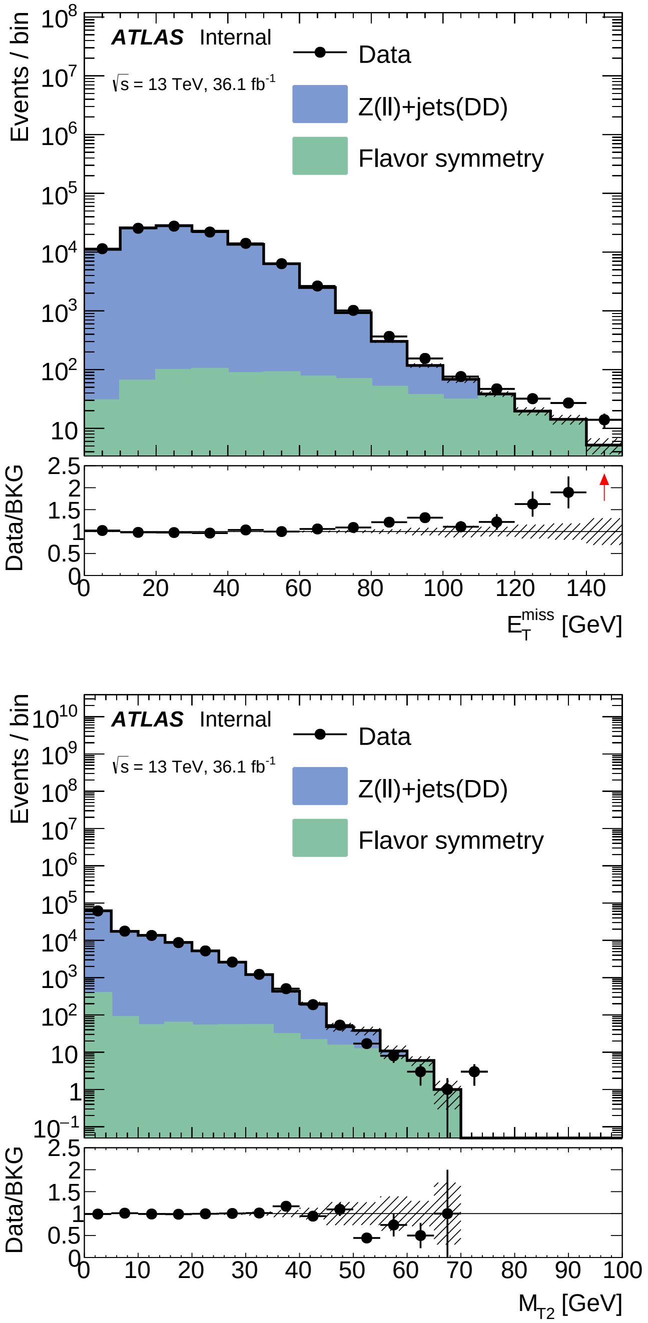

Figure 8.7: Using B-physics low p_{T} triggers, we are able to model low p_{T} $Z+$jets and low mass DY events. $E_{\mathrm{T}}^{\mathrm{miss}}$ and m_{T2} are well modeled.

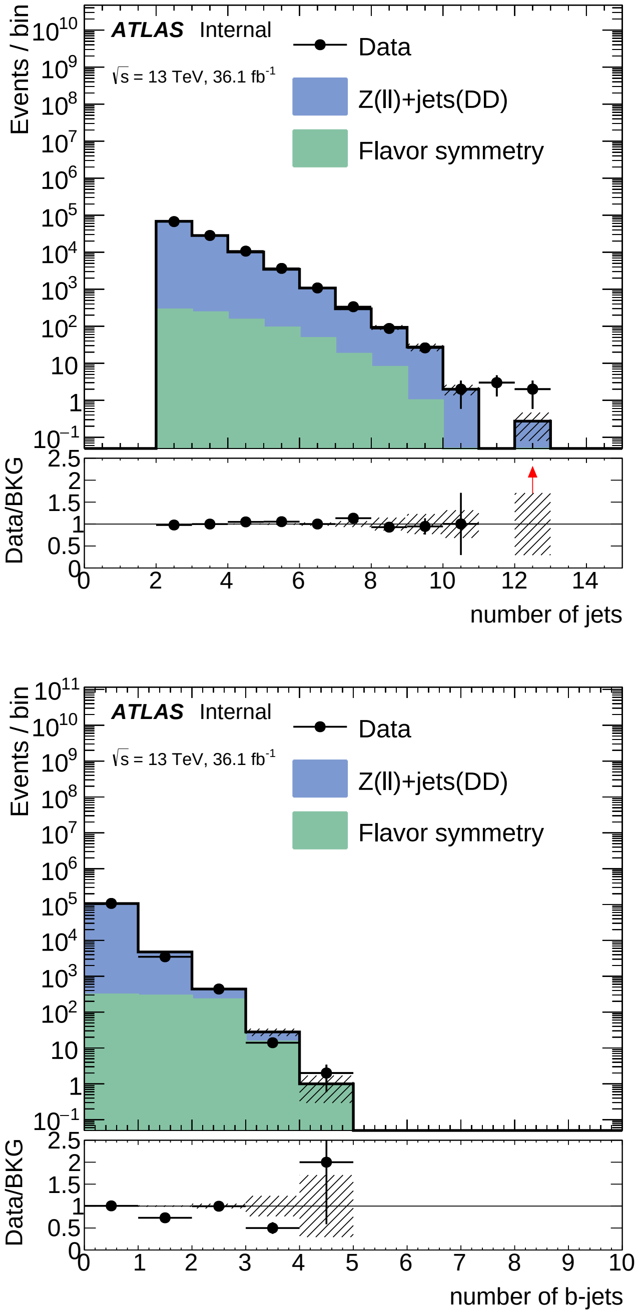

Figure 8.8: Using B-physics low p_{T} triggers, we are able to model low p_{T} $Z+$jets and low mass DY events. N_{jets} and $N_{\mathrm{b-jets}}$ are well modeled.

CHAPTER 9

CONCLUSION

The theory of Suprsymmetry provides elegant solutions to the hierarchy problem of the Higgs mass and the nature of dark matter. The Large Hadron Collider is presently the most powerful machine that offers an unique opportunity to probe the existance of Supersymmetric particles. Among them, gluinos, stops, and higgsinos, are the most essential particles to the hierarchy problem and Naturalness of Supersymmetry.

In an analysis in 2015 which using 8 TeV data to search for gluinos and squarks pair productions in the on-shell Z boson decay channel, ATLAS reported an excess with a significance of 3.0σ. On the CMS side, the analysis team did not observe excesses in the on-shell Z boson decay channel, instead they observed an excess of 2.4σ in the off-shell Z decay channel. The excesses of ATLAS and CMS Run-1 results drew a huge attention from the theory community. A careful investigation using 13 TeV data is demanded and is presented in this thesis.

Using 14.7 fb^{-1} of 13 TeV ATLAS data and keeping the ATLAS Run-1 on-shell signal region unchanged, we observed no significant excesses. We also searched the off-shell decay models and slepton models with different selectons of $E_{\text{T}}^{\text{miss}}$ and H_{T} to probe different gluino masses, and we observed no significant excesses. Based on the observation, the masses of gluinos (sqaurks) are excluded up to 1.7 TeV (980 GeV) in the simplified models of gluino-pair (squark-pair) productions.

With the null results in the strong production searches in the dilepton channel, we turned our attention to the electroweak productions of Supersymmetric particles. We searched for the neutralino ($\tilde{\chi}_2^0$) and chargino ($\tilde{\chi}_1^\pm$) pair production, with $\tilde{\chi}_2^0 \to Z\tilde{\chi}_1^0$ and $\tilde{\chi}_1^\pm \to W^\pm\tilde{\chi}_1^0$. The search result shows no excesses in the parameter space of large mass splitting $\Delta m(\tilde{\chi}_2^0/\tilde{\chi}_1^\pm, \tilde{\chi}_1^0)$. The limit on $\tilde{\chi}_2^0$ and $\tilde{\chi}_1^\pm$ masses is set as large as 580 GeV. However, the low mass $m(\tilde{\chi}_2^0) < 200$ GeV and small mass splitting $\Delta m < 100$ GeV parameter space, which favors the higgsino-like LSP, remains unprobed by this analysis.

In the future, the ATLAS SUSY program will focus on searching for Natural SUSY, which requires the higgsinos to be at electroweak scale and mass-degenerated. The compressed higgsino mass spectrum makes it difficult to probe the higgsinos, since the decay products from the higgsinos will be soft, and the distribution of which is similar to the SM backgrounds. To improve the analysis sensitivity to probe the parameter space where the higgsinos might live, a new variable is presented in this thesis, which uses the $m_{\mathrm{T}2}$ function to combine the jets, leptons, and $E_{\mathrm{T}}^{\mathrm{miss}}$, to form $m_{T2}(W, Z, E_{\mathrm{T}}^{\mathrm{miss}})$. This new variable constructs a kinematic endpoint, which corresponds to the mass differnece between the parent SUSY particles and the LSPs for the signal models. The endpoint feature will be an effective tool to discriminate signal events against the SM backgrounds. In adition, a new background method using B-physics triggers is also proposed to model the SM low p_{T} $Z + \text{jets}$ events. Low p_{T} $Z + \text{jets}$ will be an important background for the higgsino searches in the dilepton channel. The large cross-section of low p_{T} $Z + \text{jets}$ will become a heavy burden for simulation and will result in a large statistical uncertainty of the prediction. The data-driven photon method is also not able to provide estimation for low p_{T} $Z + \text{jets}$ due to the limitation of the trigger threshold. The proposed B-physics template method is able to provide estimation for $Z + \text{jets}$ with p_{T} as low as 2 GeV, and the large production rate of J/psi and Υ events will provide sufficient statistics and lower the prediction uncertianty.

REFERENCES

[1] D. E. GROOM, N. V. MOKHOV, and S. I. STRIGANOV, "MUON STOPPING POWER AND RANGE TABLES 10 MeV100 TeV," *Atomic Data and Nuclear Data Tables*, vol. 78, no. 2, pp. 183 – 356, 2001. [Online]. Available: https://www.sciencedirect.com/science/article/pii/S0092640X01908617

[2] ATLAS Collaboration, "Search for direct production of charginos, neutralinos and sleptons in final states with two leptons and missing transverse momentum in pp collisions at $\sqrt{s} = 8$ TeV with the ATLAS detector," *JHEP*, vol. 05, p. 071, 2014.

[3] M. Papucci, J. T. Ruderman, and A. Weiler, "Natural SUSY Endures," *JHEP*, vol. 09, p. 035, 2012.

[4] T. Aaltonen et al., "Inclusive Search for Squark and Gluino Production in $p\bar{p}$ Collisions at $\sqrt{s} = 1.96$-TeV," *Phys. Rev. Lett.*, vol. 102, p. 121801, 2009.

[5] V. M. Abazov et al., "Search for squarks and gluinos in events with jets and missing transverse energy using 2.1 fb^{-1} of $p\bar{p}$ collision data at $\sqrt{s}$ = 1.96- TeV," *Phys. Lett.*, vol. B660, pp. 449–457, 2008.

[6] ATLAS collaboration, "Search for the electroweak production of supersymmetric particles in $\sqrt{s}$=8 TeV pp collisions with the ATLAS detector," *Phys. Rev. D*, vol. 93, no. 5, p. 052002, 2016.

[7] CMS Collaboration, "Searches for electroweak neutralino and chargino production in channels with Higgs, Z, and W bosons in pp collisions at 8 TeV," *Phys. Rev. D*, vol. 90, no. 9, p. 092007, 2014.

[8] ATLAS Collaboration, "Performance of missing transverse momentum reconstruction for the ATLAS detector in the first proton-proton collisions at at $\sqrt{s}$= 13 TeV," ATL-PHYS-PUB-2015-027, 2015. [Online]. Available: http://cds.cern.ch/record/2037904

[9] ATLAS Collaboration, "Muon reconstruction performance of the ATLAS detector in proton–proton collision data at $\sqrt{s} = 13$ TeV," *Eur. Phys. J. C*, vol. 76, p. 292, 2016.

[10] ATLAS Collaboration, "Electron efficiency measurements with the ATLAS detector using the 2012 LHC proton–proton collision data," ATLAS-CONF-2014-032, 2014. [Online]. Available: https://cds.cern.ch/record/1706245

[11] ATLAS Collaboration, "Measurement of the photon identification efficiencies with the ATLAS detector using LHC Run-1 data," 2016.

[12] ATLAS Collaboration, "Electron and photon energy calibration with the ATLAS detector using LHC Run 1 data," *Eur. Phys. J. C*, vol. 74, p. 3071, 2014.

[13] ATLAS Collaboration, "Jet energy resolution in proton–proton collisions at $\sqrt{s} = 7$ TeV recorded in 2010 with the ATLAS detector," *Eur. Phys. J. C*, vol. 73, p. 2306, 2013.

[14] ATLAS Collaboration, "Modelling of the $t\bar{t}H$ and $t\bar{t}V$ $(V = W, Z)$ processes for $\sqrt{s} = 13$ TeV ATLAS analyses," ATL-PHYS-PUB-2016-005, 2016. [Online]. Available: http://cds.cern.ch/record/2120826

[15] M. V. Garzelli, A. Kardos, C. G. Papadopoulos, and Z. Trocsanyi, "t $\bar{t}$ W^{+-} and t $\bar{t}$ Z Hadroproduction at NLO accuracy in QCD with Parton Shower and Hadronization effects," *JHEP*, vol. 11, p. 056, 2012.

[16] J. M. Campbell and R. K. Ellis, "$t\bar{t}$ W production and decay at NLO," *JHEP*, vol. 07, p. 052, 2012.

[17] A. Lazopoulos, T. McElmurry, K. Melnikov, and F. Petriello, "Next-to-leading order QCD corrections to $t\bar{t}Z$ production at the LHC," *Phys. Lett. B*, vol. 666, p. 62, 2008.

[18] J. Alwall, R. Frederix, S. Frixione, V. Hirschi, F. Maltoni, O. Mattelaer, H. S. Shao, T. Stelzer, P. Torrielli, and M. Zaro, "The automated computation of tree-level and next-to-leading order differential cross sections, and their matching to parton shower simulations," *JHEP*, vol. 07, p. 079, 2014.

[19] ATLAS Collaboration, "Simulation of top quark production for the ATLAS experiment at $\sqrt{s} = 13$ TeV," ATL-PHYS-PUB-2016-004, 2016. [Online]. Available: http://cds.cern.ch/record/2120417

[20] M. Czakon, P. Fiedler, and A. Mitov, "Total Top-Quark Pair-Production Cross Section at Hadron Colliders Through $O(\alpha_s^4)$," *Phys. Rev. Lett.*, vol. 110, p. 252004, 2013.

[21] M. Czakon and A. Mitov, "Top++: A Program for the Calculation of the Top-Pair Cross-Section at Hadron Colliders," *Comput. Phys. Commun.*, vol. 185, p. 2930, 2014.

[22] N. Kidonakis, "Two-loop soft anomalous dimensions for single top quark associated production with a W^- or H^-," *Phys. Rev. D*, vol. 82, p. 054018, 2010.

[23] ATLAS Collaboration, "Multi-Boson Simulation for 13 TeV ATLAS Analyses," ATL-PHYS-PUB-2016-002, 2016. [Online]. Available: http://cds.cern.ch/record/2119986

[24] J. M. Campbell and R. K. Ellis, "An update on vector boson pair production at hadron colliders," *Phys. Rev. D*, vol. 60, p. 113006, 1999.

[25] J. M. Campbell, R. K. Ellis, and C. Williams, "Vector boson pair production at the LHC," *JHEP*, vol. 07, p. 018, 2011.

[26] ATLAS Collaboration, "Monte Carlo Generators for the Production of a W or Z/γ^* Boson in Association with Jets at ATLAS in Run 2," ATL-PHYS-PUB-2016-003, 2016. [Online]. Available: http://cds.cern.ch/record/2120133

[27] S. Catani, L. Cieri, G. Ferrera, D. de Florian, and M. Grazzini, "Vector boson production at hadron colliders: a fully exclusive QCD calculation at NNLO," *Phys. Rev. Lett.*, vol. 103, p. 082001, 2009.

[28] S. Catani and M. Grazzini, "An NNLO subtraction formalism in hadron collisions and its application to Higgs boson production at the LHC," *Phys. Rev. Lett.*, vol. 98, p. 222002, 2007.

[29] T. Gleisberg et al., "Event generation with sherpa 1.1," *JHEP*, vol. 02, p. 007, 2009.

[30] ATLAS Collaboration, "The ATLAS Simulation Infrastructure," *Eur. Phys. J. C*, vol. 70, pp. 823–874, 2010.

[31] S. Agostinelli et al., "GEANT4: A simulation toolkit," *Nucl. Instrum. Meth. A*, vol. 506, pp. 250–303, 2003.

[32] ATLAS Collaboration, "Search for new phenomena in events containing a same-flavour opposite-sign dilepton pair, jets, and large missing transverse momentum in $\sqrt{s} = 13$ TeV pp collisions with the ATLAS detector," *The European Physical Journal C*, vol. 77, no. 3, p. 144, 2017.

[33] ATLAS Collaboration, "Vertex Reconstruction Performance of the ATLAS Detector at $\sqrt{s} = 13$ TeV," ATL-PHYS-PUB-2015-026, 2015. [Online]. Available: http://cds.cern.ch/record/2037717

[34] ATLAS Collaboration, "Topological cell clustering in the ATLAS calorimeters and its performance in LHC Run 1," 2016.

[35] M. Cacciari, G. P. Salam, and G. Soyez, "The anti-k_t jet clustering algorithm," *JHEP*, vol. 04, p. 063, 2008.

[36] M. Cacciari and G. P. Salam, "Dispelling the N^3 myth for the Kt jet-finder," *Phys. Lett. B*, vol. 641, pp. 57–61, 2006.

[37] ATLAS Collaboration, "Jet energy measurement and its systematic uncertainty in proton–proton collisions at $\sqrt{s} = 7$ TeV with the ATLAS detector," *Eur. Phys. J. C*, vol. 75, p. 17, 2015.

[38] ATLAS Collaboration, "Jet Calibration and Systematic Uncertainties for Jets Reconstructed in the ATLAS Detector at $\sqrt{s} = 13$ TeV," ATL-PHYS-PUB-2015-015, 2015. [Online]. Available: http://cds.cern.ch/record/2037613

[39] ATLAS Collaboration, "Tagging and suppression of pileup jets with the atlas detector," ATLAS-CONF-2014-018, 2014. [Online]. Available: http://cds.cern.ch/record/1700870

[40] ATLAS Collaboration, "Characterisation and mitigation of beam-induced backgrounds observed in the ATLAS detector during the 2011 proton-proton run," *JINST*, vol. 8, p. P07004, 2013.

[41] ATLAS Collaboration, "Selection of jets produced in 13TeV proton-proton collisions with the ATLAS detector," ATLAS-CONF-2015-029, 2015. [Online]. Available: http://cds.cern.ch/record/2037702

[42] ATLAS Collaboration, "Performance of *b*-Jet Identification in the ATLAS Experiment," *JINST*, vol. 11, p. P04008, 2016.

[43] ATLAS Collaboration, "Optimisation of the ATLAS b-tagging performance for the 2016 LHC Run," ATL-PHYS-PUB-2016-012, 2016. [Online]. Available: http://cds.cern.ch/record/2160731

[44] ATLAS Collaboration, "Expected performance of missing transverse momentum reconstruction for the ATLAS detector at $\sqrt{s} = 13$ TeV," ATL-PHYS-PUB-2015-023, 2015. [Online]. Available: http://cds.cern.ch/record/2037700

[45] ATLAS Collaboration, "Search for supersymmetry in events containing a same-flavour opposite-sign dilepton pair, jets, and large missing transverse momentum in $\sqrt{s} = 8$ TeV pp collisions with the ATLAS detector," *Eur. Phys. J. C*, vol. 75, p. 318, 2015.

[46] G. Cowan, K. Cranmer, E. Gross, and O. Vitells, "Asymptotic formulae for likelihood-based tests of new physics," *Eur. Phys. J. C*, vol. 71, p. 1554, 2011.

[47] ATLAS Collaboration, "Search for squarks and gluinos in events with isolated leptons, jets and missing transverse momentum at $\sqrt{s} = 8$ TeV with the ATLAS detector," *JHEP*, vol. 04, p. 116, 2015.

[48] M. Baak, G. Besjes, D. Cte, A. Koutsman, J. Lorenz et al., "HistFitter software framework for statistical data analysis," *Eur.Phys.J.*, vol. C75, no. 4, p. 153, 2015.

[49] ATLAS Collaboration, "Search for squarks and gluinos in final states with jets and missing transverse momentum using 36 fb^{-1} of $\sqrt{s}$=13 TeV *pp* collision data with the ATLAS detector," 2017.

[50] CMS Collaboration, "Search for supersymmetry in multijet events with missing transverse momentum in proton-proton collisions at 13 TeV," *Phys. Rev. D*, vol. 96, no. 3, p. 032003, 2017.

[51] CMS Collaboration, "Search for new phenomena with the M_{T2} variable in the all-hadronic final state produced in protonproton collisions at $\sqrt{s} = 13$ TeV," *Eur. Phys. J. C*, vol. 77, no. 10, p. 710, 2017.

[52] ATLAS Collaboration, "Search for direct production of charginos and neutralinos in events with three leptons and missing transverse momentum in $\sqrt{s} = 8$ TeV *pp* collisions with the ATLAS detector," *JHEP*, vol. 04, p. 169, 2014.

[53] S. Chatrchyan et al., "Search for electroweak production of charginos and neutralinos using leptonic final states in *pp* collisions at $\sqrt{s} = 7$ TeV," *JHEP*, vol. 11, p. 147, 2012.

[54] CMS collaboration, "Searches for electroweak production of charginos, neutralinos, and sleptons decaying to leptons and W, Z, and Higgs bosons in pp collisions at 8 TeV," *Eur. Phys. J. C*, vol. 74, no. 9, p. 3036, 2014.

[55] J. Alwall, P. Schuster, and N. Toro, "Simplified Models for a First Characterization of New Physics at the LHC," *Phys. Rev. D*, vol. 79, p. 075020, 2009.

[56] ATLAS Collaboration, "Improved luminosity determination in *pp* collisions at $\sqrt{s} = 7$ TeV using the ATLAS detector at the LHC," *Eur. Phys. J. C*, vol. 73, p. 2518, 2013.

[57] ATLAS Collaboration, "Luminosity determination in *pp* collisions at $\sqrt{s} = 8$ TeV using the ATLAS detector at the LHC," *Eur. Phys. J. C*, vol. 76, p. 653, 2016.

[58] ATLAS Collaboration, "The ATLAS Simulation Infrastructure," *Eur. Phys. J. C*, vol. 70, p. 823, 2010.

[59] ATLAS Collaboration, “The simulation principle and performance of the ATLAS fast calorimeter simulation FastCaloSim,” ATL-PHYS-PUB-2010-013, 2010. [Online]. Available: https://cds.cern.ch/record/1300517

[60] ATLAS Collaboration, “Search for new phenomena in events containing a same-flavour opposite-sign dilepton pair, jets, and large missing transverse momentum in $\sqrt{s} = 13$ TeV pp collisions with the ATLAS detector,” *Eur. Phys. J. C*, vol. 77, p. 144, 2017.

[61] CMS Collaboration, “Search for physics beyond the standard model in events with a Z boson, jets, and missing transverse energy in pp collisions at $\sqrt{s} = 7$ TeV,” *Phys. Lett. B*, vol. 716, p. 260, 2012.

[62] CMS Collaboration, “Search for physics beyond the standard model in events with two leptons, jets, and missing transverse momentum in pp collisions at $\sqrt{s} = 8$ TeV,” *JHEP*, vol. 04, p. 124, 2015.